

# From Spacetime to Nucleus

Probing nuclear physics and testing general relativity

**Peter T. H. Pang**

ISBN: 978-90-393-7522-8

DOI: <https://doi.org/10.33540/1550>

Printed by: Gildeprint – [www.gildeprint.nl](http://www.gildeprint.nl)

Cover design: Alice Chan

Copyright © 2022 Tsun Ho Pang

Nik|hef



Universiteit  
Utrecht



This work originates as part of the research programme of the Foundation for Fundamental Research on Matter (FOM), and falls as of April 1, 2017 under the responsibility of Foundation for Nederlandse Wetenschappelijk Onderzoek Instituten (NWO-I), which is part of the Dutch Research Council (NWO).

# From Spacetime to Nucleus

Probing nuclear physics and testing general relativity

# Van Ruimtetijd tot Kern

Kernfysica onderzoeken en de algemene relativiteitstheorie testen  
(met een samenvatting in het Nederlands)

## Proefschrift

ter verkrijging van de graad van doctor aan de Universiteit Utrecht op gezag van de rector-magnificus, prof.dr. H.R.B.M. Kummeling, ingevolge het besluit van het college voor promoties in het openbaar te verdedigen op woensdag 14 december 2022 des middags te 14.15 uur

door

**Tsun Ho Pang**

18 May 1994

Hong Kong

First promotor:

Prof.dr. C.F.F. van den Broeck

Second promotor:

Prof.dr. R.J.M. Snellings

Assessment Committee:

Prof.dr. S.J.G. Vandoren (Chair)

Prof.dr. J.F.J. van den Brand

Prof.dr. S. Hild

Dr. S.M. Nissanke

Prof.dr. T. Peitzmann

Prof.dr. B.S. Sathyaprakash

---

*Mathematics is the language of Nature,  
statistics is the language of science.*

---



## Gravitational waves

Gravity has been static and straightforward since Newton’s law of universal gravitation in 1687 [1], in which gravity is described as an attractive force between massive objects. Such a view has been regarded as “the law of gravity” until the proposal of general relativity by Albert Einstein in 1916 [2].

General relativity describes gravity as a distortion of the spacetime continuum. In other words, the spacetime continuum is not static but dynamic. Together with this dynamic spacetime continuum, gravitational waves are also predicted. Gravitational waves are the ripples of spacetime that sketch space and time and everything in it.

## Detecting gravitational waves

Although Albert Einstein predicted gravitational waves in 1916, it was not until 1974 that its effect was observed. In 1974, with the aid of the Arecibo 305m dish, Hulse and Taylor measured the variation of the orbital period of a neutron-star–pulsar binary [3]. The variation was accurately predicted by general relativity, and it was the result of the binary radiating its energy and angular momentum via gravitational waves.

It took another 40 years for gravitational waves to be directly detected. In 2015, the Advanced Laser Interferometer Gravitational-wave Observatory (Advanced LIGO) [4] detected the first gravitational wave signal [5]. That signal, often referred to as GW150914, was emitted by a binary black hole merger of  $\sim 36$  and  $\sim 29$  solar masses at a distance of  $\sim 1.4$  billion light-years. Ever since, binary black hole mergers’ gravitational waves have been regularly detected [6–8]. Such observations allow one to access the previously invisible population of binary black holes.

In 2017, the first gravitational wave signal from a binary neutron star merger, GW170817, [9] was observed by Advanced LIGO and Advanced Virgo [10]. Moreover, it is also the first multi-messenger event that originated from a binary neutron star [11, 12], which started the era of multi-messenger astronomy.

## Gravitational-wave astronomy

The detections of gravitational waves open a whole new spectrum for physics. For instance, with the aid of gravitational waves, one can probe the properties of the binary black hole population [13, 14]. Moreover, one can put general relativity to the test in the limit of strong and dynamic field [15–18]. None of the above could be achieved before 2015.

Besides astrophysics and gravitational physics, gravitational waves also offer the opportunity for us to probe other fundamental physics, e.g., nuclear physics. Since the detection of GW170817, numerous studies have been done on extracting physics from neutron stars [19–35].

---

We are living in an amazing and exciting time. With gravitational waves, we can look into the Universe in a new way and await the surprises that nature will offer.

## Outline

This thesis is divided into four parts. Part I gives a general introduction to gravitational wave and multi-messenger data analysis. Parts II, III, and IV showcase how gravitational wave or multi-messenger observations help answer specific aspects of physics questions.

### Part I

Chapter 1 briefly introduces general relativity and how gravitational waves arise in linearized general relativity. In chapter 2, the observables of a binary black hole and neutron stars (both isolated and in binary) are presented. Chapter 3 gives an overview of Bayesian inference with the necessary computational techniques introduced in Chapter 4.

### Part II

Part II focuses on inferring the equation-of-state of supranuclear matter via observations of neutron stars on gravitational and electromagnetic channels. Chapter 5 demonstrates the feasibility of probing the presence of a phase transition in a neutron star and quantifying the transition's properties with gravitational-wave signals from binary neutron star mergers. Chapter 6 shows the robust constraint on the equation of state with nuclear theoretical calculations and the current astrophysical observations. Chapter 7 shows how to distinguish a neutron star and a low mass black hole via the information on the equation of state; in particular, GW190814 is used as an example. Chapter 8 updates the constraint with the latest X-ray observations on PSR J0740+6620. Chapter 9 further includes the results of terrestrial heavy-ion collision experiments, which lead to the state-of-the-art constraint on the equation-of-state of supranuclear matter. These chapters are based on Refs. [29, 36–39].

### Part III

Part III demonstrates the astrophysical implications of an accurate and precise constraint on the equation of state. Chapter 10 shows how to measure the magnification of a lensed binary neutron star signal with one single image; for instance, GW190425 is used as an example. This chapter is based on Ref. [40].

### Part IV

Part IV shows how to test the validity of general relativity with gravitational-wave observations. Chapter 11 introduces the methods for probing the polarization content of gravitational waves; GW170817 is used as an example. Chapter 12 demonstrates a technique for distinguishing binary black holes and other exotic compact objects; all the binary black holes in GWTC-1 have been tested. These chapters are based on Refs. [41, 42].



---

## External contribution

The work described in this thesis partially builds on contributions from others. Dr. Ingo Tews provided chiral effective field theory calculations and the corresponding equation-of-state extensions to higher and lower densities. In particular, the TWIN and KINK equations-of-state in Chapter 5 and the sets of equations-of-state used for analysis in Chapters 6, 7, 8, and 9 were made available by him. Sabrina Huth and Dr. Ingo Tews have handled the interpretation of the heavy-ion collision experimental results in Chapter 9, including the theoretical calculations. In Chapter 10, the method of estimating the magnification factor using the galactic double neutron stars' masses was derived by Dr. Otto Hannuksela and Giulia Pagano.



## ACKNOWLEDGEMENT

It has been four years since I started my Ph.D. in September 2018. That is not a long journey but a life-changing one. I have met many people during this time, and the adventure is not complete without you. There are some of you that I would like to thank explicitly.

The first one has to be my thesis supervisor, Chris. After all, you are the one who hired me, which is essential for this whole thing. Not to mention you have given me so much freedom, which allowed me to explore and work on so many different projects. Moreover, you were always there to support me, like during the (*cough*) O3b TGR paper (*cough*). I am genuinely grateful to be your student.

Tim, I still remember the day I turned my chair around and asked if you had anything for me to work on. Since that moment, I have had the chance to work with you and all the other amazing people and publish so many papers. I hope that our friendship will not end even though I am leaving academia.

Ingo and Michael, I have had such a fantastic time working with you. You guys are intelligent, hardworking, and fun, making research way more interesting than it should have been. I loved our meetings being so efficient while we still talked about all these stupid things.

Tjonnje, you and your family have helped me so much when I first arrived in the Netherlands. I still can't imagine how hard my settling in the Netherlands would have been without your help.

Of course, everyone in the Nikhef / Utrecht office, Anna, Anuradha, Chinmay, Haris, Harsh, Justin, Ka Wa, Otto, Pawan, Soumen, Yoshinta, it is a pity that we didn't have much face-to-face interaction due to Covid. But still, those table-soccer games, Nikhef party night, lunches at Utrecht pantry, were fun. Anna, please don't make that "who makes plots with C++ these days" mistake again.

Although the Netherlands is more than 9000 km away from Hong Kong, I can still feel the support from my family, especially when I am stressed and burnt out. My mom, dad and brother have made me feel like staying in a heaven whenever I travelled back to Hong Kong.

Finally, I want to show my gratitude to my girlfriend, Ben. I promised to make Amsterdam our second home in my master thesis. It turns out I can't keep it because we have moved to Purmerend. Because of you, our place at Purmerend has become our home. I wouldn't have been able to achieve what I have accomplished without you. That's all because of your love.



Peter Tsun Ho Pang  
Utrecht, 2022



<b>I</b>	<b>Introduction to gravitational-wave and multi-messenger data analysis</b>	<b>1</b>
<b>1</b>	<b>Gravitational waves in general relativity: Propagation, generation, and detection</b>	<b>3</b>
1.1	A brief overview of general relativity . . . . .	3
1.1.1	Conventions and notations . . . . .	3
1.1.2	General relativity . . . . .	4
1.2	Linearized Einstein field equation . . . . .	6
1.2.1	Linear expansion around flat spacetime . . . . .	6
1.2.2	Linearised Einstein field equation . . . . .	6
1.2.3	Gravitational waves in the vacuum . . . . .	7
1.2.4	Interaction between gravitational waves and matter . . . . .	8
1.2.5	Generation of gravitational waves . . . . .	11
1.3	Detecting gravitational waves . . . . .	15
1.3.1	Detector response and beam pattern function . . . . .	16
1.3.2	Noise characterization . . . . .	16
1.3.3	Matched filtering . . . . .	19
<b>2</b>	<b>Black holes and neutron stars</b>	<b>21</b>
2.1	Binary black holes . . . . .	21
2.1.1	Beyond the Newtonian approximation . . . . .	21
2.1.2	Post-Newtonian waveform models . . . . .	23
2.1.3	Phenomenological IMR waveform models . . . . .	26
2.2	Neutron stars . . . . .	29
2.2.1	Isolated neutron star . . . . .	29
2.2.2	Chiral effective field theory and the neutron-star equation of state . . . . .	30
2.2.3	Binary neutron star inspirals . . . . .	32
<b>3</b>	<b>Bayesian statistics</b>	<b>37</b>
3.1	Inductive logic and probability theory . . . . .	37
3.1.1	Boolean algebra . . . . .	37
3.1.2	Bayesian probability theory . . . . .	37
3.2	Parameter estimation . . . . .	39
3.3	Hypothesis testing . . . . .	40
3.3.1	Bayes' factor and odds ratio . . . . .	40
3.3.2	Background-foreground approach . . . . .	42
<b>4</b>	<b>Computational methods</b>	<b>45</b>
4.1	Monte Carlo methods . . . . .	45
4.1.1	Markov chain Monte Carlo . . . . .	45

4.1.2	Nested sampling . . . . .	47
<b>II</b>	<b>Constraining the equation-of-state of supranuclear matter</b>	<b>53</b>
<b>5</b>	<b>Parameter estimation for strong phase transitions in supranuclear matter using gravitational-wave astronomy</b>	<b>55</b>
5.1	Introduction . . . . .	55
5.2	Phase transitions and their imprint on the GW signal . . . . .	57
5.2.1	The equation of state of NS matter . . . . .	57
5.2.2	Imprint of phase transitions on the GW signal . . . . .	59
5.2.3	EOS parameterization for phase transitions . . . . .	60
5.3	Mock Data Simulation . . . . .	62
5.3.1	Bayesian Analysis . . . . .	62
5.3.2	Waveform approximants . . . . .	63
5.3.3	Injection setup . . . . .	63
5.3.4	Implementation . . . . .	64
5.4	Locating phase transitions from GW signals . . . . .	65
5.4.1	Description of the method . . . . .	65
5.4.2	Method Validation . . . . .	65
5.4.3	Limitations of our analysis . . . . .	68
5.5	Analysis of GW170817 and GW190425 . . . . .	70
5.6	Conclusion . . . . .	71
<b>6</b>	<b>Multi-messenger constraints on the neutron-star equation of state and the Hubble constant</b>	<b>75</b>
6.1	Introduction . . . . .	75
6.2	Methods . . . . .	76
6.2.1	The use of chiral effective field theory and the neutron-star equation of state . . . . .	76
6.2.2	Incorporation of the maximum mass neutron-star constraints . . . . .	76
6.2.3	Coherent incorporation of NICER data . . . . .	77
6.2.4	Gravitational-wave Analysis . . . . .	78
6.2.5	AT2017gfo . . . . .	78
6.2.6	Prior combination for distance measurement . . . . .	85
6.2.7	Estimation of the Hubble constant $H_0$ . . . . .	85
6.3	Results . . . . .	86
6.4	Investigation of possible systematics . . . . .	93
6.4.1	Gravitational-wave Analysis . . . . .	93
6.4.2	Modelling of AT2017gfo . . . . .	94
6.4.3	Ordering of the analysis steps . . . . .	96
6.4.4	Propagation of systematic uncertainties . . . . .	97
<b>7</b>	<b>On the nature of GW190814 and its impact on the understanding of supranuclear matter</b>	<b>99</b>
7.1	Introduction . . . . .	99
7.2	Analysis . . . . .	101

7.3	Results . . . . .	103
7.3.1	The nature of GW190814 . . . . .	103
7.3.2	EOS constraints from GW190814 . . . . .	105
7.4	Summary . . . . .	106
<b>8</b>	<b>Nuclear-Physics Multi-Messenger Astrophysics Constraints on the Neutron-Star Equation of State: Adding NICER’s PSR J0740+6620 Measurement</b>	<b>109</b>
8.1	Introduction . . . . .	109
8.2	Previous works . . . . .	111
8.3	Methodology . . . . .	112
8.4	Results . . . . .	114
8.4.1	Neutron-star equation of state . . . . .	115
8.4.2	Neutron-star maximum mass and GW190814 . . . . .	116
8.4.3	Existence of a phase transition . . . . .	117
8.5	Impact of EOS prior . . . . .	118
8.6	Summary . . . . .	119
<b>9</b>	<b>Constraining Neutron-Star Matter with Microscopic and Macroscopic Collisions</b>	<b>121</b>
9.1	Introduction . . . . .	121
9.2	Methods . . . . .	122
9.2.1	Nuclear equations of state from chiral effective field theory . . . . .	122
9.2.2	Multi-messenger analysis of astrophysical data . . . . .	124
9.2.3	Constraining the symmetric nuclear matter EOS at high density with heavy-ion collisions . . . . .	126
9.2.4	The ASY-EOS experiment to measure the symmetry energy . . . . .	128
9.2.5	Implementation of nuclear equation-of-state constraints from heavy-ion collisions . . . . .	128
9.2.6	Combination of the astronomical and heavy-ion collision constraints . . . . .	132
9.3	Results . . . . .	133
9.3.1	Nuclear theory input . . . . .	133
9.3.2	Multi-messenger astrophysics information . . . . .	133
9.3.3	Data from HIC experiments . . . . .	134
9.3.4	Combining information from micro- and macroscopic collisions . . . . .	135
9.4	Conclusion . . . . .	139
<b>III</b>	<b>Astrophysical implication of an accurate constraint on the equation-of-state</b>	<b>147</b>
<b>10</b>	<b>Lensed or not lensed: Determining lensing magnifications for binary neutron star mergers from a single detection</b>	<b>149</b>
10.1	Introduction . . . . .	149
10.2	Binary neutron star lensing . . . . .	151
10.3	Breaking the lensing degeneracy . . . . .	152
10.4	Discriminating between high-mass binaries and lensed binaries . . . . .	156
10.5	Beyond mock data: Discussion . . . . .	158

10.6	Conclusions . . . . .	162
10.7	Materials and methods . . . . .	162
10.7.1	Lensing analysis methods . . . . .	162
10.7.2	Results with magnification $\mu$ of 100 . . . . .	166
<b>IV</b>	<b>Testing the validity of general relativity and the nature of compact objects</b>	<b>169</b>
<b>11</b>	<b>Generic searches for alternative gravitational wave polarizations with networks of interferometric detectors</b>	<b>171</b>
11.1	Introduction . . . . .	171
11.2	Gravitational wave polarizations . . . . .	172
11.3	Methodology . . . . .	173
11.3.1	Null energy . . . . .	173
11.3.2	Null energy method and sky map method . . . . .	176
11.4	Simulations, and analyses of GW170817 . . . . .	177
11.5	Summary and conclusions . . . . .	179
<b>12</b>	<b>Probing resonant excitations in exotic compact objects via gravitational waves</b>	<b>181</b>
12.1	Introduction . . . . .	181
12.2	Methodology . . . . .	182
12.2.1	Imprint of resonant excitations on the gravitational wave phase . . . . .	182
12.2.2	Bayesian analysis . . . . .	183
12.3	Simulations . . . . .	185
12.3.1	Measurability of resonance effects in the O1 and O2 observing runs . . . . .	185
12.3.2	A note on parameter estimation . . . . .	187
12.4	Searching for resonances in GWTC-1 events . . . . .	188
12.5	Summary and future directions . . . . .	189
<b>13</b>	<b>Conclusions</b>	<b>193</b>
	<b>Public summary</b>	<b>195</b>
	<b>Openbare samenvatting</b>	<b>199</b>
	<b>Curriculum vitae</b>	<b>203</b>
	<b>List of acronyms</b>	<b>205</b>
	<b>Bibliography</b>	<b>209</b>



# LIST OF FIGURES

1.1	Effect on the ring of test masses due to gravitational waves . . . . .	11
1.2	Beam pattern function for a $90^\circ$ interferometer . . . . .	17
1.3	O3b one-sided power spectral density . . . . .	18
2.1	Showcase of multiple proposed equation-of-state models and observational constraints based on pulsars. . . . .	31
2.2	Showcase of multiple proposed equation-of-state models on the $m$ - $\Lambda$ plane. . . . .	33
3.1	A schematic example of the background distribution . . . . .	43
3.2	A schematic example of the foreground distribution . . . . .	44
4.1	A schematic example of the nested sampling algorithm with a single live point . . . . .	50
4.2	The mean and standard deviation of the shrinkage ratio as a function of the number of live points . . . . .	51
5.1	Density-pressure relations and mass–tidal-deformability relations for ALF2, TWIN and KINK . . . . .	57
5.2	The GW waveforms for a non-spinning BNS with ALF2, TWIN and KINK . . . . .	61
5.3	Sketch of the Maxwell parameterization . . . . .	62
5.4	The distribution of $\ln \mathcal{B}_{\text{NPT}}^{\text{PT}}$ for injections with ALF2, TWIN and KINK . . . . .	66
5.5	The distributions of $\ln \mathcal{B}_{\text{NPT}}^{\text{PT (cat)}}$ for injections with the ALF2, TWIN and KINK . . . . .	67
5.6	Evolution of the credible interval of $\log_{10} p_{\text{tr}}$ and $\log_{10} \Delta\rho$ . . . . .	68
5.7	The joint posteriors for $\log_{10} p_{\text{tr}}$ and $\log_{10} \Delta\rho$ . . . . .	69
5.8	The distribution of the central pressure $p_c$ for the 25 events included . . . . .	71
5.9	The joint posterior of $n_{\text{tr}}$ and $\Delta n$ . . . . .	72
5.10	Joint posterior of $\log_{10} p_{\text{tr}}$ , $\log_{10} \Delta\rho$ , $m_1$ , $m_2$ and $\tilde{\Lambda}$ for GW170817 . . . . .	73
5.11	Joint posterior of $\log_{10} p_{\text{tr}}$ , $\log_{10} \Delta\rho$ , $m_1$ , $m_2$ and $\tilde{\Lambda}$ for GW190425 . . . . .	74
6.1	Combined likelihood of the maximum mass . . . . .	77
6.2	Comparison of different NICER analysis models . . . . .	79
6.3	Geometry employed in the kilonova description of Model I . . . . .	80
6.4	Comparison of observed light curves of AT2017gfo with Model I . . . . .	81
6.5	Estimated ejecta properties for Model I . . . . .	82
6.6	Estimated BNS properties for Model I . . . . .	83
6.7	Disk mass predictions for various total masses and mass ratios . . . . .	84
6.8	Constraints on the Hubble constant . . . . .	87
6.9	Multi-step procedure to constrain the neutron-star EOS . . . . .	91
6.10	Distance-inclination constraints and Hubble constant measurement . . . . .	92

6.11	Marginalized 1D and 2D posterior probability distributions of GW170817's parameters . . . . .	94
6.12	Marginalized 1D and 2D posterior probability distributions of GW190425's parameters . . . . .	95
6.13	Distance-inclination measurements for kilonova models . . . . .	96
6.14	Radius constraints under interchange of the individual analysis steps . . .	97
6.15	Radius constraints for different gravitational-waveform models . . . . .	97
7.1	Comparison between posterior on the maximum mass of NSs and GW190814; and the resulting maximum mass's posterior for different scenarios . . . . .	101
7.2	Joint posterior of $m_2$ - $\chi_2$ for GW190814 . . . . .	102
7.3	Mass-radius relations for NSBH <sub>1</sub> , NSBH <sub>2</sub> , BBH <sub>1</sub> and BBH <sub>2</sub> . . . . .	104
8.1	Posterior for the pressure as a function of number density with NMMA and PSR J0740+6220's NICER observation . . . . .	110
8.2	Posterior for PSR J0740+6620's radius with NMMA and PSR J0740+6220's NICER observation . . . . .	111
8.3	Posterior for the press as a function of number density and mass-radius with NMMA and PSR J0740+6220's NICER observation by Miller et. al 2021 and Riley et. al 2021 . . . . .	114
8.4	Same as Fig. 8.3 but using the NICER+XMM data. . . . .	115
8.5	Posterior for $M_{\max}$ with and without the PSR J0740+6620's observations .	116
9.1	Constraints on the EOS of neutron-star matter . . . . .	122
9.2	Constraints on the mass and radius of neutron stars . . . . .	123
9.3	Constraints on $\gamma_{\text{asy}}$ versus symmetry energy $\mathbf{S}_0$ from two Quantum Molecular Dynamics models . . . . .	130
9.4	Comparison of the pressure of symmetric nuclear matter for experiment and theory . . . . .	131
9.5	Comparison between different sensitivity curves . . . . .	139
9.6	Constraint on the neutron-star mass and radius with successive astrophysics information . . . . .	144
9.7	Constraints for pure neutron matter . . . . .	145
10.1	Illustration of amplitude magnification . . . . .	150
10.2	Effect of lensing on inferred parameters . . . . .	153
10.3	Effect of lensing on the estimated tidal deformability . . . . .	155
10.4	Illustration of the magnification posterior computation for GW190425 . . .	157
10.5	Posterior distribution of magnifications inferred with posteriors of component masses and luminosity distance and that with posteriors of component masses and tidal deformability for given EOSs with various injections with $\mu = 1000$ . . . . .	159
10.6	Posterior distribution of magnifications inferred with the galactic double neutron star population assumed and posterior distribution of magnifications inferred with different EOSs assumed . . . . .	161

10.7 Posterior distribution of magnifications inferred with posteriors of component masses and luminosity distance and that with posteriors of component masses and tidal deformability for given EOSs with various injections with  $\mu = 100$  . . . . . 167

11.1 Effects of gravitational waves with non-general-relativity polarization modes on a ring of test mass . . . . . 174

11.2 Evolution of combined p-value for null energy method and skymap methos 177

11.3 Null stream inferred GW170817's sky map . . . . . 178

12.1 Distribution of log Bayes factors for the ECO hypothesis over the BBH hypothesis for BBH injections and ECO injections . . . . . 185

12.2 Efficiencies with respect to a  $5\sigma$  threshold as function of resonances' phase shift . . . . . 186

12.3 Posterior for  $f_{01}$ ,  $f_{02}$ ,  $\Delta\phi_{01}$ , and  $\Delta\phi_{02}$  when no resonances are present . . . 187

12.4 Posterior for  $f_{01}$ ,  $f_{02}$ ,  $\Delta\phi_{01}$ , and  $\Delta\phi_{02}$  with both ECOs resonance . . . . . 188

12.5 Posterior for  $f_{01}$ ,  $f_{02}$ ,  $\Delta\phi_{01}$ , and  $\Delta\phi_{02}$  with one resonance . . . . . 189

12.6 log Bayes factors for the presumed binary black hole events of GWTC-1 with respect to the BBH background distributions . . . . . 190

12.7 Posterior density functions for the resonance frequencies  $f_{02}$  and  $f_{01}$  for the GWTC-1 events . . . . . 191

12.8 Posterior density functions for the resonance frequencies  $\Delta\phi_{02}$  and  $\Delta\phi_{01}$  for the GWTC-1 events . . . . . 191

## LIST OF FIGURES

---

# LIST OF TABLES

2.1	Summary of time-domain Taylor approximants. . . . .	24
2.2	Summary of the IMRPhenomD phasing ansatz. . . . .	27
2.3	Summary of the IMRPhenomD amplitude ansatz. . . . .	27
2.4	Summary of binary Love relation’s parameters . . . . .	35
3.1	Summary of operations in Boolean algebra. . . . .	37
3.2	Summary of representations of operations in Boolean algebra in probability theory. . . . .	38
5.1	The ln Bayes factor $\ln \mathcal{B}_{\text{NPT}}^{\text{PT}}$ and the KL divergence (in nats) estimated with the two BNS events. . . . .	70
6.1	Summary of the heavy-pulsar mass measurements . . . . .	77
6.2	Comparison with selected radius constraints from multi-messenger observations. . . . .	88
6.3	Summary of the parameters of GW170817 inferred with different waveform models . . . . .	93
6.4	Summary of the parameters of GW190425 with and without inclusion of GW170817/AT2017gfo . . . . .	96
7.1	Summary of the probabilities and the resulting posteriors on the NS maximum mass and radius of a typical NS for the four scenarios . . . . .	106
8.1	Summary of the resulting posteriors with PSR J0740+6620’s NICER observation included . . . . .	118
8.2	Summary of the resulting posteriors without an uniform prior on $R_{1.4}$ imposed . . . . .	119
9.1	Final constraints on the pressure and the radius of neutron stars . . . . .	124
9.2	Impact of the EOS prior: Maximum density of chiral EFT and of prior distribution of $R_{1.4}$ . . . . .	125
9.3	Sensitivity on uncertainties of nuclear matter properties . . . . .	132
9.4	Impact of EOS extension scheme . . . . .	135
9.5	Impact of the sensitivity curve for the ASY-EOS experiment . . . . .	136
9.6	Impact of the parameterisation for symmetric nuclear matter . . . . .	137
9.7	Impact of the proton fraction in $\beta$ -equilibrium . . . . .	138
9.8	Impact of the radius constraints for J0740+6220 . . . . .	138
9.9	Impact of excluding Danielewicz et al. [313] . . . . .	140
9.10	Kullback–Leibler divergence with different observation input . . . . .	142
9.11	Future prospects for the ASY-EOS experiment . . . . .	143
10.1	Summary of the source-frame mass and the tidal deformability of the simulated binary neutron star mergers . . . . .	156

LIST OF TABLES

---

10.2 The log Bayes factor for the lensed hypothesis against unlensed hypothesis of GW190425 with various EOSs given . . . . . 160

10.3 Summary of the source-frame mass and the tidal deformability of the simulated binary neutron star mergers. Each cell shows the source-frame mass, tidal deformability pair  $(m, \Lambda)$  of the injection under different EOS and lensing scenario. . . . . 167

12.1 Values of log Bayes factors for the GWTC-1 events, together with false alarm probabilities . . . . . 184

---

---

PART I

---

INTRODUCTION TO  
GRAVITATIONAL-WAVE AND  
MULTI-MESSENGER DATA ANALYSIS





# CHAPTER 1

## GRAVITATIONAL WAVES IN GENERAL RELATIVITY: PROPAGATION, GENERATION, AND DETECTION

This chapter gives a brief overview of general relativity and gravitational wave. We will first define the notations and conventions to be used, followed by an overview of general relativity. That includes the propagation of gravitational waves and how they interact with matter. After that, we will demonstrate how gravitational waves are generated, subsequently how to detect gravitational waves.

### 1.1 A brief overview of general relativity

#### 1.1.1 Conventions and notations

Unless stated otherwise, geometric units are employed. Therefore, the speed of light  $c$  and the universal gravitational constant  $G$  are set to unity;

$$c = G = 1. \quad (1.1)$$

Moreover, unless explicitly stated, the Einstein summation convention is used. For example,

$$a^\mu b_\mu = \sum_\mu a^\mu b_\mu, \quad (1.2)$$

and similarly for any dummy index  $\mu$  appearing as both an upper and lower index.

Space-time indices are denoted by the lower-case Greek letters,  $\mu, \nu, \dots = 0, 1, 2, 3$ . The space indices are denoted by the lower-case Roman letters,  $i, j, \dots = 1, 2, 3$ . For example, the spacetime coordinates of an event  $x^\alpha$  are given by

$$x^\alpha = (t, x^i), \quad (1.3)$$

where  $t$  is the coordinate time and  $x^i$  are the spacial coordinates.

The infinitesimal line element  $ds$  is given by

$$ds^2 = g_{\mu\nu} dx^\mu dx^\nu, \quad (1.4)$$

where  $g_{\mu\nu}$  is the metric tensor. Such a line element is invariant under all possible coordinate transformations

$$x^\mu \rightarrow x'^\mu. \quad (1.5)$$

Under coordinate transformation, the transformed metric tensor is given by

$$g'_{\mu\nu} = \frac{\partial x^\rho}{\partial x'^\mu} \frac{\partial x^\sigma}{\partial x'^\nu} g_{\rho\sigma}, \quad (1.6)$$

and the transformed coordinate differential is given by

$$dx'^{\mu} = \frac{\partial x'^{\mu}}{\partial x^{\rho}} dx^{\rho}. \quad (1.7)$$

The corresponding modifications of the metric tensor and the coordinate differentials cancel each other out and keep the line element unchanged.

A  $(-, +, +, +)$  sign convention for the metric tensor is taken. For instance, the Minkowski metric tensor  $\eta_{\mu\nu}$  under the Cartesian coordinate is given by

$$\eta_{\mu\nu} = \text{diag}(-1, 1, 1, 1). \quad (1.8)$$

The Christoffel symbols  $\Gamma_{\mu\nu}^{\rho}$  are given by

$$\Gamma_{\mu\nu}^{\rho} = \frac{1}{2} g^{\rho\lambda} (\partial_{\mu} g_{\nu\lambda} + \partial_{\nu} g_{\mu\lambda} - \partial_{\lambda} g_{\mu\nu}), \quad (1.9)$$

where  $g^{\mu\nu}$  is the inverse of  $g_{\mu\nu}$ . Therefore,  $g^{\mu\alpha} g_{\alpha\nu} = \delta_{\nu}^{\mu}$ , where  $\delta_{\nu}^{\mu}$  is the Kronecker delta.

The covariant derivative is denoted by  $\nabla_{\mu}$ , which is given by

$$\begin{aligned} \nabla_{\mu} V^{\nu} &= \frac{\partial V^{\nu}}{\partial x^{\mu}} + \Gamma_{\mu\rho}^{\nu} V^{\rho} \\ &\equiv \partial_{\mu} V^{\nu} + \Gamma_{\mu\rho}^{\nu} V^{\rho}, \end{aligned} \quad (1.10)$$

where  $V^{\nu}$  is an arbitrary vector field.

The Riemann curvature tensor  $R_{\rho\mu\nu}^{\alpha}$  can be defined as the commutator between the covariant derivatives for an arbitrary covector field  $V_{\mu} = g_{\mu\nu} V^{\nu}$

$$R_{\rho\mu\nu}^{\lambda} V_{\lambda} = [\nabla_{\mu}, \nabla_{\nu}] V_{\rho} \equiv \nabla_{\mu} \nabla_{\nu} V_{\rho} - \nabla_{\nu} \nabla_{\mu} V_{\rho}. \quad (1.11)$$

The Riemann tensor can be expressed in terms of Christoffel symbols as

$$R_{\rho\mu\nu}^{\lambda} = \partial_{\mu} \Gamma_{\nu\rho}^{\lambda} - \partial_{\nu} \Gamma_{\mu\rho}^{\lambda} + \Gamma_{\mu\sigma}^{\lambda} \Gamma_{\nu\rho}^{\sigma} - \Gamma_{\nu\sigma}^{\lambda} \Gamma_{\mu\rho}^{\sigma}. \quad (1.12)$$

The Ricci tensor  $R_{\mu\nu}$  is given by

$$R_{\mu\nu} = R_{\mu\alpha\nu}^{\alpha}, \quad (1.13)$$

and the Ricci scalar is given by

$$R = g^{\mu\nu} R_{\mu\nu}. \quad (1.14)$$

### 1.1.2 General relativity

The general theory of relativity, commonly known as general relativity, was proposed by Albert Einstein in 1915. The theory can be summarised in the following way;

**“Space-time tells matter how to move; matter tells spacetime how to curve.”**  
— John Archibald Wheeler

The Einstein field equations quantify such a relation. They are given by

$$G_{\mu\nu} \equiv R_{\mu\nu} - \frac{1}{2}g_{\mu\nu}R = 8\pi T_{\mu\nu}, \quad (1.15)$$

where  $G_{\mu\nu}$  is the Einstein tensor, which encodes the curvature of spacetime, and  $T_{\mu\nu}$  is the stress-energy tensor, which describes the density of energy and momentum of matter. One can show that

$$\nabla_{\mu}T^{\mu\nu} = 0, \quad (1.16)$$

which is the local conservation of energy and momentum.

In general relativity, a free-falling particle (*i.e.*, no non-gravitational forces exerted on it) moves along a geodesic, which is a generalized notion of a “straight line” on curved spacetime. In particular, a geodesic is the “shortest path” between two points in spacetime. Using this principle, one can write an action for such a particle  $S$  as

$$S = \int ds = \int \sqrt{-g_{\mu\nu} \frac{dx^{\mu}}{d\sigma} \frac{dx^{\nu}}{d\sigma}} d\sigma. \quad (1.17)$$

By using the Euler-Lagrange equations (*i.e.*, the least action principle), the geodesic equation for a massive particle can be obtained as follow;

$$\frac{d^2x^{\mu}}{d\tau^2} + \Gamma_{\alpha\beta}^{\mu} \frac{dx^{\alpha}}{d\tau} \frac{dx^{\beta}}{d\tau} = 0, \quad (1.18)$$

where  $\tau$  is the proper time,  $d\tau^2 = -ds^2$ . For a null geodesic, the path taken by a massless particle (e.g. a photon), the geodesic equation is given by

$$\frac{d^2x^{\mu}}{d\lambda^2} + \Gamma_{\alpha\beta}^{\mu} \frac{dx^{\alpha}}{d\lambda} \frac{dx^{\beta}}{d\lambda} = 0, \quad (1.19)$$

where  $\lambda$  is an affine parameter on the geodesic.

General relativity incorporates the strong equivalence principle, therefore,

**“The outcome of any local experiment in a freely falling laboratory is independent of the laboratory’s velocity and location in spacetime,”**

*i.e.* a non-local experiment is needed for detecting the influence of gravity. One such experiment is to observe the paths of two nearby freely falling point particles. For two particles separated by  $\epsilon^{\mu}$ , their separation is governed by the geodesic deviation equation, which is given by

$$\frac{D^2\epsilon^{\mu}}{D\tau^2} = -R_{\rho\nu\sigma}^{\mu} \epsilon^{\nu} \frac{dx^{\rho}}{d\tau} \frac{dx^{\sigma}}{d\tau}, \quad (1.20)$$

where  $D/D\tau$  is the directional covariant derivative of a vector field  $V^{\mu}(x^{\nu})$  along the world line  $x^{\mu}(\tau)$ ,

$$\frac{DV^{\mu}}{D\tau} \equiv \frac{dV^{\mu}}{d\tau} + \Gamma_{\nu\rho}^{\mu} V^{\nu} \frac{dx^{\rho}}{d\tau}. \quad (1.21)$$

Based on Eq. (1.20), we can conclude that the presence of gravity is signified by a non-zero Riemann curvature tensor. In the next section, we will show how a perturbation on a flat spacetime results in a non-zero Riemann tensor, therefore, gravity.

## 1.2 Linearized Einstein field equation

### 1.2.1 Linear expansion around flat spacetime

To gain further insight into general relativity, we first expand around a Minkowski spacetime, *i.e.*

$$g_{\mu\nu} = \eta_{\mu\nu} + h_{\mu\nu} \text{ with } |h_{\mu\nu}| \ll 1, \quad (1.22)$$

and we neglect any beyond-linear-order correction from  $h_{\mu\nu}$  to the Einstein field equation. For Eq. (1.22) to hold, a set of reference frames is being chosen. As a result, the invariance of general relativity under any coordinate transformation is broken. However, the condition  $|h_{\mu\nu}| \ll 1$  continues to hold under transformation of the form

$$x'^{\mu} = x^{\mu} + \xi^{\mu}(x^{\nu}) \text{ with } |\partial_{\mu}\xi_{\nu}| \lesssim |h_{\mu\nu}|. \quad (1.23)$$

Given such a transformation, the transformation of  $h_{\mu\nu}$  is given by

$$h'_{\mu\nu} = h_{\mu\nu} - (\partial_{\mu}\xi_{\nu} + \partial_{\nu}\xi_{\mu}). \quad (1.24)$$

Eq. (1.24) demonstrates the necessity of demanding  $|\partial_{\mu}\xi_{\nu}| \lesssim |h_{\mu\nu}|$  for the condition  $|h_{\mu\nu}| \ll 1$  to hold.

In addition to the local transformation described in Eq. (1.23), a global transformation, for instance, a Lorentz transformation

$$x'^{\mu} = \Lambda^{\mu}_{\nu} x^{\nu}, \quad (1.25)$$

can be performed as long as the boost does not spoil the  $|h_{\mu\nu}| \ll 1$  condition.

### 1.2.2 Linearised Einstein field equation

Based on the above linearly perturbed metric, the Christoffel symbols and Riemann tensor are given by

$$\Gamma^{\rho}_{\mu\nu} = \frac{1}{2}(\partial_{\mu}h_{\nu}^{\rho} + \partial_{\nu}h_{\mu}^{\rho} - \partial^{\rho}h_{\mu\nu}) + O(h^2), \quad (1.26)$$

$$R^{\lambda}_{\rho\mu\nu} = \frac{1}{2}(\partial^2_{\rho\mu}h_{\nu}^{\lambda} - \partial_{\rho}\partial_{\nu}h_{\mu}^{\lambda} + \partial^{\lambda}\partial_{\nu}h_{\rho\mu} - \partial^{\lambda}\partial_{\mu}h_{\rho\nu}) + O(h^2). \quad (1.27)$$

Moreover, the Ricci tensor and Ricci scalar are given by

$$R_{\mu\nu} = \frac{1}{2}(\partial_{\nu}\partial_{\lambda}h_{\mu}^{\lambda} + \partial_{\mu}\partial_{\lambda}h_{\nu}^{\lambda} - \partial^{\lambda}\partial_{\lambda}h_{\mu\nu} - \partial_{\mu}\partial_{\nu}h^{\lambda}_{\lambda}) + O(h^2), \quad (1.28)$$

$$R = \frac{1}{2}(\partial^{\mu}\partial^{\nu}h_{\mu\nu} - \partial^{\mu}\partial_{\mu}h^{\nu}_{\nu}) + O(h^2). \quad (1.29)$$

The Einstein tensor is then, up to leading order, given by

$$\begin{aligned} G_{\mu\nu} &= R_{\mu\nu} - \frac{1}{2}Rg_{\mu\nu} \\ &= \frac{1}{2}(\partial_{\lambda}\partial_{\mu}h_{\nu}^{\lambda} + \partial_{\lambda}\partial_{\nu}h_{\mu}^{\lambda} - \partial_{\mu}\partial_{\nu}h - \square h_{\mu\nu} - \eta_{\mu\nu}\partial_{\rho}\partial_{\lambda}h^{\rho\lambda} + \eta_{\mu\nu}\square h), \end{aligned} \quad (1.30)$$

where the trace of  $h_{\mu\nu}$ ,  $h = \eta^{\mu\nu} h_{\mu\nu} = h^\mu_\mu$  and the d'Alembert operator  $\square = \eta^{\mu\nu} \partial_\mu \partial_\nu = \partial^\mu \partial_\mu$ , respectively. To simplify Eq. (1.30) one can introduce the trace-reversed  $\bar{h}_{\mu\nu}$ , which is given by

$$\bar{h}_{\mu\nu} = h_{\mu\nu} - \frac{1}{2} \eta_{\mu\nu} h. \quad (1.31)$$

Eq. (1.30) becomes

$$G_{\mu\nu} = \frac{1}{2} (\partial^\lambda \partial_\nu \bar{h}_{\mu\lambda} + \partial^\lambda \partial_\mu \bar{h}_{\nu\lambda} - \square \bar{h}_{\mu\nu} - \eta_{\mu\nu} \partial^\lambda \partial^\rho \bar{h}_{\lambda\rho}). \quad (1.32)$$

To further simplify the Einstein tensor, one can take advantage of the gauge freedom described in Eq. (1.24). In particular, the so called harmonic gauge can be chosen, which enforces

$$\partial^\nu \bar{h}_{\mu\nu} = 0. \quad (1.33)$$

Such a gauge can be achieved by choosing  $\xi_\mu$  in Eq. (1.24) to be

$$\xi_\mu(x^\alpha) = \int G(x^\alpha - y^\alpha) \partial^\nu \bar{h}_{\mu\nu}(y^\alpha) dx^\alpha, \quad (1.34)$$

where  $G(x^\alpha - y^\alpha)$  is the Green's function for the d'Alembert operator. The harmonic gauge leaves room for additional gauge freedom; any  $\xi_\mu$  that satisfies  $\square \xi_\mu = 0$ , does not spoil the harmonic gauge.

Applying the harmonic gauge, the Einstein tensor  $G$  becomes

$$G_{\mu\nu} = -\frac{1}{2} \square \bar{h}_{\mu\nu}, \quad (1.35)$$

and the linearized Einstein field equations become

$$\square \bar{h}_{\mu\nu} = -16\pi T_{\mu\nu}. \quad (1.36)$$

### 1.2.3 Gravitational waves in the vacuum

In vacuum ( $T_{\mu\nu} = 0$ ), the linearized Einstein field equations are given by

$$\square \bar{h}_{\mu\nu} = 0, \quad (1.37)$$

which admits plane-wave solutions

$$\begin{aligned} \bar{h}_{\mu\nu} &= A_{\mu\nu} \exp(ik_\sigma x^\sigma + \phi), \\ k_\mu k^\mu &= 0. \end{aligned} \quad (1.38)$$

Therefore, the gravitational influence travels like a wave, also known as a gravitational wave, at the speed of light. Because of the harmonic gauge,

$$k^\mu A_{\mu\nu} = 0, \quad (1.39)$$

so that a gravitational wave is a transverse wave.

As mentioned, a  $\xi_\mu$  satisfying  $\square \xi_\mu = 0$  leaves the harmonic gauge untouched. As a result, the trace-reversed perturbation metric tensor  $\bar{h}_{\mu\nu}$  is left with 16 - 6 (symmetric

tensor) - 4 (harmonic gauge) - 4 ( $\xi_\mu$ -freedom) = 2 degrees of freedom. As we will see next, these degrees of freedom correspond to the two independent polarization of gravitational waves. In particular, we can demand that

$$v^\mu \bar{h}_{\mu\nu} = 0, \quad (1.40)$$

where  $v^\mu$  is the 4-velocity of an arbitrary observer. This condition only consists of three constraints as one of them is repeated with  $v^\mu \partial^\nu \bar{h}_{\mu\nu} = 0$ , where we took  $\partial_\nu v^\mu = 0$ . The last gauge freedom is then used such that

$$\bar{h} = \eta^{\mu\nu} \bar{h}_{\mu\nu} = 0. \quad (1.41)$$

By choosing the 4-velocity  $v^\mu = (1, \vec{0})$ , which is the velocity of a stationary observer with respect to the coordinate system, the following constraints are satisfied;

$$\bar{h}_{\mu 0} = 0, \quad (1.42a)$$

$$\eta^{\mu\nu} \bar{h}_{\mu\nu} = \bar{h}_i^i = 0, \quad (1.42b)$$

$$\partial^\mu \bar{h}_{\mu\nu} = \partial^i \bar{h}_{ij} = 0. \quad (1.42c)$$

The gauge description above is often referred as the traceless-traverse gauge (TT gauge). In this gauge,  $h = -\bar{h} = 0$ , therefore,  $\bar{h}_{\mu\nu} = h_{\mu\nu}$ . Moreover, by specifying the gravitational wave to be propagating along the  $z$ -direction (without the loss of generality), the perturbation metric tensor is given by

$$h_{\mu\nu}^{\text{TT}} = \bar{h}_{\mu\nu}^{\text{TT}} = \begin{pmatrix} 0 & 0 & 0 & 0 \\ 0 & h_+ & 0 & 0 \\ 0 & 0 & -h_+ & 0 \\ 0 & 0 & 0 & 0 \end{pmatrix} + \begin{pmatrix} 0 & 0 & 0 & 0 \\ 0 & 0 & h_\times & 0 \\ 0 & h_\times & 0 & 0 \\ 0 & 0 & 0 & 0 \end{pmatrix}, \quad (1.43)$$

where the superscript TT denotes the traverse-traceless gauge. The  $h_+$  and  $h_\times$  are the two residual degrees of freedom, referred to as the plus and cross polarization of a gravitational wave, respectively.

### 1.2.4 Interaction between gravitational waves and matter

One way to observe the influence of gravitational waves on matter is to calculate the motion of a free-falling point particle under the perturbed metric. By applying the geodesic equation Eq. (1.18), on a particle at rest  $dx^i/d\tau = 0$ ,

$$\begin{aligned} \frac{d^2 x^i}{d\tau^2} &= -\Gamma_{00}^i \left( \frac{dx^0}{d\tau} \right)^2 \\ &= \frac{1}{2} (\partial^i h_{00} - 2\partial_0 h_0^i) \left( \frac{dx^0}{d\tau} \right)^2 \\ &= 0. \end{aligned} \quad (1.44)$$

A particle initially at rest does not experience any effect due to the gravitational wave under the TT gauge. The reason for such a phenomenon is not a physical one, but because

we specify  $v^\mu = (1, \vec{0})$  throughout the whole spacetime. As a result, the effect from the gravitational wave is canceled out by the coordinate system's correction.

To observe the gravitational wave, we can first calculate the behavior of the proper distance between two points. Given two points separated along the  $x$ -axis,  $(t, x_1, 0, 0)$  and  $(t, x_2, 0, 0)$ , the proper distance  $s$  between them is given by

$$\begin{aligned} s &= \int ds \\ &= \int_{x_1}^{x_2} dx \sqrt{1 + h_+ \cos(\omega t + \phi)} \\ &\approx (x_2 - x_1) \left( 1 + \frac{1}{2} h_+ \cos(\omega t + \phi) \right), \end{aligned} \quad (1.45)$$

where in the second line we made explicit the time dependence of the plane wave. Thus, proper distance between two points oscillates under the influence of gravitational waves.

In order to observe the coordinate distance between two points to reflect the presence of gravitational wave, a different gauge is needed. One of such choice is the so called Local Lorentz gauge. Based on the strong equivalence principle, for any point  $P$  in the spacetime there exist a coordinate transformation such that

$$g_{\mu\nu}(P) = \eta_{\mu\nu} + \mathcal{O}\left(\left(\frac{x}{R}\right)^2\right), \quad (1.46)$$

where  $R$  is the radius of curvature of the metric tensor at that point. This locally flat metric is the tangent plane of the spacetime manifold at point  $P$ . Given the Local Lorentz gauge and assuming a non-relativistic limit ( $dx^0/d\tau \gg dx^i/d\tau$ ), the geodesic deviation equation (1.20) is given by

$$\frac{d^2 \epsilon^i}{d\tau^2} \approx -R_{0j0}^i \epsilon^j \left( \frac{dx^0}{d\tau} \right)^2. \quad (1.47)$$

Because the metric is locally flat,  $d^2 x^0/d\tau^2 = d^2 t/d\tau^2 = 0$ . The equation is then given by

$$\frac{d^2 \epsilon^i}{dt^2} = \ddot{\epsilon}^i \approx -R_{0j0}^i \epsilon^j, \quad (1.48)$$

where the double overdot denotes double time derivative. As the Riemann curvature tensor is gauge-invariant, it can be computed under the TT gauge, where it is given by

$$R_{0j0}^i = -\frac{1}{2} \ddot{h}_{ij}^{\text{TT}}, \quad (1.49)$$

Therefore, the equations of motion are given by

$$\ddot{\epsilon}^i = \frac{1}{2} \ddot{h}_{ij}^{\text{TT}} \epsilon^j. \quad (1.50)$$

Let us consider a ring of test particles sitting on the  $x$ - $y$  plane where the gravitational wave is traveling along the  $z$ -direction (normal to the plane). Because the gravitational wave is transverse, we ignore a particle's motion along the  $z$ -axis. The positions of the particles are denoted as  $(x_0 + \delta x, y_0 + \delta y)$ , where  $(x_0, y_0)$  is the unperturbed position and  $(\delta x, \delta y)$  is the variation induced by the gravitational wave. The equations of motion are

give by

$$\begin{aligned} \begin{pmatrix} \delta \ddot{x} \\ \delta \ddot{y} \end{pmatrix} &= \frac{1}{2} \left[ \begin{pmatrix} \ddot{h}_+ & 0 \\ 0 & -\ddot{h}_+ \end{pmatrix} + \begin{pmatrix} 0 & \ddot{h}_\times \\ \ddot{h}_\times & 0 \end{pmatrix} \right] \begin{pmatrix} x_0 + \delta x \\ y_0 + \delta y \end{pmatrix} \\ &\approx \frac{1}{2} \left[ \begin{pmatrix} \ddot{h}_+ & 0 \\ 0 & -\ddot{h}_+ \end{pmatrix} + \begin{pmatrix} 0 & \ddot{h}_\times \\ \ddot{h}_\times & 0 \end{pmatrix} \right] \begin{pmatrix} x_0 \\ y_0 \end{pmatrix}, \end{aligned} \quad (1.51)$$

where the leading-order approximation has been taken. The motion of the particle is give by

$$\begin{pmatrix} \delta x \\ \delta y \end{pmatrix} = \frac{1}{2} \left[ \begin{pmatrix} \ddot{h}_+ & 0 \\ 0 & -\ddot{h}_+ \end{pmatrix} + \begin{pmatrix} 0 & \ddot{h}_\times \\ \ddot{h}_\times & 0 \end{pmatrix} \right] \begin{pmatrix} x_0 \\ y_0 \end{pmatrix}. \quad (1.52)$$

Let us consider the two polarization separately. For a monochromatic gravitational-wave  $h_{+,\times} = A_{+,\times} \cos(\omega t)$ , the motion due to the plus polarization is given by

$$\begin{aligned} \begin{pmatrix} \delta x \\ \delta y \end{pmatrix} &= \frac{1}{2} \begin{pmatrix} \ddot{h}_+ & 0 \\ 0 & -\ddot{h}_+ \end{pmatrix} \begin{pmatrix} x_0 \\ y_0 \end{pmatrix} \\ &= \frac{1}{2} A_+ \cos(\omega t) \begin{pmatrix} x_0 \\ -y_0 \end{pmatrix}. \end{aligned} \quad (1.53)$$

For the cross polarization, it is given by

$$\begin{aligned} \begin{pmatrix} \delta x \\ \delta y \end{pmatrix} &= \frac{1}{2} \begin{pmatrix} 0 & \ddot{h}_\times \\ \ddot{h}_\times & 0 \end{pmatrix} \begin{pmatrix} y_0 \\ x_0 \end{pmatrix} \\ &= \frac{1}{2} A_\times \cos(\omega t) \begin{pmatrix} y_0 \\ x_0 \end{pmatrix}. \end{aligned} \quad (1.54)$$

Their corresponding motions are shown in Fig 1.1, which explains the naming of plus and cross for the polarizations.



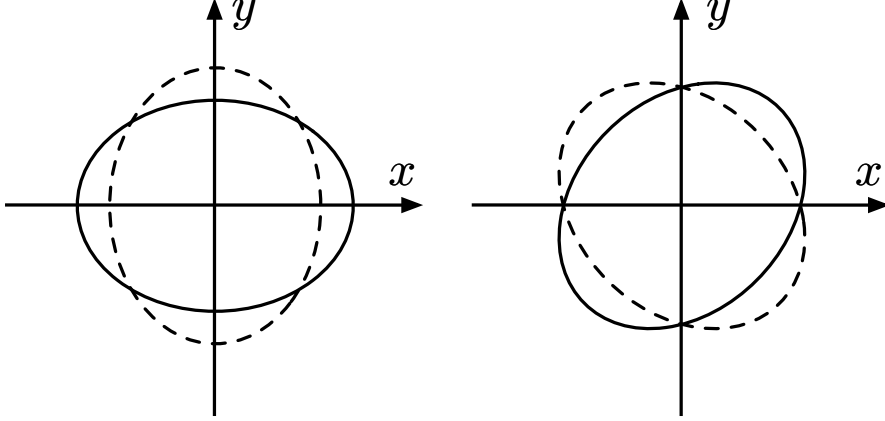


Figure 1.1: The impact on a ring of test particles of a gravitational wave in plus polarization (*left*) and cross-polarization (*right*). In both cases, the wave is traveling in the  $z$ -direction. The solid and dotted lines are the shape of the ring with a phase difference of  $\pi$ .

### 1.2.5 Generation of gravitational waves

To study the generation of gravitational waves, we have to revisit the linearized Einstein field equations, which state

$$\square \bar{h}_{\mu\nu} = -16\pi T_{\mu\nu}. \quad (1.55)$$

To solve these equations, boundary conditions have to be imposed. We will assume no incoming gravitational radiations and the source is confined. The general solution of Eq. (1.55) is then given by

$$\bar{h}_{\mu\nu}(t, \vec{x}) = 4 \int d\vec{y} \frac{T_{\mu\nu}(t - |\vec{x} - \vec{y}|, \vec{y})}{|\vec{x} - \vec{y}|}. \quad (1.56)$$

One can introduce a projection operator  $\Lambda_{ijkl}$  so that

$$\Lambda^i{}_{jkl} A_{kl} = 0, \quad (1.57a)$$

$$\Lambda_{ijkl} A_{kl} n^i = 0, \quad (1.57b)$$

where  $A_{kl}$  and  $n_i$  are an arbitrary tensor and the propagation direction of the gravitational wave, respectively. These conditions uniquely define  $\Lambda_{ijkl}$  as

$$\Lambda_{ijkl} \equiv P_{ik}P_{jl} - \frac{1}{2}P_{ij}P_{kl}, \quad (1.58)$$

where  $P_{ij}$  is given by

$$P_{ij} \equiv \delta_{ij} - n_i n_j. \quad (1.59)$$

As a result, the metric perturbation in the TT gauge is given by

$$h_{ij}^{\text{TT}}(t, \vec{x}) = 4\Lambda_{ijkl} \int d\vec{y} \frac{T^{kl}(t - |\vec{x} - \vec{y}|, \vec{y})}{|\vec{x} - \vec{y}|}. \quad (1.60)$$

To simplify the expression in Eq. (1.60), one can impose approximations to its spatial and temporal dependence. First, if we focus on the metric perturbation far away from the source, one can take the far field approximation, which states

$$\begin{aligned}
 |\vec{x} - \vec{y}| &= |\vec{x}| + y^i \partial_i |\vec{x}| + \mathcal{O}\left(\frac{d^2}{|\vec{x}|}\right) \\
 &\approx |\vec{x}| - y^i \partial_i |\vec{x}| \\
 &= |\vec{x}| - y^i \frac{x_i}{|\vec{x}|} \\
 &= |\vec{x}| - y^i n_i \\
 &\equiv r - y^i n_i,
 \end{aligned} \tag{1.61}$$

Subsequently in the integrand of Eq. (1.60),

$$\begin{aligned}
 \frac{1}{|\vec{x} - \vec{y}|} &= \frac{1}{|\vec{x}|} + \frac{1}{|\vec{x}|^2} n_i y^i + \mathcal{O}\left(\frac{d^2}{|\vec{x}|^3}\right) \\
 &\approx \frac{1}{|\vec{x}|} = \frac{1}{r},
 \end{aligned} \tag{1.62}$$

where  $d$  is the typical length scale of the source and  $r$  is the distance from the origin to the observer. Moreover, we also assume that the stress-energy tensor is slow varying, therefore,

$$\omega d \ll 1, \tag{1.63}$$

where  $\omega$  is the angular frequency of the gravitational wave. The stress-energy tensor is then given by

$$\begin{aligned}
 T^{ij}(t - |\vec{x} - \vec{y}|, \vec{y}) &\approx T(t - r + n_k y^k, \vec{y}) \\
 &= T^{ij}(t - r, \vec{y}) + n_k y^k \partial_0 T^{ij}(t - r, \vec{y}) \\
 &\quad + \frac{1}{2} n_k n_l y^k y^l \partial_0 \partial_0 T^{ij}(t - r, \vec{y}) + \mathcal{O}(\omega^3 d^3 T) \\
 &\approx T^{ij}(t - r, \vec{y}) + n_k y^k \partial_0 T^{ij}(t - r, \vec{y}) \\
 &\quad + \frac{1}{2} n_k n_l y^k y^l \partial_0 \partial_0 T^{ij}(t - r, \vec{y}),
 \end{aligned} \tag{1.64}$$

where  $T$  is the typical stress-energy scale of the source. We can further simplify the expression Eq. (1.64) by defining the moments of the stress-energy tensor;

$$S^{ij}(t) \equiv \int d\vec{y} T^{ij}(t, \vec{y}), \tag{1.65a}$$

$$S^{ijk}(t) \equiv \int d\vec{y} T^{ij}(t, \vec{y}) y^k, \tag{1.65b}$$

$$S^{ijkl}(t) \equiv \int d\vec{y} T^{ij}(t, \vec{y}) y^k y^l. \tag{1.65c}$$

Eq. (1.64) then becomes

$$T^{ij}(t - |\vec{x} - \vec{y}|, \vec{y}) \approx S^{ij}(t - r) + n_k \dot{S}^{ijk}(t - r) + \frac{1}{2} n_k n_l \ddot{S}^{ijkl}(t - r). \tag{1.66}$$

One can extract the physical meaning of each term in Eq. (1.66) by considering the mass moments,

$$M(t) \equiv \int d\vec{y} T^{00}(t, \vec{y}), \quad (1.67a)$$

$$M^i(t) \equiv \int d\vec{y} T^{00}(t, \vec{y}) y^i, \quad (1.67b)$$

$$M^{ij}(t) \equiv \int d\vec{y} T^{00}(t, \vec{y}) y^i y^j, \quad (1.67c)$$

and the linear momentum moments

$$P^i(t) \equiv \int d\vec{y} T^{0i}(t, \vec{y}), \quad (1.68a)$$

$$P^{ij}(t) \equiv \int d\vec{y} T^{0i}(t, \vec{y}) y^j, \quad (1.68b)$$

$$P^{ijk}(t) \equiv \int d\vec{y} T^{0i}(t, \vec{y}) y^j y^k. \quad (1.68c)$$

By using the conservation of energy and momentum Eq. (1.16) and the source being confined in space, one can derive the following identities.

$$\dot{M} = 0, \quad (1.69a)$$

$$\dot{M}^i = P^i, \quad (1.69b)$$

$$\dot{M}^{ij} = P^{ij} + P^{ji}, \quad (1.69c)$$

$$\dot{M}^{ijk} = P^{ijk} + P^{jki} + P^{kij}, \quad (1.69d)$$

$$\dot{P}^i = 0 \quad (1.70a)$$

$$\dot{P}^{ij} = S^{ij} \quad (1.70b)$$

$$\dot{P}^{ijk} = S^{ijk} + S^{ikj}. \quad (1.70c)$$

To leading order, Eq. (1.60) is given by

$$\begin{aligned} h_{ij}^{\text{TT}} &= \frac{4}{r} \Lambda_{ijkl} S^{kl}(t-r) \\ &= \frac{2}{r} \Lambda_{ijkl} \ddot{M}^{kl}(t-r), \end{aligned} \quad (1.71)$$

which shows that the leading order contribution to the gravitational wave is quadrupole radiation. Because mass is always positive (unlike electric charge), the mass dipole mo-

ment vanishes by translating the origin to the center-of-mass. Mathematically,

$$\begin{aligned}
 \text{mass dipole} &= \sum_i m_i \vec{x}'_i \\
 &= \sum_i m_i (\vec{x}_i - \vec{x}_c) \\
 &= \sum_i m_i \left( \vec{x}_i - \frac{1}{M} \sum_j m_j \vec{x}_j \right) \\
 &= \sum_i m_i \vec{x}_i - \sum_j m_j \vec{x}_j \\
 &= \vec{0},
 \end{aligned} \tag{1.72}$$

where  $M$  and  $\vec{x}_c$  are the total mass and the center-of-mass, respectively. The above reasoning only holds if the total mass is always non-zero. As a result, the contribution of dipole moment radiation is absent in gravitational waves.

Without loss of generality, we assume the gravitational wave is traveling towards the positive  $z$ -direction. Eq. (1.71) becomes

$$h_{ij}^{\text{TT}}(t) = \frac{2}{r} \begin{pmatrix} \frac{1}{2}(\ddot{M}_{11} - \ddot{M}_{22})(t_{\text{ret}}) & \ddot{M}_{12}(t_{\text{ret}}) & 0 \\ \ddot{M}_{21}(t_{\text{ret}}) & -\frac{1}{2}(\ddot{M}_{11} - \ddot{M}_{22})(t_{\text{ret}}) & 0 \\ 0 & 0 & 0 \end{pmatrix}, \tag{1.73}$$

where  $t_{\text{ret}} = t - r$ . Comparing Eq. (1.73) to Eq. (1.43), the two gravitational-wave polarizations are

$$\begin{aligned}
 h_+(t) &= \frac{1}{r} (\ddot{M}_{11} - \ddot{M}_{22})(t_{\text{ret}}), \\
 h_\times(t) &= \frac{2}{r} \ddot{M}_{12}(t_{\text{ret}}).
 \end{aligned} \tag{1.74}$$

Let us consider one of the simplest systems with significant gravitational wave emission, a binary system with two point masses. The two masses  $m_1$  and  $m_2$  are circularly orbiting around their center-of-mass with a mutual separation of  $R$  and an angular frequency  $\omega_{\text{orb}}$ . We have the origin placed at the center-of-mass and the angle between their plane of orbit and the  $z$ -axis is denoted by  $\iota$ . The position of the masses,  $\vec{y}_1$  and  $\vec{y}_2$ , are then given by

$$\begin{aligned}
 \vec{y}_1 &= \frac{m_2}{m_1 + m_2} R \hat{e}(t), \\
 \vec{y}_2 &= -\frac{m_1}{m_1 + m_2} R \hat{e}(t),
 \end{aligned} \tag{1.75}$$

where  $\hat{e}(t)$  is given by

$$\hat{e}(t) = (\cos(\omega_{\text{orb}}t), \cos(\iota) \sin(\omega_{\text{orb}}t), -\sin(\iota) \sin(\omega_{\text{orb}}t)), \tag{1.76}$$

where we have taken  $t = 0$  to be the time at which the two masses' separation is parallel with the  $x$ -axis. Using Eq. (1.67) and  $T^{00} = m_1 \delta(\vec{y} - \vec{y}_1) + m_2 \delta(\vec{y} - \vec{y}_2)$ , the mass quadrupole

is given by

$$M_{ij} = \frac{m_1 m_2}{m_1 + m_2} R^2 \begin{pmatrix} \cos^2(\omega_{\text{orb}} t) & \cos(\iota) \cos(\omega_{\text{orb}} t) \sin(\omega_{\text{orb}} t) & 0 \\ \cos(\iota) \cos(\omega_{\text{orb}} t) \sin(\omega_{\text{orb}} t) & \cos^2(\iota) \sin^2(\omega_{\text{orb}} t) & 0 \\ 0 & 0 & 0 \end{pmatrix}, \quad (1.77)$$

the  $M_{i3}$  and  $M_{3i}$  are omitted as they do not contribute to the gravitational wave as seen in Eq. (1.73). The resulting gravitational wave is

$$\begin{aligned} h_+(t) &= \frac{1}{r} \frac{4m_1 m_2 R^2 \omega_{\text{orb}}^2}{m_1 + m_2} \frac{1 + \cos^2(\iota)}{2} \cos(2\omega_{\text{orb}} t_{\text{ret}}), \\ h_\times(t) &= -\frac{1}{r} \frac{4m_1 m_2 R^2 \omega_{\text{orb}}^2}{m_1 + m_2} \cos(\iota) \sin(2\omega_{\text{orb}} t_{\text{ret}}). \end{aligned} \quad (1.78)$$

By employing Kepler's third law

$$\omega_{\text{orb}}^2 = \frac{m_1 + m_2}{R^3}, \quad (1.79)$$

and defining chirp mass  $\mathcal{M}_c$  as

$$\mathcal{M}_c = \frac{(m_1 m_2)^{3/5}}{(m_1 + m_2)^{1/5}}, \quad (1.80)$$

Eq. (1.78) becomes

$$\begin{aligned} h_+(t) &= \frac{4\mathcal{M}_c^{5/3} \omega_{\text{orb}}^{2/3}}{r} \frac{1 + \cos^2(\iota)}{2} \cos(2\omega_{\text{orb}} t_{\text{ret}}), \\ h_\times(t) &= -\frac{4\mathcal{M}_c^{5/3} \omega_{\text{orb}}^{2/3}}{r} \cos(\iota) \sin(2\omega_{\text{orb}} t_{\text{ret}}). \end{aligned} \quad (1.81)$$

A few things are to be noted in the gravitational-wave waveform, as shown in Eq. (1.81).

1. The amplitude and frequency of the waveform are constant. This is because we have assumed the masses to undergo Newtonian motion. The back-reaction due to energy and momentum carried away by gravitational waves is neglected.
2. The gravitational wave's frequency is twice the orbital frequency. This is because the mass quadrupole moment is invariant under parity transformation  $\vec{y} \rightarrow -\vec{y}$ . This relation does not hold if higher mass moments are included.
3. At  $\iota = 0$ , often referred as "face-on", amplitudes of  $h_+$  and  $h_\times$  are equal and highest. At  $\iota = \pi/2$ , often referred as "edge-on",  $h_\times$  vanishes and amplitude of  $h_+$  is half of its maximum.

### 1.3 Detecting gravitational waves

As described in Sec. 1.2.4, gravitational waves can physically affect the test mass experiencing it. Therefore one can utilize such behavior for detecting the presence of

gravitational waves. The following section will give an overview of the interferometric gravitational wave detector and basic techniques to detect a signal embedded in the data.

### 1.3.1 Detector response and beam pattern function

An interferometer consists of two arms, pointing along the two directions  $u^i$  and  $v^i$ , respectively. The output of an interferometer is the strain, which is the relative distance difference between the two arms.

Let us consider an interferometer sitting at the origin with arm length of  $L$  pointing along  $u^i = (1, 0, 0)$  and  $v^i = (0, 1, 0)$ , with a gravitational wave traveling along the  $z$ -direction. Using Eq. (1.53) and (1.54), the length of the  $x$ -axis arm is changed by  $\delta x = \frac{1}{2}h_+(t)L$ , and that of the  $y$ -axis arms is changed by  $\delta y = -\frac{1}{2}h_+(t)L$ . The strain  $h(t)$  is given by

$$h(t) = \frac{\delta x - \delta y}{L} = h_+(t), \quad (1.82)$$

showing a direct relation with the gravitational wave.

In general, the strain is given by [43]

$$h(t) = D^{ij}h_{ij}(t), \text{ where } D^{ij} \equiv \frac{1}{2}(u^i u^j - v^i v^j). \quad (1.83)$$

Because the detector tensor  $D_{ij}$  acts linearly, one can write the strain as

$$h(t) = F_+ h_+(t) + F_\times h_\times(t), \quad (1.84)$$

where  $F_+$  and  $F_\times$  are the beam pattern functions for the plus and cross polarizations, respectively.<sup>1</sup> For a detector with arms at right angle, the beam pattern function for gravitational-wave radiating from the direction  $(\theta, \phi)$  relative to the detector's origin is given by

$$\begin{aligned} F_+^{90^\circ} &= \frac{1}{2}(1 + \cos^2 \theta) \cos 2\phi \cos 2\psi - \cos \theta \sin 2\phi \sin 2\psi \\ F_\times^{90^\circ} &= \frac{1}{2}(1 + \cos^2 \theta) \cos 2\phi \sin 2\psi + \cos \theta \sin 2\phi \cos 2\psi, \end{aligned} \quad (1.85)$$

where  $\psi$  is the polarization angle which fixes an orientation in the plane perpendicular to the propagation direction. The beam pattern functions with  $\psi = 0$  are shown in Fig. 1.2.

### 1.3.2 Noise characterization

Because the amplitude of the gravitational waves observed on Earth is weak ( $\sim 10^{-21}$ ), the effect of noise on the detector is not negligible. These noises result from multiple contributions, e.g., gravitational disruption from nearby mass, seismic activity, etc. (see Ref. [4, 10] for details). The time-series output from the detector  $d(t)$  can be expressed as

$$d(t) = h(t) + n(t), \quad (1.86)$$

---

<sup>1</sup>In general, the beam pattern functions have a time dependence due to Earth's rotation. It is common to ignore it as the signals in a second-generation gravitational-wave detector have a much shorter duration than the rotation timescale.

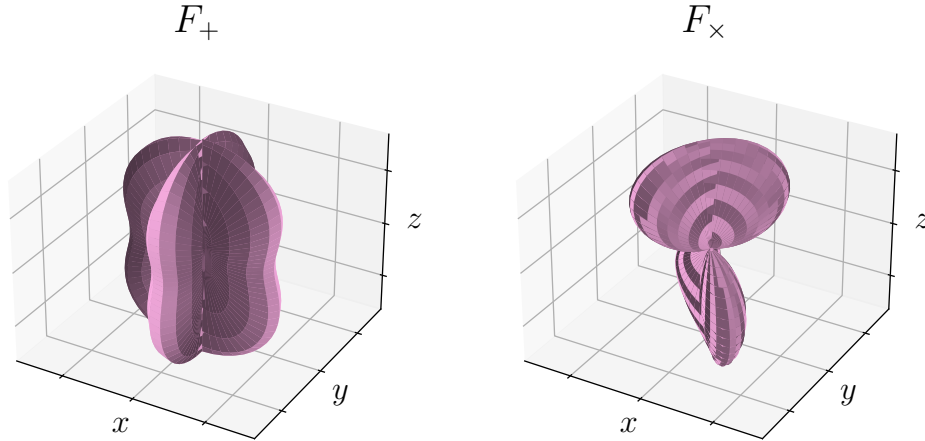


Figure 1.2: The beam pattern function of a  $90^\circ$  interferometer for the plus polarization (*left*) and cross polarization (*right*) with  $\psi = 0$  are shown.

where  $h(t)$  is the embedded gravitational-wave signal and  $n(t)$  is the noise. Due to the abundance of noise, understanding its nature is crucial for detecting gravitational waves.

Suppose the noise in the detector can be described by a stationary Gaussian stochastic process [44]<sup>2</sup> with

$$\langle n(t) \rangle = 0, \quad (1.87)$$

where the  $\langle \cdot \rangle$  bracket is referring to an ensemble average. In reality, one can only access to a single realization of the noise. Therefore, ergodicity is assumed and the ensemble average is replaced by a time average, e.g.

$$\langle n(t) \rangle = \lim_{T \rightarrow \infty} \frac{1}{T} \int_0^T dt n(t). \quad (1.88)$$

The autocorrelation  $R(\tau)$  is given by

$$\begin{aligned} R(\tau) &\equiv \langle n(t + \tau)n(t) \rangle \\ &= \lim_{T \rightarrow \infty} \int_0^T dt n(t + \tau)n(t), \end{aligned} \quad (1.89)$$

which qualify how related are the noise separated by  $\tau$ .

As it is a common practice to perform a time-series analysis in the Fourier domain, one can define the power spectral density  $P_n(f)$  as

$$P_n(f) \equiv \int_{-\infty}^{\infty} d\tau R(\tau) \exp(-i2\pi f\tau). \quad (1.90)$$

Note that

1.  $n(t)$  is real, so is  $R(\tau)$ , therefore  $P_n(-f) = P_n^*(f)$ ,
2. time translational symmetry, therefore  $R(\tau) = R(-\tau)$ ,

<sup>2</sup>Such an approximation turns out to be accurate for describing the noise in second-generation ground-based detector like LIGO and Virgo [45].

where the  $*$  denotes complex conjugate. The power spectral density  $P_n(-f) = P_n^*(f) = P_n(f)$ , and the integral

$$\int_{-\infty}^{\infty} df P_n(f) = 2 \int_0^{\infty} df P_n(f) \equiv \int_0^{\infty} df S_n(f), \quad (1.91)$$

where  $S_n(f)$  is the one-sided power spectral density. The properties described above and the usage of one-sided power spectral density justifies gravitational-wave data analysis to be conducted for positive frequency only. Moreover, the one-sided power spectral density has the following properties

$$\begin{aligned} \langle n^2(t) \rangle &= R(0) \\ &= \int_0^{\infty} df S_n(f), \end{aligned} \quad (1.92)$$

and

$$\langle \tilde{n}(f) \tilde{n}^*(f') \rangle = \frac{1}{2} S_n(f) \delta(f - f'), \quad (1.93)$$

where the overhead tilde refers to the Fourier transform. The representative one-sided power spectral densities for LIGO and Virgo during the second half of the third observation run (O3b) are shown in Fig. 1.3.

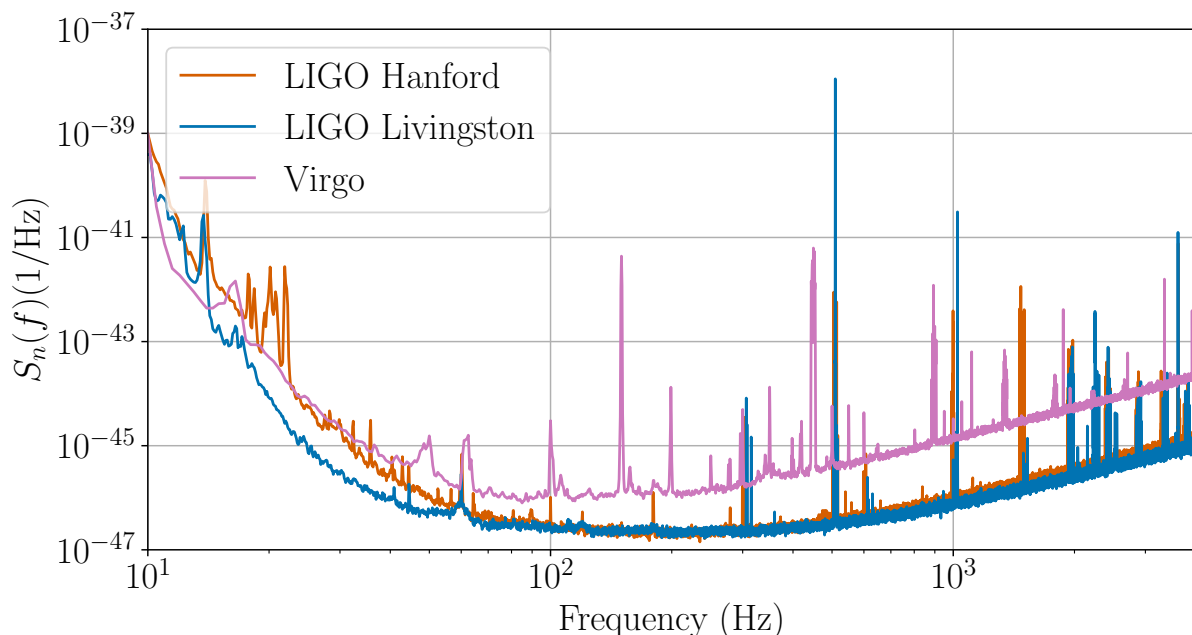


Figure 1.3: The representative one-sided power spectral density for LIGO Hanford (*orange*), LIGO Livingston (*blue*), and Virgo (*purple*) during the second half of the third observation run.

Because of the Gaussian process nature of the noise, the probability density of having



a particular noise realization  $\text{pdf}(n(t))$  is

$$\begin{aligned} \text{pdf}(n(t)) &= \text{pdf}(\tilde{n}(f)) \\ &\propto \exp\left(-\frac{1}{2} \int_0^\infty df \frac{|\tilde{n}|^2}{S_n(f)}\right) \\ &\equiv \exp\left(-\frac{1}{2} \langle n|n \rangle\right), \end{aligned} \quad (1.94)$$

In the above expression, a common notion of noise-weighted inner product  $\langle a|b \rangle$  is used, which is given by

$$\langle a|b \rangle \equiv 4\Re \int_0^\infty df \frac{\tilde{a}(f)\tilde{b}^*(f)}{S_n(f)} \approx 4\Re \sum_i \Delta f \frac{\tilde{a}(f_i)\tilde{b}^*(f_i)}{S_n(f_i)}. \quad (1.95)$$

Such an inner product incorporates the strength of the noise at different frequencies (in the form of one-sided power spectral density), which is commonly used in gravitational-wave data analysis.

### 1.3.3 Matched filtering

With the knowledge of the noise described in the previous section, one can develop the technique for searching for gravitational-wave signals hidden within the noise. In particular, the details of the matched filtering technique are presented in this section.

Suppose we are searching for the gravitational-wave signal in the form of  $h(t)$  with a filter  $W(t)$ . We define the matching between the data  $d(t)$  and the filter to be

$$\begin{aligned} \hat{d} &\equiv \int_{-\infty}^\infty dt d(t)W(t) \\ &= \int_{-\infty}^\infty df \tilde{d}(f)\tilde{W}^*(f). \end{aligned} \quad (1.96)$$

Furthermore, the signal-to-noise ratio is defined to be  $\rho \equiv S/N$ , where  $S$  is the mean of  $\hat{d}$  in the presence of a gravitational-wave signal, and  $N$  is the root-mean-square value of  $\hat{d}$  when no gravitational wave is present. Therefore,

$$\begin{aligned} S &\equiv \langle \hat{d} \rangle, \text{ with } d(t) = h(t) + n(t) \\ &= \left\langle \int_{-\infty}^\infty dt d(t)W(t) \right\rangle \\ &= \int_{-\infty}^\infty dt \langle d(t) \rangle W(t) \\ &= \int_{-\infty}^\infty dt h(t)W(t) \\ &= \int_{-\infty}^\infty df \tilde{h}(f)\tilde{W}^*(f) \\ &= 2\Re \int_0^\infty df \tilde{h}(f)\tilde{W}^*(f), \end{aligned} \quad (1.97)$$

and

$$\begin{aligned}
 N^2 &\equiv \langle \hat{d}^2 \rangle - \langle \hat{d} \rangle^2, \text{ with } d(t) = n(t) \\
 &= \langle \hat{d}^2 \rangle \\
 &= \int_{-\infty}^{\infty} \int_{-\infty}^{\infty} dt dt' \langle n(t)n(t') \rangle W(t)W(t') \\
 &= \frac{1}{2} \int_{-\infty}^{\infty} df S_n(f) \tilde{W}(f) \tilde{W}^*(f) \\
 &= \int_0^{\infty} df S_n(f) \tilde{W}(f) \tilde{W}^*(f).
 \end{aligned} \tag{1.98}$$

The resulting signal-to-noise ratio  $\rho$  is given by

$$\begin{aligned}
 \rho &= 2\Re \int_0^{\infty} df \tilde{h}(f) \tilde{W}^*(f) / \sqrt{\int_0^{\infty} df S_n(f) \tilde{W}(f) \tilde{W}^*(f)} \\
 &= 4\Re \int_0^{\infty} df \tilde{h}(f) \tilde{W}^*(f) / \sqrt{4\Re \int_0^{\infty} df S_n(f) \tilde{W}(f) \tilde{W}^*(f)} \\
 &= 4\Re \int_0^{\infty} df \tilde{h}(f) \tilde{W}^*(f) / S_n(f) / \sqrt{4\Re \int_0^{\infty} df \tilde{W}(f) \tilde{W}^*(f) / S_n(f)} \\
 &= \frac{\langle h | \hat{W} \rangle}{\sqrt{\langle \hat{W} | \hat{W} \rangle}},
 \end{aligned} \tag{1.99}$$

where the noise-weighted inner product (Eq. (1.95)) is used at the last line to simplify the expression, and  $\tilde{W}$  is given by

$$\tilde{W} = \tilde{W}(f) S_n(f). \tag{1.100}$$

To maximize the signal-to-noise ratio  $\rho$ , the optimal filter to be used is given by

$$\tilde{W}(f) \propto \frac{\tilde{h}(f)}{S_n(f)}, \tag{1.101}$$

and the corresponding signal-to-noise ratio is referred as the optimal signal-to-noise ratio, which is given by

$$\rho_{\text{opt}} = \sqrt{\langle h | h \rangle}. \tag{1.102}$$

Ninety candidate signals [46] have been detected so far by the Advanced LIGO [4] and Advanced Virgo [10] gravitational wave detectors, the bulk of which are from merging binary black holes [5–7, 47, 48], as well as two binary neutron star inspirals [9, 49] and two neutron star-black hole coalescences [50]. Moreover, the electromagnetic counterparts of GW170817 [9], namely, a kilonova AT2017gfo [51–59] and a gamma-ray burst GRB170817A [11, 12] were detected. Together with the radio and X-ray observations of isolated neutron stars [60–66], this marks the beginning of the multi-messenger era.

This chapter briefly reviews the physics of binary black holes and neutron stars. We will first introduce the orbit of binary point masses beyond the Newtonian approximation, then describe inspiral-only and inspiral-merger-ringdown gravitational-wave waveform models. After that, the physics of isolated neutron stars will be described, together with the corresponding observations made on them. Finally, we will discuss both the electromagnetic and gravitational signals emitted by binary neutron stars.

## 2.1 Binary black holes

A black hole is one of the simplest objects in the Universe. By the no-hair theorem, a stationary black hole is fully characterized by its mass, electric charge, and angular momentum [67]. In Sec. 1.2.5, we described the gravitational waves emitted by binary point masses, which turns out to be the lowest order approximation for the behavior of a binary black hole. This section will discuss the higher-order corrections to binary black hole orbits and how it leads to accurate waveform models.

### 2.1.1 Beyond the Newtonian approximation

In Sec. 1.2.5, we have assumed the orbit to be fully Newtonian. This assumption neglected the loss of energy and angular momentum by the emission of gravitational waves. Based on the second-order expansion of the linearized Einstein field equation, one can derive the expression for the stress-energy tensor of gravitational waves. Under TT gauge, the power  $\mathcal{P}$  of gravitational waves far away from the source is given by [68]

$$\mathcal{P} \equiv \dot{E}_{\text{GW}} = \frac{r^2}{16\pi} \int d\Omega \langle \dot{h}_{ij}^{\text{TT}} \dot{h}_{ij}^{\text{TT}} \rangle_t, \quad (2.1)$$

where  $\langle \cdot \rangle_t$  denotes average over a time interval much longer than the gravitational wave's period, and  $\Omega$  is the solid angle.

By assuming the binary's rate of energy loss to be equal to the gravitational wave power,

$$\frac{dE}{dt} = -\mathcal{P}, \quad (2.2)$$

one can solve for the motion of the binary iteratively. By taking the waveform of a Newtonian binary as shown in Eq. (1.81), the power is given by

$$\begin{aligned}
 \mathcal{P} &= \int d\Omega \frac{2}{\pi} (\mathcal{M}_c \omega_{\text{orb}})^{10/3} \left( \left( \frac{1 + \cos^2(\iota)}{2} \right)^2 + \cos^2(\iota) \right) \\
 &= 4 (\mathcal{M}_c \omega_{\text{orb}})^{10/3} \int_0^\pi d\iota \sin(\iota) \left( \left( \frac{1 + \cos^2(\iota)}{2} \right)^2 + \cos^2(\iota) \right) \\
 &= \frac{32}{5} (\mathcal{M}_c \omega_{\text{orb}})^{10/3} \\
 &\equiv \frac{32}{5} (\pi \mathcal{M}_c f_{\text{GW}})^{10/3},
 \end{aligned} \tag{2.3}$$

where  $f_{\text{GW}} = 2f_{\text{orb}} = \omega_{\text{orb}}/\pi$ . Moreover, the total energy of the binary  $E$  is

$$\begin{aligned}
 E &= \frac{1}{2} m_1 v_1^2 + \frac{1}{2} m_2 v_2^2 - \frac{m_1 m_2}{R} \\
 &= -\frac{1}{2} \frac{m_1 m_2}{R} \\
 &= -\frac{1}{2} \mathcal{M}_c (\pi \mathcal{M}_c f_{\text{GW}})^{2/3}.
 \end{aligned} \tag{2.4}$$

By using Eq. (2.2), one obtains

$$\dot{f}_{\text{GW}} = \frac{96}{5} \frac{f_{\text{GW}}}{\mathcal{M}_c} (\pi \mathcal{M}_c f_{\text{GW}})^{8/3}, \tag{2.5}$$

and

$$f_{\text{GW}}(t) = \frac{1}{\pi \mathcal{M}_c} \left( \frac{5}{256} \frac{\mathcal{M}_c}{t_c - t} \right)^{3/8}, \tag{2.6}$$

where  $t_c$  is the time of coalescence and  $f_{\text{GW}}(t)$  is the instantaneous gravitational wave frequency. These expressions match our physical intuition; as the binary loses energy, the two masses spiral towards each other with increasing velocity. Because we have assumed the two black holes to be point masses, the frequency diverges at  $t = t_c$ .

Given the frequency evolution, the associated gravitational-wave waveform is given by

$$\begin{aligned}
 h_+(t) &= \frac{\mathcal{M}_c}{r} \left( \frac{5\mathcal{M}_c}{t_c - t} \right)^{1/4} \frac{1 + \cos^2(\iota)}{2} \cos(\Phi_{\text{GW}}(t)), \\
 h_\times(t) &= -\frac{\mathcal{M}_c}{r} \left( \frac{5\mathcal{M}_c}{t_c - t} \right)^{1/4} \cos(\iota) \sin(\Phi_{\text{GW}}(t)),
 \end{aligned} \tag{2.7}$$

where

$$\begin{aligned}
 \Phi_{\text{GW}}(t) &= -\int_t^{t_c} dt' 2\pi f_{\text{GW}}(t') + \Phi_c \\
 &= -2 \left( \frac{t_c - t}{5\mathcal{M}_c} \right)^{5/8} + \Phi_c,
 \end{aligned} \tag{2.8}$$

where  $\Phi_c$  is the phase of the gravitational wave at  $t = t_c$ .

For binary black holes, the point mass approximation fails when the separation of the

two black holes is comparable to their event horizon radii. To resolve the evolution of the horizons during inspiral requires techniques of numerical relativity, which take a significant amount of computational resources. Therefore it is common to use the innermost stable circular orbit (ISCO) as a proxy for where the approximation breaks down. The ISCO of a black hole is the closest marginally stable circular orbit for a test particle to orbit around it [67]. For a non-spinning, chargeless black hole with mass  $M$ , the ISCO locates at  $6M$  from the center of it. The corresponding gravitational wave frequency for ISCO is given by

$$f_{\text{GW,ISCO}} = \frac{1}{6^{3/2}\pi M}, \quad (2.9)$$

which is also taken to be the frequency at which the inspiral picture no longer holds.

### 2.1.2 Post-Newtonian waveform models

We have a first glance of the behavior of a binary beyond Newtonian gravity in Sec. 2.1.1, which gives a qualitative picture of how a binary behaves in general relativity. To obtain an accurate representation of the binary's motion, especially the corresponding gravitational-wave waveform, the post-Newtonian (PN) expansion formalism is introduced. The PN expansion is a series expansion in terms of the characteristic velocity  $v$  of the binary. Therefore, by including higher powers of  $v$ , the resulting series would be representative at higher velocity. The term ‘‘PN order’’ is often used for stating the powers of  $v$  beyond leading order is included in an expression; in particular, an  $n$ -PN order expression includes up to  $v^{2n}$  beyond the leading order.

The PN formalism based on Kepler's third law and the energy-power equation Eq. (2.2). Those equations are often rewritten in terms of  $v$  [69]

$$\frac{d\Phi_{\text{orb}}}{dt} = \frac{v^3}{m_1 + m_2} \equiv \frac{v^3}{M}, \quad (2.10)$$

$$\frac{dv}{dt} = -\frac{\mathcal{P}(v)}{dE(v)/dv} \equiv -\frac{\mathcal{P}(v)}{E'(v)}, \quad (2.11)$$

or, equivalently,

$$\Phi_{\text{orb}}(v) = \Phi_{\text{ref}} + \int_v^{v_{\text{ref}}} dv \frac{v^3 E'(v)}{M \mathcal{P}(v)}, \quad (2.12)$$

$$t(v) = t_{\text{ref}} + \int_v^{v_{\text{ref}}} dv \frac{E'(v)}{\mathcal{P}(v)}, \quad (2.13)$$

where  $\Phi_{\text{orb}} = \int^t dt' \omega_{\text{orb}}(t') = \Phi_{\text{GW}}/2$  is the orbital phase and the subscript ‘‘ref’’ denotes an arbitrary reference quantity. One can see that the expressions for  $\mathcal{P}(v)$  and  $E$  are the foundation for any PN calculation. Once they are known, the associated waveform can be calculated.

The energy  $E(v)$  (up to 3PN order) and the flux  $\mathcal{P}(v)$  (up to 3.5PN order) are [70–80]

$$E(v) = -\frac{1}{2}\eta M v^2 \left[ 1 - \left( \frac{3}{4} + \frac{1}{12}\eta \right) v^2 - \left( \frac{27}{8} - \frac{19}{8}\eta + \frac{1}{24}\eta^2 \right) v^4 - \left( \frac{675}{64} - \left( \frac{34445}{576} - \frac{205}{96}\pi^2 \right) \eta + \frac{155}{96}\eta^2 + \frac{35}{5184}\eta^3 \right) v^6 \right], \quad (2.14)$$

Quantity	$\mathcal{P}(v)/E'(v)$	$\Phi_{\text{orb}}(v)$	$t(v)$	$\Phi_{\text{orb}}(t)$
TaylorT1	-	-	-	Numerically solve
TaylorT2	Power series in $v$	Power series in $v$	Power series in $v$	Numerically solve
TaylorT3	Power series in $v$	Power series in $v$	Power series in $v$	Power series in $\theta$
TaylorT4	Power series in $v$	-	-	Numerically solve

Table 2.1: Summary of time-domain Taylor approximants.

Different approaches taken by different Taylor approximants are shown. The “-” denotes that the quantity is not used or no treatment is done. “Numerically solve” refers to numerically solving Eq. (2.10) and Eq. (2.11) simultaneously. With  $\theta = (\eta(t_{\text{ref}} - t)/5M)^{-1/8}$ . Details can be found in Ref. [69].

$$\begin{aligned}
 \mathcal{P}(v) = & \frac{32}{5}\eta^2 v^{10} \left[ 1 - \left( \frac{1247}{336} + \frac{35}{12}\eta \right) v^2 + 4\pi v^3 - \left( \frac{44711}{9072} - \frac{9271}{504}\eta - \frac{65}{18}\eta^2 \right) v^4 \right. \\
 & - \left( \frac{8191}{672} + \frac{583}{24}\eta \right) \pi v^5 + \left\{ \frac{6643739519}{69854400} + \frac{16}{3}\pi^2 - \frac{1712}{105}\gamma + \left( \frac{41}{48}\pi^2 - \frac{134543}{7776} \right) \eta \right. \\
 & \left. \left. - \frac{94403}{3024}\eta^2 - \frac{755}{324}\eta^3 - \frac{856}{105} \ln(16v^2) \right\} v^6 - \left( \frac{16285}{504} - \frac{214745}{1728}\eta - \frac{193385}{3024}\eta^2 \right) \pi v^7 \right],
 \end{aligned} \tag{2.15}$$

where  $\eta = m_1 m_2 / M^2$  and  $\gamma = 0.57721 \dots$  are the symmetric mass ratio and the Euler-Mascheroni constant, respectively. Because one is dealing with a perturbative series, one is free to “re-expand” or “re-sum” the series in whatever way one wants while the order in the perturbation expansions is kept consistent. The resulting waveforms are referred as the Taylor approximants; their approaches are summarised in Tab. 2.1.

As shown in Sec. 1.3.3, gravitational-wave data analysis is done in the frequency domain. Therefore, it is beneficial to have the waveform analytically Fourier transformed for lower computational cost. Yet, an approximation has to be taken for the Fourier transform, referred to as the stationary phase approximation (SPA).

Given a time-domain waveform

$$h(t) = A(t) \cos(2\Phi_{\text{orb}}(t)), \tag{2.16}$$

the frequency-domain waveform is

$$\begin{aligned}
 \tilde{h}(f) &= \int_{-\infty}^{\infty} dt A(t) \cos(2\Phi_{\text{orb}}(t)) \exp(-i2\pi ft) \\
 &= \frac{1}{2} \int_{-\infty}^{\infty} dt A(t) (\exp(i2\Phi_{\text{orb}}(t) - i2\pi ft) + \exp(-i2\Phi_{\text{orb}}(t) - i2\pi ft)).
 \end{aligned} \tag{2.17}$$

In SPA, we assume the orbital phase to be rapidly varying. Therefore, the second exponential is neglected as it is oscillating rapidly and averages to zero. By contrast, the first exponent can be approximated as

$$2\Phi_{\text{orb}}(t) - 2\pi ft \approx 2\Phi_{\text{orb}}(t_*) + \ddot{\Phi}_{\text{orb}}(t - t_*)^2 - 2\pi ft_*, \tag{2.18}$$

where  $t_*$  is the saddle point at which  $d\Phi_{\text{orb}}(t)/dt|_{t=t_*} = \pi f$ . Assuming the variation of

In  $A(t)$  to be slow around  $t_*$ , the resulting waveform  $\tilde{h}_{\text{SPA}}(f)$  is given by

$$\begin{aligned}\tilde{h}_{\text{SPA}}(f) &= \frac{1}{2}A(t_*) \exp(i2\Phi_{\text{orb}}(t_*) - i2\pi ft_*) \int_{-\infty}^{\infty} dt \exp(i\ddot{\Phi}_{\text{orb}}(t_*)(t - t_*)^2) \\ &= \frac{1}{2}A(t_*) \sqrt{\frac{\pi}{\ddot{\Phi}_{\text{orb}}(t_*)}} \exp\left(i2\Phi_{\text{orb}}(t_*) - i2\pi ft_* + \frac{\pi}{4}\right).\end{aligned}\quad (2.19)$$

To solve for  $t_*$  and  $\Phi_{\text{orb}}$ , one make use of the equations

$$t_* = t_{\text{ref}} + \int_{v_*}^{v_{\text{ref}}} dv \frac{E'(v)}{\mathcal{P}(v)}, \quad (2.20)$$

$$\Phi_{\text{orb}}(t_*) = \phi_{\text{ref}} - 2 \int_{v_*}^{v_{\text{ref}}} dv (v_*^3 - v^3) \frac{E'(v)}{\mathcal{P}(v)}, \quad (2.21)$$

where  $v_* = (\pi Mf)^{1/3}$  based on the definition of the saddle point. Because the fraction  $E'(v)/\mathcal{P}(v)$  is expanded in a power series of  $v$  in TaylorT2, it allows for analytical calculation for Eq. (2.20) and Eq. (2.21). The resulting waveform model, TaylorF2, is the most commonly used PN approximant. The TaylorF2 waveform is given by

$$\tilde{h}_{+, \times}(f) = \mathcal{A}_{+, \times} f^{-7/6} \exp(i\phi(f)), \quad (2.22)$$

where

$$\begin{aligned}\mathcal{A}_+ &= \frac{1 + \cos^2 \iota}{2r} \sqrt{\frac{5\pi}{96}} \mathcal{M}_c^{5/6} \pi^{-7/6}, \\ \mathcal{A}_\times &= \frac{\cos \iota}{r} \sqrt{\frac{5\pi}{96}} \mathcal{M}_c^{5/6} \pi^{-7/6} \exp\left(i\frac{\pi}{2}\right),\end{aligned}\quad (2.23)$$

and

$$\phi(f) = 2\pi f t_{\text{ref}} + \phi_{\text{ref}} + \frac{\pi}{4} + \frac{3}{128\eta} v^{-5} \left[ \sum_{k=0}^7 \varphi_k v^k + \sum_{k=5}^6 \varphi_k^l \ln(v) v^k \right], \quad (2.24)$$

where  $v = (\pi M f)^{1/3}$ . The PN coefficients are give by

$$\begin{aligned}
 \varphi_0 &= 1, \\
 \varphi_1 &= 0, \\
 \varphi_2 &= \frac{20}{9} \left( \frac{743}{336} + \frac{11}{4} \eta \right), \\
 \varphi_3 &= -16\pi, \\
 \varphi_4 &= 10 \left( \frac{3058673}{1016064} + \frac{5429}{1008} \eta + \frac{617}{144} \eta^2 \right), \\
 \varphi_5 &= \pi \left( \frac{38645}{756} - \frac{65}{9} \eta \right) (1 - 3 \ln(v_{\text{ISCO}})), \\
 \varphi_5^l &= \pi \left( \frac{38645}{756} - \frac{65}{9} \eta \right), \\
 \varphi_6 &= \frac{11583231236531}{4694215680} - \frac{640}{3} \pi^2 - \frac{6848}{21} (\gamma - \ln 4) \\
 &\quad + \left( -\frac{15737765635}{3048192} + \frac{2255\pi^2}{12} \right) \eta + \frac{76055}{1728} \eta^2 \\
 &\quad - \frac{127825}{1296} \eta^3, \\
 \varphi_6^l &= -\frac{6848}{21}, \\
 \varphi_7 &= \pi \left( \frac{77096675}{254016} + \frac{378515}{1512} \eta - \frac{74045}{756} \eta^2 \right).
 \end{aligned} \tag{2.25}$$

These PN coefficients describe the waveform for non-spinning point masses in a binary. In addition, the contribution of spins can be calculated and can be included in the TaylorF2 waveform [81–83], which allows the waveform to be used for analyzing binary black hole signals. Moreover, the contribution due to matter’s tidal effect is also calculated, which allows for binary neutron star studies [84, 85]. We will further discuss this tidal effect in Sec. 2.2.3.

Undoubtedly, TaylorF2 is a successful model that allows numerous gravitational-wave studies. Because of its completely analytical form, it is quick to evaluate. This is a substantial advantage for parameter estimation as that requires the waveform for different parameters to be generated millions or billions of times. Yet, this model is a so-called inspiral-only approximant, which does not include the waveform beyond inspiral, namely, merger and ringdown. Moreover, it has been shown that the TaylorF2 waveform is less accurate for massive systems as SPA breaks down when the phase variation is slow [69].

To overcome these issues, inspiral-merger-ringdown (IMR) waveform models have been developed, which will be introduced in Sec. 2.1.3.

### 2.1.3 Phenomenological IMR waveform models

A phenomenological IMR waveform model is an analytical extension of TaylorF2 to include the merger and ringdown regimes. This class of waveforms is referred to as IMRPhenom. An analytical extension, ansatz, is calibrated against numerical relativity simulations. The resulting waveform is validated with numerical relativity. Note, however, that unlike numerical waveforms, analytical IMR waveforms are fast to generate on a



computer, as is needed for use in data analysis. This section will give a brief review of the IMRPhenomD waveform model [86, 87], which is the foundation for the IMRPhenomPv2 waveform model [88], one of the most used waveform models.

IMRPhenomD starts with a frequency domain waveform given by

$$\begin{aligned}\tilde{h}(f) &= \tilde{h}_+(f) - i\tilde{h}_\times \\ &= \sum_{m=-2,2} \tilde{h}_{2m}(f)^{-2} Y_{2m},\end{aligned}\tag{2.26}$$

where  $^{-2}Y_{2m}(\iota, \psi)$  is the spin weighted spherical harmonic with weight  $-2$ , which gives the waveforms angular dependence, and  $\tilde{h}_{-2}(f) = \tilde{h}_{22}^*(-f)$ . Therefore the source dependence of the waveform is all captured in  $\tilde{h}_{22}(f)$ , which can be written as

$$\tilde{h}_{22}(f) = A(f) \exp(-i\phi(f)).\tag{2.27}$$

The phase  $\phi(f)$  and the amplitude  $A(f)$  are split into three regions: inspiral, intermediate, and merger-ringdown.

Region	Ansatz	Range for $f$
Inspirational $\phi_{\text{Insp}}$	$\phi_{\text{TF2}} + \left[ \sigma_0 + \sigma_1 f + 3\sigma_2 f^{4/3}/4 + 3\sigma_3 f^{5/3}/5 + \sigma_4 f^2/2 \right] / \eta$	$[0.0035/M, 0.018/M]$
Intermediate $\phi_{\text{Int}}$	$[\beta_0 + \beta_1 f + \beta_2 \ln(f) - \beta_3 f^{-3}/3] / \eta$	$[0.018/M, 0.5 f_{\text{RD}}]$
Merger-ringdown $\phi_{\text{MR}}$	$\left[ \alpha_0 + \alpha_1 f - \alpha_2 f^{-1} + \frac{4}{3} \alpha_3 f^{3/4} + \alpha_4 \tan^{-1} \left( \frac{f - \alpha_5 f_{\text{RD}}}{f_{\text{damp}}} \right) \right] / \eta$	$[0.5, 1.15] f_{\text{RD}}$

Table 2.2: Summary of the IMRPhenomD phasing ansatz.

The parameters  $\{\{\sigma_i\}, \{\beta_i\}, \{\alpha_i\}\}$  are calibrated against numerical relativity simulations.

The phasing ansatzes are summarised in Tab. 2.2. For inspiral, additional higher PN order terms  $\{\sigma_i\}$  are added to the spin-included TaylorF2 phase  $\phi_{\text{TF2}}$ . These additional terms allow the frequency power series to be valid towards a higher frequency. The intermediate region acts as a bridge connecting the inspiral and the merger-ringdown region. This phasing region is used up to  $0.5 f_{\text{RD}}$ , which is half of the ringdown frequency for the resulting black hole. For the merger-ringdown region, the information of the final black hole is used, in particular, its ringdown frequency  $f_{\text{RD}}$  and damping frequency  $f_{\text{damp}}$ .

Region	Ansatz	Range for $f$
Inspirational $A_{\text{Insp}}$	$\sum_{i=0}^6 \mathcal{A}_i (\pi f)^{i/3} + \sum_{i=1}^3 \rho_i f^{(6+i)/3}$	$[0, 0.014/M]$
Intermediate $A_{\text{Int}}$	$\delta_0 + \delta_1 f + \delta_2 f^2 + \delta_3 f^3 + \delta_4 f^4$	$[0.014/M, f_{\text{peak}}]$
Merger-ringdown $A_{\text{MR}}$	$\gamma_1 \gamma_3 f_{\text{damp}} / ((f - f_{\text{RD}})^2 + (\gamma_3 f_{\text{damp}})^2) \times \exp(-\gamma_2 (f - f_{\text{RD}}) / (\gamma_3 f_{\text{damp}}))$	$[f_{\text{peak}}, 1.2 f_{\text{RD}}]$

Table 2.3: Summary of the IMRPhenomD amplitude ansatz.

The parameters  $\{\{\rho_i\}, \{\gamma_i\}\}$  are calibrated against numerical relativity simulations.

Similarly, the amplitude is also proposed to be a piecewise function of frequency. The amplitude ansatzes are normalized by a factor  $A_0$ , which is defined by

$$(2.28)$$

The normalized amplitude ansatzes are summarised in Tab. 2.3. For the inspiral's amplitude, the ansatz starts with a re-expansion of the PN amplitude  $A_{\text{PN}}$  as

$$A_{\text{PN}} = A_0 \sum_{i=0}^6 \mathcal{A}_i(\pi f)^{i/3}. \quad (2.29)$$

with the  $\{\rho_i\}$  included for better high frequency performance. In the merger-ringdown regime, a Lorentzian that peaks at  $f_{\text{RD}}$  is combined with an exponential. The resulting function peaks at  $f_{\text{peak}}$ , which is given by

$$f_{\text{peak}} = f_{\text{RD}} + f_{\text{damp}} \frac{\gamma_3}{\gamma_2} (\sqrt{1 - \gamma_2^2} - 1). \quad (2.30)$$

Again, the intermediate region bridges the gap between inspiral and merger-ringdown regions for  $Mf \in [0.014, Mf_{\text{peak}}]$ . Instead of being free parameters, the  $\{\delta_i\}$  are the solution for the amplitude to be  $C(1)$  continuous at  $Mf = 0.014, f_{\text{peak}}$ . Moreover, the amplitude at  $f_2^A = (0.014/M + f_{\text{peak}})/2$  is enforced to match the numerical relativity simulations. Thus the parameters involved  $\{\Lambda^i\}$  are

$$\{\Lambda^i\} = \left\{ \overbrace{\{\{\rho_j\}, \{A_{\text{Int}}(f_2^A)\}\}}^{\text{Amplitude coefficients}}, \overbrace{\{\{\gamma_j\}, \{\sigma_j\}, \{\beta_j\}, \{\alpha_j\}\}}^{\text{Phase coefficients}} \right\}. \quad (2.31)$$

These are set to be a power series as

$$\Lambda^i(\eta, \chi_{\text{PN}}) = \sum_{j=0}^2 \sum_{k=0}^3 \lambda_{jk}^i \eta^j (\chi_{\text{PN}} - 1)^k, \quad (2.32)$$

where the  $\lambda_{jk}^i$  are fitted against numerical relativity waveforms. In the above,  $\chi_{\text{PN}}$  is the leading-order spin contribution on the binary's phasing in the post-Newtonian formalism [89–91], which is given by

$$\chi_{\text{PN}} = \frac{m_1 \chi_1 + m_2 \chi_2}{M} - \frac{38\eta}{113} (\chi_1 + \chi_2), \quad (2.33)$$

where the  $\chi_i$  are the dimensionless spins of the two black holes along the orbital angular momentum  $\vec{L}$ ,

$$\chi_i = \frac{\vec{S}_i}{m_i^2} \cdot \vec{L}, \quad (2.34)$$

with  $\vec{S}_i$  the rotational angular momenta of the black holes. To connect the phases and amplitudes for different region, the step functions

$$\theta(f - f_0) = \begin{cases} -1, & f < f_0, \\ 1, & f \geq f_0, \end{cases} \quad (2.35)$$

and

$$\theta_{f_0}^{\pm} = \frac{1}{2}(1 \pm \theta(f - f_0)), \quad (2.36)$$

are used. The resulting waveform phase  $\phi_{\text{IMR}}$  is given by

$$\phi_{\text{IMR}} = \phi_{\text{Insp}}\theta_{f_1}^- + \theta_{f_1}^+\phi_{\text{Int}}\theta_{f_2}^- + \theta_{f_2}^+\phi_{\text{MR}}, \quad (2.37)$$

where  $Mf_1 = 0.018$  and  $f_2 = 0.5f_{\text{RD}}$ . The associated amplitude  $A_{\text{IMR}}$  is given by

$$\frac{A_{\text{IMR}}}{A_0} = A_{\text{Insp}}\theta_{f_1}^- + \theta_{f_1}^+A_{\text{Int}}\theta_{f_2}^- + \theta_{f_2}^+A_{\text{MR}}, \quad (2.38)$$

where  $Mf_1 = 0.014$  and  $f_2 = f_{\text{peak}}$ .

In general, the spin vectors of binary black holes are not aligned, leading them to precess. Such a general spin waveform is often referred as precession waveform, as it allows the spins to precess as the two black holes merge. To transform a non-precessing waveform  $h_{2m'}^{\text{non-prec}}(t)$  (e.g. IMRPhenomD) to a precessing one  $h_{2m}^{\text{prec}}(t)$ , one “twists” the waveform as [92]

$$h_{2m}^{\text{prec}} = \exp(-im\alpha(t)) \sum_{|m'=2|} \exp(im'\epsilon(t))d_{mm'}^2(-\beta(t))h_{2m'}^{\text{non-prec}}(t), \quad (2.39)$$

where  $d_{mm}^l$  are the Wigner d-matrices. Different twisting schemes have different approaches for the angles  $\alpha(t), \beta(t), \epsilon(t)$ . By applying the method described in Ref. [92] to IMRPhenomD, the resulting waveform is IMRPhenomPv2.

## 2.2 Neutron stars

Neutron stars are the collapsed cores of massive stars. They are the smallest and densest stellar objects except for black holes. A canonical neutron stars of 1.4 solar mass will have a typical size of 10 km, which is an object with a mass of 460000 Earths and the size of Amsterdam. This section will introduce different aspects of neutron stars. We first show how an isolated neutron star behaves as described in general relativity and the associated observations. After that, we will introduce binary neutron stars with their gravitational and electromagnetic signatures.

### 2.2.1 Isolated neutron star

The Tolman-Oppenheimer-Volkoff (TOV) equations [93, 94] describe a static neutron star. The TOV equations are the relativistic hydrostatic equations. First, we modeled the matter as a perfect fluid, with stress-energy tensor

$$T^{\mu\nu} = (\epsilon + P)u^\mu u^\nu + Pg^{\mu\nu}, \quad (2.40)$$

where  $\epsilon$ ,  $P$  and  $u^\mu$  are the energy density, pressure and the 4-velocity of the fluid. Assuming spherical symmetry, the metric takes the form

$$ds^2 = -\exp(2\Phi(r))dt^2 + \left(1 - \frac{2m(r)}{r}\right)^{-1} dr^2 + r^2 d\Omega, \quad (2.41)$$

where  $m(r)$  is the gravitational mass enclosed by a spherical surface with coordinate radius  $r$ . Plugging the stress-energy tensor Eq. (2.40) and the metric Eq. (2.41) into the Einstein field equations, one obtains the TOV equations:

$$\frac{dm}{dr} = 4\pi r^2 \epsilon, \quad (2.42a)$$

$$\frac{dP}{dr} = -\frac{m\epsilon}{r^2} \left(1 + \frac{P}{\epsilon}\right) \left(1 + \frac{4\pi r^3 P}{m}\right) \left(1 - \frac{2m}{r}\right)^{-1}, \quad (2.42b)$$

$$\frac{d\Phi}{dr} = -\frac{1}{\epsilon + P} \frac{dP}{dr}. \quad (2.42c)$$

One can easily see that the TOV equations become the Newtonian hydrostatic equations in the weak field limit  $m \ll r$  and low-pressure limit  $P \ll \epsilon$ , and  $\Phi$  is the Newtonian gravitational potential in such a limit. However, the TOV pressure gradient equation (2.42b) gives a clear physical picture of the difference between Newtonian gravity and Einstein gravity. The factors in the first two brackets show that, in addition to energy, pressure also plays a role in gravity, and the factor in the last bracket represents the metric deviation due to the presence of mass.

In Newtonian gravity, there is no upper bound for the mass of a stellar object; one can add more mass as long as the pressure can support it. But in general relativity, pressure is also a source of gravity, and there exists a point such that with more mass added, the resulting mass and pressure would cause the star to collapse into a black hole.

The TOV equations are not complete. To obtain a solution, one needs to provide the equation-of-state (EOS)  $\epsilon(P)$ , which is a relation between the energy density and the pressure. Yet, the exact nature of nuclear matter at such a high density is still an open scientific question. Numerous EOS models have been proposed: in Fig. 2.1, the mass-radius relation for 65 EOS models tabulated in Refs. [95–97] are shown. The resulting mass-radius relation and the maximum mass can be vastly different between different EOSs.

## 2.2.2 Chiral effective field theory and the neutron-star equation of state

Microscopic nuclear interactions are governed by multiple processes, e.g., various longer-range meson exchanges between two or more nucleons or short-range processes that are typically modeled by contact interactions. Nuclear effective field theories, like chiral EFT [98–102], provide a framework for arranging the large number of operator structures for nuclear interactions.

Nuclear EFTs start from the most general Lagrangian that is consistent with all symmetries of the fundamental theory of strong interactions, quantum chromodynamics, and that describes the various interaction mechanisms. In chiral EFT, this Lagrangian is

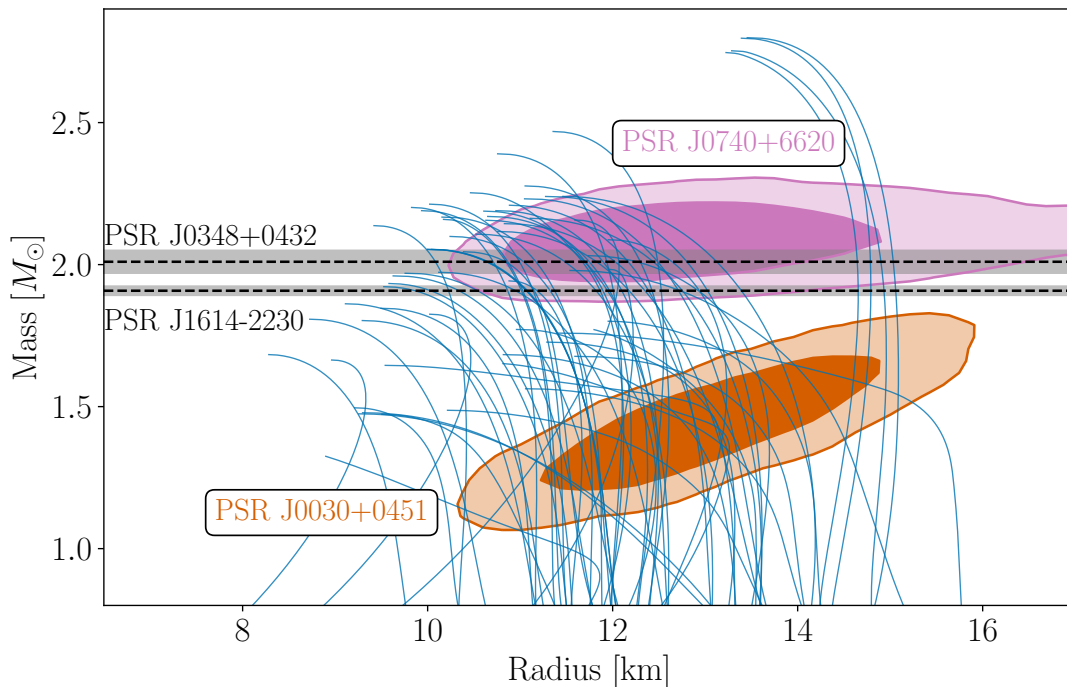


Figure 2.1: The mass-radius relations of 65 EOS models are shown, together with the mass measurement (with  $1\text{-}\sigma$  uncertainties) of the pulsars in PSR J0348+0432 and PSR J1614-2230 are shown (*dashed black lines*). The 68% and 95% credible contours for the pulsar in PSR J0740+6620 (*purple*) and PSR J0030+0451 (*orange*) are also shown.

written in terms of nucleon and pion degrees of freedom, and includes pion-exchange interactions as well as nucleon-contact interactions [98, 99]. The latter absorb short-range effects, e.g., exchanges of heavier mesons, and depend on coupling constants that have to be adjusted to experimental data. Because this Lagrangian contains an infinite number of terms, it is then expanded in powers of momenta  $p$  over the breakdown scale  $\Lambda_b$ . In addition to two-nucleon interactions, the chiral EFT expansion includes many-body forces, where three or more nucleons interact with each other. This results in a systematic and consistent expansion of two- and many-body nuclear forces, which can be truncated at a chosen order. By going to higher orders in the expansion, nuclear interactions can be systematically improved. By calculating results order-by-order, theoretical uncertainties due to our incomplete understanding of nuclear interactions can be quantified [103].

Chiral interactions allow an extrapolation of nuclear interactions away from experimentally accessible systems to those that are difficult or impossible to measure in terrestrial laboratories, e.g., the neutron-rich matter in the core of NSs. However, chiral interactions are limited to momenta  $p < \Lambda_b \approx 600$  MeV [104]. At larger momenta, chiral interactions are not reliable because short-range (high-energy) physics that was absorbed by the coupling constants needs to be explicitly included.

The EOSs used in this thesis are constrained at low densities by quantum Monte Carlo calculations of neutron matter [105, 106] at temperature  $T = 0$ , using the auxiliary field diffusion Monte Carlo approach and chiral EFT interactions in their local formulation [107–109]. The unknown coupling constants in chiral EFT are determined by fitting the nuclear Hamiltonians order-by-order to experimental data [110]. The interac-

tions used here were fitted to two-nucleon scattering data, the  ${}^4\text{He}$  ground state energy, and neutron- $\alpha$  scattering phase shifts [108, 109]. The order-by-order convergence of this approach remains valid up to densities of twice the nuclear saturation density [111].

## Pulsars

A pulsar, short for pulsing radio source, is a rotating, strongly magnetized neutron star whose magnetic poles generate beams of electromagnetic radiation. This radiation is responsible for the pulsed appearance of emission since it can only be seen when a beam is oriented toward Earth.

Observing the electromagnetic signatures of pulsars allows one to measure their macroscopic parameters. For instance, by combining radio timing and precise spectroscopy, the mass of the visible pulsar in the binary PSR J0348+0432 is estimated to be  $2.01 \pm 0.04 M_{\odot}$  [60]. Moreover, one can also measure the mass using Shapiro delay, e.g., the mass of the pulsar in the binary PSR J1614-2230 is estimated to be  $1.908 \pm 0.016 M_{\odot}$  [61]. The masses of these pulsars act as a lower bound for the maximum mass for a neutron star. Therefore, the EOSs predicting a maximum mass below these pulsars' masses are ruled out.

Moreover, by analyzing the thermal X-ray waveform of the pulsars, one can measure both the mass and the radius of a neutron star. For instance, by using a Bayesian approach to the data observed by the Neutron Star Interior Composition Explorer (NICER), the mass and radius of PSR J0030+0451 are measured to be  $1.44^{+0.15}_{-0.14} M_{\odot}$  and  $13.02^{+1.24}_{-1.06}$  km, respectively [63, 64]. The mass and radius of the most massive pulsar even observed, PSR J0740+6620, are also measured with the same approach. The mass and radius are found to be  $2.08 \pm 0.07 M_{\odot}$  and  $13.7^{+2.6}_{-1.3}$  km, respectively. As shown in Fig. 2.1, these mass-radius contours allow more EOS to be ruled out.

### 2.2.3 Binary neutron star inspirals

In 2017, the first gravitational-wave signal of a binary neutron star merger was observed [9], together with its electromagnetic signals [11, 51–59]. Numerous studies on the nuclear equation of state have been conducted with them. All these signals carry a piece of information about the equation-of-state. By analyzing them, one can obtain robust constraints on it.

#### Gravitational waves

Like a binary black hole, a binary neutron star undergoes an inspiral-merger process. However, one major difference between a binary black hole merger and a binary neutron star merger is the tidal effect of matter.

Because of the presence of the companion neutron star, both neutron stars experience an external tidal field  $\mathcal{E}_{ij}$ . In response, the neutron stars deform in a way that can approximately be described through a quadrupole moment  $Q_{ij}$ . To linear order in  $\mathcal{E}_{ij}$ , the induced quadrupole  $Q_{ij}$  is given by [112]

$$Q_{ij} = -\Lambda m^5 \mathcal{E}_{ij}, \quad (2.43)$$

where  $m$  is the neutron star's mass and  $\Lambda$  is the tidal deformability. The tidal deformability is given by

$$\Lambda = \frac{2}{3}k_2 \left(\frac{R}{m}\right)^5, \quad (2.44)$$

where  $k_2$  and  $R$  are the second tidal love number and the neutron star's radius, respectively. As shown in Fig. 2.2, the tidal deformability strongly depends on the EOS. Because different EOSs can predict tidal deformabilities that differ by orders of magnitude, it is an ideal parameter for constraining the EOS.

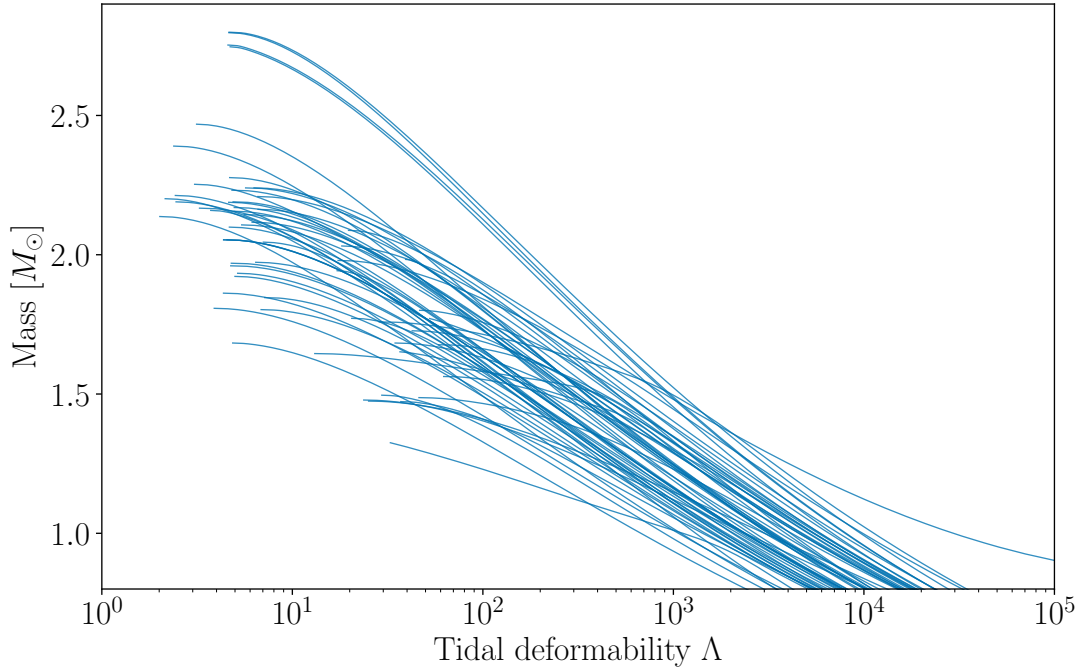


Figure 2.2: The mass-tidal-deformability relations of 65 EOS models are shown.

The effects of tidal deformations on the orbital motion can be calculated in the post-Newtonian formalism. Within the stationary phase approximation, their contribution to the phasing  $\phi_{\text{Tidal}}$  is given by [85, 113, 114]

$$\begin{aligned} \phi_{\text{Tidal}}(v) = & \frac{3}{128\eta} v^{-5} \sum_{i=1}^2 \Lambda_i X_i^4 \left[ -24(12 - 11X_i)v^{10} \right. \\ & + \frac{5}{28}(3179 - 919X_i - 2286X_i^2 + 260X_i^3)v^{12} \\ & + 24\pi(12 - 11X_i)v^{13} \\ & - 24 \left( \frac{39927845}{508032} - \frac{480043345}{9144576} X_i + \frac{9860575}{127008} X_i^2 - \frac{421821905}{2286144} X_i^3 \right. \\ & \left. \left. + \frac{4359700}{35721} X_i^4 - \frac{10578445}{285768} X_i^5 \right) v^{14} \right. \\ & \left. + \frac{\pi}{28}(27719 - 22127X_i + 7022X_i^2 - 10232X_i^3)v^{15} \right], \quad (2.45) \end{aligned}$$

where  $v = (\pi M f)^{1/3}$ ,  $X_i = m_i/M$  and  $\eta = m_1 m_2 / M^2$ . It has been shown that the tidal phasing can be conveniently re-parameterized in terms of  $(\tilde{\Lambda}, \delta\tilde{\Lambda})$  [84, 115]

$$\tilde{\Lambda} = \frac{16}{13} \Lambda_1 \frac{m_1^4}{M^4} \left( 12 - 11 \frac{m_1}{M} \right) + \frac{16}{13} \Lambda_2 \frac{m_2^4}{M^4} \left( 12 - 11 \frac{m_2}{M} \right), \quad (2.46a)$$

$$\delta\tilde{\Lambda} = \left( \frac{1690}{1319} \eta - \frac{4843}{1319} \right) \left( \frac{m_1^4}{M^4} \Lambda_1 - \frac{m_2^4}{M^4} \Lambda_2 \right) + \frac{6162}{1319} \sqrt{1 - 4\eta} \left( \frac{m_1^4}{M^4} \Lambda_1 + \frac{m_2^4}{M^4} \Lambda_2 \right), \quad (2.46b)$$

where  $\eta$  is the symmetric mass ratio.  $\tilde{\Lambda}$  is the best measured tidal parameter because it determines the leading-order 5PN contribution, while  $\delta\tilde{\Lambda}$  determines the 6PN contribution.

One can see that the contribution of tidal effects only comes in at 5<sup>th</sup> PN order or higher. Such a high PN order means that the influence only contributes to the late inspiral or the merger portion of the waveform, where the PN formalism becomes less accurate. It has been shown that the PN tidal phasing is not accurate enough for gravitational-wave parameter estimation on detections [21].

To construct an accurate description of the tidal phasing, a PN induced phasing Padé approximant was introduced and calibrated against numerical relativity simulations [116, 117]. These numerical-relativity-calibrated tidal phasings are referred to as NRTidal (or NRTidalv2 for the updated version). The NRTidal phasing has been widely used to analyze GW170817 [9] and GW190425 [49], leading to robust constraints on the nuclear equation of state.

## Quasi-universal relations

As described above, most of the neutron star properties are determined by the EOS. The resulting properties can be vastly different because of the variation between EOS models. However, it has been discovered that the relations between some properties do not depend strongly on the EOS [118]. These relations are called quasi-universal relations, also known as EOS-independent relations.

Numerous relations have been discovered ever since [20, 29, 118–121]. These relations can be helpful for astrophysical data analysis as they can reduce the number of free parameters and give rise to a tighter constraint on parameters of interest [121].

One such quasi-universal relation is the so-called *binary Love relation* [120, 121]. This relation connects the symmetric tidal deformability  $\Lambda_s \equiv (\Lambda_1 + \Lambda_2)/2$ , antisymmetric tidal deformability  $\Lambda_a \equiv (\Lambda_2 - \Lambda_1)/2$ , and the mass ratio  $q \equiv m_2/m_1$  of a binary neutron star. In particular, the relation can be expressed as

$$\frac{\Lambda_a}{\Lambda_s} = \frac{1 - q^{10/(3-n)} \left( 1 + \sum_{i=1}^3 \sum_{j=1}^2 b_{ij} q^j \Lambda_s^{-i/5} \right)}{1 + q^{10/(3-n)} \left( 1 + \sum_{i=1}^3 \sum_{j=1}^2 c_{ij} q^j \Lambda_s^{-i/5} \right)}, \quad (2.47)$$

where the parameters  $\{b_{ij}, c_{ij}\}$  are calibrated with a set of realistic EOSs and  $n = 0.743$  is the average polytropic index for the set. The values of the parameters  $\{b_{ij}, c_{ij}\}$  are shown in Tab. 2.4. This relation has been shown to achieve a  $\leq 10\%$  relative error on reproducing the tidal deformabilities predicted by the set of realistic EOSs.



$b_{11}$	-27.7408	$c_{11}$	-25.5593
$b_{12}$	8.42358	$c_{12}$	5.58527
$b_{21}$	122.686	$c_{21}$	92.0337
$b_{22}$	-19.7551	$c_{22}$	26.8586
$b_{31}$	-175.496	$c_{31}$	-70.247
$b_{32}$	133.708	$c_{32}$	-56.3076

Table 2.4: Summary of binary Love relation’s parameters  
The numerical values for the binary love relation are given in Ref. [121].

### Kilonovae

A kilonova is an electromagnetic signal in the optical, infrared, and ultraviolet emission bands due to the radioactive decay of atomic nuclei created during a binary neutron star merger. The light curve of the kilonova, *i.e.*, the time evolution of the brightness across electromagnetic frequency, depends on the source and the equation of state.

The light curves are analyzed with theoretical modeling of kilonovae [122]. The equation-of-state can be constrained by connecting the kilonova observables (e.g., ejecta mass) to the EOS via quasi-universal relations or numerical-relativity-inspired fitting relations. For details on these constraints, we refer to Refs. [26, 28].



Bayesian statistics, named after the Reverend Bayes, is the backbone of modern data analysis. It allows us to estimate the parameters of gravitational-wave sources and quantitatively compare hypotheses. This chapter will first introduce the basic concept of inductive logic, followed by Bayesian analysis for parameter estimation and hypothesis testing.

## 3.1 Inductive logic and probability theory

### 3.1.1 Boolean algebra

Boolean algebra is widely used. Boolean algebra deals with the operations on propositions. Propositions (commonly denoted by upper case roman letter, e.g.  $A, B, \dots$ ) can be statements like “apple grows on tree” or “the value  $x$  is within 3 and 4”. The operations in Boolean algebra are summarised in Table 3.1.

Instead of assigning either true or false to the propositions, one can set a degree of certainty or plausibility to them. Together with the notion of plausibility, Boolean algebra includes the idea of conditional plausibility. The conditional plausibility is denoted by

$$A|B, \tag{3.1}$$

which states “ $A$  is true given  $B$  is true”.

### 3.1.2 Bayesian probability theory

To build a mathematical framework for plausibility reasoning, Cox proposed a list of axioms [44]. By denoting the plausibility of proposition  $A$  by  $w(A)$ , the axioms can be stated as

Name	Symbol	Proposition
Conjunction	$AB$ or $A \cap B$	Both $A$ and $B$ are true
Disjunction	$A + B$ or $A \cup B$	Either $A$ or $B$ is true
Negation	$\bar{A}$ or $\neg A$	$A$ is false
Implication	$A \rightarrow B$	If $A$ is true, $B$ is true
Bi-implication	$A = B$	$B$ is true if and only if $A$ is true
Equal by definition	$A \equiv B$	By definition, $B$ is true if and only if $A$ is true

Table 3.1: Summary of operations in Boolean algebra.

Name	Probability Representation
Conjunction	$\Pr(AB) \equiv \Pr(A \cap B) \equiv \Pr(A, B) = \Pr(A B)\Pr(B)$
Disjunction	$\Pr(A + B) \equiv \Pr(A \cup B) = \Pr(A) + \Pr(B) - \Pr(AB)$
Negation	$\Pr(\neg A) \equiv \Pr(\bar{A}) = 1 - \Pr(A)$
Implication	$\Pr(B A) = 1, \Pr(B) \geq \Pr(A)$
Bi-implication	$\Pr(A) = \Pr(B)$

Table 3.2: Summary of representations of operations in Boolean algebra in probability theory.

1. Plausibilities can be ordered. If  $A$  is more plausible than  $B$  and  $B$  is more plausible than  $C$ , then  $w(A) > w(B) > w(C)$ .
2. The plausibility of a proposition's negation is determined by the plausibility of the proposition. Therefore, there exist a function  $f$  such that

$$w(\bar{A}) = f(w(A)). \quad (3.2)$$

3. The plausibility of  $A$  and  $B|A$  determines the plausibility of the conduction  $AB$ . Therefore, there exist a function  $g$  such that

$$w(AB) = g(w(A), w(B|A)). \quad (3.3)$$

Based on Boolean algebra and the proposed axioms, Cox showed that the plausibility of a proposition can be mapped onto probability. In particular, impossibility and certainty are mapped onto 0 and 1, respectively. Moreover, the rules of logical reasoning are consistent with probability theory. The representations of the Boolean operations in the context of probability theory are summarised in Table 3.2.

Based on these rules, one can derive Bayes' theorem,

$$\Pr(A|B) = \frac{\Pr(B|A)\Pr(A)}{\Pr(B)}, \quad (3.4)$$

which is the foundation of Bayesian inference. In addition one has the marginalization rule,

$$\Pr(A) = \sum_i \Pr(A, B_i), \quad (3.5)$$

where  $\{B_i\}$  is a set of mutually exclusive and exhaustive propositions, where mutually exclusive and exhaustive implies  $\Pr(B_i|B_j) = \delta_{ij}$  and  $\sum_i \Pr(B_i) = 1$ , respectively.

The above statements on probability can be extended to a continuum limit by using a probability density function  $\text{pdf}(x)$ . The probability density for propositions about real variables  $x$  is defined to be

$$\Pr(x \in [a, b]) = \int_a^b \text{pdf}(x)dx. \quad (3.6)$$

The marginalization rule in the continuum limit is given by

$$\text{pdf}(\phi) = \int_{\text{whole space}} \text{pdf}(\phi, \theta) d\theta, \quad (3.7)$$

where both  $\phi$  and  $\theta$  are a continuous variables.

## 3.2 Parameter estimation

In the context of data analysis, Bayes' theorem of Eq. (3.4) takes the form

$$p(\mathcal{H}|d, \mathcal{I}) = \frac{p(d|\mathcal{H}, \mathcal{I})p(\mathcal{H}|\mathcal{I})}{p(d|\mathcal{I})} \quad (3.8)$$

where  $d$ ,  $\mathcal{H}$  and  $\mathcal{I}$  are the data, hypothesis of interest, and the background information available before conducting the experiment, respectively. Because the above equation holds for both probability and probability density, all objects are represented by  $p(x)$ . The *prior*  $p(\mathcal{H}|\mathcal{I})$  quantifies the plausibility of the hypothesis given the background information (e.g., previous experiments). The *likelihood*  $p(d|\mathcal{H}, \mathcal{I})$  gauges how likely it is that data of a particular form are obtained given that the hypothesis is true. The *posterior*  $p(\mathcal{H}|d, \mathcal{I})$  is the primary quantity of interest, since it describes the updated plausibility of the hypothesis after the additional data is included. finally, the *evidence*  $p(d|\mathcal{I})$ , acts as a normalization constant as it is independent of the hypothesis.

One common hypothesis of interest is “the source parameter  $\vec{\theta}$  is in  $[\vec{\theta}, \vec{\theta} + d\vec{\theta}]$ ”. In such a context, the Bayes' theorem can be written as

$$p(\vec{\theta}|d, \mathcal{M}, \mathcal{I}) = \frac{p(d|\vec{\theta}, \mathcal{M}, \mathcal{I})}{p(d|\mathcal{M}, \mathcal{I})} p(\vec{\theta}|\mathcal{M}, \mathcal{I}), \quad (3.9)$$

where the hypothesis  $\mathcal{M}$  is called a generative model; it specifies the likelihood function. Here to, the evidence acts as a normalization constant, which is given by

$$p(d|\mathcal{M}, \mathcal{I}) = \int_{\text{whole space}} d\vec{\theta} p(d|\vec{\theta}, \mathcal{M}, \mathcal{I}) p(\vec{\theta}|\mathcal{M}, \mathcal{I}). \quad (3.10)$$

In cases where the parameters of interest are expected to be the same across detections  $\{d_i\}$  (e.g. neutron star equation-of-state parameters, or parameters determining population), information from multiple detections can be combined. When combing multiple detections, there is often a selection bias involved as some sources are easier to be observed than the others. This is described by the detection probability

$$p_{\text{det}}(\vec{\theta}) = \int_{d > \text{detection threshold}} dd p(d|\vec{\theta}, \mathcal{M}, \mathcal{I}). \quad (3.11)$$

Let the hyper-parameters which are shared across detections be denoted by  $\vec{\lambda}$ , and the

parameters of the  $i$ -th detection by  $\vec{\theta}_i$ . Then the joint posterior is given by [123]

$$p(\vec{\lambda}|\{d_i\}) = p(\vec{\lambda})^{1-N_{\text{obs}}} \prod_{i=1}^{N_{\text{obs}}} \frac{\int d\vec{\theta}_i p(d_i|\vec{\theta}_i) p(\theta_i|\vec{\lambda})}{\int d\vec{\theta} p_{\text{det}}(\vec{\theta}) p(\vec{\theta}|\vec{\lambda})}, \quad (3.12)$$

where the generative model and the background information are omitted for simplicity.  $N_{\text{obs}}$  is the number of detections to be combined. The inclusion of the dominator factor is to account for the selection bias [123], which is the intrinsic bias towards particular  $\vec{\lambda}$  due to different detection probability.

To apply Bayesian parameter estimation for particular field of science (e.g. gravitational-wave data analysis), the likelihood function and the detection probability has to be defined. By assuming the noise in a gravitaitonal-wave detector to be stationary Gaussian (see Ch. 3), the associated likelihood  $p(d|\vec{\theta}, \mathcal{M}, \mathcal{I})$  is given by

$$p(d|\vec{\theta}, \mathcal{M}, \mathcal{I}) \propto \exp\left(-\frac{1}{2}\langle d - h(\vec{\theta}; \mathcal{M}) | d - h(\vec{\theta}; \mathcal{M}) \rangle\right), \quad (3.13)$$

where  $h(\vec{\theta}; \mathcal{M})$  is the gravitational-wave waveform of parameters  $\vec{\theta}$  generated using the generative model  $\mathcal{M}$ . The detection probability is given by

$$p_{\text{det}}(\vec{\theta}) = \int dd \Theta(\rho - \rho_{\text{threshold}}) p(d|\vec{\theta}, \mathcal{M}, \mathcal{I}), \quad (3.14)$$

where  $\Theta(x)$  is the Heaviside step function.  $\rho$  and  $\rho_{\text{threshold}}$  are are signal-to-noise ratio given the particular noise realization and the signal-to-noise ratio threshold for detection, respectively.

## 3.3 Hypothesis testing

### 3.3.1 Bayes' factor and odds ratio

For parameter estimation, the evidence only acts as a normalization constant which is mostly neglected. Yet, it plays the main role in the context of hypothesis testing. Based on the Bayes' theorem as in Eq. (3.8), we can write

$$\frac{p(\mathcal{H}_1|d, \mathcal{I})}{p(\mathcal{H}_2|d, \mathcal{I})} = \frac{p(d|\mathcal{H}_1, \mathcal{I}) p(\mathcal{H}_1|\mathcal{I})}{p(d|\mathcal{H}_2, \mathcal{I}) p(\mathcal{H}_2|\mathcal{I})}, \quad (3.15)$$

or

$$\mathcal{O}_2^1 = \mathcal{B}_2^1 \Pi_2^1, \quad (3.16)$$

where  $\mathcal{O}_2^1$ ,  $\mathcal{B}_2^1$  and  $\Pi_2^1$  are the odds ratio, Bayes' factor and prior odds, respectively. The odds ratio quantifies the plausibility ratio between the two hypothesis  $\mathcal{H}_1$  and  $\mathcal{H}_2$  in given the data. The Bayes' factor quantifies the likelihood ratio for the two hypotheses to lead to the given data realization, and the prior odds quantifies the plausibility ratio between two hypotheses prior to the experiment.

One can understand the above equation as the Bayes' factor updates our relative belief for the two hypotheses, which is previous the prior odds, to the odds ratio. If  $\mathcal{O}_2^1 > 1$ ,  $\mathcal{H}_1$  is more plausible than  $\mathcal{H}_2$  given the data, and vice versa.

The advantage of using the Bayes' factor over the likelihood-ratio test is the inclusion of Occam's razor. The Occam's razor is a principle for problem-solving, stating;

**“Entities should not be multiplied beyond necessity.”**  
— William of Ockham.

In other words, if two hypotheses explain the data equally well, the simpler model should be more plausible.

Let us consider a toy model example with two hypotheses, namely  $\mathcal{H}_1$  and  $\mathcal{H}_2$ .  $\mathcal{H}_1$  is a hypothesis without any free parameter, *i.e.*

$$p(d|\mathcal{H}_1, \mathcal{I}) = \mathcal{L}_0. \quad (3.17)$$

$\mathcal{H}_2$  is a hypothesis with one free parameter  $\theta$ , the likelihood is given by

$$p(d|\theta, \mathcal{H}_2, \mathcal{I}) = \mathcal{L}_0 \exp\left(-\frac{1}{2} \left(\frac{\theta - \theta_0}{\sigma}\right)^2\right), \quad (3.18)$$

and

$$p(\theta|\mathcal{H}_2, \mathcal{I}) = \frac{1}{\sigma_\theta \sqrt{2\pi}} \exp\left(-\frac{1}{2} \left(\frac{\theta - \theta_0}{\sigma_\theta}\right)^2\right). \quad (3.19)$$

The maximum likelihood for the two hypotheses are the same, therefore the two hypotheses fit the data equally well with a likelihood ratio of 1. The corresponding evidences are given by

$$p(d|\mathcal{H}_1, \mathcal{I}) = \mathcal{L}_0, \quad (3.20)$$

and

$$\begin{aligned} p(d|\mathcal{H}_2, \mathcal{I}) &= \int d\theta p(d|\theta, \mathcal{H}_2, \mathcal{I})p(\theta|\mathcal{H}_2, \mathcal{I}) \\ &= \mathcal{L}_0 \sqrt{\frac{\sigma^2}{\sigma^2 + \sigma_\theta^2}}. \end{aligned} \quad (3.21)$$

The odds ratio  $\mathcal{O}_2^1$  is then given by

$$\begin{aligned} \mathcal{O}_2^1 &\equiv \frac{p(\mathcal{H}_1|d, \mathcal{I})}{p(\mathcal{H}_2|d, \mathcal{I})} \\ &= \Pi_2^1 \sqrt{1 + \frac{\sigma_\theta^2}{\sigma^2}}. \end{aligned} \quad (3.22)$$

By assuming the prior odds  $\Pi_2^1 = 1$ , the odds ratio  $\mathcal{O}_2^1$  is always larger than one. That is because the two hypotheses can explain the data equally well, but  $\mathcal{H}_2$  is penalised due to its complexity. Such a finding is a quantitative representation of Occam's razor.

Similar to parameter estimation, one can combine the information from multiple observations to strengthen the plausibility of one hypothesis over the other. The combined odds ratio, often referred as the catalog odds ratio  $\mathcal{O}_2^{1(\text{cat})}$ , is given by

$$\mathcal{O}_2^{1(\text{cat})} = \Pi_2^1 \prod_{i=1}^{N_{\text{obs}}} \mathcal{B}_{2,i}^1, \quad (3.23)$$

where  $N_{\text{obs}}$  and  $\mathcal{B}_{2,i}^1$  are the number of detections to be combined and the Bayes' factor of the  $i$ -th detection, respectively. This approach does not use the knowledge that one hypothesis can assume common parameters between detections. In such a case, a simple multiplication of Bayes' factors is a suboptimal yet conservative approach.

### 3.3.2 Background-foreground approach

Although the odds ratio can quantify the plausibility between two hypotheses, there is no quantitative cutoff for us to reject one of the hypotheses. Moreover, due to noise, the odds ratio inherits variance.

One common approach to overcoming this shortcoming is treating the odds ratio as a ranking statistic. Given two hypotheses, a null hypothesis  $\mathcal{H}_{\text{null}}$  and an alternative hypothesis  $\mathcal{H}_{\text{alt}}$ , one estimates the distribution of the odds ratio  $\mathcal{O}_{\text{null}}^{\text{alt}}$  given that the null hypothesis is true, and the noise is present. Such a distribution  $p(\mathcal{O}_{\text{null}}^{\text{alt}}|\mathcal{H}_{\text{null}})$  is called the *background* or null distribution. In most cases, one cannot analytically calculate the background; instead, the background is sampled by calculating the odds ratios for multiple realizations of the data simulated with the null hypothesis being true.

With the background estimated, given a detection with  $\mathcal{O}_{\text{null}}^{\text{alt}} = \mathcal{O}$ , the associated *false alarm probability*  $\beta$  and the *statistical significance level*  $\alpha$  are given by

$$\int_{\mathcal{O}}^{\infty} d\mathcal{O}_{\text{null}}^{\text{alt}} p(\mathcal{O}_{\text{null}}^{\text{alt}}|\mathcal{H}_{\text{null}}) = \beta = 1 - \alpha. \quad (3.24)$$

On the other hand, one can establish an odds ratio threshold  $\mathcal{O}_{\text{null,thr}}^{\text{alt}}$  given a threshold false alarm probability  $\beta_{\text{thr}}$  or a threshold statistical significance  $\alpha_{\text{thr}}$  (e.g.  $5\text{-}\sigma$ ) such that

$$\int_{\mathcal{O}_{\text{null,thr}}^{\text{alt}}}^{\infty} d\mathcal{O}_{\text{null}}^{\text{alt}} p(\mathcal{O}_{\text{null}}^{\text{alt}}|\mathcal{H}_{\text{null}}) = \beta_{\text{thr}} = 1 - \alpha_{\text{thr}}. \quad (3.25)$$

Therefore, if one observes  $\mathcal{O}_{\text{null}}^{\text{alt}} > \mathcal{O}_{\text{null,thr}}^{\text{alt}}$ , the null hypothesis can be rejected with  $\alpha_{\text{thr}}$  statistical significance. A schematic example of the background, odds ratio threshold, threshold false alarm probability, and threshold statistical significance is shown in Fig. 3.1. The hypothesis testing methodology is then completed with the background and threshold odds ratio established. The methodology can then be used against actual observations and make statistically robust statements.

Yet, the performance of the pipeline is not estimated; therefore, one does not know how likely one can reject the null hypothesis, given the alternative hypothesis is true. To estimate the performance, one can estimate the distribution of the odds ratio  $\mathcal{O}_{\text{null}}^{\text{alt}}$  given the alternative hypothesis is true. Such a distribution  $p(\mathcal{O}_{\text{null}}^{\text{alt}}|\mathcal{H}_{\text{alt}})$  is called the *foreground*. Similar to the background, the foreground is commonly sampled using multiple simulations. Given the previously chosen odds ratio threshold and estimated foreground, one can estimate the efficiency  $\xi$ , which is given by

$$\xi = \int_{\mathcal{O}_{2,\text{thr}}^1}^{\infty} d\mathcal{O}_{\text{null}}^{\text{alt}} p(\mathcal{O}_{\text{null}}^{\text{alt}}|\mathcal{H}_2). \quad (3.26)$$

Therefore, the efficiency  $\xi$  is the probability for  $\mathcal{O}_{\text{null}}^{\text{alt}}$  being higher than the threshold given the alternative hypothesis is true. A schematic example of the foreground and efficiency is shown in Fig. 3.2.



An ideal scenario is that the background and foreground distributions are highly separable. One can establish a threshold odds ratio with a false alarm probability of 0 and an efficiency of 1. In practice, it is more likely for the efficiency to be too low for the pipeline to be considered sensitive. In such a case, one case boosts the method’s sensitivity by considering the background and foreground of the catalog odds ratio instead.

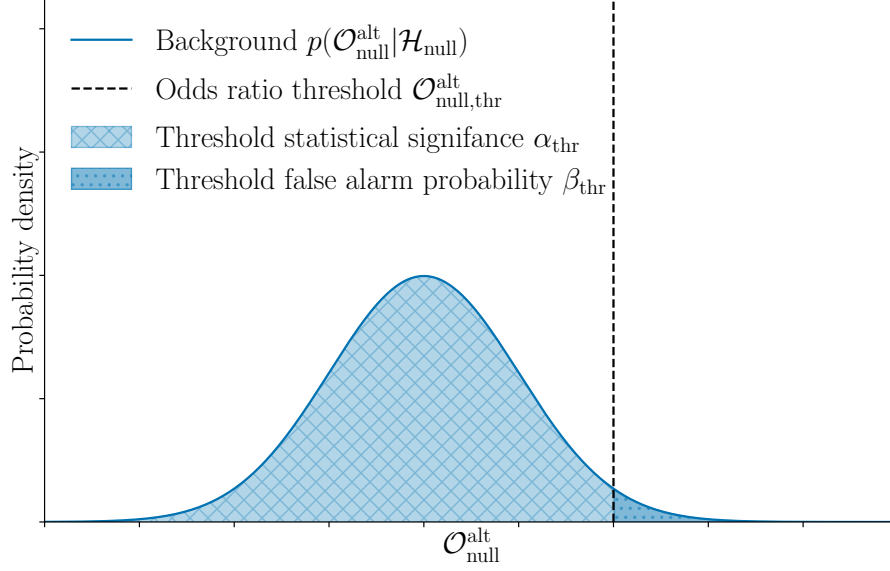


Figure 3.1: A example of the odds ratio’s background distribution is shown (*blue*). The odds ratio threshold  $O_{\text{null,thr}}^{\text{alt}}$  (*dashed black*), the corresponding statistical significance  $\alpha$  (*shaded blue cross*), and the false alarm probability (*shaded blue dotted*) are also shown.

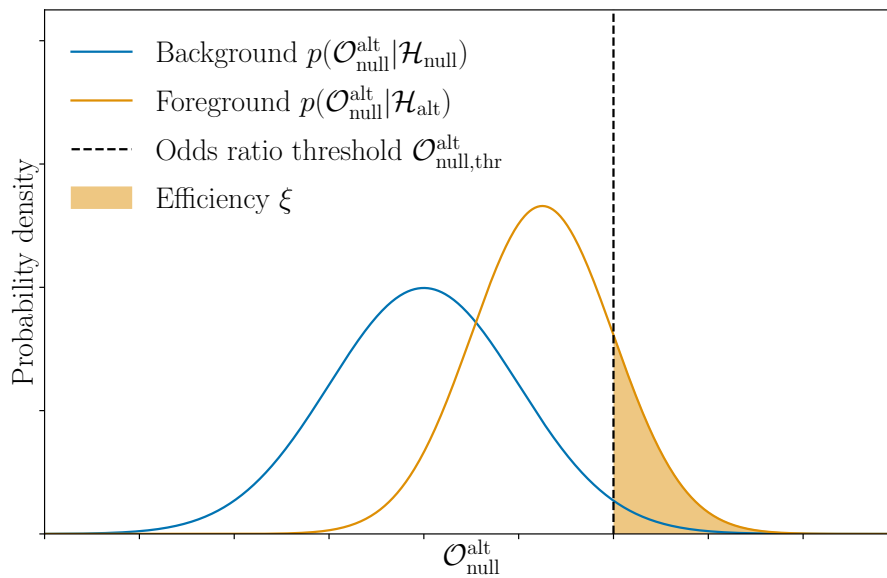


Figure 3.2: A example of the odds ratio's foreground distribution is shown (*orange*). The odds ratio threshold  $\mathcal{O}_{\text{null,thr}}^{\text{alt}}$  (*dashed black*) and the corresponding efficiency (*shaded orange dotted*) are also shown.

With the improvement in computers, numerical methods have become more popular and essential, especially in data analysis. This chapter introduces the computational techniques used in gravitational wave and multi-messenger data analysis. We will focus on the Monte Carlo methods. These methods are the practical alternatives when the curse of dimensionality makes brute-force methods impractical.

## 4.1 Monte Carlo methods

Monte Carlo methods are a class of algorithms in which repeated random sampling is utilized, thus named after the Casino de Monte Carlo in Monaco. This section will introduce two Monte Carlo methods: Markov chain Monte Carlo and nested sampling. Both methods can obtain posterior distribution samples ( $\{\vec{\theta}_i\} \sim p(\vec{\theta}|d, \mathcal{H})$ ) and estimate the evidence  $p(d|\mathcal{H})$ . Because of their advantage over brute-force methods, they are widely used in the gravitational-wave data analysis community.

### 4.1.1 Markov chain Monte Carlo

Markov chain Monte Carlo is a subclass of Monte Carlo for sampling from a target probability distribution. A Markov chain Monte Carlo method iteratively transforms the distribution using a transition probability  $T(\vec{\theta}', \vec{\theta})$  given an initial distribution  $p_0(\vec{\theta})$ . The probability density at the  $t$ -th iteration of the Markov chain  $p_t(\vec{\theta})$  is [44]

$$p_t(\vec{\theta}') = \int d\vec{\theta} T(\vec{\theta}', \vec{\theta}) p_{t-1}(\vec{\theta}). \quad (4.1)$$

When constructing a Markov chain Monte Carlo method, the resulting chain must have the following properties [44]:

1. The desired distribution  $\pi(\vec{\theta})$  has to be invariant for the chain, therefore

$$\pi(\vec{\theta}') = \int d\vec{\theta} T(\vec{\theta}', \vec{\theta}) \pi(\vec{\theta}), \quad (4.2)$$

which can be accomplished if the chain has detailed balance, meaning,

$$T(\vec{\theta}', \vec{\theta}) \pi(\vec{\theta}) = T(\vec{\theta}, \vec{\theta}') \pi(\vec{\theta}'). \quad (4.3)$$

2. The  $t$ -th iteration's chain converges to the invariant distribution as  $t$  approaches infinity for any given initial distribution. This property is referred to as ergodicity.

### Metropolis-Hasting algorithm

Metropolis-Hasting algorithm [124, 125] is a Markov chain Monte Carlo method for generating a sequence of samples from the desired distribution  $\pi(\vec{\theta})$ . The algorithm is beneficial when the desired distribution is challenging to sample.

Given the current state  $\vec{\theta}_t$ , a new state  $\vec{\theta}'$  is proposed using a proposal density  $Q(\vec{\theta}'|\vec{\theta})$ . The new state  $\vec{\theta}'$  is accepted as the next state, therefore,  $\vec{\theta}_{t+1} = \vec{\theta}'$ , with a probability  $a$ . The probability  $a$  is given by

$$a = \min \left( 1, \frac{\pi(\vec{\theta}')}{\pi(\vec{\theta}_t)} \frac{Q(\vec{\theta}_t|\vec{\theta}')}{Q(\vec{\theta}'|\vec{\theta}_t)} \right). \quad (4.4)$$

If the new state is rejected, then

$$\vec{\theta}_{t+1} = \vec{\theta}_t. \quad (4.5)$$

There are two disadvantages of the Metropolis-Hasting algorithm. At first, some iterations are needed before the dependence on the starting location of the chain is lost. The samples generated from this burn-in period must be discarded as they are not guaranteed to be drawn from the target distribution. Moreover, the adjacent samples in the chain are correlated. Because numerous statistical calculations require the samples to be independent, such a correlation is undesirable. One can remove the correlation by keeping the samples every  $n$ -th iteration, where  $n$  must be greater or equal to the chain's autocorrelation time  $\tau$ . This process is often referred to as thinning.

In the context of Bayesian analysis, the target distribution is the posterior distribution  $p(\vec{\theta}|d, \mathcal{H})$ , therefore, the probability of acceptance  $a$  is given by

$$a = \min \left( 1, \frac{p(\vec{\theta}'|d, \mathcal{H})}{p(\vec{\theta}_t|d, \mathcal{H})} \frac{Q(\vec{\theta}_t|\vec{\theta}')}{Q(\vec{\theta}'|\vec{\theta}_t)} \right). \quad (4.6)$$

### Parallel tempering

In general, the posterior distribution can be in any form. In particular, it is not uncommon for the distribution to have multiple modes separated by low probability density regions. Given such a distribution, it is challenging to choose a proposal density  $Q(\vec{\theta}'|\vec{\theta})$  such that the chain can frequently jump between the modes while maintaining a healthy acceptance rate.

To solve this problem, one can resort to the method of tempering [126, 127]. The tempering method introduces an inverse temperature  $1/T$  to the likelihood function, such that the modified posterior  $p_T(\vec{\theta}|d, \mathcal{H})$  is given by

$$p_T(\vec{\theta}|d, \mathcal{H}) \propto p(d|\vec{\theta}, \mathcal{H})^{\frac{1}{T}} p(\vec{\theta}|\mathcal{H}), \quad (4.7)$$

where  $T \in [1, \infty)$ . With a temperature  $T > 1$ , the likelihood surface's contrast is reduced and smoothed. With the posterior distribution flattened, it is easier for the chain to jump between previously distinct modes.

In practice, an ensemble of tempered chains is constructed, with their temperature covering  $T = 1$  up to a chosen maximum temperature  $T_{\max}$ . The high temperature chain can transit between different modes more easily and explore a larger region in the

parameter space. The locations of adjacent temperature chains periodically swap with an acceptance probability  $r_s$ , which is given by

$$r_s = \min \left( 1, \left( \frac{p(d|\vec{\theta}_j, \mathcal{H})}{p(d|\vec{\theta}_i, \mathcal{H})} \right)^{\frac{1}{T_i} - \frac{1}{T_j}} \right), \quad (4.8)$$

where  $T_i < T_j$ .

In addition to resulting in a more robust Markov chain Monte Carlo method, parallel tempering also allows the Bayesian evidence  $p(d|\mathcal{H})$  to be estimated. Consider the evidence as a function of temperature,

$$p(d|\mathcal{H}, \beta) = \int d\vec{\theta} p(d|\vec{\theta}, \mathcal{H})^\beta p(\vec{\theta}|\mathcal{H}), \quad (4.9)$$

where  $\beta \equiv 1/T$ . By differentiating the log-evidence with respect to  $\beta$ , one finds

$$\frac{d}{d\beta} \ln p(d|\mathcal{H}, \beta) = \langle \ln p(d|\vec{\theta}, \mathcal{H}) \rangle_\beta, \quad (4.10)$$

where  $\langle \cdot \rangle_\beta$  refers to the expected value with respect to the posterior distribution at temperature  $T = 1/\beta$ . The log-evidence of interest  $\ln p(d|\mathcal{H})$  is then given by

$$\begin{aligned} \ln p(d|\mathcal{H}) &= \ln p(d|\mathcal{H}, \beta = 1) \\ &= \int_0^1 d\beta \frac{d \ln p(d|\mathcal{H}, \beta)}{d\beta} + \ln p(d|\mathcal{H}, \beta = 0) \\ &= \int_0^1 d\beta \langle \ln p(d|\vec{\theta}, \mathcal{H}) \rangle_\beta + \ln \int d\vec{\theta} p(\vec{\theta}|\mathcal{H}) \\ &= \int_0^1 d\beta \langle \ln p(d|\vec{\theta}, \mathcal{H}) \rangle_\beta \\ &\approx \sum_{\beta=1/T_{\max}}^{\beta=1} \Delta\beta \langle \ln p(d|\vec{\theta}, \mathcal{H}) \rangle_\beta. \end{aligned} \quad (4.11)$$

The expected value of the log-likelihood with respect to the posterior at different temperatures  $\langle \ln p(d|\vec{\theta}, \mathcal{H}) \rangle_\beta$  can be estimated using the sample mean for each tempered chain.

### 4.1.2 Nested sampling

The Bayesian evidence  $p(d|\mathcal{H})$  is given by

$$p(d|\mathcal{H}) = \int d\vec{\theta} p(d|\vec{\theta}, \mathcal{H}) p(\vec{\theta}|\mathcal{H}), \quad (4.12)$$

or

$$Z = \int d\vec{\theta} \mathcal{L}(\vec{\theta}) \pi(\vec{\theta}), \quad (4.13)$$

where  $Z$ ,  $\mathcal{L}(\vec{\theta})$ , and  $\pi(\vec{\theta})$  are the evidence, likelihood, and the prior, respectively. Nested sampling [128], developed by John Skilling, is a Monte Carlo technique for estimating the evidence  $Z$ . The nested sampling approximates a, in general, high dimensional integral with a one-dimensional one, and the posterior samples can be obtained as a byproduct

with minimal additional computational cost.

### Algorithm overview

To transform the evidence integration (4.13) into a one-dimensional integration, the prior mass  $X(\lambda)$  is introduced. For given  $\lambda$ , the prior mass is defined to be the prior volume with  $\mathcal{L} > \lambda$ , *i.e.*,

$$X(\lambda) = \int_{\vec{\theta}: \mathcal{L}(\vec{\theta}) > \lambda} d\vec{\theta} \pi(\vec{\theta}). \quad (4.14)$$

The region of space with  $X = 0$  corresponds to the hyper-volume in parameter space enclosed by the maximum likelihood  $\mathcal{L}_{\max}$ . On the other hand, the region of space with  $X = 1$  corresponds to the hyper-volume enclosed by the minimum likelihood  $\mathcal{L}_{\min}$ . The evidence is given by

$$Z = \int_0^1 dX \hat{\mathcal{L}}(X), \quad (4.15)$$

where  $\hat{\mathcal{L}}(X)$  is defined as

$$\hat{\mathcal{L}}(X(\lambda)) \equiv \lambda. \quad (4.16)$$

Therefore  $\hat{\mathcal{L}}(X)$  is a monotonically decreasing function of  $X$ .

The key idea of nested sampling is to probabilistically estimate the prior mass instead of numerically calculating it. Suppose we have a set of samples  $\{\vec{\theta}_i\}$  of size  $K$  distributed accordingly to the prior:

$$\vec{\theta} \sim \pi(\vec{\theta}). \quad (4.17)$$

Based on Eq. (4.14), we can deduce that the prior mass samples  $\{X_i\}$  are distributed as

$$X \sim U(0, 1), \quad (4.18)$$

where  $U(a, b)$  is a continuous uniform distribution in an interval  $[a, b)$ . The cumulative distribution function  $F(X)$  is then given by

$$\begin{aligned} F(X) &= \int_0^X dX' \\ &= X. \end{aligned} \quad (4.19)$$

Considering a random variable  $\chi \in [0, 1)$ , the probability for it to be higher than the prior masses in a given set of prior masses is given by

$$\begin{aligned} \Pr(\{X_i\} < \chi) &= \prod_{i=0}^{N-1} F(X_i = \chi) \\ &= \chi^K, \end{aligned} \quad (4.20)$$

in which we assume that the samples are independent of each other. Subsequently the probability density  $p(\chi)$  is given by

$$\begin{aligned} p(\chi) &= \frac{d}{d\chi} \Pr(\{X_i\} < \chi) \\ &= K\chi^{K-1}, \end{aligned} \quad (4.21)$$

or

$$\chi \sim \text{Beta}(K, 1), \quad (4.22)$$

where  $\text{Beta}(\alpha, \beta)$  is the beta distribution. In the above derivation, we have assumed both  $X$  and  $\chi$  span from 0 to 1. If instead, both of them are bounded by a value  $X^*$ , one can define the shrinkage ratio  $t \equiv \chi/X^*$  and

$$t \sim \text{Beta}(K, 1). \quad (4.23)$$

With the probabilistic properties of the prior mass established, nested sampling proceeds as shown in Algorithm 1. A schematic example of nested sampling with a single “live” point is shown in Fig 4.1.

---

**Algorithm 1:** Nested sampling

---

```

// Live points initialization
Draw  $K$  “live” points  $\{\vec{\theta}_1, \vec{\theta}_2, \dots, \vec{\theta}_K\}$  from the prior  $\pi(\vec{\theta})$ .
 $i = 0$ 
// Main sampling loop
while stopping criterion not met do
  Compute the likelihoods for the current set of live points
  Find the live point  $\vec{\theta}_{\min}$  associated with the minimum likelihood  $\mathcal{L}_{\min}$ 
  // Likelihood constrained prior sampling loop
  while  $\mathcal{L}(\vec{\theta}')$  <  $\mathcal{L}_{\min}$  do
    | Sample a new point  $\vec{\theta}'$  from the prior  $\pi(\vec{\theta})$ 
  end
  Add  $\vec{\theta}_{\min}$  to the list of “dead” points
  Replace  $\vec{\theta}_{\min}$  with  $\vec{\theta}'$ 
   $\mathcal{L}_i = \mathcal{L}_{\min}$ 
  if  $i = 0$  then
    | Draw  $X_i$  from  $\text{Beta}(K, 1)$ 
  end
  else
    | Draw  $t$  from  $\text{Beta}(K, 1)$ 
    |  $X_i = tX_{i-1}$ 
  end
  // Check whether to stop.
  Evaluate stopping criterion
  // Increment  $i$ 
   $i = i + 1$ 
end

```

---

One might worry that this probabilistic approach introduces substantial inaccuracy to the algorithm. Fortunately, the uncertainty associated with the shrinkage ratio  $t$  decreases rapidly with the number of live points  $K$  increases, as the standard deviation  $\sigma$

$$\sigma = \sqrt{\frac{K}{(K+1)^2(K+2)}}. \quad (4.24)$$

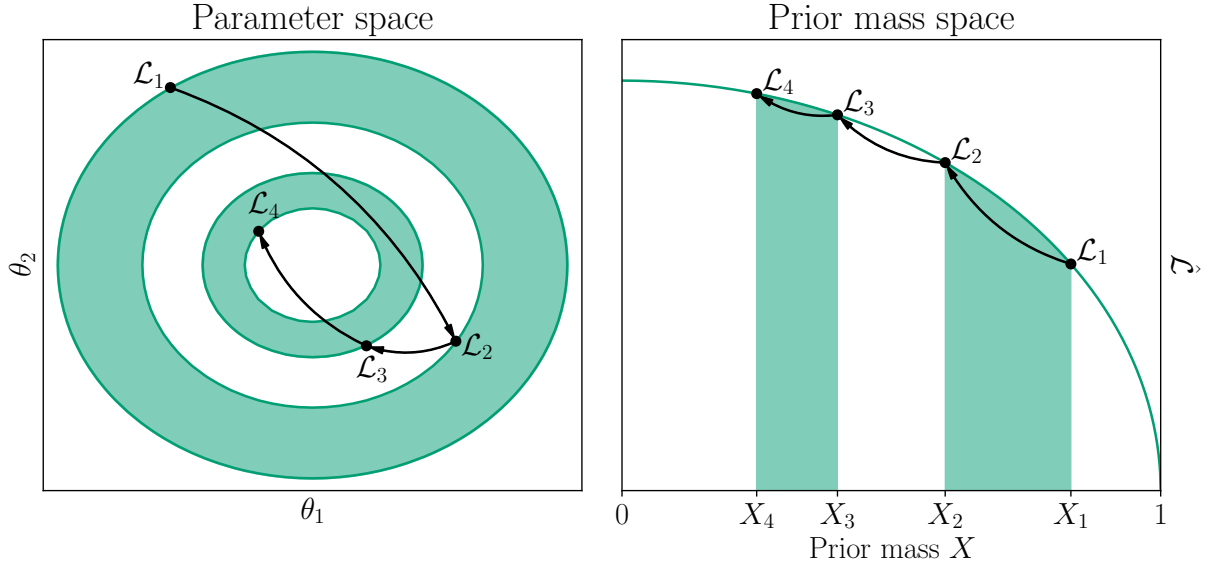


Figure 4.1: The likelihood surface as a function of the parameters  $\vec{\theta} = \{\theta_1, \theta_2\}$  is shown (left). The corresponding surface as a function of the prior mass is also shown (right). The dots represent the location and the associated prior mass of the live point, with arrows indicating its evolution.

Moreover, the shrinkage ratio's mean  $\mu$  is given by

$$\mu = \frac{K}{K+1}. \quad (4.25)$$

Subsequently, both absolute and relative uncertainty decrease as the number of live points increases. Therefore, with sufficient live points, the shrinkage is almost deterministic. A plot with the mean  $\mu$  and the standard deviation against the number of live points is shown in Fig. 4.2.

### Evidence and posterior estimation

With the set of dead points, also referred as nested samples, the evidence  $Z$  can be estimated by

$$\begin{aligned} Z &= \int_0^1 dX \hat{\mathcal{L}}(X) \\ &\approx \frac{1}{2} \sum_{i=1}^K (\mathcal{L}_{i-1} + \mathcal{L}_i)(X_{i-1} - X_i) \\ &\equiv \sum_{i=1}^K w_i. \end{aligned} \quad (4.26)$$

Moreover, the posterior samples can be obtained by sampling from the dead points with the importance weight  $p_i$

$$p_i = \frac{w_i}{\sum_{i=1}^K w_i} \quad (4.27)$$

associated to each of them.



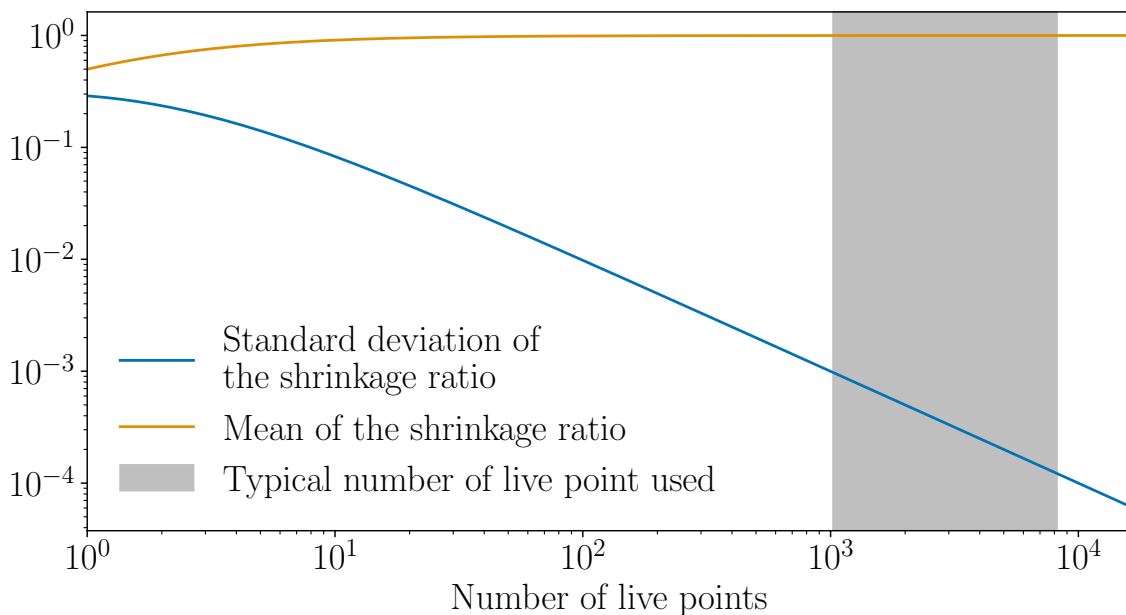


Figure 4.2: Shrinkage ratio’s mean (*orange*) and standard deviation (*blue*) are plotted against the number of live points. The typical range of live points used in gravitational wave and multi-messenger analysis is also shown (*grey*).

### Stopping criterion

Since the main goal of nested sampling is to estimate the evidence, it is straightforward to terminate the sampling when the evidence yet to be accumulated is below some preset threshold. In particular, one might terminate the sampling at the  $i$ -th iteration if

$$\epsilon > \ln(Z_i + \mathcal{L}_{\max} X_i) - \ln(Z_i) \quad (4.28)$$

is satisfied, where  $\epsilon$  is the user-specified threshold and  $\mathcal{L}_{\max}$  is the maximum likelihood ever encountered during the sampling.

### Sampling the likelihood constrained prior

The main portion of the runtime of the nested sampling algorithm is for sampling from the likelihood constrained prior. Moreover, efficiently sampling the likelihood constrained prior is non-trivial as simple rejection sampling results in a low acceptance rate.

The community has made numerous efforts to counter this problem. In most of these methods, attempts have been made to extract the information of the iso-likelihood contour from the current set of live points. For example, the contour is approximated by a single  $D$ -dimensional ellipsoid [129, 130], with multiple overlapping  $D$ -dimensional ellipsoids [131] or with a machine learning algorithm [132]. Once the contour is calculated, the new live point can then be proposed using inverse transform sampling or Markov chain Monte Carlo methods.

### Limitations

Nested sampling has a number of limitations [133]:

1. Independent samples are hard to achieve.
2. Effect of the discretization of posterior inference is unknown.
3. Not massively parallelizable.
4. The stopping criterion is somewhat arbitrary.

Still, nested sampling is one of the most used algorithms for Bayesian inference, because apart from posterior samples it directly provides the evidence without substantial additional computational cost.

---

---

## PART II

---

# CONSTRAINING THE EQUATION-OF-STATE OF SUPRANUCLEAR MATTER

Neutron stars (NSs) are remnants of core-collapse supernovae and contain matter at the highest densities that we can observe in the Universe, up to several times nuclear saturation density,  $n_{\text{sat}} = 0.16 \text{ fm}^{-3}$ , which corresponds to a mass density of  $\rho_{\text{sat}} = 2.7 \times 10^{14} \text{ g cm}^{-3}$ . Hence, NSs are perfect laboratories to determine the unknown equation of state (EOS) of dense matter. The EOS relates the pressure with the energy density in the NS interior and is determined by the fundamental degrees of freedom inside the NS and their interactions among each other. Each possible EOS determines the global structure of NSs, i.e., their masses and radii, in a unique way. Therefore, detailed astronomical observations of NSs, in particular of binary NS (BNS) coalescences, are of extreme importance to nuclear physicists and allow us to constrain the dense-matter EOS. To date, most EOS constraints stem from NS mass measurement [60, 134, 135] or radius extractions from X-ray observations [63, 64, 136]. In addition to electromagnetic (EM) observations, the remarkable observation of gravitational waves (GWs) from a BNS merger in 2017, GW170817, by Advanced LIGO [4] and Advanced Virgo [10] provided another avenue to determine NS properties and the EOS [9, 11, 12]. Numerous efforts have been made to extract information on the EOS from the GW signal of BNS mergers, see e.g., Refs. [29–32, 34, 35, 85, 137–149]; cf. Ref. [150] for a recent review and further references.

Constraints from GW170817 arise either purely from the analysis of the GW signal, e.g., Refs. [6, 9, 19–22], from a combination of GW and EM information, e.g., Refs. [23–29], or from analyses of large sets of possible EOSs constrained by nuclear-physics theory at low densities, e.g., Refs. [29–35]. Furthermore, the NS mass distribution, and therefore also the maximum density in the NS core, is bounded from above by the NS maximum-mass configuration. This is the highest NS mass that can be supported against gravitational collapse by the dense matter in the NS interior and depends on the EOS. While this maximum mass can in principle be as high as  $3 - 4 M_{\odot}$  (see e.g. Ref. [32]), the observation of the kilonova AT2017gfo has constrained the maximum mass to be much smaller, of the order of  $2.2 - 2.3 M_{\odot}$  [25, 151, 152]. In addition, NASA’s Neutron Star Interior Composition Explorer (NICER) mission [63–66] has led to novel constraints on the EOS [22, 24, 27, 29–31, 33, 65, 153, 154]. Most NS observations so far have explored NSs in a mass range of  $1.4 - 2.1 M_{\odot}$ , and hence below the maximal possible density. In contrast, the coalescence of two typical NSs of approximately  $1.4 M_{\odot}$  creates an object that is likely above the maximum mass, and truly explores the EOS at the highest densities in the Universe.

In Chapter 5, we will introduce the technique developed by us for probing phase transition in supranuclear matter via gravitational-wave signals from BNSs. In Chapter 6,

---

the multi-messenger analysis method will be described, which led to a robust constraint on EOS and an independent measurement for the Hubble constant. In Chapter 7, we will show how one can tell if GW190814 is a binary black hole merger or a neutron star black hole merger by using the knowledge on the equation of state. After that, we will show the impact on the EOS constraint by the NICER observation on PSR J0740+6620 in Chapter 8. Finally, the most stringent constraint to date, based on the combination of nuclear theory, astrophysical multi-messenger observations, and terrestrial nuclear experiments, is presented in Chapter 9. These works are published as Refs. [29, 36–39].

## CHAPTER 5

# PARAMETER ESTIMATION FOR STRONG PHASE TRANSITIONS IN SUPRANUCLEAR MATTER USING GRAVITATIONAL-WAVE ASTRONOMY

### 5.1 Introduction

In the context of the dense-matter EOS, an important problem is to determine the nature of matter inside of NSs. For example, at very high energy densities the fundamental theory of strong interactions, Quantum Chromodynamics, predicts that matter undergoes a phase transition to quark matter but it is unknown at what densities such a transition occurs. A long-standing question is whether NSs explore such phase transitions to new and exotic forms of matter in their cores or whether they solely consist of nucleonic matter [155–157], and whether these transitions are observable [158, 159]. Among NSs that explore a phase transition, “twin stars” are a particular family. For these stars, the phase transition in the EOS is sufficiently strong so that the mass-radius curve around the phase transition is disconnected and contains two or more branches [160, 161].

For EOSs where a phase transition is present, two scenarios can be distinguished based on its onset density. First, it is possible that the transition happens at very high densities, i.e., only in heavy stars. In this case, the phase transition is probed only after the collision of the two individual stars; see, e.g., Refs. [162–167]. A second possibility is that the onset density of the phase transition is at lower densities explored in typical NS around  $1.4 M_{\odot}$ , that are probed already during the inspiral phase of the NS merger, e.g., Refs. [168, 169]. In the latter case, one could imagine scenarios in which a mass asymmetry between the two stars in the BNS leads to one (lighter) star containing only nuclear matter, while in the other (more massive) star a quark core is already present. In such a case the two individual stars could have very different radii and tidal deformabilities while their masses are comparable<sup>1</sup>. This is of particular importance since a number of existing GW analyses, e.g., Refs. [20, 22], and multi-messenger constraints on the EOS, e.g., Refs. [23, 24, 26–28], rely on the assumption that both inspiraling objects are NSs following some given quasi-universal relations [20, 119, 121]. In the presence of a phase transitions those quasi-universal relations might be violated, in which case their employment in GW analyses are likely to lead to biases of the determined binary properties and the EOS.

While the current analysis of GW170817 seems to disfavor NSs with radii and tidal deformabilities on the large side, consistent with the appearance of phase transitions, the data from this single event is insufficient to conclusively answer this question; see, e.g., Ref. [146]. Many recent works have addressed the question whether GWs allow to constrain the existence of hybrid stars, i.e., NSs that explore strong phase transitions to

---

<sup>1</sup>As explained in Ch. 2, the tidal deformability  $\Lambda = (2/3)k_2(R/M)^5$  with the second tidal Love number  $k_2$ , radius  $R$ , and mass  $M$  determines the deformation of the star in an external gravitational field [112, 170, 171].

exotic forms of matter in their cores, and in particular twin stars [35, 148, 162, 163, 166, 168, 172]. For example, Ref. [148] searched for the presence of a phase transition by applying quasi-universal relations. In particular, the presence of a strong phase transition was probed via observing the breakdown of quasi-universal relations. Ref. [148] found that the mass at which the phase transition occurs,  $M_t$ , can be measured with 50 – 100 detections and the corresponding microscopic parameters can be estimated via quasi-universal relations. Furthermore, Refs. [146, 147] looked for indications of phase transitions in GW data using a non-parametric inference approach to the EOS. By combining heavy pulsar observations, GW170817, and the recent NICER observation [63], a Bayes factor in favor of the presence of multiple stable branches of  $1.8 \pm 0.2$  [147] was found.

When looking for the imprint of a phase transition in the GW170817 data, these previous works have mainly searched for the presence of multiple stable branches in the mass-radius relation. However, this is only one among various scenarios. In this chapter, we aim at quantifying whether we are capable of determining the presence of a strong phase transition from GW data even when only one stable branch is present. In particular, we ask the question how many GW observations are necessary to observe a phase transition and recover the parameters of an injected EOS from GW data. We focus on three different EOSs that experience a phase transition in the typical mass range explored in BNS systems and which show 3 different behaviors in the mass-radius relation.

For this purpose, we introduce a novel method, based on a new parameterization for EOSs at supranuclear densities, of testing GW data from the inspiral phase of a BNS merger for the appearance of a strong phase transition. This new approach is based on Bayesian inference methods, and can be used with current GW detectors. Simulating 600 signals for three different EOSs, we find that already 12 events might be sufficient to confidently find the presence of a phase transition. However, when analyzing the signals GW170817 and GW190425 with our method, we do not find a hint of a strong phase transition.

The major differences between previous studies and our work are that we simultaneously (i) analyze EOSs with different phase-transition signatures, i.e., one EOS with a twin-star solution which is commonly searched for, but also two EOSs with phase transitions leading to single-branch solutions, (ii) analyze both simulated data and actual events with state-of-the-art Bayesian GW data analysis techniques, which allows for hypothesis testing and parameter estimation at once, and (iii) explicitly demonstrate that our method is able to measure the microscopic characteristics of strong phase transitions, by comparing injected with recovered parameters. Hence, our method allows us to make statistically robust statements on the presence of strong phase transitions.

The chapter is structured as follows. We describe our methods and our mock data setup in Secs. 5.2 and 5.3, respectively. Main results are shown in Sec. 5.4, and in Sec. 5.5 we apply our method to GW170817 and GW190425. We conclude in Sec. 5.6.

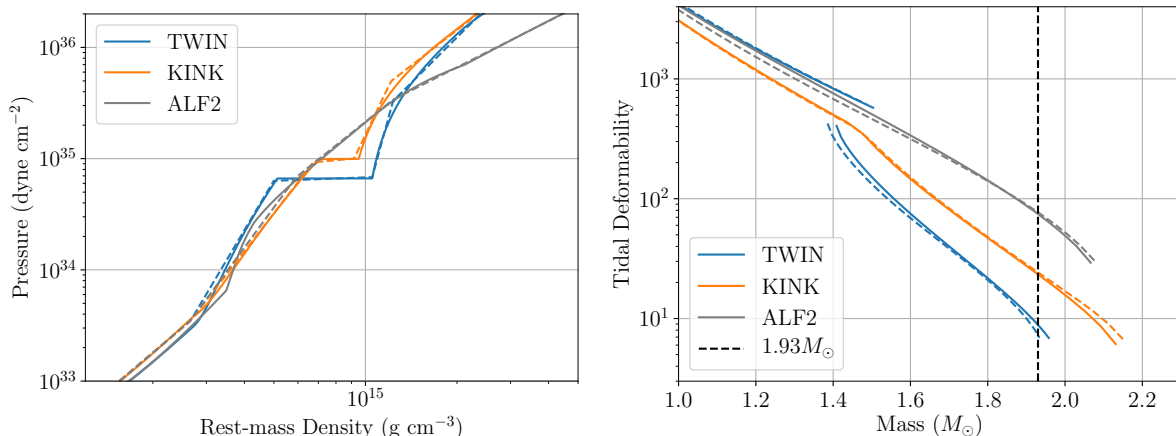


Figure 5.1: Density-pressure relations (*left panel*) and mass–tidal-deformability relations of the three EOSs (solid) used in this chapter, and the least-squares Maxwell fits (dashed) to the the EOSs. The Maxwell parameterization successfully captures all features, including the phase transition, for both the EOS and the mass-radius curve. Moreover, both the EOSs and the EOSs’ best-fits support heavy NSs.

## 5.2 Phase transitions and their imprint on the GW signal

### 5.2.1 The equation of state of NS matter

As explained in Ch. 2, the structure of NSs is determined by solving the Tolman-Oppenheimer-Volkoff (TOV) equations. The only necessary input is the EOS, a relation between the pressure, energy density, temperature, and composition inside the NS. The EOS is determined by the microscopic degrees of freedom in the NS interior and their interactions. At lower densities, these are mostly neutrons with a few percent protons interacting via nuclear forces, but at higher densities new degrees of freedom might appear. With typical radii of the order of 12 km and masses of  $1 - 2 M_{\odot}$ , the densities inside NSs are so large that thermal energies are much smaller than typical Fermi energies, except in the most violent astrophysical scenarios. Hence, for isolated NSs and NSs during the inspiral phase of a BNS merger, finite temperature effects can be neglected and the EOS is simply a relation of pressure and energy density for a given composition.

From the theoretical side, the EOS of cold dense matter at the densities explored in the NS core is very uncertain. There exists a multitude of models for the EOS which explore a wide range of pressures at densities beyond  $n_{\text{sat}}$ , leading to large uncertainties for the radii of typical NSs. The models can differ both in the degrees of freedom that they assume and in the effective interactions among them. At low densities explored in the NS crust and outermost core, where experimental input on, e.g., saturation properties or extractions of the symmetry energy are available to constrain models, the EOS can instead be constrained rather reliably. In this density regime, approaches ranging from density functionals [173] or relativistic mean-field models [174, 175] to ab initio calculations using a variety of models for the nuclear interactions, e.g., Refs. [176, 177], lead to consistent

results.

In recent years, important constraints on the EOS of NS matter at low densities have been obtained from microscopic calculations of neutron matter using systematic interactions from chiral effective field theory (EFT) [111, 177–181]; see Sec. 2.2.2 for more details.

However, while we know the relevant degrees of freedom at lower densities to be nucleons, it is not clear which degrees of freedom appear at larger densities. While many astrophysical EOSs assume nucleonic degrees of freedom to be valid in the whole NS, a phase transition to new degrees of freedom, e.g., quark matter or exotic condensates, might occur [172]. This phase transition might be strong and of first order, in which case it can lead to interesting features in the mass-radius relation, like kinks or disconnected branches [159].

To extend microscopic low-density results for the EOS to higher densities, the uncertainty in the degrees of freedom must be taken into account. This is typically done by applying general extension schemes, e.g., by using sets of polytropes for the energy density and pressure [30, 177, 182] or an expansion in the speed of sound [32, 145, 148]. An extension of this approach are nonparametric inference schemes which have prior support for all possible EOS curves [183] and have recently been combined with chiral EFT calculations [35]. Such extension schemes abandon explicit assumption about the degrees of freedom at higher densities but instead model all EOS curves permitted by the chosen functional form in the case of parametric extensions<sup>2</sup> and general physics considerations such as causality. By sampling all allowed functions, uncertainties at low densities can be systematically extended to high densities.

These general EOS sets contain both smooth EOSs, i.e., EOSs for which the change of pressure with energy density is continuous at all densities, as well as EOSs with drastic changes in the pressure. While EOSs of the first type might be obtained by using a purely nucleonic description of NSs, the latter type contains EOSs with strong first-order phase transitions. Such transitions can be modeled within a Maxwell or Gibbs construction, depending on the properties of the considered phases.

In a Maxwell construction, no mixed phases appear and the phase transitions can be modeled by an EOS segment where the speed of sound,  $c_s^2 = \partial p / \partial \epsilon = 0$ , vanishes. This EOS segment, and hence the phase transition, can be described by its onset density, where the speed of sound becomes 0, and its width, i.e., the density jump between the two phases with nonvanishing speed of sound. Depending on these properties, different features might be observed in the  $M$ - $R$  relation (or the  $M$ - $\Lambda$  relation). In Fig. 5.1, we show two examples of such phase transitions, which we have selected from the EOS set of Ref. [32]. This EOS set was constrained by microscopic chiral EFT calculations below nuclear saturation density, including a consistent NS crust [184], and extended to larger densities by using a speed-of-sound extension scheme. Hence, it ensures NS stability ( $c_s > 0$ ) and causality ( $c_s < c$ , with  $c$  the speed of light) by design. For one of the two chosen EOS (labeled KINK, orange line), an intermediate width is chosen for the phase transition which leads to a visible kink in the mass-radius curve. For the other EOS (labeled TWIN, blue line), a larger width leads to a stronger phase transition which

---

<sup>2</sup>Because no particular choice for the functional form of the EOS is made in nonparametric inference schemes, they are less limited in this sense. However, in this chapter we choose a parameterized approach for the EOS because it is straightforward to implement a  $c_s^2 = 0$  segment that appears in case of a strong first-order phase transition.



results in the appearance of two disconnected branches in the mass-radius relation, a so-called twin-star solution. For both EOS, the onset density is chosen such that the interesting feature appears already in typical NSs.

In the Gibbs construction, on the other hand, a mixed phase appears and smoothens the resulting EOS around the phase transition. In that case an EOS with a phase transition might be indistinguishable from a purely nucleonic EOS, which is known as the masquerade problem [158]. We compare the two EOSs TWIN and KINK with the model ALF2 [158], which is a hybrid EOS with a phase transition to quark matter that leads to the formation of a mixed phase. For all three EOS models, the maximum mass is greater than  $1.93 M_\odot$  and, hence, consistent with observed masses of heavy NSs [60, 135].

### 5.2.2 Imprint of phase transitions on the GW signal

A possible phase transition can imprint itself upon the GW signal in different ways during the inspiral and during the postmerger phase.

*Inspiral:* During the inspiral, the GW signal depends on the properties of the two binary stars (masses, spins, and tidal deformabilities), as well as on the source location and orientation. As explained in Ch. 2, of particular importance for the description of tidal effects are the parameters

$$\tilde{\Lambda} = \frac{16}{13} \Lambda_1 \frac{m_1^4}{M^4} \left( 12 - 11 \frac{m_1}{M} \right) + \frac{16}{13} \Lambda_2 \frac{m_2^4}{M^4} \left( 12 - 11 \frac{m_2}{M} \right), \quad (5.1)$$

which captures the leading-order contribution at fifth Post-Newtonian (PN) order, and

$$\delta\tilde{\Lambda} = \left( \frac{1690}{1319} \eta - \frac{4843}{1319} \right) \left( \frac{m_1^4}{M^4} \Lambda_1 - \frac{m_2^4}{M^4} \Lambda_2 \right) + \frac{6162}{1319} \sqrt{1 - 4\eta} \left( \frac{m_1^4}{M^4} \Lambda_1 + \frac{m_2^4}{M^4} \Lambda_2 \right), \quad (5.2)$$

with the symmetric mass ratio  $\eta = m_1 m_2 (m_1 + m_2)^{-2} = m_1 m_2 / M^2$ , which captures additional contributions at sixth PN order.

The presence of a phase transition in the EOS might lead to a significant change in the radii and tidal deformabilities for almost equal mass systems, if in any of the two stars the onset density for the transition is already reached in the core, cf. Fig. 5.1. In Fig. 5.2, we show the expected GW signal for a non-spinning BNS system with component masses of  $1.50 M_\odot$  and  $1.45 M_\odot$  for the three EOSs that we have chosen in this chapter. For the two EOSs with strong first-order phase transitions, due to the different tidal deformabilities of both stars, we find a dephasing of the waves compared to the ALF2 EOS. Since the leading-order tidal contribution enters at the fifth PN order [112, 114, 170, 171], the dephasing is most prominent in the late-inspiral phase.

In addition to the GWs for the EOSs described above, we also present as dashed lines the waveforms when we assume that the quasi-universal relation of Refs. [120, 121] holds for TWIN, KINK, and ALF2. To apply this relation, we fix the tidal deformability of the lower-mass star and compute the tidal deformability of the primary component by using the quasi-universal relation. We find that the resulting waveform significantly deviates from the full waveform for EOSs with a very strong phase transitions, i.e., TWIN, but approximates the waveform well in the other cases. These differences suggest the failure of the quasi-universal relation with respect to EOSs with strong phase transitions like TWIN, while the relation holds approximately for the KINK EOS. For smooth EOSs,

like ALF2, there is no observable difference and the quasi-universal relation seems to be valid. This suggests that detecting a phase transition that does not result in a twin-star solution will be challenging if a methodology purely based on quasi-universal relations is employed.

*Postmerger:* In cases in which the phase transition happens at densities beyond the ones probed during the inspiral, the postmerger signature can change if a phase transition is present, as outlined in, e.g., Refs. [148, 162, 163, 166–168, 172]. In most cases, the presence of a phase transition will lead to a different (often shorter) lifetime of the remnant and a shift of the main postmerger GW emission mode. However, due to the limited sensitivity of existing GW detectors in the high-frequency range [10, 185] and the absence of high-quality GW models describing the postmerger evolution of BNS mergers – see Refs. [186–191] for some first attempts – it seems natural to investigate, at the current stage, possible phase transition effects that can be extracted from the GW signal during the inspiral.

### 5.2.3 EOS parameterization for phase transitions

When analyzing NS observations, one needs to assume a general form for the EOS describing the relation between pressure and energy density. For the “true” NS EOS realized in nature, however, the functional form is unknown. Hence, an EOS parameterization needs to be flexible enough to capture the various effects one might encounter in nature, in particular phase transitions. In this chapter, we consider the three EOSs of Fig. 5.1 as three possible “true” EOSs. In order to capture all features of these EOSs, in particular the first-order phase transitions, here we propose to use a 5-parameter piecewise-polytrope EOS parameterization scheme, which we refer to as Maxwell parameterization. This scheme is similar to the parameterization proposed in Ref. [182].

In our Maxwell parametrization, at low densities up to nuclear saturation density, we use an EOS constrained by the chiral EFT calculation of Ref. [111] ( $V_{E,1}$  parametrization). This EOS contains a consistent inner crust and uses the BPS model for the outer crust [192, 193]. For the high-density part beyond  $n_{\text{sat}}$ , we use a modified 5-parameter 4-piece polytrope. Each polytrope is characterized by the starting pressure  $p_i$  and the adiabatic index  $\Gamma_i$ . Therefore, our extension starts with 8 free parameters:  $\{p_1, p_2, p_3, p_4\}$  and  $\{\Gamma_1, \Gamma_2, \Gamma_3, \Gamma_4\}$ .

To ensure continuity for the first polytrope, the starting pressure  $p_1$  is chosen to be the pressure of the chiral EFT EOS at the nuclear saturation density,  $p_{\text{CEFT}}(\rho_0)$ . The adiabatic index of the second polytrope,  $\Gamma_2$ , is set to be zero to represent a Maxwell construction for a phase transition extended across a density gap of  $\Delta\rho$ . Therefore,  $p_2 = p_3 = p_{\text{tr}}$ , where  $p_{\text{tr}}$  is the phase transition pressure. Furthermore, we choose the transition pressure between the third and fourth polytropes to be 5 times the phase transition pressure,  $p_4 = 5p_{\text{tr}}$ . Fixing  $p_4$  reduces the numbers of free parameters and, therefore, helps during the recovery. The particular value of  $5p_{\text{tr}}$  is chosen ad-hoc by comparison against various different EOSs. We have also explored leaving this parameter free, but this only improved the fitting performance marginally. Therefore, to reduce dimensionality, we have fixed this parameter. A sketch of the parameterization is shown in Fig. 5.3 and its capability of representing the three EOSs is shown in Fig. 5.1. We find that the Maxwell parametrization works well for EOSs where phase transitions appear between  $1-4n_{\text{sat}}$ , corresponding to a NS in a typical mass range. As suggested in [194, 195], we have

found that our parametrization introduces systematic uncertainties due to imperfect fits to the “true” EOSs. Yet, as shown in the right panel of Fig. 5.1, the error is overall small and will be below the statistical uncertainty of an EOS measurement [84]. However, it might be necessary to verify the generality of this assumption assuming different parametrizations. Because of the large computational cost, this is not part of this chapter. Furthermore, we do not expect systematics induced by our parametrization to significantly affect the present study and its main goal, namely to identify strong phase transitions and their parameters.

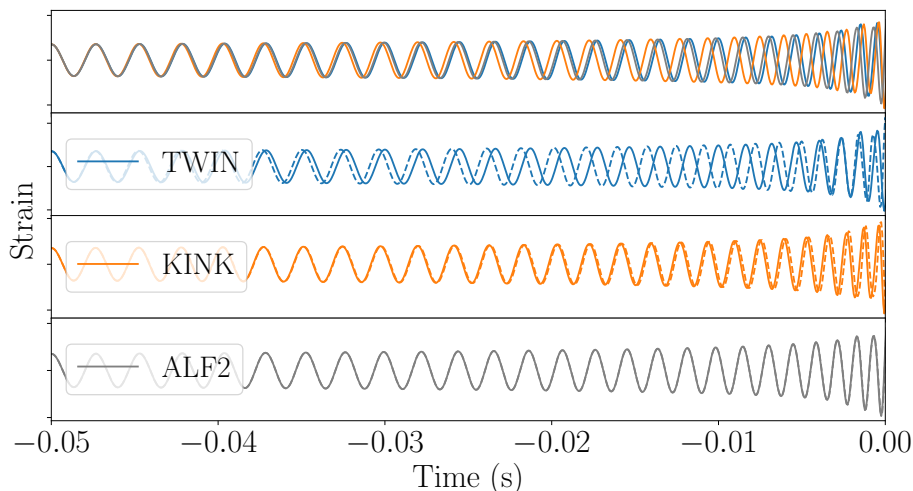


Figure 5.2: The GW waveforms for a non-spinning BNS system with component masses of  $1.50M_{\odot}$  and  $1.45M_{\odot}$  for the three EOS used in this chapter. The dashed lines are the waveforms assuming that the Binary-Love relation [120, 121] holds.

In total, our parametrization is described by five parameters  $\Gamma_1, \Gamma_3, \Gamma_4$ , the phase transition onset pressure  $p_{\text{tr}}$ , and the transition density jump  $\Delta\rho$ . In practice, in case of an EOS with a twin-star solution, it is possible to have NSs with the same mass but different radii, i.e., NSs that live on different branches of the  $M$ - $R$  relation. These NSs have central densities around the onset density of the phase transition. Because in this case the NS mass cannot be used to distinguish the individual stars – see Fig. 5.1 (right panel) – we need to add two extra parameters  $B_1$  and  $B_2$  for each of the two NSs to indicate on which branch the star lives. Therefore, the EOS parameters  $\vec{E}$  are given by

$$\begin{aligned} \vec{E} &= \{\log_{10} p_{\text{tr}}, \log_{10} \Delta\rho, \Gamma_1, \Gamma_3, \Gamma_4, B_1, B_2\} \\ &= \{\vec{E}_c, \{B_i\}\}, \end{aligned} \tag{5.3}$$

where  $\vec{E}_c$  denotes the common parameters of all stars, assuming they follow the same EOS.

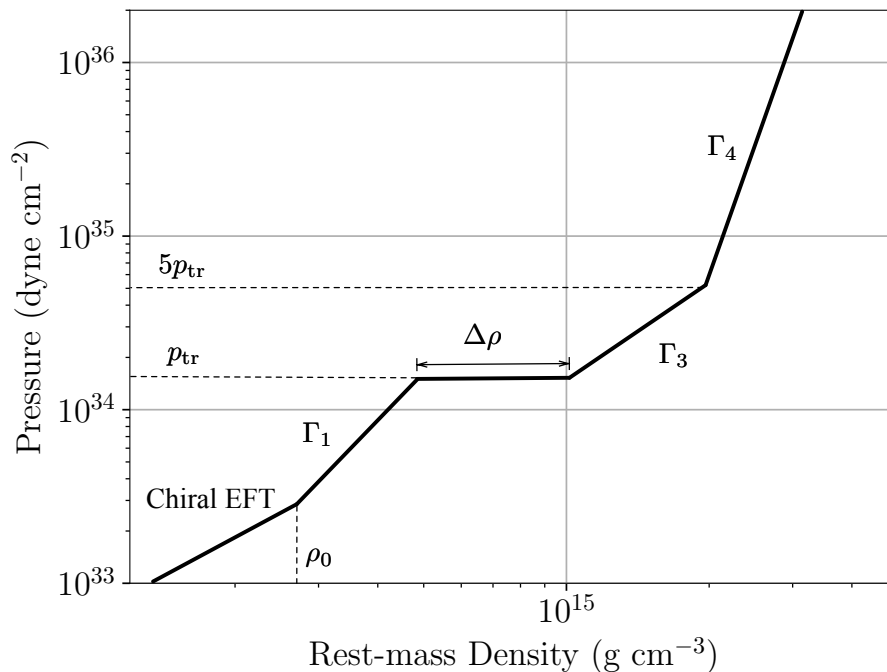


Figure 5.3: Sketch of the Maxwell parameterization, which is characterized by the adiabatic indices  $\{\Gamma_1, \Gamma_3, \Gamma_4\}$ , the phase transition onset pressure  $p_{\text{tr}}$ , and the transition density jump  $\Delta\rho$ .

## 5.3 Mock Data Simulation

### 5.3.1 Bayesian Analysis

As explained in Ch. 3, within the Bayesian framework we can combine the information from multiple detections. For parameters that are expected to be the same across several detections (e.g. EOS parameters), the combined posterior for common parameters  $\mathcal{P}_c(\vec{\theta}_c)$  can be obtained as

$$\mathcal{P}_c(\vec{\theta}_c) = \pi(\vec{\theta}_c)^{1-N} \prod_{i=1}^N \mathcal{P}_i(\vec{\theta}_c), \quad (5.4)$$

where  $\vec{\theta}_c$  are the common parameters and  $\mathcal{P}_i(\vec{\theta}_c)$  is the posterior including the  $i$ -th detection. We can also combine the odds ratios into a catalog odds ratio  $\mathcal{O}_2^{1(\text{cat})}$ , which is given by<sup>3</sup>

$$\mathcal{O}_2^{1(\text{cat})} = \Pi_2^1 \prod_{i=1}^N \mathcal{B}_{2,i}^1 = \Pi_2^1 \mathcal{B}_2^{1(\text{cat})}, \quad (5.5)$$

where  $\mathcal{B}_{2,i}^1$  is the Bayes factor for the  $i$ -th detection and  $\mathcal{B}_2^{1(\text{cat})}$  is the catalog Bayes factor. As we have the prior odds set to 1, the catalog odd ratio  $\mathcal{O}_2^{1(\text{cat})}$  is the same as the catalog Bayes factor  $\mathcal{B}_2^{1(\text{cat})}$ .

<sup>3</sup>By cataloging odd ratios with simple multiplication, the information that some parameters are shared across detections is not included. This conservative choice is dictated by computational limitations; see the discussion in Sec. IV.B.

### 5.3.2 Waveform approximants

In this chapter, we restrict our studies to the PN model `TaylorF2`; see Ch. 2. This model was also employed in the analysis of GW170817 and GW190425 by the LIGO and Virgo Collaborations; see e.g. Refs. [6, 21, 49].

The version of `TaylorF2` we use is based on a 3.5 PN order point-particle description [70, 73, 196–198] that includes spin-orbit effects [83] and spin-spin effects [81, 82, 199, 200]. Tidal effects are added up to 7.5 PN following Refs. [113, 114]. We note that we also incorporate the EOS-dependency of the 2PN and 3PN spin-spin contributions. For this purpose, we use quasi-universal relations outlined in [119] to connect the spin-induced quadrupole moments to the tidal deformability of the NS stars. This approach is commonly used for GW data analysis and was by default used here, but a phase transition could also affect the employed quasi-universal relation. This might introduce additional biases. Sampling over the individual quadrupole moments of the NSs (see, e.g., Ref. [201]), would cause an increase of the computational costs and it seemed more appropriate to employ the quasi-universal relations of [119] than simply neglecting the EOS imprint on the quadrupole moment. However, since all simulated signals are non-spinning, we do not expect that any significant biases appear during our analysis and refer to the study of Ref. [202], where it was shown that potential biases only arise for high spins.

### 5.3.3 Injection setup

We choose to use an astrophysically motivated distribution for the parameters of the simulated sources. We distribute the sources uniformly in a co-moving volume with the optimal network SNR range  $\rho \in [30, 100]$ . Thus, a relatively high lower bound on SNR is assumed. Indeed, to probe the phase transition, an accurate measurement of  $\Lambda_i$  is needed, which can not be achieved with BNS signals that have low or medium SNR [84]. The orientation  $(\iota, \psi)$  and the sky location  $(\alpha, \delta)$  of the sources are placed uniformly on a sphere. Since NS spins are expected to be small [203], we set them to zero for all simulated sources. The component masses of the binaries are sampled from the uniform distribution  $[1 M_\odot, M_{\text{TOV}}]$ , where  $M_{\text{TOV}}$  is the maximum allowed mass of a NS with the given EOS.

For the EOSs, we want to investigate under what circumstances one can distinguish between the existence and the absence of a strong phase transition. Therefore, we choose two EOSs that have phase transitions with different onset pressure and density jumps but that lead to an observable and distinct feature within the mass range of  $[1, 2]M_\odot$  in the mass-radius curve, labeled as TWIN and KINK; cf. Sec. 5.2. In addition, we choose another EOS with phase transition but a smooth density dependence of the pressure. As the phase transition masquerades, this model is indistinguishable from a purely nucleonic EOS model, see Fig. 5.1. Here, we choose the ALF2 EOS described in Ref [157] because of its plausibility based on the multi-messenger analysis of GW170817 [23, 28]. The three EOSs are all able to support the observed heavy NSs [60, 134, 135].

The simulated GW signals are injected coherently into the data of the Advanced LIGO and Advanced Virgo detectors. The detector noise is simulated as stationary Gaussian noise with the power spectral density to be that of the design sensitivities of each detector [10, 185].

### 5.3.4 Implementation

Our analysis follows a similar approach as previous works [142, 146, 149]. The analysis consist of a two-stage process:

- I. Estimation of the posterior of the macroscopic parameters  $\mathcal{P}(\vec{\theta}_{\text{macro}})$  based upon a GW analysis, where  $\vec{\theta}_{\text{macro}} = \{m_i, \Lambda_i\}$ .
- II. Estimation of the posterior of the microscopic parameters (*i.e.* the EOS parameters)  $\mathcal{P}(\vec{E})$  with  $\mathcal{P}(\vec{\theta}_{\text{macro}})$  given.

For stage I, the posterior  $\mathcal{P}(\vec{\theta}_{\text{macro}})$  is estimated with the Nested Sampling algorithm [128] implemented in `LALInference` [204] with a prior of  $m_i \in [0.5, 3.0] M_\odot$  and  $\Lambda_i \in [0, 5000]$ . For stage II, the posterior  $\mathcal{P}(\vec{E})$  is given by

$$\begin{aligned} \mathcal{P}(\vec{E}) &\propto \pi(\vec{E})\mathcal{L}(\vec{E}) \\ &= \pi(\vec{E}) \int d\vec{\theta}_{\text{macro}} \frac{\pi(\vec{\theta}_{\text{macro}}|\vec{E})}{\pi(\vec{\theta}_{\text{macro}}|I)} \mathcal{P}(\vec{\theta}_{\text{macro}}), \end{aligned} \quad (5.6)$$

where  $\pi(\vec{\theta}_{\text{macro}}|\vec{E})$  and  $\pi(\vec{\theta}_{\text{macro}}|I)$  are the priors on  $\vec{\theta}_{\text{macro}}$  with and without the EOS given, respectively. For our study, the macroscopic parameters of interest are the component masses  $m_{1,2}$  and the corresponding tidal deformabilities  $\Lambda_{1,2}$ . Therefore the likelihood  $\mathcal{L}(\vec{E})$  is given by

$$\begin{aligned} \mathcal{L}(\vec{E}) &= \int dm_1 dm_2 d\Lambda_1 d\Lambda_2 \frac{\pi(m_1, m_2, \Lambda_1, \Lambda_2|\vec{E})}{\pi(m_1, m_2, \Lambda_1, \Lambda_2|I)} \mathcal{P}(m_1, m_2, \Lambda_1, \Lambda_2) \\ &= \int dm_1 dm_2 d\Lambda_1 d\Lambda_2 \frac{\prod_i \delta(\Lambda_i - \Lambda(m_i; \vec{E}))}{\pi(\Lambda_1, \Lambda_2|m_1, m_2, I)} \frac{\pi(m_1, m_2|\vec{E})}{\pi(m_1, m_2|I)} \mathcal{P}(m_1, m_2, \Lambda_1, \Lambda_2) \\ &= \int dm_1 dm_2 \left. \frac{\mathcal{P}(m_1, m_2, \Lambda_1, \Lambda_2)}{\pi(\Lambda_1, \Lambda_2|m_1, m_2, I)} \right|_{\Lambda_1=\Lambda(m_1; \vec{E}), \Lambda_2=\Lambda(m_2; \vec{E})}, \end{aligned} \quad (5.7)$$

where  $\Lambda(m, \vec{E})$  is the tidal deformability as a function of mass with an EOS given. We have also chosen the priors  $\pi(m_1, m_2|\vec{E})$  and  $\pi(m_1, m_2|I)$  to be the same.

Therefore, the joint posterior  $\mathcal{P}(\vec{E}, m_i)$  is given by

$$\mathcal{P}(\vec{E}, m_1, m_2) \propto \pi(\vec{E}) \left. \frac{\mathcal{P}(m_1, m_2, \Lambda_1, \Lambda_2)}{\pi(\Lambda_1, \Lambda_2|m_1, m_2, I)} \right|_{\Lambda_1=\Lambda(m_1; \vec{E}), \Lambda_2=\Lambda(m_2; \vec{E})}. \quad (5.8)$$

The joint posterior is estimated with the Nested Sampling algorithm `Multinest` [131] implemented in `PyMultinest` [205, 206]. The posterior  $\mathcal{P}(\vec{E})$  is then obtained via marginalizing  $\mathcal{P}(\vec{E}, m_i)$ .

For the stage II process, we choose the prior for the parameters to be  $m_i \in [0.5, 3.0] M_\odot$ ,  $\Gamma_i \in (1, 10]$ ,  $\log_{10} p_{\text{tr}}[\text{dyne cm}^{-2}] \in [33.7, 38.0]$  and  $\log_{10} \Delta\rho[\text{g cm}^{-3}] \in [13.85, 16]$ . We also impose the constraints of  $M_{\text{TOV}} \geq 1.93 M_\odot$  as part of the prior. To increase efficiency, sampling over masses is done in terms of the chirp mass  $\mathcal{M}$  and  $\ln \Delta\eta$  rather than indi-

vidual masses. The chirp mass  $\mathcal{M}$  and  $\ln \Delta\eta$  are given by

$$\mathcal{M} = \frac{(m_1 m_2)^{3/5}}{(m_1 + m_2)^{1/5}}, \quad (5.9)$$

$$\ln \Delta\eta = \ln \left( \frac{1}{4} - \eta \right). \quad (5.10)$$

## 5.4 Locating phase transitions from GW signals

### 5.4.1 Description of the method

Because the pressure  $p$  within a compact star is monotonically decreasing from  $p_c$  in the center to  $p = 0$  at the surface, only the part of the EOS with pressures below the central pressure  $p_c$  is observable. With this in mind, we define the hypotheses to be tested as follows:

- $\mathcal{H}_{\text{PT}}$ : The phase transition pressure  $p_{\text{tr}}$  is below  $p_c$  for one or both of the stars and the phase transition involves a density jump  $\Delta\rho > 0$ ;
- $\mathcal{H}_{\text{NPT}}$ : The phase transition density jump  $\Delta\rho$  is zero or  $p_{\text{tr}}$  is larger than  $p_c$ , and therefore the transition is not observable.

For  $\mathcal{H}_{\text{NPT}}$ , we found that it is sufficient to test for the condition  $\Delta\rho = 0$ . Indeed, within our parameterization, the condition  $p_{\text{tr}} > p_c$  is equivalent to fitting the whole observable EOS with a single polytrope (instead of 3-4 polytropes in the case of  $p_{\text{tr}} < p_c$ ), which is automatically penalized by the analysis due to its low likelihood. Moreover, a significant decrease of the number of fit degrees of freedom complicates our interpretation of the evidence and, correspondingly, the Bayes factors.

The evidences for the two hypotheses are given by

$$\begin{aligned} \mathcal{Z}_{\text{PT}} = & \int d\vec{E} dm_1 dm_2 \mathcal{L}(\vec{E}, m_1, m_2) \\ & \times \pi(\vec{E}, m_1, m_2 \mid (p_{\text{tr}} < p_{c,1} \cup p_{\text{tr}} < p_{c,2}) \cap \Delta\rho > 0), \end{aligned} \quad (5.11)$$

and

$$\mathcal{Z}_{\text{NPT}} = \int d\vec{E}_c dm_1 dm_2 \mathcal{L}(\vec{E}_c, m_1, m_2) \pi(\vec{E}_c \mid \Delta\rho = 0), \quad (5.12)$$

where the central pressure  $p_{c,i}$  is estimated via interpolation of  $m_i - p_{c,i}$  for given EOS parameters  $\vec{E}$ .

The Bayes factor  $\mathcal{B}_{\text{NPT}}^{\text{PT}}$  between  $\mathcal{H}_{\text{PT}}$  and  $\mathcal{H}_{\text{NPT}}$  is given by

$$\mathcal{B}_{\text{NPT}}^{\text{PT}} = \frac{\mathcal{Z}_{\text{PT}}}{\mathcal{Z}_{\text{NPT}}}. \quad (5.13)$$

By examining the Bayes factor  $\mathcal{B}_{\text{NPT}}^{\text{PT}}$ , one can deduce if a phase transition is observed.

### 5.4.2 Method Validation

With 200 BNS inspiral signals for each EOS, the parameter estimation is performed and the evidences are estimated as described in Sec. 5.4.1.

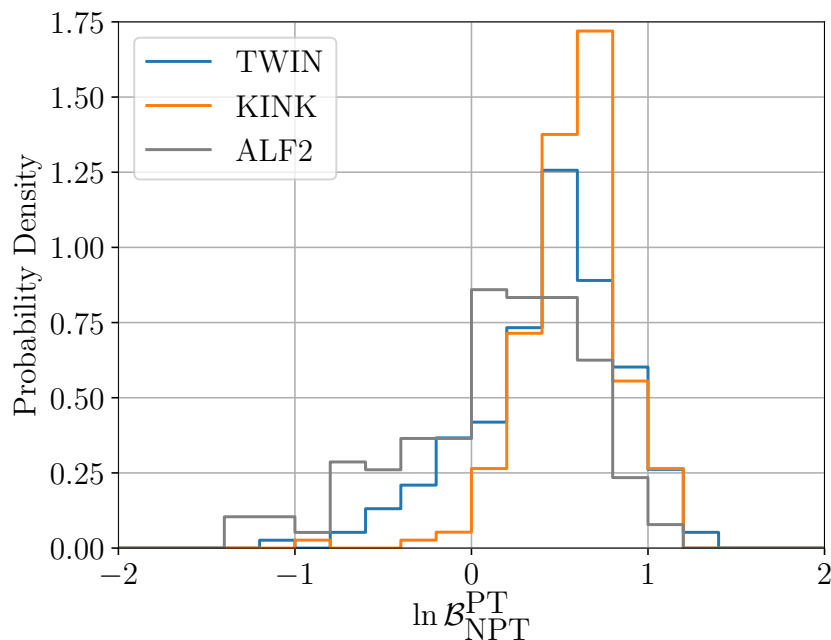


Figure 5.4: The distribution of  $\ln \mathcal{B}_{\text{NPT}}^{\text{PT}}$  for injections with the TWIN, KINK, and ALF2 EOSs. The presence of a strong phase transition does shift the distribution of  $\ln \mathcal{B}_{\text{NPT}}^{\text{PT}}$  towards larger values.

The probability distribution functions of the  $\ln$  Bayes factors  $\ln \mathcal{B}_{\text{NPT}}^{\text{PT}}$  obtained from all 200 injections for each of the three EOSs are shown in Fig. 5.4. In our simulations, 85%, 98% and 70% of the injections lead to a positive  $\ln \mathcal{B}_{\text{NPT}}^{\text{PT}}$  for the TWIN, KINK, and ALF2 EOSs, respectively. Even though the EOSs with a strong phase transition, KINK and TWIN, do shift the distribution of  $\ln \mathcal{B}_{\text{NPT}}^{\text{PT}}$  towards larger values, the shift is not pronounced enough to draw a statistically robust conclusion. Furthermore, while there is no strong first-order phase transition in the ALF2 EOS,  $\mathcal{H}_{\text{PT}}$  is favored over  $\mathcal{H}_{\text{NPT}}$  for the ALF2 injections. However, in  $\mathcal{H}_{\text{PT}}$ , the EOS below  $p_c$  is fitted with 3 – 4 polytropes while in  $\mathcal{H}_{\text{NPT}}$  it is fitted with only 1 – 3 polytropes. The additional degrees of freedom for  $\mathcal{H}_{\text{PT}}$  improve the fit to the  $M$ - $\Lambda$  curve and lead to a higher evidence.

To improve on the situation, we follow the catalog technique described in Sec. 5.3.1, and estimate the catalog log Bayes factors  $\ln \mathcal{B}_{\text{NPT}}^{\text{PT}(\text{cat})}$ . In Fig. 5.5, we show the distributions of  $\ln \mathcal{B}_{\text{NPT}}^{\text{PT}(\text{cat})}$  with 5, 9, and 12 events per catalog for the three EOSs. We find that the presence of a strong phase transition in the EOS can be clearly recognized from the distributions for 9 or more events per catalog. For both the TWIN and KINK EOSs, with 12 events per catalog, all the catalogs result in a higher than  $5\sigma$  statistical significance with respect to the catalogs estimated for the ALF2 EOS.

Before continuing, we note that by combining the Bayes factors with simple multiplication we are not making use of the knowledge that all BNSs share the same EOS. The inclusion of this additional constraint would require us to do the analysis on all BNSs in a catalog simultaneously, which would be computationally very demanding. While our procedure is sub-optimal, it is a conservative one. Most importantly, we see that by using our catalog Bayes factor as a detection statistic for strong phase transitions, with



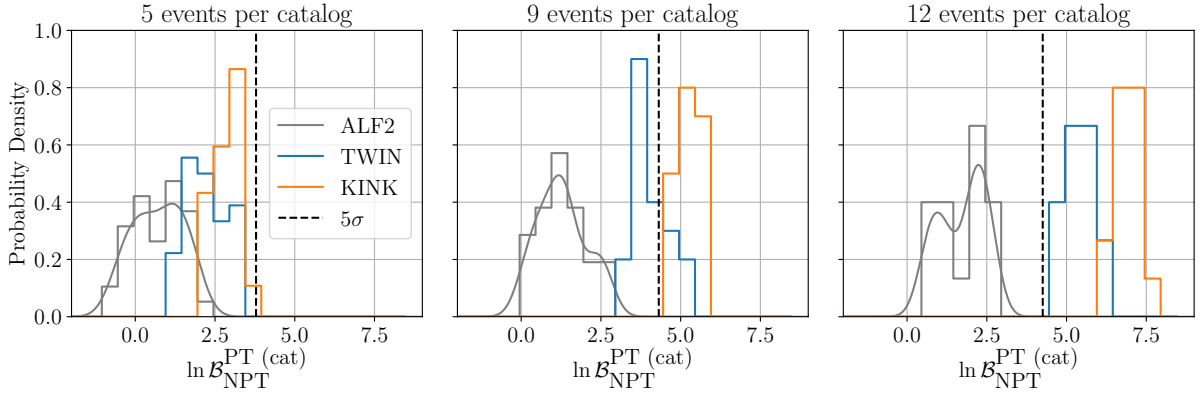


Figure 5.5: The distributions of  $\ln \mathcal{B}_{\text{NPT}}^{\text{PT}}(\text{cat})$  for injections with the TWIN, KINK, and ALF2 EOSs. Each catalog consists of 5 events (*left*), 9 events (*center*), or 12 events (*right*). The presence of a strong phase transition can be recognized from the distributions for 9 or more events. The  $5\sigma$  threshold, indicated by the black dashed line, is estimated with respect to the  $\ln$  Bayes factor distribution for the ALF2 EOS using a Gaussian kernel density estimation (the smooth grey curve).

12 sources we can already draw significant conclusions, regardless of the interpretation of the Bayes factor.

Returning to Fig. 5.5, we see that the phase transition in the KINK EOS is easier to identify than the TWIN EOS, even though the TWIN EOS has the more pronounced feature in the  $M$ - $R$  relation. Moreover, in the case of TWIN, the parameters  $B_1$  and  $B_2$ , which indicate on which branch the stars live, are not redundant, and one would think that this should boost the evidence in that case. However, the individual  $\Lambda_i$  for each component in a BNS are not well measured<sup>4</sup>; as a result, the inclusion of the  $\{B_i\}$  does not necessarily lead to the evidence being elevated. In addition, as seen in Fig. 5.1, our parameterization can fit the KINK EOS better than the TWIN EOS, which contributes to the higher evidence of KINK compared to TWIN.

In addition to observing the presence of a phase transition with statistical significance, we can also probe its characteristics. In particular, the phase transition onset pressure  $p_{\text{tr}}$ , and the phase transition density jump  $\Delta\rho$ , can be measured. In Fig. 5.6, we show the maximum *a posteriori* (MAP) and 95% credible interval evolution for  $\log_{10} p_{\text{tr}}$  and  $\log_{10} \Delta\rho$  with an increasing number of events, where we only include events with positive  $\ln \mathcal{B}_{\text{NPT}}^{\text{PT}}$  for TWIN and KINK. Indeed, we expect that events with positive  $\ln \mathcal{B}_{\text{NPT}}^{\text{PT}}$  will tend to have  $p_c > p_{\text{tr}}$ , and hence be informative for the estimation of  $\log_{10} p_{\text{tr}}$  and  $\log_{10} \Delta\rho$ ; this is something we will return to momentarily. Looking at the results, for both EOSs the true phase transition parameters are recovered within the 95% credible interval. For  $\log_{10} \Delta\rho$ , the true value is recovered after  $\sim 10$  events are included. We note that the credible intervals for the parameters of the phase transition are not dominated by the one or two loudest events. Instead, in order to detect the phase transition, we need to map-out a significant part of the  $M$ - $\Lambda$  curve, which requires multiple detections.

In Fig. 5.7, we show the joint posteriors for  $\log_{10} p_{\text{tr}}$  and  $\log_{10} \Delta\rho$  with 25 combined events for the TWIN and KINK EOSs. For both EOSs, the phase transition parameters

<sup>4</sup>This results from the poor measurement of  $\delta\tilde{\Lambda}$  with second-generation detectors [84].

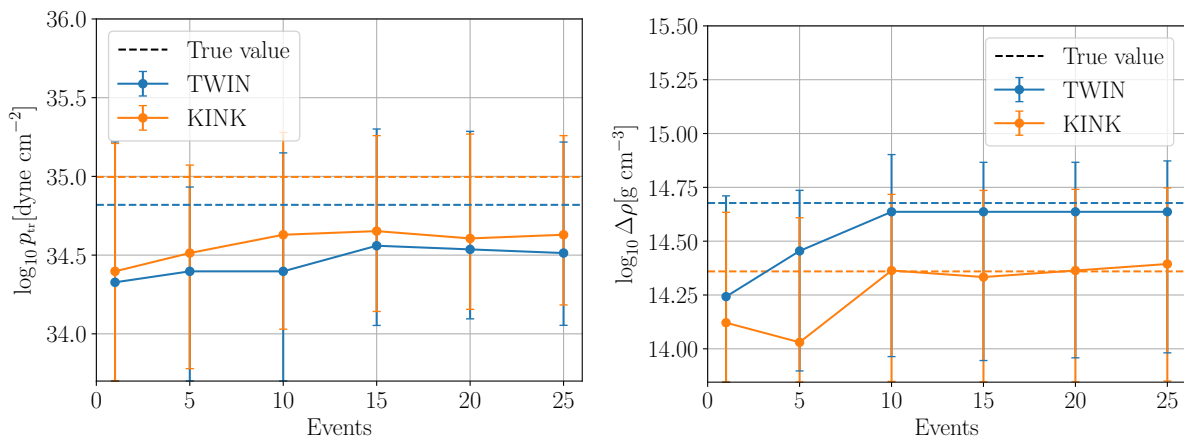


Figure 5.6: Maximum *a posteriori* (MAP) and 95% credible interval evolution for  $\log_{10} p_{\text{tr}}$  (left panel) and  $\log_{10} \Delta\rho$  (right panel) for the TWIN and KINK EOSs. The dashed lines indicate the true values, which are found to lie within the extracted 95% credible interval for both EOS.

$(\log_{10} p_{\text{tr}}, \log_{10} \Delta\rho)$  are measured with  $\lesssim 10\%$  statistical uncertainty, with the true values lying within the 95% credible interval.

Finally, for the same 25 events, we show the distribution of the central pressure  $p_c$  for both stars in Fig. 5.8. For the majority of the events, both stars have a central pressure above the phase transition onset pressure. This matches our expectation from the positive  $\ln \mathcal{B}_{\text{NPT}}^{\text{PT}}$  and provides a valuable crosscheck for our analysis.

Based on our findings, we conclude that:

- (i) It is possible to establish the presence of a strong first-order phase transition with twelve BNS observations;
- (ii) With  $\sim 10$  BNSs, the phase transition parameters  $(\log_{10} p_{\text{tr}}, \log_{10} \Delta\rho)$  can be measured with  $\lesssim 10\%$  statistical uncertainty.

Because we are imposing a strict bound on the  $M_{\text{TOV}}$  during the stage II analysis, systematics might be induced as suggested in Refs. [147, 207]. However, since we are not interested in recovering the full EOS or  $M_{\text{TOV}}$  but the parameters of the phase transition, the simple hard cut on  $M_{\text{TOV}}$  is sufficient for the purposes of this analysis. Also, no significant systematics are observed with respect to the simulation.

### 5.4.3 Limitations of our analysis

As we have shown in the previous section, it is possible to confirm the existence of a phase transition and extract its parameters. However, our approach is limited to such EOSs where the phase transition is Maxwell-like, i.e., it is described by a segment with  $c_S = 0$ . As the comparison with the ALF2 EOS clearly shows, our approach cannot establish the existence of a phase transition in case a mixed phase appears, that smears out an observable EOS feature. Due to this masquerade problem [157], macroscopic structure properties ( $M$ - $R$  or  $M$ - $\Lambda$  relations) for such EOSs cannot be distinguished from purely nucleonic EOSs. As only such properties affect the GW waveforms, the inspiral

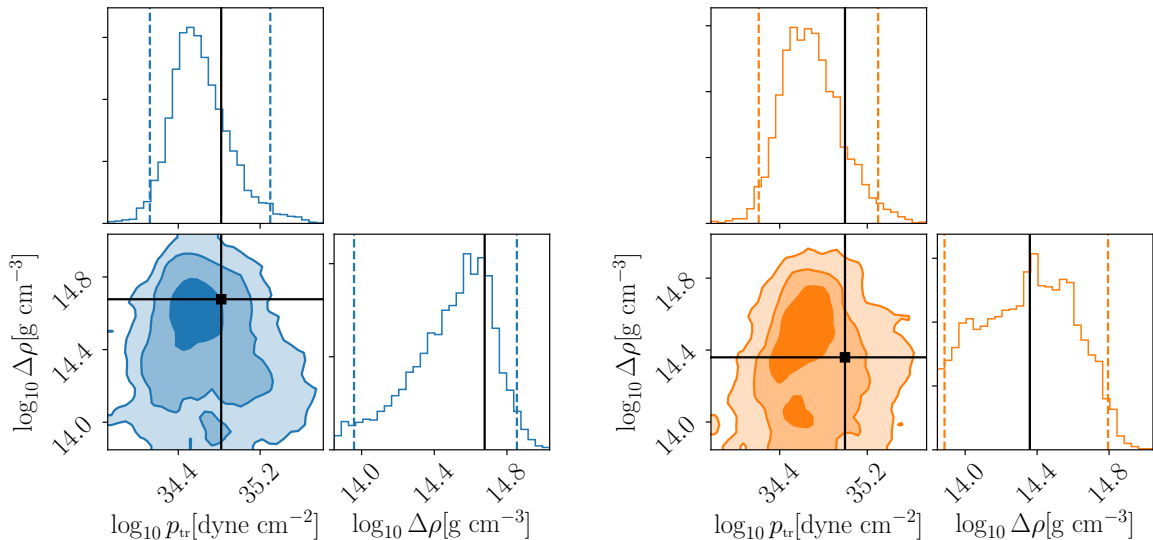


Figure 5.7: The joint posteriors for  $\log_{10} p_{\text{tr}}$  and  $\log_{10} \Delta \rho$  with 25 combined events for the TWIN EOS (*left panel*) and the KINK EOS (*right panel*). The dashed lines indicate the 95% credible interval and the solid lines the true value. For both EOSs, the true values of the phase transition parameters ( $\log_{10} p_{\text{tr}}, \log_{10} \Delta \rho$ ) are constrained with  $\lesssim 10\%$  statistical uncertainty.

phase does not provide information on the phase transition in this case. Should such a case be realized in nature, information might only be obtained from the postmerger GW signal.

Furthermore, we can only observe a Maxwell-like transition that is strong enough to leave an observable feature, e.g., at least a kink, in the  $M$ - $\Lambda$  curve. Should the density jump be too small, the  $M$ - $\Lambda$  curve would be smooth and, again, the inspiral phase would not provide information on the phase transition.

Finally, our method only works if inspiraling NSs have central pressures above the onset of the phase transition. If NS masses in binaries are limited to be around  $1.4 M_{\odot}$ , exploring lower central pressures, but phase transitions appear at much higher pressures in heavier stars, it will only be probed by the postmerger GW signal. However, the observation of GW190425 shows that also BNS mergers of heavy NS might be observed by GW interferometers (note that GW190425 could potentially have been a neutron-star–black-hole merger [208–210]). Should the phase transition appear at low pressures/densities, in NS below  $1 M_{\odot}$ , such that both NS in a binary are hybrid stars, our method might also not be able to identify its presence. In this case, while the observed macroscopic NS observables represent integrals over the EOS at all densities in the star, and, hence, in principle include information of the phase transition, observations might not be able to distinguish between the “true” EOS and an EOS that connects smoothly between the low-density nuclear-physics constraints and the observed part of the  $M$ - $R$  curve. However, in this case the phase transition onset would likely be between  $(1 - 2)n_{\text{sat}}$ , at low energy densities, which might be identified using other analysis techniques [35].

These shortcomings highlight that GW observations alone might not be able to answer

Event	$\ln \mathcal{B}_{\text{NPT}}^{\text{PT}}$	KL divergence
GW170817	$0.889 \pm 0.113$	0.809
GW190425	$0.441 \pm 0.085$	0.371
Combined	$1.330 \pm 0.141$	0.865

Table 5.1: The  $\ln$  Bayes factor  $\ln \mathcal{B}_{\text{NPT}}^{\text{PT}}$  and the KL divergence (in nats) estimated with the two BNS events.

the question of whether phase transitions exists in NSs or not. Hence, interdisciplinary studies including both nuclear physics and GW astrophysics are crucial.

## 5.5 Analysis of GW170817 and GW190425

Having shown with simulations that our methodology is in principle capable of uncovering and characterizing strong phase transitions, we now apply it to the real signals GW170817 [9] and GW190425 [49]. The former can confidently be assumed to have come from a BNS inspiral. We will also assume that the latter was emitted by a BNS. For both events, we take the publicly available posterior samples [211, 212] as the input for the stage II analysis as described in Sec. 5.3.4.

Table 5.1 shows the  $\ln$  Bayes factors  $\ln \mathcal{B}_{\text{NPT}}^{\text{PT}}$  and the Kullback–Leibler (KL) divergence for the two events separately and combined. The KL divergence is estimated from the posterior and prior for the EOS parameters, i.e.,

$$\text{KL divergence} = \int \mathcal{P}(\vec{E}_c) \ln \frac{\mathcal{P}(\vec{E}_c)}{\pi(\vec{E}_c)} d\vec{E}_c, \quad (5.14)$$

and it quantifies to what extent the posterior distribution is different from the prior distribution. A KL divergence of zero indicates that the two distributions are identical.

Based on the values of KL divergence for the two events, it would seem that GW170817 is carrying more information regarding the EOS, while GW190425 is not very informative, similar to the findings of Ref. [147].

In order to make a statistically robust statement, we would need to have a reliable distribution of  $\ln \mathcal{B}_{\text{NPT}}^{\text{PT}(\text{cat})}$  in the absence of strong phase transitions, which we could use as “background” to estimate the significance of the “foreground” values in Table 5.1. This would require (i) an accurate or at least representative simulated BNS population, and (ii) a justifiable representation of EOSs without a strong phase transition. One can systematically generate a representative ensemble of EOSs by using parameteric or non-parameteric methods and used them to calculate a background distribution for  $\ln \mathcal{B}_{\text{NPT}}^{\text{PT}(\text{cat})}$ , but the required computational resources will be significant. Due to the uncertainty in the BNS population and the limitation of available computational resources, such an estimation is currently not achievable. Clearly, we find no strong evidence for or against the presence of a strong phase transition [213].

In addition to the Bayes factors, a small value for the KL divergence indicates similarity of posterior and prior, and the extracted phase transition parameters are strongly influenced by the priors. The combined posteriors for the phase transition onset density, number density at the phase transition  $n_{\text{tr}}$ , and the corresponding density jump in terms

of  $n_{\text{sat}}$ ,  $\Delta n = \Delta\rho/\rho_{\text{sat}}$ , are shown together with the prior in Fig. 5.9.<sup>5</sup> The posteriors distributions for  $\log_{10} p_{\text{tr}}$ ,  $\log_{10} \Delta\rho$ ,  $m_1$ ,  $m_2$ , and  $\tilde{\Lambda}$  for GW170817 and GW190425 are shown in Figs. 5.10 and 5.11, respectively. We conclude that our measurements of  $n_{\text{tr}}$  and  $n_{\text{sat}}$  are not very informative, as could be expected based on the KL divergence.

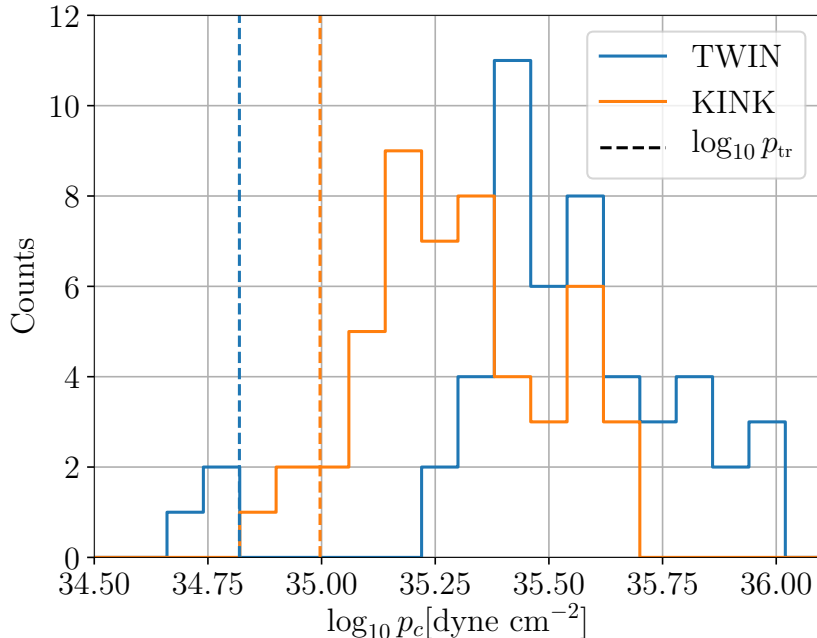


Figure 5.8: The distribution of the central pressure  $p_c$  for the 25 events included in the joint parameter-estimation analysis with the phase transition pressure for the two EOSs indicated by the dashed line. Most of the events have both of the components' central pressure above the phase transition pressure. In particular, none of the events have both components' central pressure below phase transition pressure.

## 5.6 Conclusion

We have presented a reliable way of searching for phase transitions in supranuclear matter using the inspiral waveform of binary NS mergers, which is successful both if the resulting mass-radius relation has only one or multiple stable branches. In contrast to previous works, which calculated the preference for multiple stable branches to search for strong phase transitions [35, 146, 147], our approach searches for an extended segment with  $c_S = 0$ , i.e., we do not explicitly assume a multiple-branch feature in the  $M$ - $R$  curve.

As long as there is some observable imprint of the phase transition in the mass-radius relation, our method can recover injected phase-transition parameters, and, hence, represents an important step forward in the search for a possible phase transition. We have explicitly demonstrated this by injecting simulated BNS mergers with different equations of state into synthetic stationary Gaussian noise. We have shown that our method can

<sup>5</sup>Initially we have priors  $n_{\text{tr}} \in [1, 4]n_{\text{sat}}$  and  $\Delta n \in [0.26, 37]n_{\text{sat}}$ , but the presence of heavy pulsars constrained both priors to more narrow ranges.

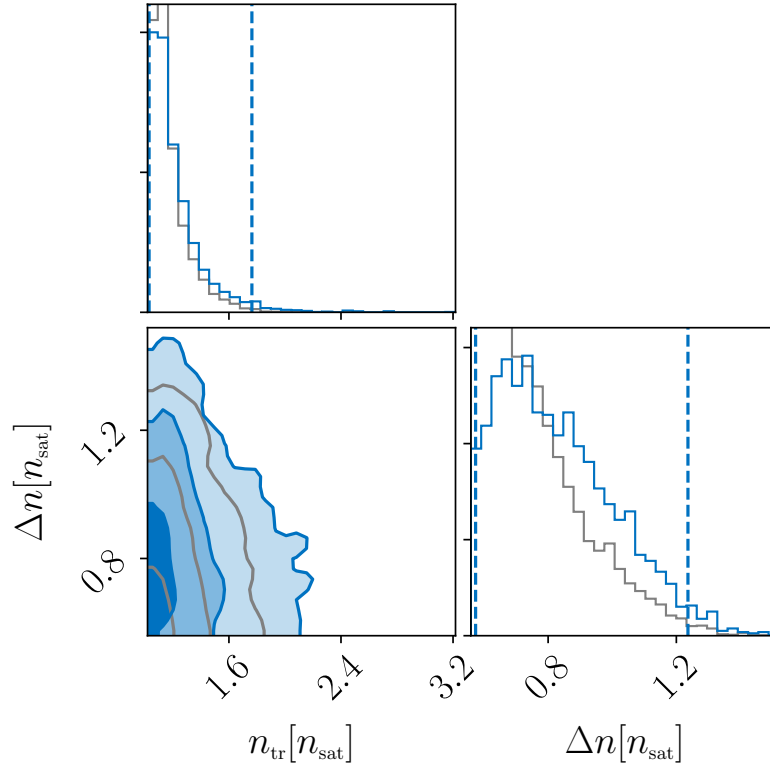


Figure 5.9: Corner plots showing the posterior distribution of  $n_{\text{tr}}$  and  $\Delta n$  in terms of  $n_{\text{sat}}$  with GW170817 and GW190425 combined (*blue*) on top of the prior with heavy pulsars constraint (*grey*). The dashed lines mark the 95% credible intervals. The posterior does not significantly deviate from the prior.

detect the presence of phase transitions at  $5\sigma$  confidence with 12 signals. Moreover, the phase-transition onset pressure and the corresponding density jump ( $\log_{10} p_{\text{tr}}, \log_{10} \Delta\rho$ ) were recovered with  $\lesssim 10\%$  statistical uncertainty with  $\sim 10$  events. Finally, we have applied the method to GW170817 and GW190425, but found no strong evidence for or against the presence of strong phase transitions.

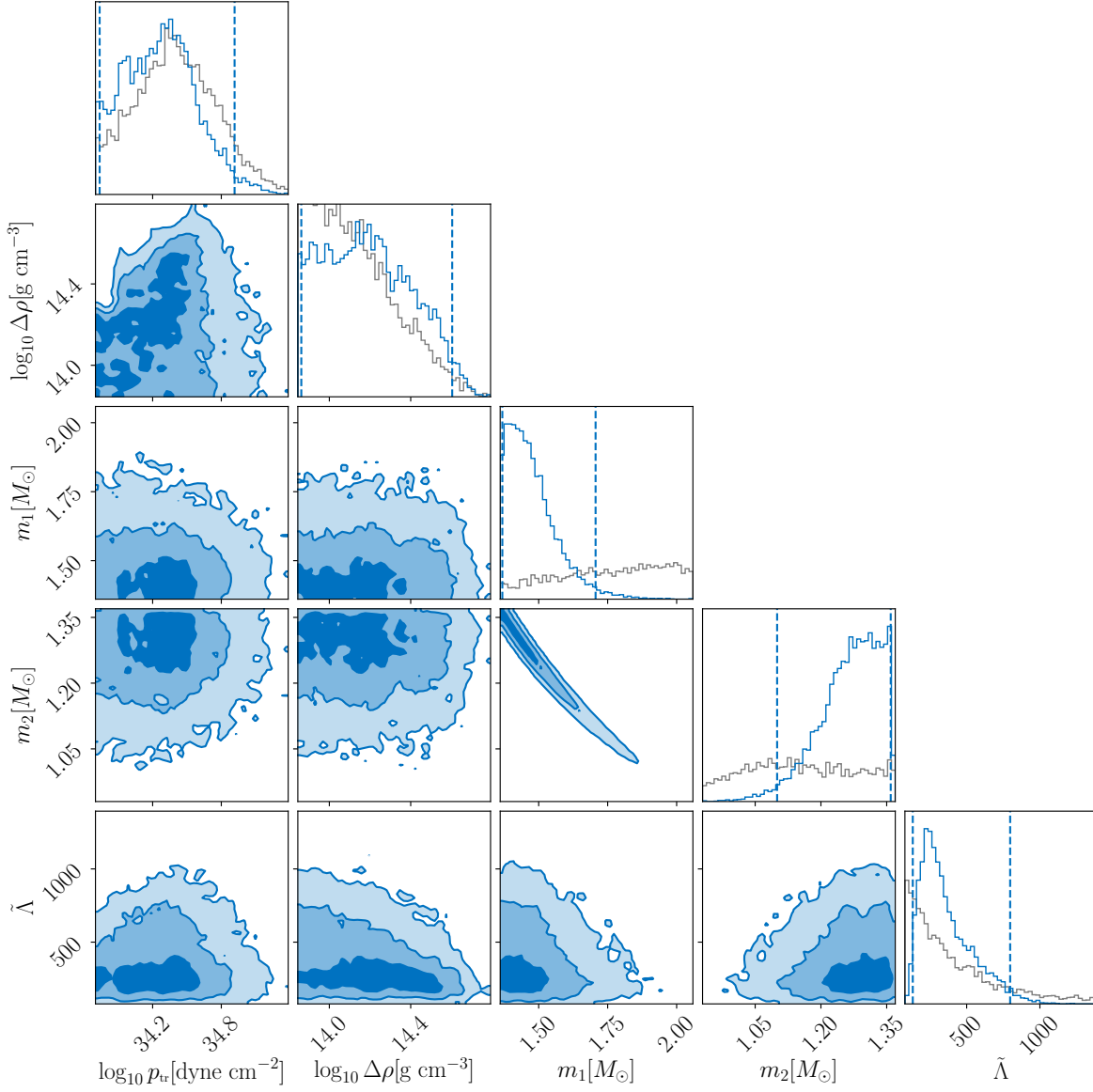


Figure 5.10: Corner plot showing the posterior distribution of  $\log_{10} p_{\text{tr}}$ ,  $\log_{10} \Delta\rho$ ,  $m_1$ ,  $m_2$  and  $\tilde{\Lambda}$  for GW170817 (*blue*) on top of the prior distribution across parameters (*grey*). The dashed lines marks the 95% credible intervals.

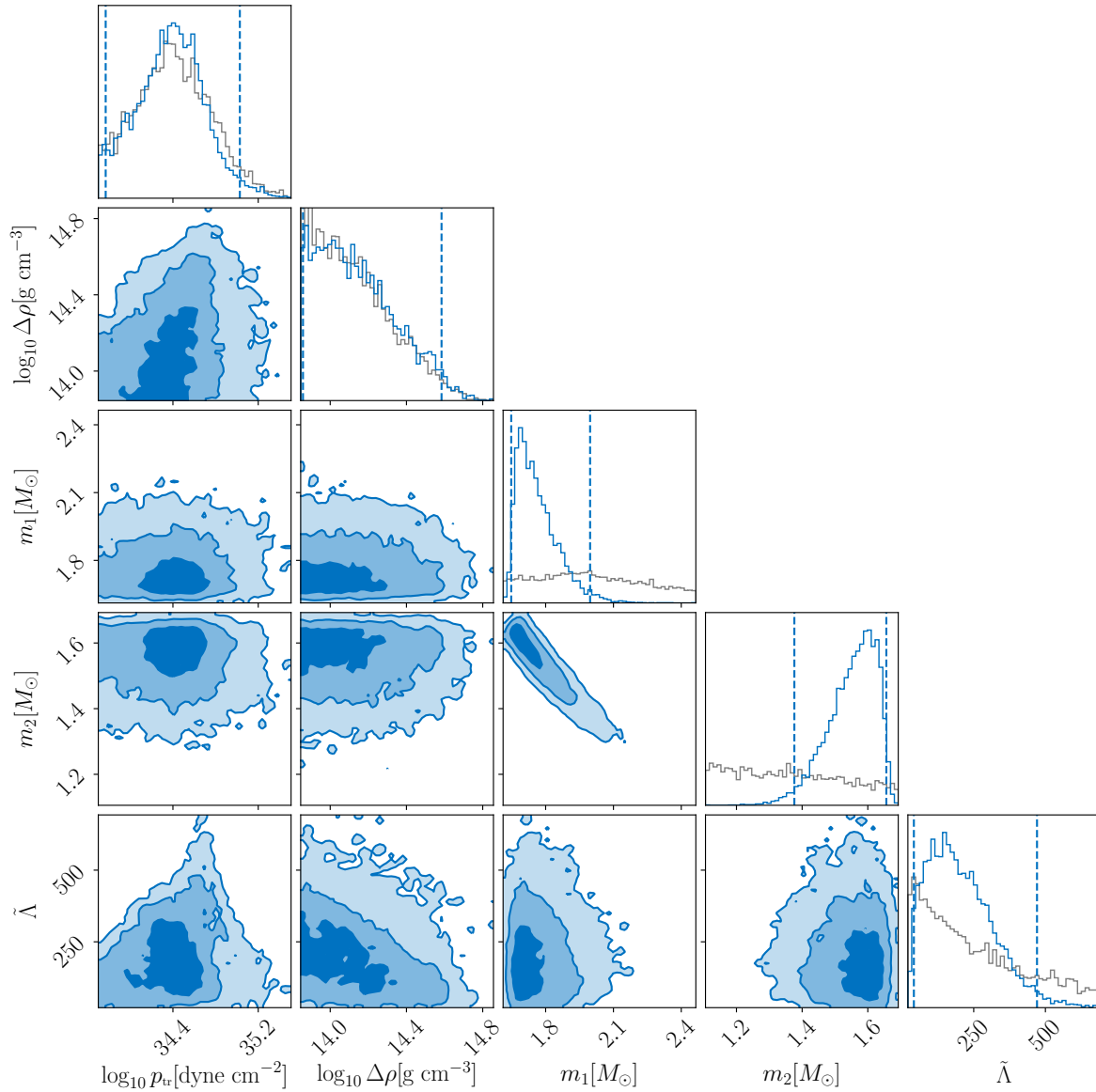


Figure 5.11: Corner plot showing the posterior distribution of  $\log_{10} p_{\text{tr}}$ ,  $\log_{10} \Delta\rho$ ,  $m_1$ ,  $m_2$  and  $\tilde{\Lambda}$  for GW190425 (*blue*) on top of the prior distribution across parameters (*grey*). The dashed lines marks the 95% credible intervals.



---

# MULTI-MESSENGER CONSTRAINTS ON THE NEUTRON-STAR EQUATION OF STATE AND THE HUBBLE CONSTANT

## 6.1 Introduction

Multi-messenger observations of binary neutron-star (BNS) mergers, which employ different probes to observe the same astrophysical process, elucidate the properties of matter under extreme conditions and can be used to determine the expansion rate of the Universe described by the Hubble constant. An example was the joint detection of gravitational waves (GWs), GW170817 [9], a gamma-ray burst (GRB), GRB170817A, a GRB afterglow arising from synchrotron radiation [11], and the kilonova AT2017gfo, i.e., an electromagnetic (EM) signal in the optical, infrared, and ultraviolet bands originating from the radioactive decay of atomic nuclei created during a merger from the same astrophysical source [12]. Using only GWs and the redshift of the host galaxy, this event led to an independent measurement of the Hubble constant [214]. It also placed constraints on the equation of state (EOS) of matter at densities higher than in the center of an atomic nucleus, e.g., [22]. Moreover, GWs have been detected from another presumed BNS merger, GW190425 [49], but no EM counterpart was observed [215]. Joint observations of the mass and radius of the rapidly rotating neutron star (pulsar) PSR J0030+0451 by the Neutron Star Interior Composition Explorer (NICER), e.g., [63], have provided independent constraints on NS properties [216]. These build upon mass measurements of the pulsars PSR J0740+6620 [135], PSR J0348+4042 [60], and PSR J1614-2230 [61] using radio observations.

In this chapter we combine the results from GW170817, GW190425, AT2017gfo, GRB170817A, PSR J0030+0451, PSR J0740+6620, PSR J0348+4042, and PSR J1614-2230 with nuclear-theory calculations of the EOS, the latter using chiral effective field theory (EFT) predictions at low densities, see Sec. 2.2.2. Previous studies have connected GW analyses to nuclear-physics predictions, e.g., [30, 33], or performed Bayesian analyses of EM and GW signals, e.g., [27, 28], or combined GW and NICER results [34, 217]. We combine all of these approaches, with the goal of providing improved constraints on the supranuclear EOS and measuring the Hubble constant.

## 6.2 Methods

### 6.2.1 The use of chiral effective field theory and the neutron-star equation of state

As mentioned before, chiral effective field theory (EFT) can be used to describe the neutron star equation-of-state at low densities; In particular, we use the result of these calculations up to densities of  $1.5 n_{\text{sat}}$  to constrain the NS EOS below that density, extended to matter in  $\beta$ -equilibrium and with a crust added [184]. Then, we extend our EOS models to densities beyond  $1.5 n_{\text{sat}}$  by employing a model-agnostic parametric expansion scheme that represents the EOS in the speed of sound plane [32, 33, 145, 218]. For each EOS, we sample a set of six randomly distributed points in the speed of sound plane at baryon densities between  $1.5 n_{\text{sat}}$  and  $12 n_{\text{sat}}$  and connect them by line segments. The NS properties are found to be not very sensitive to the number of line segments when varying it between 5-10. This construction by design remains causal and stable at all densities,  $0 \leq c_S \leq c$ , with  $c_S$  the speed of sound and  $c$  the speed of light. From the speed-of-sound curves, we reconstruct the EOSs and solve the Tolman-Oppenheimer-Volkoff (TOV) equations [93, 94] to extract NS structure properties. For each sampled EOS, we construct a second EOS that includes a segment with  $c_S = 0$  with random onset density and width, to simulate EOSs with strong first-order phase transitions. We sampled 5000 different EOSs to produce a uniform prior on the radius of a typical  $1.4M_{\odot}$  NS.

Similar to commonly used polytropic expansion schemes [177], the speed-of-sound extension does not make any assumptions about degrees of freedom at higher densities, and includes many possible density dependencies for the EOS at high densities. For example, this extension includes regions of sudden stiffening or sudden softening, as would be expected from a strong first-order phase transition.

### 6.2.2 Incorporation of the maximum mass neutron-star constraints

For the inclusion of the astronomical constraints on the EOSs, we adopt a Bayesian approach [207, 219], and express the constraints in terms of likelihood functions that can be used for the GW and EM analysis.

We have used constraints on the lower bound of the maximum NS mass  $M_{\text{max}}$  given by the mass measurements of pulsars PSR J0740+6620 [135], PSR J0348+0432 [60], PSR J1614-2230 [61], and a constraint on the upper bound on  $M_{\text{max}}$  [151] of  $M_{\text{max}} = 2.16_{-0.15}^{+0.17}M_{\odot}$  at 95% credence. Similar upper bounds on  $M_{\text{max}}$  have also been obtained in different studies, e.g.,  $M_{\text{max}} \lesssim 2.17M_{\odot}$  at 90% credence [25],  $M_{\text{max}} \lesssim 2.3M_{\odot}$  [220], or  $M_{\text{max}} \lesssim 2.16 - 2.28M_{\odot}$  [221]. The corresponding likelihood  $\mathcal{L}_{M_{\text{max}}}$  is given by

$$\begin{aligned} \mathcal{L}_{M_{\text{max}}}(\text{EOS}) &= \mathcal{L}_{M_{\text{max}}}(M_{\text{max}}) \\ &= \prod_i \text{CDF}(M_{\text{max}}, \mathcal{N}(M_i^{\text{PSR}}, \sigma_i^{\text{PSR}})) \\ &\quad \times (1 - \text{CDF}(M_{\text{max}}, \mathcal{N}(2.16M_{\odot}, 0.17M_{\odot}))), \end{aligned} \tag{6.1}$$

where  $\text{CDF}(x, \mathcal{N}(\mu, \sigma))$  is the cumulative distribution function corresponding to a normal distribution  $\mathcal{N}(\mu, \sigma)$  evaluated at  $x$ .  $M_i^{\text{PSR}}$  and  $\sigma_i^{\text{PSR}}$  are the mass measurement and the

1- $\sigma$  uncertainty reported for the pulsars that we included for the analysis, respectively. The values for  $M_i^{\text{PSR}}$  and  $\sigma_i^{\text{PSR}}$  are tabulated in Tab. 6.1. For the upper bound on  $M_{\text{max}}$ , we take a more conservative uncertainty, adopting the 95% credible range as the standard deviation for the likelihood input. In the likelihood  $\mathcal{L}_{M_{\text{max}}}$ , we have approximated the measurements [60, 61, 135] and estimates [151] as Gaussian. The final likelihood is shown in Fig. 6.1.

Pulsar	$M^{\text{PSR}} [M_{\odot}]$	$\sigma^{\text{PSR}} [M_{\odot}]$	Reference
PSR J0740+6620	2.14	0.1	[135]
PSR J0348+0432	2.01	0.04	[60]
PSR J1614-2230	1.908	0.016	[61]

Table 6.1: **Summary of the heavy-pulsar mass measurements.** The masses  $M^{\text{PSR}}$  and their 1- $\sigma$  uncertainties  $\sigma^{\text{PSR}}$  reported for the pulsars included in this analysis.

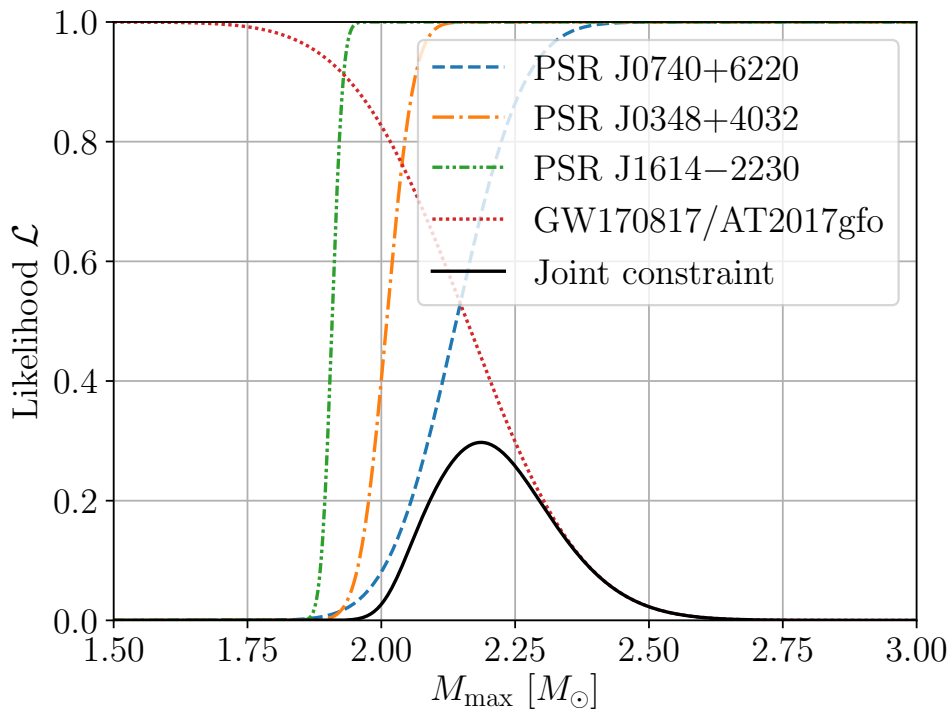


Figure 6.1: **Combined likelihood of the maximum mass.** Shown are the constraints from radio observations of PSR J0740+6620 [135], PSR J0348+0432 [60], and PSR J1614-2230 [61] (lower bounds) from the remnant classification of GW170817/AT2017gfo as a black hole [151] (upper bound), and the joint constraint (black line).

### 6.2.3 Coherent incorporation of NICER data

For the NICER data [222], we use the results from Ref. [63] where a Bayesian inference approach was used to analyze the energy-dependent thermal X-ray waveform of PSR J0030+0451. We employ the samples obtained with a three-oval, uniform-temperature

spots model [63, 223]. This model provides agreement with the observed NICER data and constrains the mass and radius of PSR J0030+0451 to be  $M = 1.44_{-0.14}^{+0.15}M_{\odot}$  and  $R = 13.02_{-1.06}^{+1.24}\text{km}$  (both at  $1\sigma$  uncertainty). The inferred mass-radius posterior probability distributions are not dominated by systematic uncertainties and inferred parameters are in agreement for different models [63, 64]; as a comparison, the results for the two-oval spot model are shown together with the three-oval spots model in Fig. 6.2. Further comparisons can be found in Refs. [63, 64].

The corresponding likelihood  $\mathcal{L}_{\text{NICER}}$  is given by

$$\begin{aligned}\mathcal{L}_{\text{NICER}}(\text{EOS}) &= \int dM dR p_{\text{NICER}}(M, R)\pi(M, R|\text{EOS}) \\ &= \int dM dR p_{\text{NICER}}(M, R)\delta(R - R(M, \text{EOS})) \\ &= \int dM p_{\text{NICER}}(M, R = R(M, \text{EOS})),\end{aligned}\tag{6.2}$$

where  $p_{\text{NICER}}(M, R)$  is the joint-posterior probability distribution of mass and radius of PSR J0030+0451 as measured by NICER and we use the fact that the radius is a function of mass for a given EOS.

The joint-constraint likelihood  $\mathcal{L}_{\text{Joint}}$  combining the maximum mass and the NICER information is given by

$$\mathcal{L}_{\text{Joint}}(\text{EOS}) = \mathcal{L}_{\text{NICER}}(\text{EOS}) \times \mathcal{L}_{M_{\text{max}}}(\text{EOS}).\tag{6.3}$$

$\mathcal{L}_{\text{Joint}}(\text{EOS})$  is then taken as an input for our further analysis of GW170817, AT2017gfo, and GW190425.

## 6.2.4 Gravitational-wave Analysis

We use the BILBY software [224] to reanalyze the observational data for GW170817 [225] and GW190425 [226]. We ran PARALLEL BILBY [227] on 800 cores to obtain posterior probability distributions within a few hours on the high-performance computing (HPC) clusters Minerva at the Max-Planck-Institute for Gravitational Physics, on SuperMUC-NG at the Leibniz Supercomputing Centre, or on the HAWK cluster of the High-Performance Computing Center Stuttgart. The GW signals are analysed within a frequency interval  $f \in [23, 2048]\text{Hz}$  which covers the full inspiral of the BNS coalescence. Frequency-dependent spline calibration envelopes [228] are introduced into the waveform templates to counteract the potential systematics due to the uncertainties in the detectors' calibrations [229, 230]. We adopt the power spectral density estimated with BAYESWAVE [45, 231]. For our analysis, we employ the IMRPhenomPv2\_NRTidalv2 (NRTidalv2) waveform model [117].

## 6.2.5 AT2017gfo

### Kilonova modelling

For the assessment of systematic uncertainties, we compare multiple light curve models [122, 232].

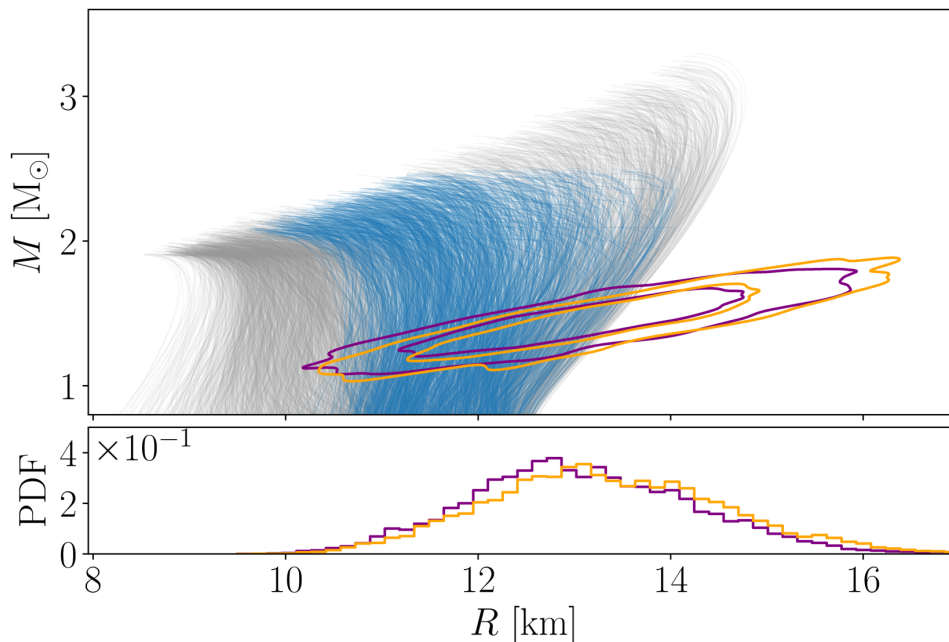


Figure 6.2: **Comparison of different NICER analysis models.** Shown are the 2D posterior probability distributions for the mass and radius of PSR J0030+0451 inferred with a three-oval spot model (purple) and a two-oval spot model (orange) [63] in comparison with our EOS constraint at this analysis step, cf. Fig. 6.9. Contours are shown at 68% and 95% credibility.

*Model I (standard model):* This model uses Spectral Energy Distributions (SEDs) simulated using the multi-dimensional Monte Carlo radiative transfer code POSSIS [122]. We use a model grid with modifications to the underlying physics and the assumed geometry for the ejecta. Compared to previous work [122], we introduce two changes to the physics: thermalization efficiencies are taken from Ref. [233] and the temperature is estimated in each grid cell and at each time from the mean intensity of the radiation field (inferred from the density and local energy deposition from radioactive decay). In terms of the adopted geometry, we run calculations for geometries similar to, e.g., Refs. [234–236], see Fig. 6.3, which were obtained from numerical relativity simulations. A first component represents the dynamical ejecta, which have velocities ranging from the minimum velocity of the dynamical ejecta  $v_{\min}^{\text{dyn}} = 0.08c$  to the maximum velocity of the dynamical ejecta  $v_{\max}^{\text{dyn}} = 0.3c$ , are characterised by an ejecta mass  $M_{\text{ej}}^{\text{dyn}}$ , and have a lanthanide-rich composition within an angle  $\pm\Phi$  about the equatorial plane and a lanthanide-free composition otherwise. The dynamical ejecta correspond to a high-velocity portion of the geometry adopted in Ref. [122]. The main source of opacity in kilonova ejecta is given by bound-bound line transitions, in which electrons move between two bound states of atoms or ions. The bound-bound opacities  $\kappa_{\text{bb}}$  assumed for the dynamical ejecta are wavelength- and time-dependent, reaching values of  $\kappa_{\text{bb}} = 1 \text{ cm}^2 \text{ g}^{-1}$  at  $1\mu\text{m}$  and 1.5 d for the lanthanide-rich and  $\kappa_{\text{bb}} = 5 \times 10^{-3} \text{ cm}^2 \text{ g}^{-1}$  at  $1\mu\text{m}$  and 1.5 d for the lanthanide-free portion of the ejecta [122]. A second spherical component represents the ejecta released from the merger remnant and debris disk, extending from minimal velocities  $v_{\min}^{\text{pm}} = 0.025c$  up to maximal velocities  $v_{\max}^{\text{pm}} = 0.08c$  and with an ejecta mass  $M_{\text{ej}}^{\text{pm}}$ . The bound-bound opacities adopted for the postmerger ejecta are intermediate [235] to those in the lanthanide-rich

and lanthanide-free components of the dynamical ejecta ( $\kappa_{\text{bb}} = 0.1 \text{ cm}^2 \text{ g}^{-1}$  at  $1 \mu\text{m}$  and 1.5 d). SEDs and corresponding light curves are then controlled by four parameters:  $M_{\text{ej}}^{\text{dyn}}$ ,  $M_{\text{ej}}^{\text{pm}}$ ,  $\Phi$ , and the observer viewing angle  $\Theta_{\text{obs}}$ .

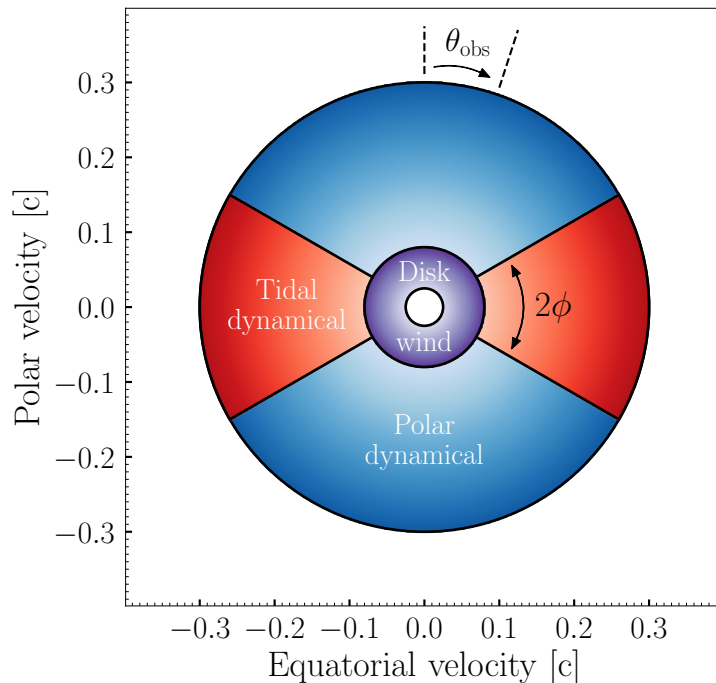


Figure 6.3: **Geometry employed in the kilonova description of Model I.** Different colors refer to the different lanthanide fractions of the individual ejecta components: tidal dynamical (red), polar dynamical (blue), and disk wind (purple).

*Model II:* This model adopts a kilonova without an additional wind ejecta component [122], which makes standardization and extraction of the Hubble constant easier due to the smaller number of free parameters. Tighter constraints on the distance and inclination angle are extracted compared to our standard choice (Model I); cf. Fig. 6.13.

*Model III:* This model adopts the radiative transfer model of Ref. [232] and employs a multi-dimensional Monte Carlo code to solve the multi-wavelength radiation transport equation for an expanding medium. We use one spherically symmetric ejecta component characterized by the mass of the ejecta  $M_{\text{ej}}$ , the mass fraction of lanthanides  $X_{\text{lan}}$ , and the ejecta velocity  $v_{\text{ej}}$ . While using only one ejecta component reduces the consistency between the observational data and the model prediction, it provides easier standardization and therefore puts a tighter constraint on the measured distance, but no information about inclination can be extracted due to the assumption of spherical symmetry.

*Surrogate Construction:* We use the approach outlined in Refs. [237, 238], where a Gaussian-Process-Regression framework is employed; cf. Refs. [26, 215] for a detailed discussion.

We show the performance of our standard model (Model I) in Fig. 6.4 and find that it is consistent with the observed data. The extracted properties of the ejecta are shown in Fig. 6.5. The disk wind ejecta are about 10 times larger than the dynamical ejecta. The angle  $\Phi$  peaks around  $50^\circ$ , while the observation angle  $\Theta_{\text{obs}}$  peaks around  $40^\circ$  (cf. Fig. 6.3).

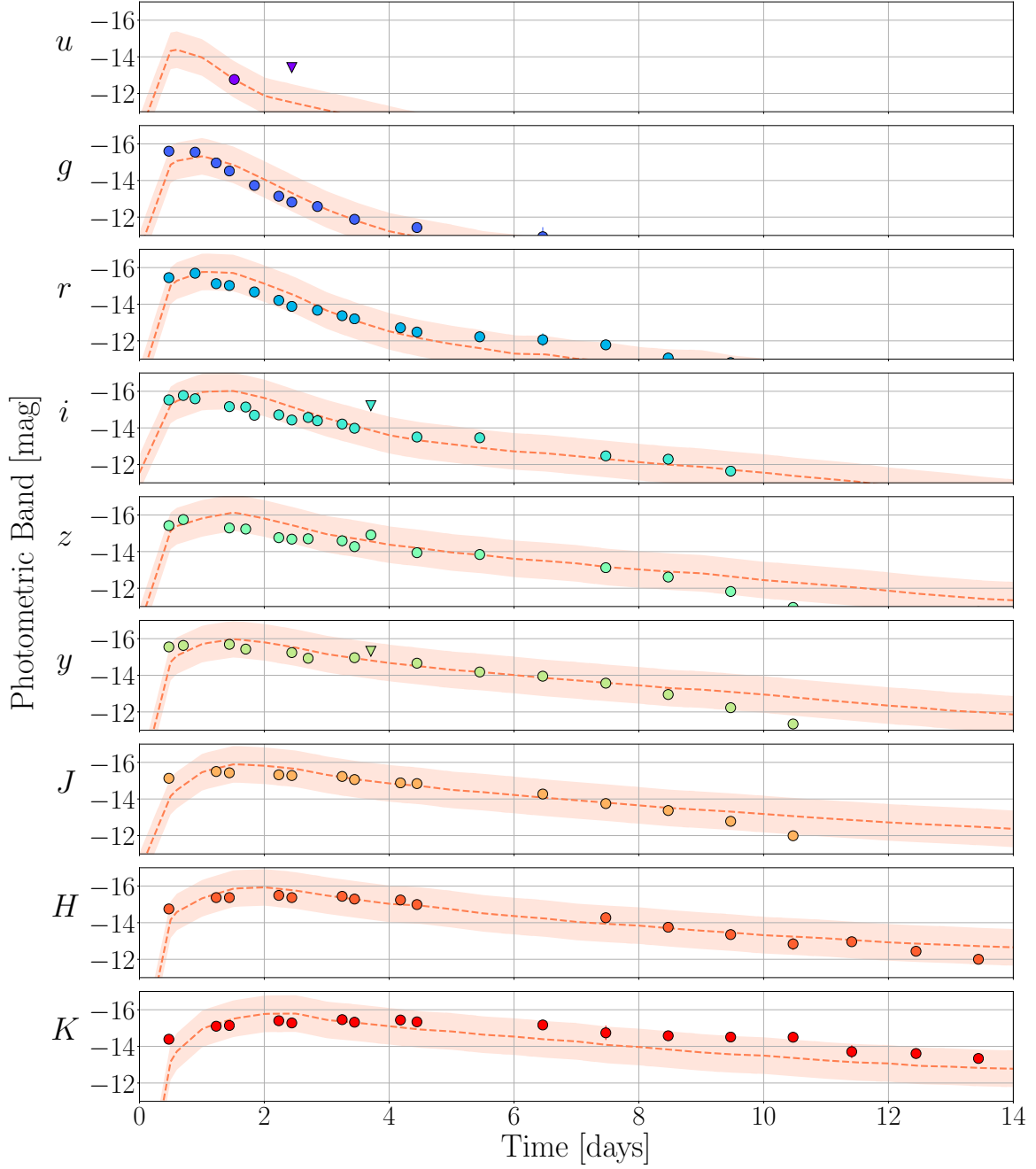


Figure 6.4: **Comparison of observed light curves of AT2017gfo with Model I.** Predictions of Model I (shaded bands) are compared to observational data (points) in different photometric bands collected in [26] using the original data of [52, 54–57, 59, 239–245].

To connect the individual ejecta components to the different ejecta mechanisms, we assume that the total ejecta mass is a sum of multiple components. The first component is related to the dynamical ejecta  $M_{\text{ej}}^{\text{dyn}}$ . The second component is caused by disk wind ejecta and proportional to the disk mass surrounding the final remnant  $M_{\text{ej}}^{\text{pm}} = \zeta M_{\text{disk}}$ .

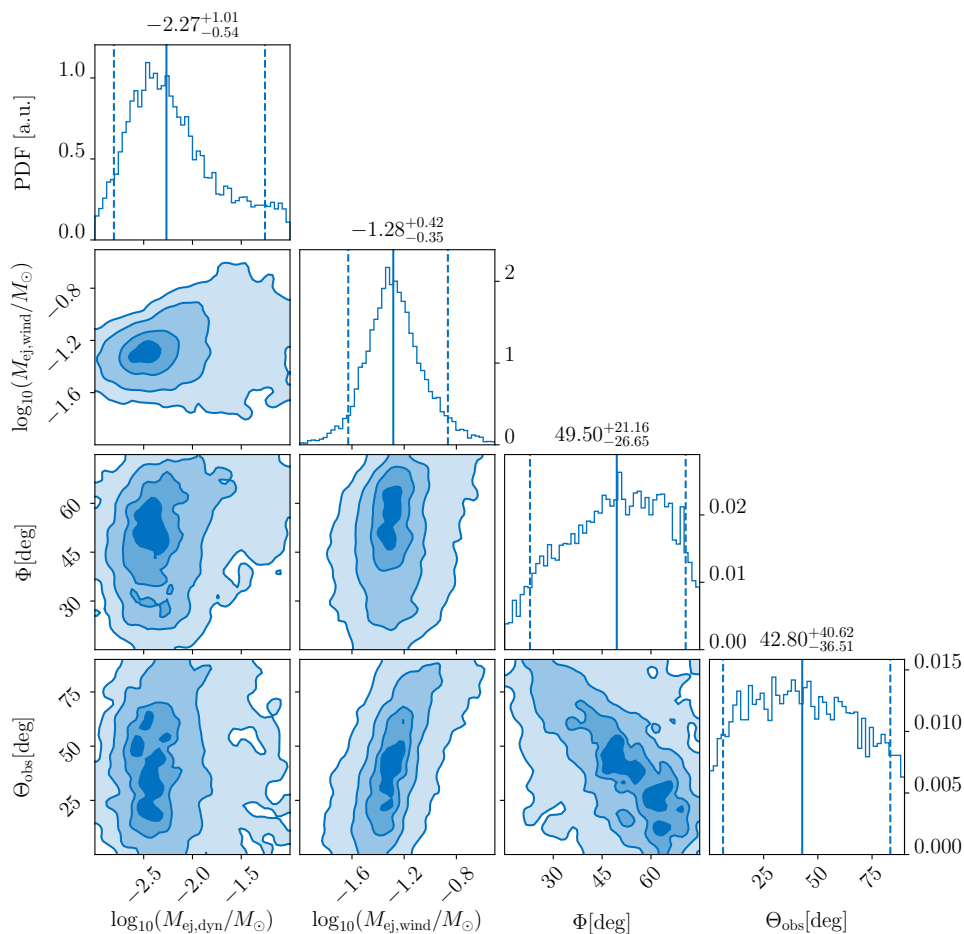


Figure 6.5: **Estimated ejecta properties for Model I.** Corner plot for the mass of the dynamical ejecta  $M_{\text{ej,dyn}}$ , the mass of the disk wind ejecta  $M_{\text{ej,wind}}$ , the opening angle between lanthanide-rich and lanthanide-poor dynamical ejecta components  $\Phi$ , and the viewing angle  $\Theta_{\text{obs}}$  at 10%, 32%, 68% and 95% credence. For the 1D posterior probability distributions, we mark the median (solid lines) and the 90% credible interval (dashed lines) and report these above each panel.

For a conservative estimate, we also add a third component  $\alpha$  that we keep as a free parameter during the sampling procedure.

For the dynamical ejecta, we use the description in Ref. [28], while we assume that the disk wind ejecta are proportional to the disk mass. Based on recent works on predicting the disk mass for systems with low mass ratios [246], we include an explicit mass-ratio dependence as described below.

The extracted binary properties are shown in Fig. 6.6, in which we report the chirp mass, the mass ratio, the deformability  $\tilde{\Lambda}$ , the fraction of the dynamical ejecta  $\alpha$ , the disk conversion factor  $\zeta$ , and the maximum TOV mass.

### Disk mass prediction

We utilise results from 73 numerical relativity simulations performed by different groups [246–249]. The full dataset is shown in Fig. 6.7A which shows the disk mass versus the ratio of the total mass of the system and the threshold mass. The threshold mass  $M_{\text{threshold}}$  is the



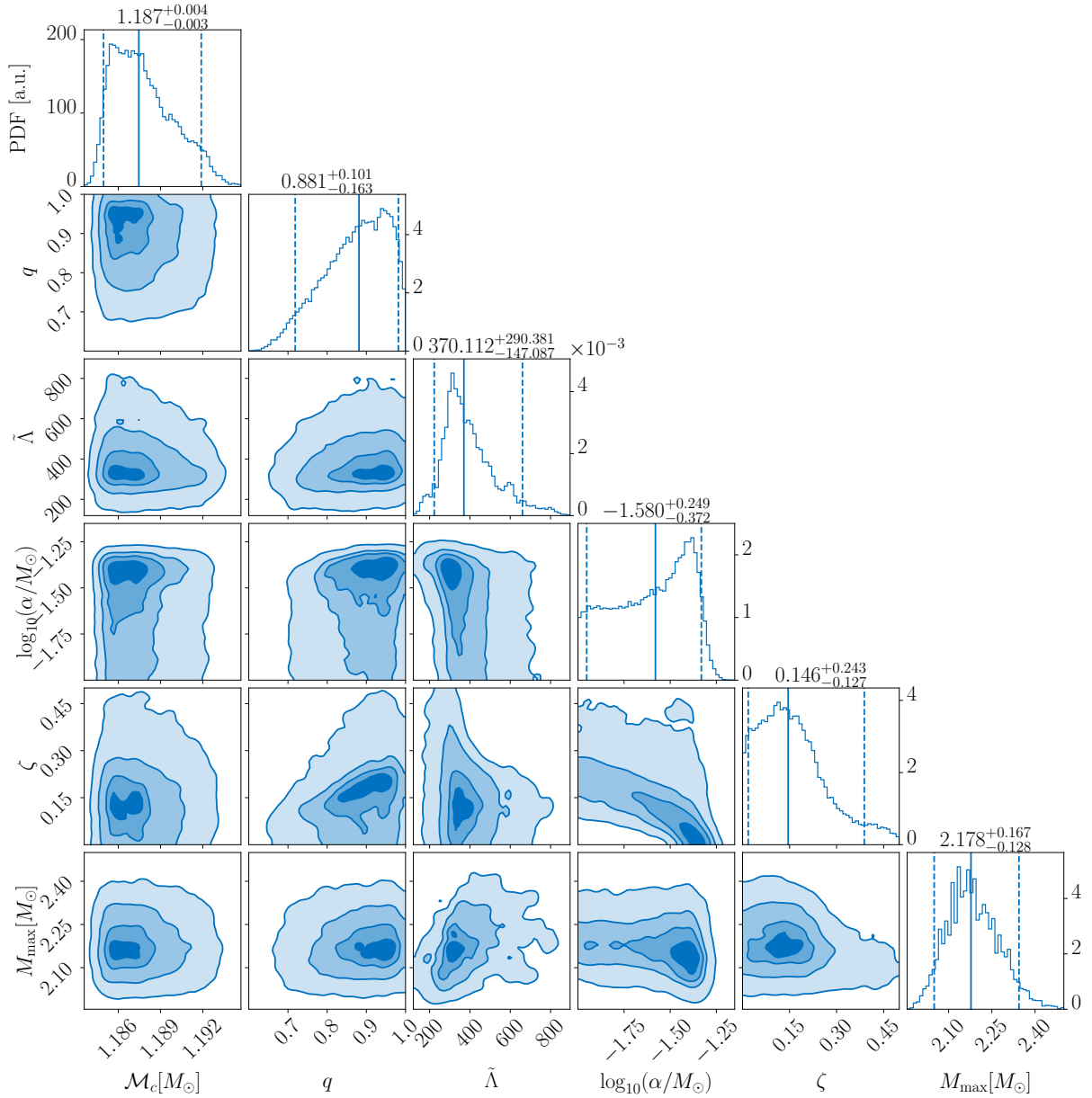


Figure 6.6: **Estimated BNS properties for Model I.** Similar to Fig. 6.5 but for the chirp mass  $\mathcal{M}_c$ , mass ratio  $q$ , tidal deformability  $\tilde{\Lambda}$ , free ejecta parameter  $\alpha$ , disk conversion factor  $\zeta$ , and maximum NS mass. Model II and Model III provide very similar binary properties.

limiting total mass of the BNS system beyond which a prompt collapse to a black hole occurs. For the estimate of the threshold mass, we use the predictions of Ref. [250]. We compare the data with the estimate of Ref. [28] confirming that an decreasing mass ratio leads to an increased disk mass [246]. We use a similar functional behavior to Ref. [28], but we incorporate mass-ratio dependent fitting parameters such that

$$\log_{10} \left( \frac{M_{\text{disk}}}{M_{\odot}} \right) = \max \left( -3, a \left( 1 + b \tanh \left( \frac{c - (m_1 + m_2) M_{\text{threshold}}^{-1}}{d} \right) \right) \right), \quad (6.4)$$

with  $a$  and  $b$  given by

$$\begin{aligned} a &= a_o + \delta a \cdot \xi, \\ b &= b_o + \delta b \cdot \xi, \end{aligned} \quad (6.5)$$

where  $a_o$ ,  $b_o$ ,  $\delta a$ ,  $\delta b$ ,  $c$ , and  $d$  are free parameters. The parameter  $\xi$  is given by

$$\xi = \frac{1}{2} \tanh(\beta(q - q_{\text{trans}})), \quad (6.6)$$

where  $\beta$  and  $q_{\text{trans}}$  are free parameters. Fig. 6.7B shows how the model fitting changes as the mass ratio changes.

The best-fitting model parameters are given by minimizing  $r = \langle (\log_{10}(M_{\text{disk}}) - \log_{10}(M_{\text{disk}}^{\text{fit}}))^2 \rangle$ ; we find  $a_o = -1.581$ ,  $\delta a = -2.439$ ,  $b_o = -0.538$ ,  $\delta b = -0.406$ ,  $c = 0.953$ ,  $d = 0.0417$ ,  $\beta = 3.910$ ,  $q_{\text{trans}} = 0.900$ .

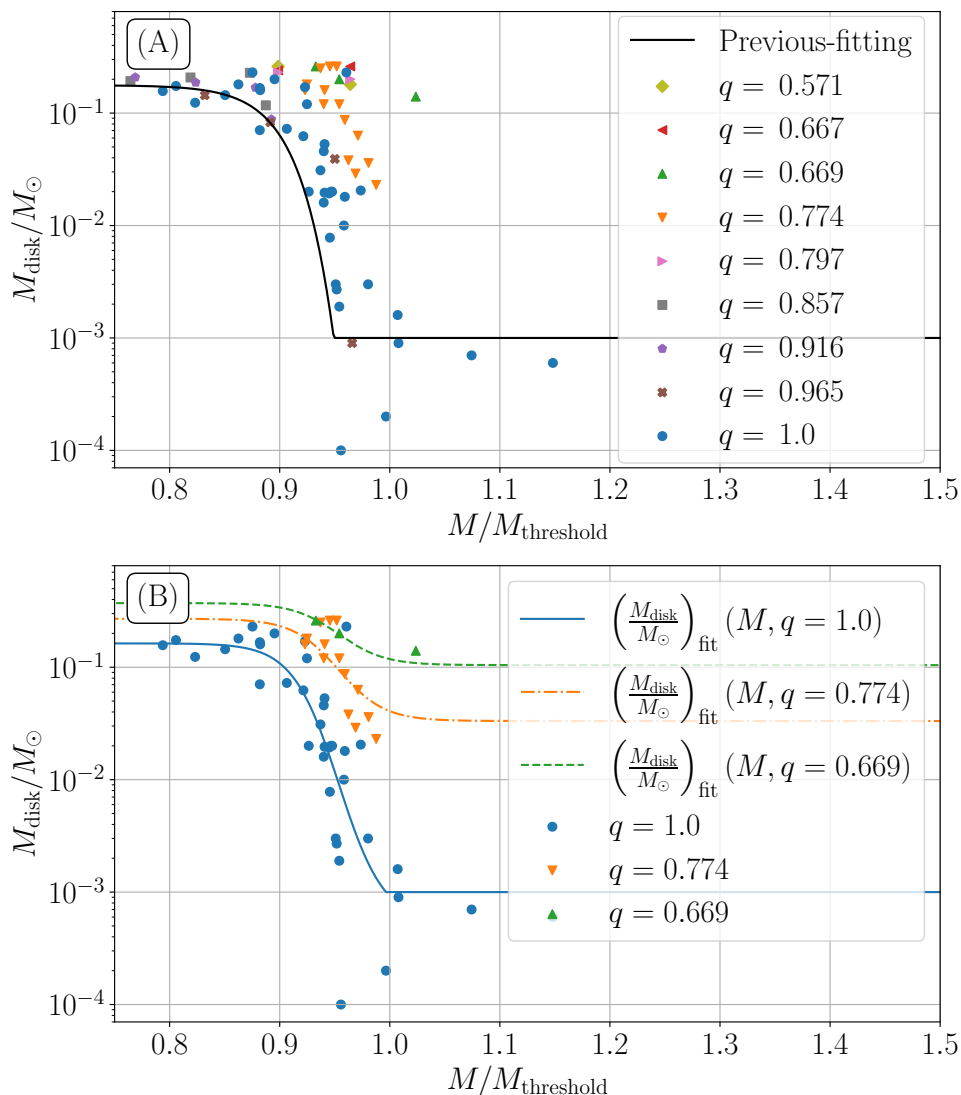


Figure 6.7: **Disk mass predictions for various total masses and mass ratios.** (A) Data employed for the construction of the model fitting in Eq. (6.4), compared to the model of [28]. (B) Three examples, where data from numerical-relativity simulations (symbols) are compared to the fit for different mass ratios (lines).

## 6.2.6 Prior combination for distance measurement

Due to the strong correlation between the luminosity distance  $D$  and inclination  $\iota_0$  across different analyses, we combine the information on the  $D$ - $\iota_0$  plane and then marginalize over the inclination. We take the GRB170817A-VLBI measurement  $p_{\text{GRB}}(D, \iota_0)$  as the prior for the other two analyses. Therefore, the combined posterior probability distribution  $p_{\text{com}}(D, \iota_0)$  is given by

$$p_{\text{com}}(D, \iota_0) = \mathcal{L}_{\text{GW}}(D, \iota_0) \times \mathcal{L}_{\text{EM}}(D, \iota_0) \times p_{\text{GRB}}(D, \iota_0), \quad (6.7)$$

where  $\mathcal{L}_{\text{GW}}$  and  $\mathcal{L}_{\text{EM}}$  are the likelihoods for the parameters  $(D, \iota_0)$  for the GW170817 and AT2017gfo analyses, respectively.

Because we are combining the information in the post-processing stage, we do not have access to the likelihood but only the posterior probability distributions of GW170817,  $p_{\text{GW}}$ , and AT2017gfo,  $p_{\text{EM}}$ . Therefore, we evaluate the combined posterior probability distribution by

$$p_{\text{com}}(D, \iota_0) = \frac{p_{\text{GW}}(D, \iota_0)}{\pi_{\text{GW}}(D, \iota_0)} \times \frac{p_{\text{EM}}(D, \iota_0)}{\pi_{\text{EM}}(D, \iota_0)} \times p_{\text{GRB}}(D, \iota_0), \quad (6.8)$$

where  $\pi_{\text{GW}}(D, \iota_0)$  and  $\pi_{\text{EM}}(D, \iota_0)$  are the priors for the parameters  $(D, \iota_0)$  used for analysing GW170817 and AT2017gfo, respectively.

The combined posterior probability distribution on the distance is then given by

$$p_{\text{com}}(D) = \int d\iota_0 p_{\text{com}}(D, \iota_0) \quad (6.9)$$

which we use below in the Hubble constant measurement.

## 6.2.7 Estimation of the Hubble constant $H_0$

The Hubble constant  $H_0$  relates the center-of-mass recession velocity of a galaxy relative to the cosmic microwave background (CMB) [251]  $v_r$  with the comoving distance  $D_c$  and the peculiar velocity  $v_p$  by

$$v_r = H_0 D_c + v_p. \quad (6.10)$$

The distance between Earth and NGC 4993, the host galaxy of GW170817, is small,  $\sim 40$  Mpc [51], so we can approximate the comoving distance with the luminosity distance  $D$ . Combining the distance measurement with the redshift  $z$  of the host galaxy,  $z = 0.009783 \pm 0.000023$ , constrains the Hubble constant [214].

GW170817's host galaxy NGC 4993 belongs to the galaxy cluster ESO 508, which has a radial velocity of  $v_r$  of  $3327 \pm 72 \text{ km s}^{-1}$  [252] and the peculiar velocity  $v_p$  of NGC 4993 is  $310 \pm 69 \text{ km s}^{-1}$  [253]. To reduce possible systematics introduced by imperfect modelling of the bulk flow motion [253], we take the uncertainty on  $v_p$  to be  $150 \text{ km s}^{-1}$  [254].

We model the likelihoods of  $v_r$ ,  $\mathcal{L}(v_r)$ , and  $v_p$ ,  $\mathcal{L}(v_p)$ , to be Gaussians given by

$$\mathcal{L}(v_r) \propto \exp\left(-\frac{1}{2} \left(\frac{v_r - \langle v_r \rangle}{\sigma_{v_r}}\right)^2\right), \quad \mathcal{L}(v_p) \propto \exp\left(-\frac{1}{2} \left(\frac{v_p - \langle v_p \rangle}{\sigma_{v_p}}\right)^2\right), \quad (6.11)$$

where  $\langle v_r \rangle = 3327 \text{ km s}^{-1}$ ,  $\sigma_{v_r} = 72 \text{ km s}^{-1}$ ,  $\langle v_p \rangle = 310 \text{ km s}^{-1}$  and  $\sigma_{v_p} = 150 \text{ km s}^{-1}$ .

As a result, the multi-dimensional posterior probability distribution  $p(H_0, D, v_p)$  is given by

$$\begin{aligned}
 p(H_0, D, v_p) &= \mathcal{L}(H_0, D, v_p) \pi(H_0, D, v_p) \times \frac{1}{\mathcal{N}_s(H_0)} \\
 &\propto \exp\left(-\frac{1}{2} \left(\frac{v_p - \langle v_p \rangle}{\sigma_{v_p}}\right)^2\right) \times \exp\left(-\frac{1}{2} \left(\frac{H_0 D + v_p - \langle v_r \rangle}{\sigma_{v_r}}\right)^2\right) \\
 &\times p(D) \times \pi(H_0) \times \pi(v_p) \times \frac{1}{\mathcal{N}_s(H_0)},
 \end{aligned} \tag{6.12}$$

where  $p(D)$ ,  $\pi(H_0)$  and  $\pi(v_p)$  are the posterior probability distribution of the distance, the prior on the Hubble constant, and the prior on the peculiar velocity, respectively.  $\mathcal{N}_s(H_0)$  is the selection effect term [214]. We take  $\pi(H_0)$  to be uniform in  $[20, 160] \text{ km s}^{-1} \text{ Mpc}^{-1}$ ,  $\pi(v_p)$  to be uniform in  $[-c, c]$  and  $\mathcal{N}_s(H_0) \propto H_0^3$ . This choice of selection effect term is rooted in a volumetric prior on the redshift [214].

For the posterior probability distribution of the distance, we take the posterior probability distribution based on the combined analysis as described above, including the use of standardizable kilonovae light curves to measure their distances [255, 256]. Because we have a set of posterior probability distribution samples  $\{d_i\}$  that follow the posterior probability distribution  $p_{\text{com}}(D)$ , we obtain the marginalized posterior probability distribution  $p(H_0, v_p)$  by

$$\begin{aligned}
 p(H_0, v_p) &= \int dD p(H_0, D, v_p) \\
 &= \int dD p_{\text{com}}(D) \frac{p(H_0, D, v_p)}{p_{\text{com}}(D)} \\
 &= \left\langle \frac{p(H_0, D, v_p)}{p_{\text{com}}(D)} \right\rangle_{\{d_i\}},
 \end{aligned} \tag{6.13}$$

in which we approximate  $\int dD p_{\text{com}}(D)$  by an average over posterior probability distribution samples denoted  $\langle \dots \rangle_{\{d_i\}}$ . We sample over  $p(H_0, v_p)$  with EMCEE [257] and obtain the corner plot shown in Fig. 6.8.

### 6.3 Results

We use a multi-step procedure, illustrated in Fig. 6.9, to incorporate constraints from nuclear theory and from astrophysical observations. Our analysis begins with a newly-constructed set of 5000 EOSs (Sec. 6.2.1) that provide possible descriptions of the structure of NSs (Fig. 6.9A). At low densities, these EOSs are constrained by microscopic calculations using chiral EFT interactions and computational many-body methods. Chiral EFT is a systematic theory for nuclear forces that describes the interactions in terms of nucleon and pion degrees of freedom and is consistent with the symmetries of quantum chromodynamics [101]. The resulting forces are arranged in an order-by-order expansion, which is then truncated at a certain level. This systematic scheme allows for the estimation of theoretical uncertainties from missing higher-order contributions to the nuclear

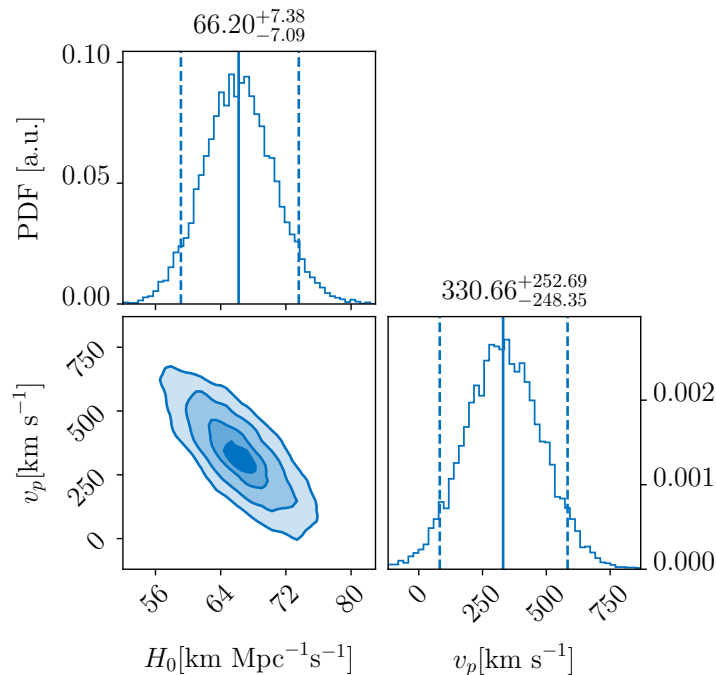


Figure 6.8: **Constraints on the Hubble constant.** Corner plot of the inferred  $H_0$ - $v_p$  posterior probability distribution using the inferred distance from our analysis, cf. Fig. 6.10. For the 1D posterior probability distributions, we mark the median (solid lines) and the 90% credible interval (dashed lines) and report these above each panel.

interactions. The resulting nuclear Hamiltonians are inserted into the Schrödinger equation, which has been solved using quantum Monte Carlo methods [105]. Chiral EFT might be valid up to  $2n_{\text{sat}}$  [111], where  $n_{\text{sat}}$  is the nuclear saturation density,  $n_{\text{sat}} = 0.16 \text{ fm}^{-3}$ . Beyond that, chiral EFT interactions and their uncertainty estimates are not reliable. We adopt a more conservative limit and constrain our EOSs with chiral EFT calculations up to densities of  $1.5n_{\text{sat}}$ . At densities above that limit, we employ a model-agnostic parametric expansion scheme that represents the EOS in the speed of sound plane [111] and ensures consistency with causality.

We then restrict the set of EOSs by including astrophysical constraints. In a first step, we begin by enforcing a maximum NS mass  $M_{\text{max}}$  with an upper bound of  $M_{\text{max}} \leq 2.16_{-0.15}^{+0.17}$  solar masses ( $M_{\odot}$ ) at  $2\sigma$  uncertainty [151] (Sec. 6.2.2). This upper bound was derived by assuming that the final merger remnant of GW170817 was a black hole [151]. We derived a lower bound for the maximum mass by combining radio observations of PSR J0740+6620 [135], PSR J0348+4042 [60], and PSR J1614-2230 [61]. The resulting distribution for the maximum mass and the updated EOS set are shown in Fig. 6.9B. For comparisons with other works, we calculate the radius of a typical  $1.4M_{\odot}$  NS at 90% credence. The corresponding radii at each stage of our analysis are shown in Fig. 6.9H.

In the next step, we include the NICER results (Sec. 6.2.3) using the joint posterior probability density function for mass and radius for the best fit model of Ref. [63] shown in Fig. 6.9C. We assign a probability to each EOS based on the maximum NS mass and NICER constraints.

By sampling over the obtained EOS set using their precomputed probabilities, we analyze GW170817 (Sec. 6.2.4), where NS properties are inferred from GW signals through

Reference	Chiral EFT	Heavy PSRs	$M_{\max}$ (remnant)	GW170817	AT2017gfo	GRB170817A	NICER	GW190425	$R_{1.4M_{\odot}}$ [km]
This chapter	yes	✓	✓	✓	✓	✓	✓	✓	$11.75^{+0.86}_{-0.81}$
[34]	yes	✓	✗	✓	✗	✗	✓	✗	[11.63, 13.26]
[33]	yes	○	○	✓	✗	✗	✗	✗	$11.0^{+0.9}_{-0.6}$
[28]	no	✓	○	✓	✓	○	✗	✗	[11.3, 13.5]
[27]	no	✗	✗	✓	○	✗	✗	✗	$(12.2^{+1.0}_{-0.8} \pm 0.2)$
[22]	no	○	✗	✓	✗	✗	✗	✗	$11.9^{+1.4}_{-1.4}$
[30]	yes	○	✗	○	✗	✗	✗	✗	[9.9, 13.6]

Table 6.2: Comparison with selected radius constraints from multi-messenger observations.

For each reference, we indicate if chiral EFT input, constraints from heavy-pulsar mass measurements (Heavy PSRs), maximum-mass constraints obtained from GW170817/AT2017gfo ( $M_{\max}$ ), GW constraints from GW170817 or GW190425, constraints from kilonova light curves (AT2017gfo), constraints from the GRB afterglow (GRB170817A), and constraints from NICER have been used. We indicate with ✓ if either the full posterior probability distribution or a Bayesian inference was employed, ○ if some information was included without performing a Bayesian analysis or including the full posterior probability distribution, and ✗ if the information was not included in the study. Stated radius uncertainties represent 90% credible intervals, where for [27] we also include systematic uncertainties as stated by the authors.

tidal effects that are larger for NSs with smaller masses and larger radii. We employ the PARALLEL BILBY software [227] and the GW waveform model IMRPhenomPv2\_NRTidalv2 [117] for cross-correlation with the observed GW data [9], inferring the binary properties from the measured signal. This model is an updated version of the waveform approximant IMRPhenomPv2\_NRTidal which has been used in previous analyses of GW170817 [21] and GW190425 [49].

In the fourth step, we add constraints from AT2017gfo using a published light curve model [122] (Sec. 6.2.5). We use a Gaussian-Process-Regression framework to compute generic light curves for various ejecta-mass properties. To connect the individual ejecta parameters to the properties of the system, we assume that the total ejecta mass  $M_{\text{ej}}$  is a sum of multiple components: dynamical ejecta  $M_{\text{ej}}^{\text{dyn}}$ , the material released during the merger process via shocks and torque, and disk-wind ejecta  $\zeta M_{\text{disk}}$ :  $M_{\text{ej}} = M_{\text{ej}}^{\text{dyn}} + \zeta M_{\text{disk}} + \alpha$ . The parameters  $\alpha$ , corresponding to a potentially unmodelled ejecta component, and  $\zeta$ , determining how much mass of the disk is ejected, are unknown free parameters. Our treatment of the dynamical ejecta follows previous work [28]. Existing disk-wind ejecta models are known to be inappropriate for systems with low mass ratios. To overcome this issue, we include an explicit mass-ratio dependence in the disk-mass prediction (Sec. 6.2.5). The GW results for the chirp mass  $\mathcal{M}_c = (m_1 m_2)^{3/5} (m_1 + m_2)^{-1/5}$ , with  $m_1$  and  $m_2$  being the masses of the heavier and lighter NS, respectively, the mass ratio  $q = m_2 m_1^{-1}$ , and

the EOS are used as priors for our analysis of AT2017gfo. This further constrains the EOS models (Fig. 6.9D). Including all steps so far, we obtain the radius of a  $1.4M_{\odot}$  NS of  $R_{1.4M_{\odot}} = 11.67_{-0.87}^{+0.95}$  km at 90% credence.

These results can be further constrained by combining them with another observed BNS merger, GW190425 [49]. Due to the high total mass of GW190425 of  $3.4_{-0.1}^{+0.3}M_{\odot}$  at 90% credence, which suppresses tidal effects, we find that the inclusion of GW190425 does not improve the precision, but does slightly shift the median value within the uncertainty. Our final estimate on the radius of a  $1.4M_{\odot}$  NS is  $R_{1.4M_{\odot}} = 11.75_{-0.81}^{+0.86}$  km with 90% credence. Later in this chapter, we also explore an alternative ordering of individual analysis steps (Fig. 6.14) and systematic uncertainties due to the use of different GW models (Fig. 6.15), but obtain a consistent radius constraint (see Sec. 6.4.3 and Sec. 6.4.4).

Several independent EM searches for counterparts to GW190425 observed large fractions of the possible sky area [215], suggesting that most of the appropriate region was searched but no EM signal was detected. To include this non-detection, we employ the same kilonova analysis as for GW170817, combining it with upper limits reported by the optical EM counterpart searches. Using the distance information from the GW data,  $159_{-71}^{+69}$  Mpc at 90% credence level [49], we obtain limits on the absolute magnitude of a potential counterpart. Using our light curve models, we rule out parts of the parameter space for which the predicted absolute magnitude would be above the obtained limit. Following this procedure, we arrive at a radius estimate of  $R_{1.4M_{\odot}} = 11.74_{-0.77}^{+0.88}$  km (90% credence) under the assumption that if GW190425 produced a detectable signal, it would have been found. To be conservative, we omit this step from the subsequent analysis.

Our study includes information from GW170817, AT2017gfo, GRB170817A, GW190425, the NICER observation of PSR J0030+0451, and the radio observations of PSR J0740+6620, PSR J0348+0432, PSR J1614-2230. Our approach allows for strong phase transitions in the EOS, the combination of multiple events, and the incorporation of EM non-detections. We compare our final result of  $R_{1.4M_{\odot}} = 11.75_{-0.81}^{+0.86}$  km with a selection of previous studies in Tab. 6.2. We note that the inclusion of additional astrophysical observations does not necessarily lead to tighter constraints (Fig. 6.9H) as (i) the full combined posterior probability distributions are incorporated in the analysis and (ii) the number of events detected with multiple messengers remains very small.

In addition to EOS studies, we perform a measurement of the Hubble constant (Sec. 6.2.7). For this purpose, we assume that measurable properties related to the kilonova, e.g., time-scale and color evolution of the ejecta, are connected to its intrinsic luminosity. Theoretical kilonova predictions can be used to standardize kilonovae light curves and thereby measure their distances [255]. Combining the distance measurement with the redshift  $z$  of the host galaxy NGC 4993,  $z = 0.009783 \pm 0.000023$ , constrains the Hubble constant [214]. We combine the distance and inclination measurements of the GW and kilonova analyses with the measurement using radio observations of the GRB afterglow (Fig. 6.10) [258]. The comparison of a kilonova observation to a light curve model permits a large parameter range, due to the complexity of the model. Adopting two other kilonova models (see Sec. 6.4.2) indicates that our kilonova constraints are conservative, but we note that it is not possible to test the robustness of different kilonova models with only one well-sampled kilonova observation (AT2017gfo). Combining all these measurements leads to an improved distance constraint and an estimate of the Hubble constant of  $H_0 = 66.2_{-4.2}^{+4.4}$  km Mpc $^{-1}$  s $^{-1}$  at  $1\sigma$  uncertainty (Fig. 6.10). We find that the radio inclination measurement reduces the existing uncertainty on the Hubble constant by more

than the kilonova measurement, at least for this single event. The uncertainty does not allow us to resolve the tension between measurements via type-Ia supernovae [259] and the Planck measurement of the Cosmic Microwave Background [260], but our results indicate a preference for the latter and disfavor the measurement via type-Ia supernovae [259].



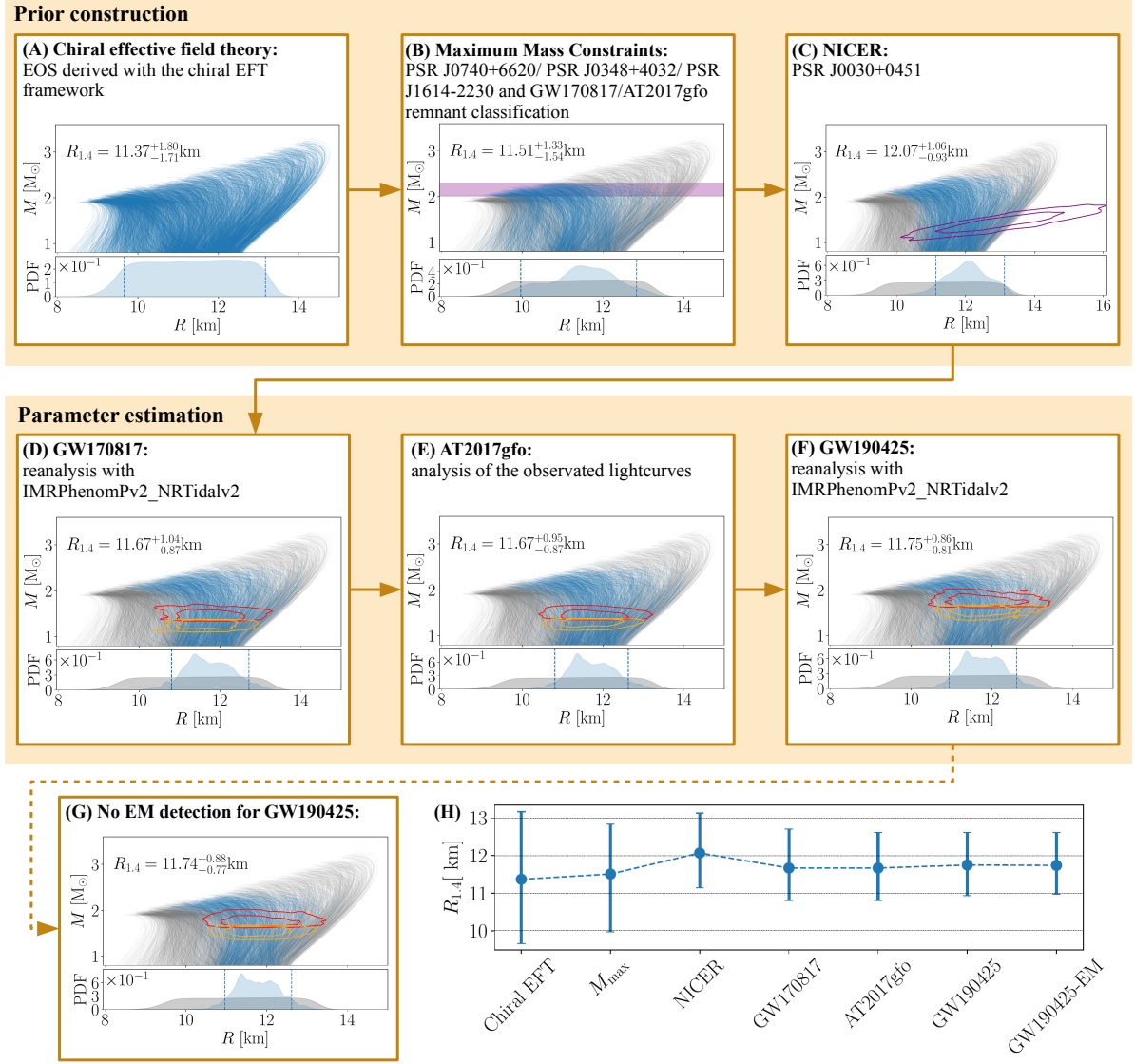


Figure 6.9: **Multi-step procedure to constrain the neutron-star EOS.** In each panel, allowed (disallowed) EOSs are shown as blue (gray) lines. Lower plots indicate the probability distribution function (PDF) for the radius of a 1.4 solar mass neutron star, with the 90% credible range indicated by dashed lines. (A) The set of EOSs from chiral EFT. (B) The EOS set restricted by incorporating information from mass measurements of PSR J0740+6620, PSR J0348+4032, PSR J1614-2230, and the maximum-mass constraints obtained from GW170817/AT2017gfo. The 90% credible interval of the maximum mass posterior probability distribution is shown by a purple band. (C) The EOS set further restricted by the NICER mass-radius measurement of PSR J0030+0451 (purple contours at 68% and 95% credence). (D) Further restriction of the EOS set using Bayesian inference from our reanalysis of the GW170817 waveform. Contours at 68% and 95% credence show the mass-radius measurements of the primary (red) and secondary (orange) neutron stars. (E) We use the chirp mass, mass ratio, and the EOSs as Bayesian prior for our analysis of AT2017gfo. (F) Further restrictions by analysing GW190425. This is our fiducial result. (G) Additional analysis assuming that GW190425 did not produce a detectable EM signal. (H) The radius constraint at each step of this analysis, with 90% credible ranges.

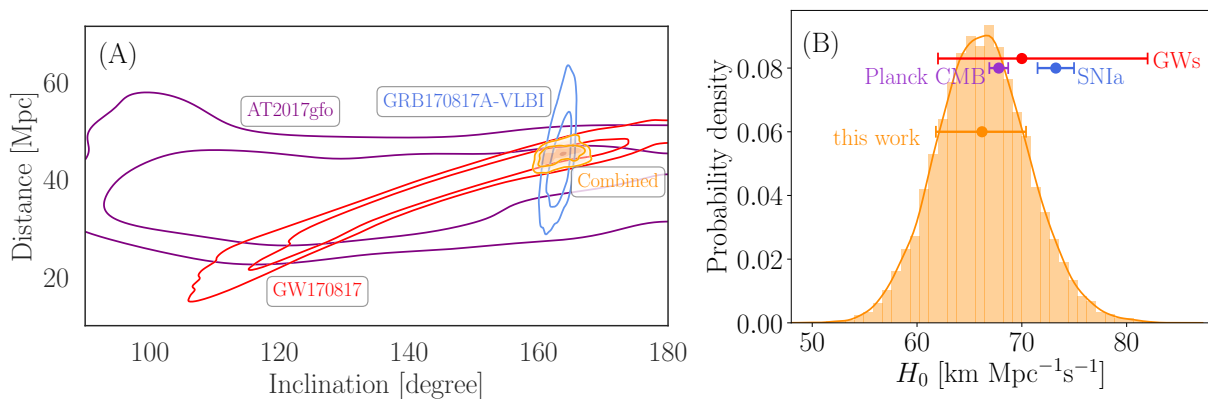


Figure 6.10: **Distance-inclination constraints and Hubble constant measurement.** (A) Estimated distance and inclination of GW170817 from the GW waveform (red) and AT2017gfo analysis (purple) and the radio interferometry constraint [258] derived from GRB170817A (blue). The combined distance-inclination measurement is shown in orange. Contours are shown at 68% and 95% credence. (B) Hubble constant estimate from our combined inclination measurement (orange histogram). Symbols mark the most probable values and  $1\sigma$  uncertainties from this chapter (orange), the Planck measurement of the Cosmic Microwave Background [260] (Planck CMB, purple), the Hubble measurement via type-Ia supernovae [259] (SNIa, blue), and the Hubble estimate from GW170817 alone [214] (GWs, red).

## 6.4 Investigation of possible systematics

### 6.4.1 Gravitational-wave Analysis

As mentioned above, we use the `IMRPhenomPv2_NRTidalv2` (`NRTidalv2`) waveform model. The approximant uses the description of tidal effects introduced in Ref. [117] to augment the precessing binary black-hole waveform model [92]. `NRTidalv2` has a different tidal and spin description to the `IMRPhenomPv2_NRTidal` model [116, 261], which was the waveform model employed by the LIGO Scientific and Virgo Collaborations to interpret GW170817 [6, 21, 22, 262, 263] and GW190425 [49]. We present the parameter-estimation results for GW170817 in Fig. 6.11. For comparison, we also show the posterior probability distributions obtained with the `IMRPhenomPv2_NRTidal` waveform model to allow for an assessment of `NRTidalv2`. We find no noticeable difference in the measured component masses, distance, and inclination; cf. Tab. 6.3. The agreement is likely caused by the same underlying point-particle base line of both models. There is a small difference in the estimated tidal deformability, where `NRTidalv2` predicts a slightly larger tidal deformability which consequently results in a slightly larger radius estimate. This behavior is expected because the `NRTidalv2` approximant incorporates slightly smaller tidal contributions for the same physical parameters than the original `IMRPhenomPv2_NRTidal` model, which consequently leads to a larger estimated tidal deformability. In addition, we show posterior probability distributions obtained with the `SEOBNRv4T` waveform model [264], where we employ its surrogate model of Ref. [265] for the parameter estimation runs. `SEOBNRv4T` has a point-particle and tidal description that differs from `IMRPhenomPv2_NRTidal` and `NRTidalv2` and, therefore, provides an independent check for possible systematic uncertainties. We find no noticeable difference between parameters, suggesting that no systematic errors are introduced by the choice of waveform model in our analysis; cf. Fig. 6.11 and Tab. 6.3.

Parameter	<code>NRTidal</code>	<code>NRTidalv2</code>	<code>SEOBNRv4T</code>
Primary mass $m_1$ [ $M_\odot$ ]	$1.48^{+0.15}_{-0.10}$	$1.48^{+0.17}_{-0.10}$	$1.45^{+0.16}_{-0.07}$
Secondary mass $m_2$ [ $M_\odot$ ]	$1.26^{+0.09}_{-0.11}$	$1.26^{+0.09}_{-0.12}$	$1.29^{+0.07}_{-0.12}$
Mass-weighted tidal deformability $\tilde{\Lambda}$	$357.86^{+259.49}_{-173.26}$	$370.54^{+296.33}_{-160.57}$	$349.25^{+383.87}_{-129.77}$
Luminosity distance $D$ [Mpc]	$37.85^{+9.95}_{-16.95}$	$37.33^{+10.29}_{-16.46}$	$36.81^{+9.30}_{-13.69}$
Inclination $\iota_0$ [deg]	$143.41^{+29.07}_{-30.31}$	$142.19^{+30.08}_{-29.15}$	$141.21^{+27.48}_{-24.48}$

Table 6.3: **Summary of the parameters of GW170817 inferred with different waveform models.** We give the median of the parameters of GW170817, together with their corresponding 90% credible intervals for analyses using different waveform models.

For the analysis of GW190425 we also use the `NRTidalv2` model. In Fig. 6.12, we show extracted source parameters for GW190425 when we include or do not include the GW170817 and AT2017gfo information (chirp mass, mass ratio, and EOS constraints); cf. Tab. 6.4. The extracted source parameters differ in the estimated tidal deformability  $\tilde{\Lambda}$ , and the inclusion of GW170817 and AT2017gfo in our analysis leads to a smaller value. The incorporation of additional information from GW170817 and AT2017gfo changes the prior of the GW190425 analysis such that NSs with large radii (large tidal deformabilities) are already disfavored.

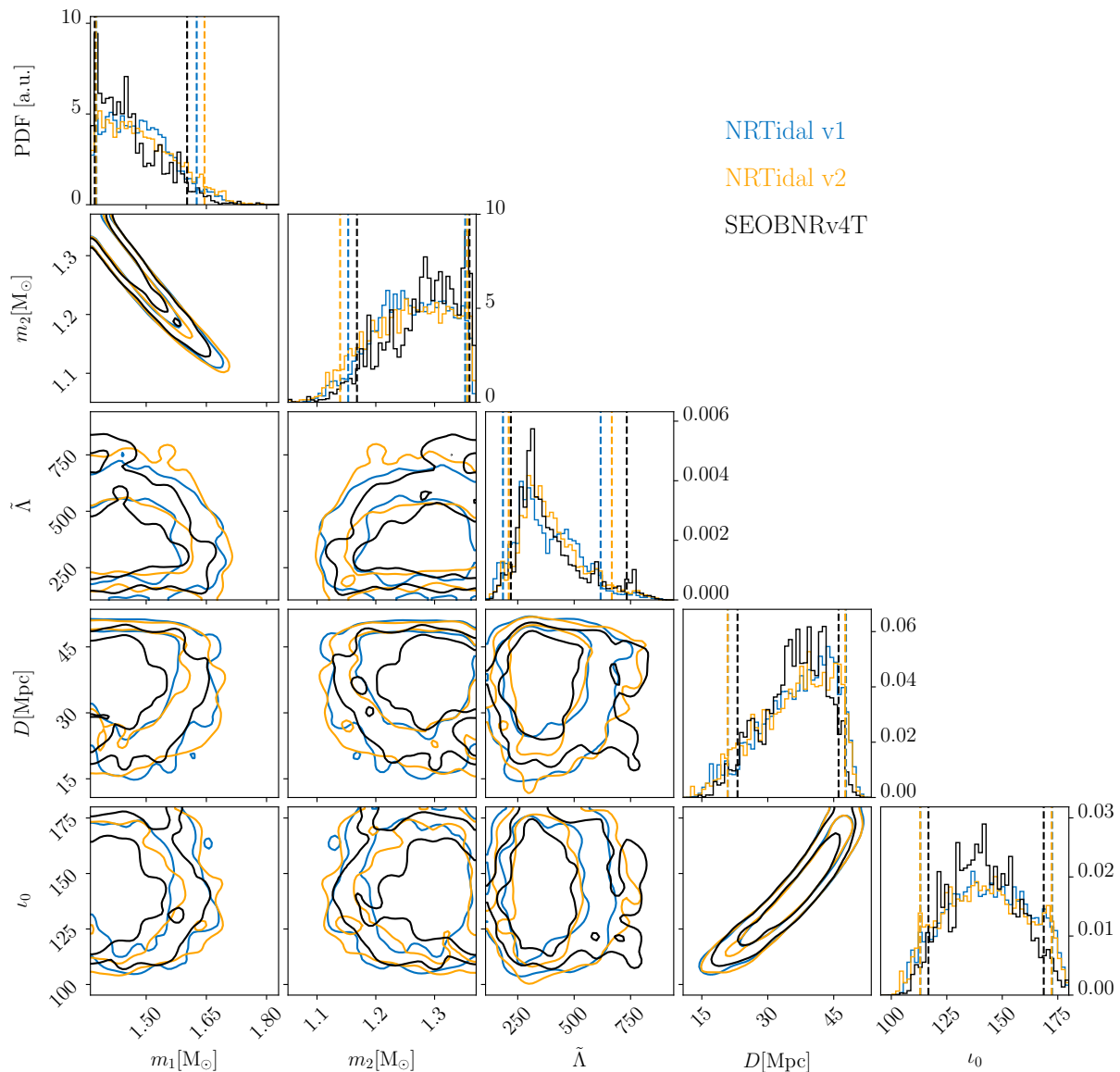


Figure 6.11: **Marginalized 1D and 2D posterior probability distributions of GW170817’s parameters.** Visualization of the 1D and 2D marginalized posterior probability distributions (corner plot) of the parameters of GW170817 at 68% and 95% credence, obtained with IMRPhenomPv2\_NRTidal (blue), IMRPhenomPv2\_NRTidalv2 (orange) and SEOBNRv4T (black) for the primary source mass  $m_1$ , secondary source mass  $m_2$ , mass-weighted tidal deformability  $\tilde{\Lambda}$ , luminosity distance  $D$ , and inclination  $i_0$ . For the 1D posterior probability distributions, we show the probability distribution function (PDF) in arbitrary units (a.u.) and mark the 90% credible interval by dashed lines. The main difference between the posterior probability distributions inferred with the three waveform models is the distribution of  $\tilde{\Lambda}$ , which is expected due to the different tidal description of the three models.

### 6.4.2 Modelling of AT2017gfo

There is good agreement between the three kilonova models, which differ mostly in the predicted inclination and distance. We show the distance-inclination measurements in

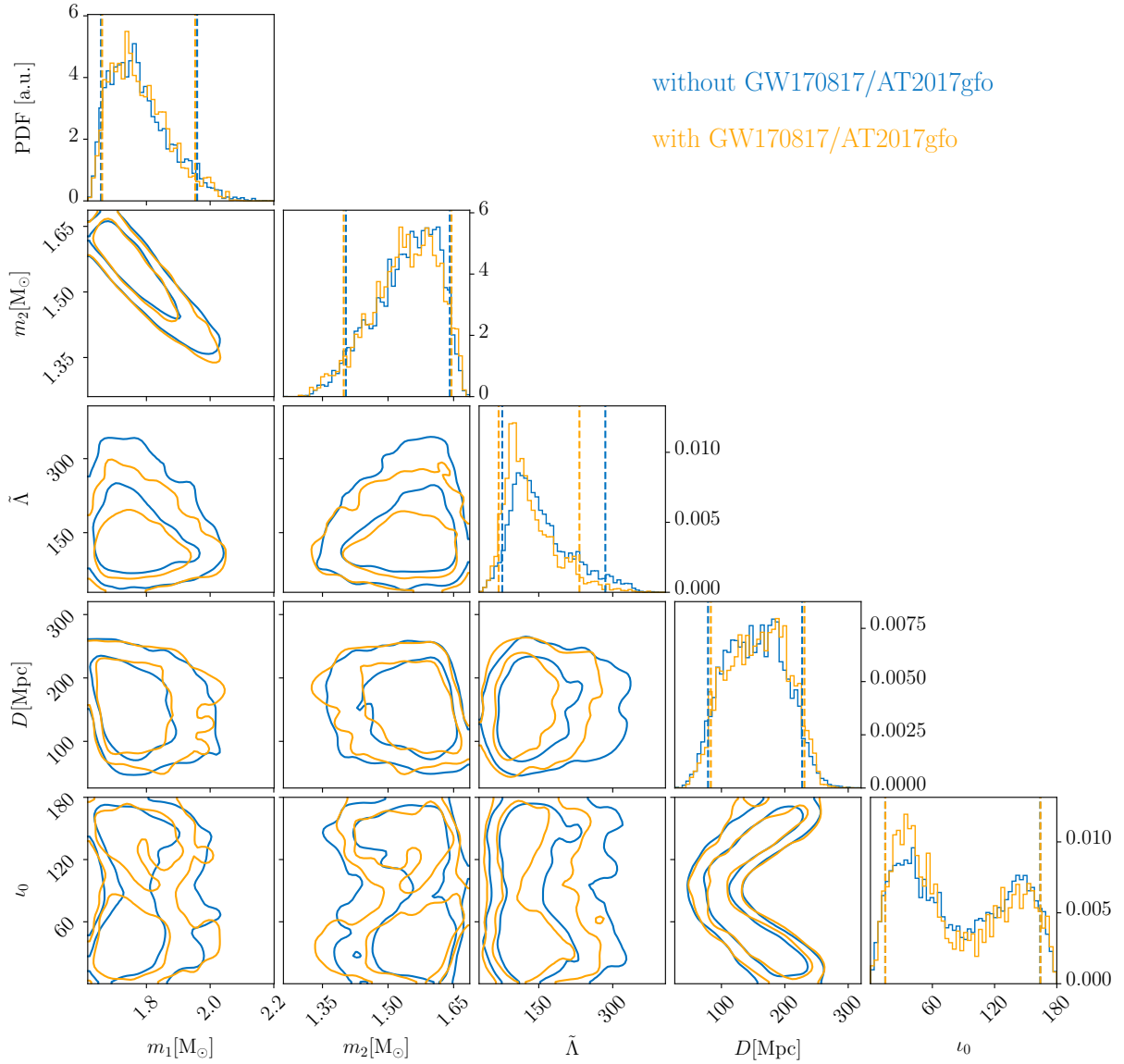


Figure 6.12: **Marginalized 1D and 2D posterior probability distributions of GW190425’s parameters.** Same as Fig. 6.11 but for the posterior probability distribution of GW190425’s parameters obtained without (blue) and with (orange) the inclusion of GW170817/AT2017gfo. With the inclusion of GW170817/AT2017gfo, the tidal measurement is more tightly constrained.

Fig. 6.13. Model I is the least constraining due to the additional complexity of the wind ejecta component. Model III is spherically symmetric and therefore only enables a distance measurement. All three models agree within their statistical uncertainties, which suggests that our analysis is dominated by statistical effects and not systematics.

For the analysis of the non-observed EM counterpart of GW190425, we use the same kilonova analysis as discussed above, but restricted to Model I. We use information from the Asteroid Terrestrial-impact Last Alert System (ATLAS) [266] that covered 37%, the Gravitational-wave Optical Transient Observer (GOTO) [267] that covered 30%, the Master Global Robotic Telescopes Net (MASTER) [268] that covered 37%, and the Zwicky Transient Facility (ZTF) [269] that covered 25% of the sky area derived from the GW data

Parameter	without GW170817/AT2017gfo	with GW170817/AT2017gfo
Primary mass $m_1 [M_\odot]$	$1.76^{+0.20}_{-0.11}$	$1.77^{+0.19}_{-0.10}$
Secondary mass $m_2 [M_\odot]$	$1.55^{+0.09}_{-0.15}$	$1.54^{+0.10}_{-0.15}$
Mass-weighted tidal deformability $\tilde{\Lambda}$	$140.80^{+144.22}_{-64.73}$	$117.90^{+114.60}_{-49.24}$
Luminosity distance $D$ [Mpc]	$152.87^{+74.52}_{-73.99}$	$159.08^{+71.91}_{-75.73}$
Inclination $\iota_0$ [deg]	$79.22^{+84.81}_{-64.67}$	$64.54^{+99.66}_{-49.88}$

Table 6.4: **Summary of the parameters of GW190425 with and without inclusion of GW170817/AT2017gfo.** We give the median of the parameters of GW190425, together with their corresponding 90% credible intervals for analyses with and without input from GW170817/AT2017gfo.

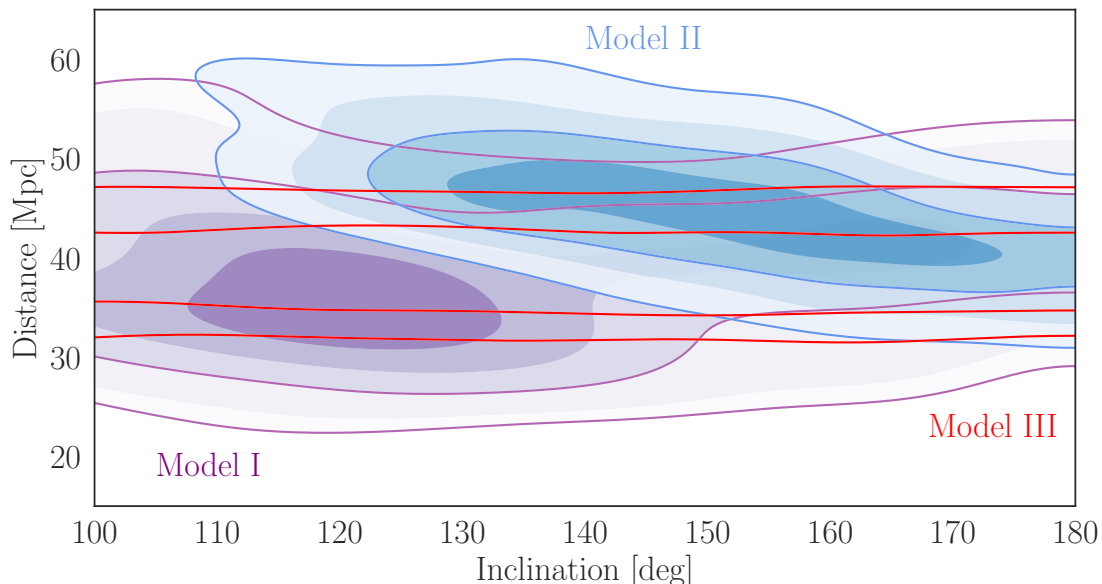


Figure 6.13: **Distance-inclination measurements for kilonova models.** Shown are results for Model I (purple), Model II (blue), and Model III (red) at 68% and 95% credible levels. Model I is the least constraining.

to obtain apparent magnitude limits on potential counterparts from optical surveys. An exact computation of the total sky coverage is not possible because not all groups released their covered tiles and search information. However, the published limits, together with the distance information from the GW event, lead to limits on the absolute magnitude of a potential kilonova [215]. Accounting for the distance of the transient, we rule out all ejecta parameters for which the predicted magnitude would exceed the obtained apparent magnitude limit.

### 6.4.3 Ordering of the analysis steps

We test the effect of changing the order of analysis steps in Fig. 1 by moving the NICER results to the final stage. To reduce computational costs, we focus on the combination of GW170817, AT2017gfo, NICER, and the maximum-mass constraints. Fig. 6.14 shows

that the measured radius is slightly larger for our original analysis than for our analysis in which NICER results are included in the final step. This change is due to the kernel density estimation that is used to obtain the prior for our individual analysis steps. However, the 90% credible intervals remain unchanged. We conclude that our method is robust to the order of the procedure.

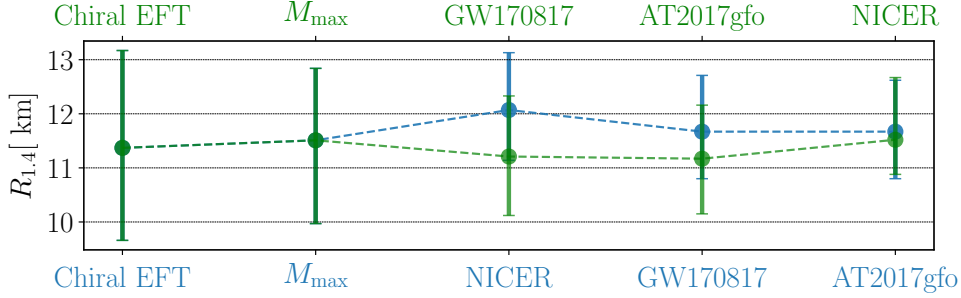


Figure 6.14: **Radius constraints under interchange of the individual analysis steps.** The blue line is the same as in Fig. 6.9H. We show the highest probability interval of 90% credence and the median of the posterior probability distribution.

#### 6.4.4 Propagation of systematic uncertainties

We also show how small differences in individual analysis steps influence the entire analysis. We analyse the GW events GW170817 and GW190425 with the SEOBNRv4T waveform model, but keep all other steps the same. Figure 6.15 shows our final result for the radius using IMRPhenom\_NRTidalv2 and SEOBNRv4T. IMRPhenom\_NRTidalv2 predicts slightly larger radii than SEOBNRv4T but the difference is well within uncertainties and remains almost unchanged when analysing AT2017gfo and GW190425.

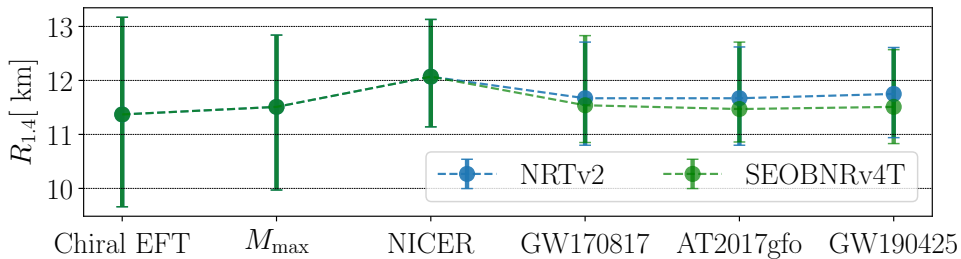


Figure 6.15: **Radius constraints for different gravitational-waveform models.** Similar to Fig. 6.14 but for different gravitational-wave models used in the analyses of GW170817 and GW190425.

Given the small sensitivity of our results to the choice of the GW model (Fig. 6.15), the order of the analysis steps (Fig. 6.14), and the consistent results employing different kilonova models (Fig. 6.13), we conclude that our results are generally robust.





## 7.1 Introduction

Neutron stars (NSs) are the densest objects in the observable universe and allow us to probe matter under the most extreme conditions realized in nature. In particular, NSs close to the maximum mass, i.e., the highest mass  $M_{\max}$  that can be supported against gravitational collapse to a black hole (BH), truly probe matter at its limits. Even though NS masses could historically be inferred quite accurately through timing measurements [270], the exact value of  $M_{\max}$  is still not known. For a long time, because observed NSs had masses around  $1.4M_{\odot}$ , one assumed that  $M_{\max}$  was not much higher. However, this situation changed with several observations of pulsars with  $M \sim 2M_{\odot}$  in the last decade: PSR 1614-2230 with  $M = 1.908 \pm 0.016M_{\odot}$  [61, 134], PSR J0348+0432 with a mass of  $M = 2.01 \pm 0.04M_{\odot}$  [60], and PSR J0740+6620 with a mass of  $M = 2.14 \pm 0.10M_{\odot}$  [135]. These observations firmly established that the equation of state (EOS) of NSs has to be sufficiently stiff to support such heavy stars. Combining the likelihoods for these three observations, they provide a strong lower bound  $M_{\max} \geq 2.03M_{\odot}$  at 90% credence (see Ch. 6). An upper bound on  $M_{\max}$ , on the other hand, is impossible to obtain from NS mass measurements alone. Assuming that BH and NS mass distributions do not overlap, it might be extracted from population studies or observations of BHs, e.g., Refs. [271–273], or from nuclear-physics considerations, e.g., Ref. [274].

In addition, the first observation of a binary neutron-star (BNS) merger, GW170817 [9, 21] performed by the LIGO Scientific and Virgo collaborations (LVC), and the observations of the associated kilonova, AT2017gfo, and the short gamma-ray burst, GRB170817A [7] led several groups to propose upper limits on  $M_{\max}$ , e.g., Refs. [25, 151]. These bounds are based on the conjecture that the ejecta properties disfavor both a prompt collapse to a BH as well as a long-lived NS. This delayed-collapse scenario, with an expected remnant lifetime of several 100 ms [275], provides an upper limit on  $M_{\max}$ , because larger  $M_{\max}$  typically lead to longer remnant lifetimes, see, e.g., Ref. [276] and references therein. Given the observed remnant mass of  $M_R = 2.7M_{\odot}$  [9, 21], limits on  $M_{\max}$  have been proposed in the range of  $2.3 - 2.4 M_{\odot}$ , see, e.g., Refs. [25, 151, 220, 221]. While generally robust, these upper limits on  $M_{\max}$  are based on numerical simulations and on the reasonable but unproven assumption that the final remnant was a BH.

A recent detection by Advanced LIGO [4] and Advanced Virgo [10] adds a fascinating new piece of information to this puzzle. In its third observing run, on August 14, 2019, the LVC discovered gravitational waves (GWs) from a binary compact-object merger of a  $22.2 - 24.3 M_{\odot}$  BH with an unidentified compact companion of  $2.50 - 2.67M_{\odot}$  [277]. While in the future, gravitational-wave detectors might be able to distinguish the type

of the event and, in particular, identify the secondary, i.e., lighter component purely based on the GW signal [278, 279], this was not possible for GW190814 due to the large mass ratio  $q \equiv m_1/m_2 \geq 1$  of the event<sup>1</sup>. The tidal deformability of a binary black hole (BBH) system,  $\tilde{\Lambda} = 0$ , is almost indistinguishable from an NS–BH merger with  $\tilde{\Lambda} = \frac{16}{13}\Lambda_{\text{NS}}(1 + 12q)/(1 + q)^5 \lesssim 10^{-2}$  for the given system parameters, where  $\Lambda_{\text{NS}}$  is the NS tidal deformability. In addition, the missing electromagnetic counterpart does not provide additional information because from an NS–BH system with such a heavy primary component no electromagnetic signal is likely to be detected, unless the BH has a very high spin,  $\chi = cJ/(Gm^2)$  with speed of light  $c$ , angular momentum  $J$ , gravitational constant  $G$  and the object’s mass  $m$  (e.g., Refs. [280, 281]). This is disfavored for GW190814 with the primary spin magnitude bounded to be  $\chi_1 < 0.07$  at 90% credence [277]. Therefore, from observations alone, it cannot be determined if the secondary component of GW190814 is the lightest BH or the heaviest NS discovered to date, and its nature needs to be constrained differently. Using the GW170817-informed EOS samples of [22], obtained with a spectral EOS parameterization [282, 283], the LVC found that the probability for GW190814 to be an NS–BH merger is less than 3% [277]. Using EOS-independent pulsar-mass distributions [273], they also reported a probability of less than 29%.

Additional information on the nature of the secondary component of GW190814 might be obtained by considering the many new pieces of NS data obtained in the last years. Besides mass measurements and observations of gravitational waves from BNS mergers, improved nuclear-physics constraints with uncertainty estimates from chiral effective field theory (EFT; [109, 177, 181]), recent X-ray observations by NICER [63, 64], or detailed modeling of the kilonova associated with GW170817 [122, 232] allow us to reduce the uncertainty on the EOS [29–31, 33–35, 145, 147, 148], see Ref. [150] for a recent review. For example, Ref. [284] addressed GW190814 by using a mass-based classification scheme employing Bayesian model selection and informed by compact-object populations and posteriors on  $M_{\text{max}}$  from the EOS model of Ref. [147], which includes information from mass measurements, BNS mergers, and NICER. They found the probability of GW190814 to be an NS–BH merger to be less than 6%, and less than 0.1% when they additionally enforced the limit on  $M_{\text{max}}$  from Ref. [220].

Here, we go further and use the Nuclear Physics – Multimessenger Astrophysics (NMMA) framework developed in Ch. 6 to analyze GW190814 and identify the nature of its secondary component. Our NMMA framework employs all of the additional sources of observational data (NS masses, GW data from GW170817 and GW190425, NICER data, and detailed kilonova modeling of GW170817) as well as EOS constrained by modern nuclear-physics theory, and hence, presents the first systematic multimessenger analysis of GW190814 using a wealth of interdisciplinary input. We point out that the inclusion of multiple channels in our analysis provides the most complete understanding of GW190814, in contrast to previous studies that used only a subset of possible constraints. Moreover, our analysis is based on a framework with controlled systematic uncertainties for all of its components (see Ch. 6). We investigate the two different scenarios and also determine their constraints on the NS EOS. Our study strongly suggests that GW190814 was a BBH and not an NS–BH merger, see also similar conclusions in Refs. [277, 284, 285]. To be conservative, we perform our analysis with and without assuming upper limits on  $M_{\text{max}}$  obtained from GW170817. We find that the existence of a heavy NS in GW190814 leads

---

<sup>1</sup>Please note that the definition of the mass ratio used here is the inverse of the definition used in Ref. [277].

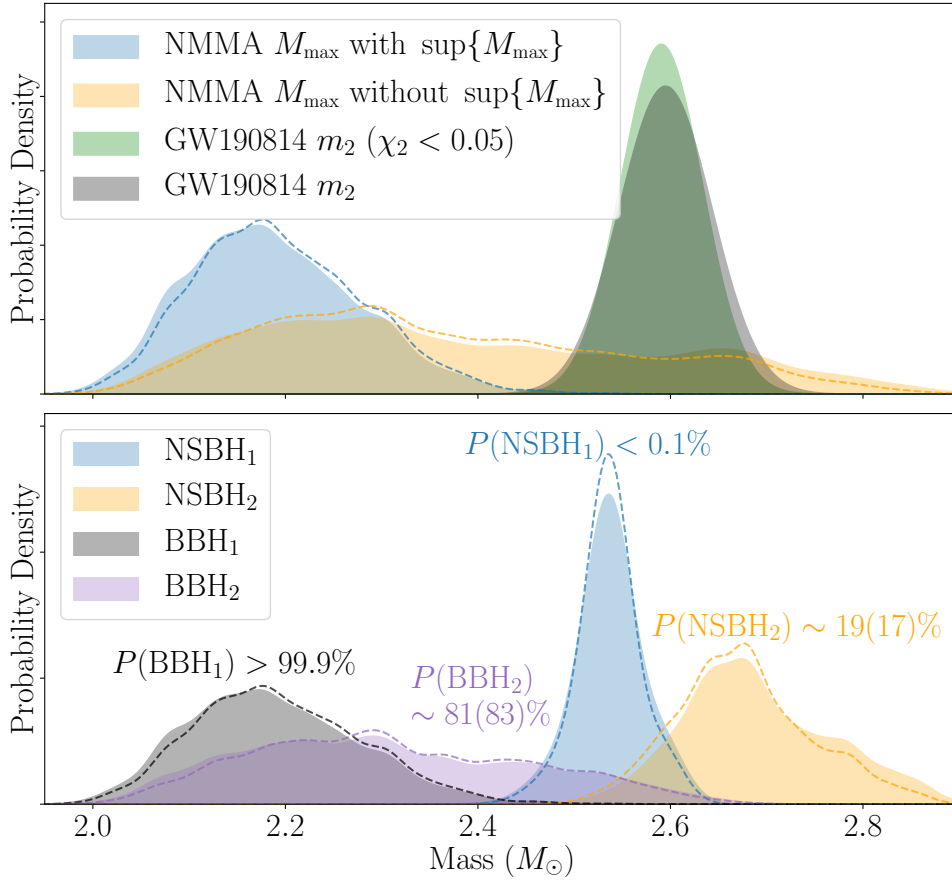


Figure 7.1: Upper panel: posteriors on the maximum mass of NSs,  $M_{\max}$ , from the NMMA analysis of Ch. 6 when enforcing the upper limit on  $M_{\max}$  from Ref. [151] (blue) and when relaxing this constraint (orange). We also show the posteriors for an EOS prior that is not flat in  $R_{1,4}$  (dashed lines). We compare with the posterior on the mass of the secondary component of GW190814, assuming its spin  $\chi_2 < 0.05$  (green) or with no limit on  $\chi_2$  (black). Lower panel: the resulting posteriors on  $M_{\max}$  for our four scenarios with their probabilities. The probabilities for the alternative EOS prior are shown in brackets.

to tension with current nuclear-physics constraints, see also Refs. [286, 287].

## 7.2 Analysis

Our analysis starts from the NMMA framework introduced in Ch. 6. This approach is based on a set of 5000 EOSs that are constrained below 1.5 times the nuclear saturation density,  $n_{\text{sat}} \approx 2.7 \times 10^{14} \text{ g cm}^{-3}$  by state-of-the-art microscopic calculations using chiral EFT [101, 102]; see Sec. 2.2.2 for more details.

Using Bayesian inference, these EOSs are analyzed with respect to their agreement with the posteriors on  $M_{\max}$  from heavy-pulsar observations [60, 134, 135], the upper limit on  $M_{\max}$  ( $M_{\max}^{\text{up}} = 2.16_{-0.15}^{+0.17} M_{\odot}$ ) from Ref. [151], which is consistent with the limits inferred in Refs. [25, 220, 221], the full mass-radius (MR) posterior from the NICER observation of PSR J0030+0451 [63, 64], the GW observations of GW170817 [9, 21] and GW190425 [49], and the kilonova observation AT2017gfo [7], where both the pulsar mass

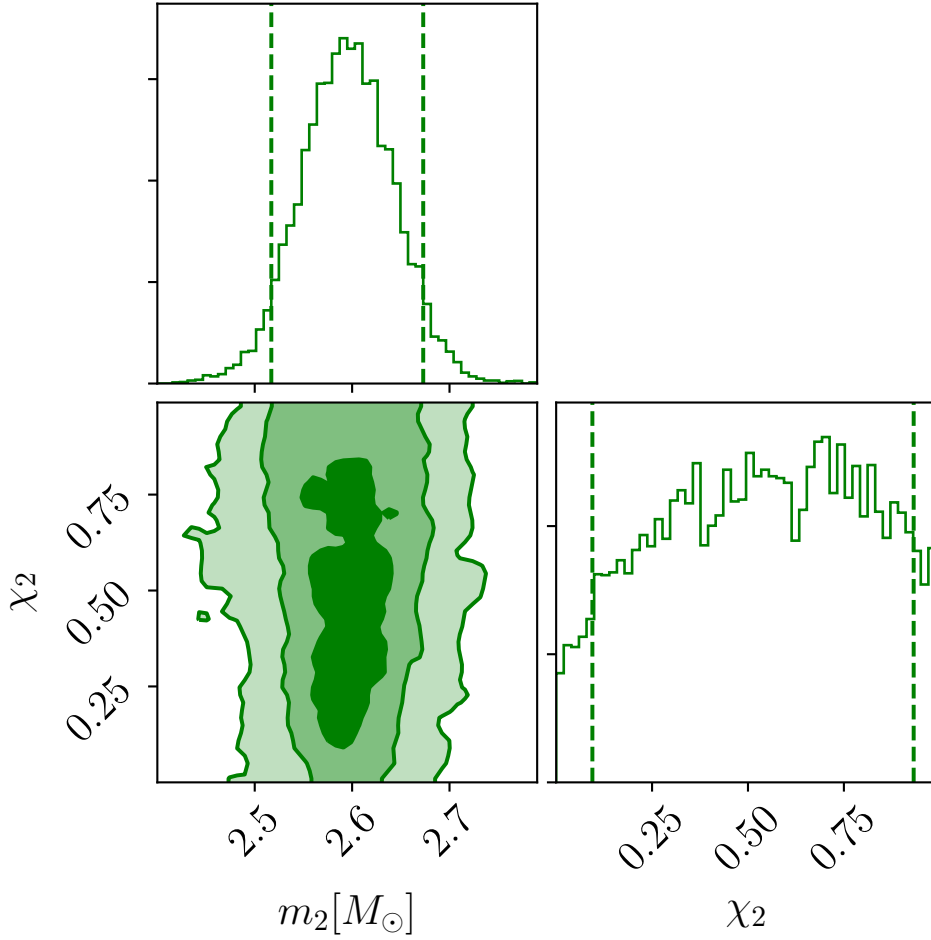


Figure 7.2: Corner plot showing the posterior distribution of  $m_2$ - $\chi_2$  for GW190814. The dashed lines mark the 90% credible intervals.

measurements and the upper limit on  $M_{\max}$  are approximated with Gaussian likelihoods. Hence, the posterior of the NMMA analysis takes into account a wealth of available data on NSs; see Ch. 6 for detailed information and discussions. From the 5000 initial EOSs analyzed in Ch. 6, about 20% are within the 95% credible interval given all observational constraints. Our analyses allowed us to constrain the radius of a typical  $1.4M_{\odot}$  NS,  $R_{1.4}$ , to be  $R_{1.4} = 11.8_{-0.8}^{+0.9}$ km, as shown in Ch. 6.

We now use the final posterior of our NMMA analysis to investigate the nature of GW190814, which includes all analysis steps except the absence of EM emission from GW190425. In particular, we study four scenarios. In the first scenario, NSBH<sub>1</sub>, we assume that GW190814 was an NS–BH merger. Hence, GW190814 leads to an additional lower limit on  $M_{\max}$ . Even though rotation could stabilize such a heavy NS against gravitational collapse for a lower  $M_{\max}$  [151, 285, 288, 289], the long lifetimes of BNS systems suggest NS spins to be small. Therefore, we adopt the same low-spin prior used in the LVC studies,  $\chi_2 < 0.05$  [9], suggesting  $M_{\max} \geq 2.5M_{\odot}$  at 90% credence. Because upper limits on  $M_{\max}$  from GW170817 might suffer from systematic uncertainties and are based on assumptions about the fate of the remnant, in the second scenario, NSBH<sub>2</sub>, we again assume that GW190814 was an NS–BH merger but relax the upper bound on  $M_{\max}$

of Ref. [151]. In our third scenario,  $\text{BBH}_1$ , we assume that GW190814 was a BBH merger, i.e., that the secondary component is a BH<sup>2</sup>. This scenario is the contrary to  $\text{NSBH}_1$ . In this case, GW190814 leads to an additional upper limit on  $M_{\text{max}}$ , consistent with the upper bound of Ref. [151]. Finally, the scenario  $\text{BBH}_2$  is the contrary to  $\text{NSBH}_2$  and assumes GW190814 was a BBH merger but relaxes the  $M_{\text{max}}$  bound of Ref. [151]. The information on GW190814's secondary component's mass measurement is incorporated via the method described in Ch. 6 with the posterior samples taken from Ref. [291].

## 7.3 Results

In the following, we discuss what we can learn about the nature of GW190814 and the dense-matter EOS probed in the core of NSs from our four scenarios.

### 7.3.1 The nature of GW190814

In Fig. 7.1, we compare the posterior on  $M_{\text{max}}$  of the NMMA analysis (blue),  $M_{\text{max}} = 2.18_{-0.13}^{+0.15} M_{\odot}$ , with the posterior of the mass of the secondary component of GW190814 depending on two choices for its spin: (1)  $\chi_2 < 0.05$  (green), expected for NS, and (2) without any constraint on the spin (black), which is relevant in case of a BH. Please note that the posterior widens slightly if higher spins are allowed, see Fig. 7.2. Furthermore, we show the posterior of the NMMA analysis when we relax the upper bound on  $M_{\text{max}}$  of Ref. [151] (orange),  $M_{\text{max}} = 2.30_{-0.25}^{+0.34} M_{\odot}$ .

$\text{NSBH}_1$  is described by the overlap of the NMMA and mass posteriors (blue and green). Due to the great tension between the upper limit on  $M_{\text{max}}$  extracted from the BNS merger GW170817 [151] and the assumption that this new object, close to the remnant mass of GW170817, is an NS, this is the most restrictive of the four scenarios. From the overlap of both posteriors, we can estimate the probability that the secondary component of GW190814 had a mass below  $M_{\text{max}}$  by using

$$P(\Delta m > 0) = \int_0^{\infty} d\Delta m \int_{-\infty}^{\infty} dm p_{M_{\text{max}}}(m + \Delta m) p_{m_2}(m), \quad (7.1)$$

where  $\Delta m \equiv M_{\text{max}} - m_2$ , and  $p_{M_{\text{max}}}(m)$  and  $p_{m_2}(m)$  are the probability distribution for  $M_{\text{max}}$  from the NMMA analysis and the posterior on  $m_2$  from GW190814, respectively. The overlap region is extremely small, and hence, the probability  $P(\Delta m > 0)$  is less than 0.1%, in excellent agreement with Ref. [284] with an upper limit on  $M_{\text{max}}$ . Neutron-star EOS for this maximum-mass range are heavily penalized by the upper  $M_{\text{max}}$  limit. In the  $\text{NSBH}_1$  case, we find that the resulting  $M_{\text{max}}$  is constrained to a very narrow range,  $M_{\text{max}} = 2.53_{-0.06}^{+0.07} M_{\odot}$ ; see the lower panel of Fig. 7.1. This finding is in good agreement with the limit on  $M_{\text{max}}$  obtained from spin-polarized neutron matter in Ref. [292]. However, this  $M_{\text{max}}$  would imply that the remnant of GW170817 was either a supramassive or long-lived NS, which is in conflict with the observed kilonova lightcurve and the GRB afterglow, e.g., Ref. [25].

For  $\text{NSBH}_2$ , the relaxation of the upper bound on  $M_{\text{max}}$  widens the NMMA posterior, see the orange curve in Fig. 7.1. However,  $M_{\text{max}}$  is still constrained to be  $M_{\text{max}} \lesssim$

<sup>2</sup>It has been suggested that the secondary component might be a primordial black hole, see, e.g., Ref. [290].

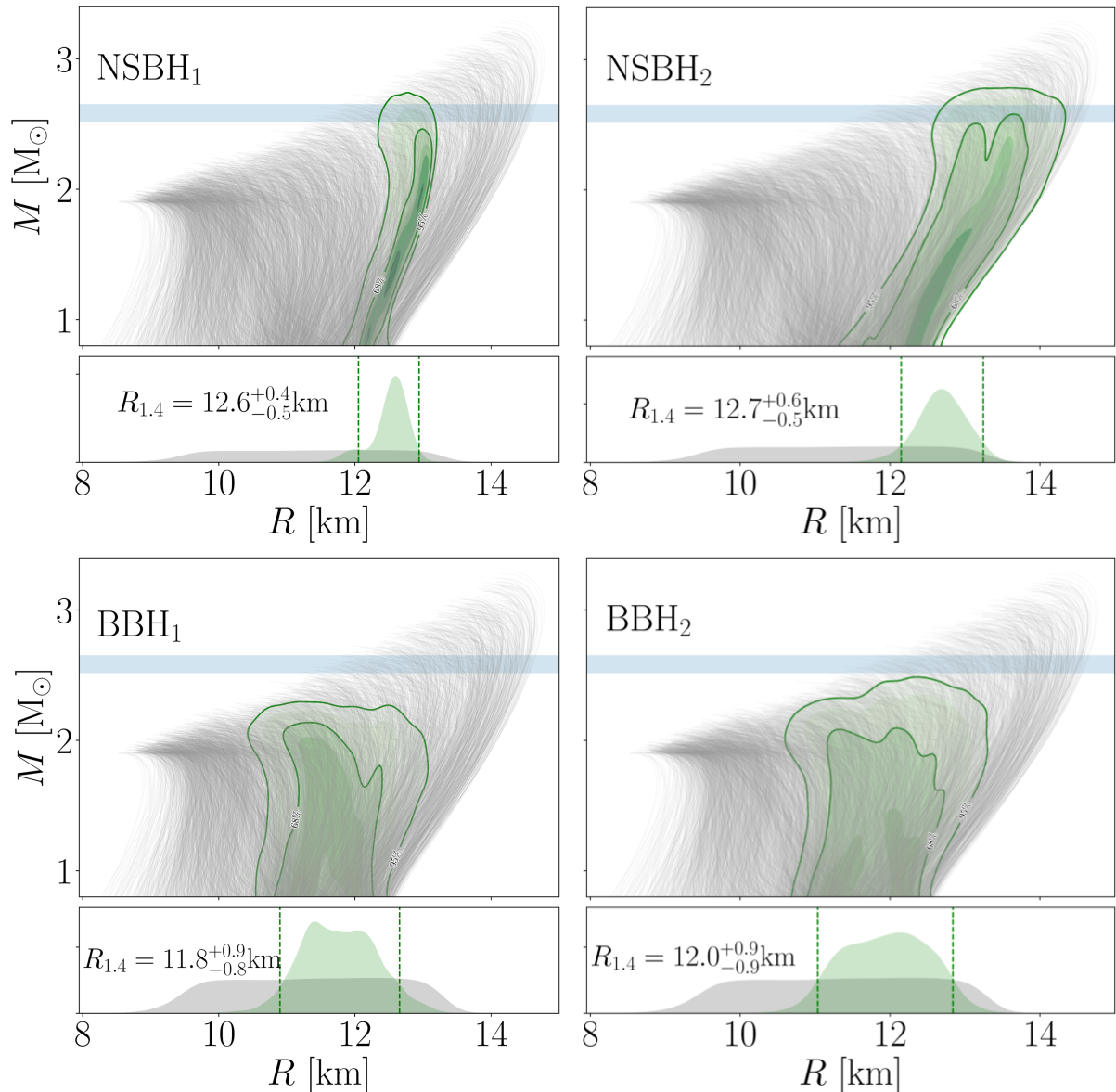


Figure 7.3: Mass-radius relations for NSBH<sub>1</sub> (*upper left*), NSBH<sub>2</sub> (*upper right*), BBH<sub>1</sub> (*lower left*) and BBH<sub>2</sub> (*lower right*), and the corresponding constraint on the radius of a typical neutron star,  $R_{1.4}$ . We show all EOS in our set (gray) and the 95% credible interval on the mass-radius relations that survive in each scenario (green-shaded areas). For comparison, we also show the 90% credible interval of the mass of GW190814’s secondary component (blue). For NSBH<sub>1</sub> and NSBH<sub>2</sub>, a constraint of  $\chi_2 < 0.05$  is imposed, while it is relaxed for BBH<sub>1</sub> and BBH<sub>2</sub>.

$2.8M_{\odot}$  because of the required softness of the EOS at low densities to be consistent with GW170817, and the requirement for the EOS to explain the kilonova observations within our kilonova models, that depend on  $M_{\max}$  through disk ejecta [28, 29]. While GW190814 again leads to an additional lower limit on  $M_{\max}$ , similarly to NSBH<sub>1</sub>, the overlap region is now larger. This results in an increase of  $P(\Delta m > 0)$  to about 19%. For NSBH<sub>2</sub>, we find that  $M_{\max}$  is constrained to  $M_{\max} = 2.68_{-0.11}^{+0.14}M_{\odot}$ .

NSBH<sub>2</sub> is also the ideal case to highlight the importance of the various aspects of our NMMA analysis. When including only nuclear-physics constraints and heavy-pulsar masses,  $P(\Delta m > 0) \sim 33\%$  which even increases to  $\sim 44\%$  when NICER data are included. This is because heavy pulsars favor high  $M_{\max}$  and NICER data prefers stiff EOS that also tend to have higher  $M_{\max}$ . The limitations on  $M_{\max}$ , and hence  $P(\Delta m > 0)$ , stem from the inclusion of the GW signal GW170817 and its associated kilonova, which reduce  $P(\Delta m > 0)$  to  $\sim 27\%$  and  $\sim 20\%$ , respectively. Finally, GW190425 reduces  $P(\Delta m > 0)$  to the 19% quoted above.

For the scenario BBH<sub>1</sub>, the observation of GW190814 adds an upper limit on  $M_{\max}$ , which now excludes the small overlap region of the blue and black curves in Fig. 7.1 (note that for BBH<sub>1,2</sub> we do not constrain  $\chi_2$ ). In this sense, BBH<sub>1</sub> is the contrary of NSBH<sub>1</sub>, and the probability for the mass  $m_2$  of GW190814 to be above  $M_{\max}$ ,  $P(\Delta m < 0)$ , is above 99.9%. As expected, this scenario does not visibly impact the posterior on  $M_{\max}$  from the NMMA analysis and we obtain  $M_{\max} = 2.18_{-0.13}^{+0.15}M_{\odot}$ . Finally, BBH<sub>2</sub> is the contrary to NSBH<sub>2</sub>. In this case, we find  $P(\Delta m < 0) \sim 81\%$  and  $M_{\max} = 2.29_{-0.21}^{+0.26}M_{\odot}$ .

We have also tested the dependence of our findings on the EOS prior. In Ch. 6, the NMMA analysis used an EOS prior that is uniform in  $R_{1.4}$ . Using the EOS prior provided directly by the parametric speed-of-sound extension scheme developed in Refs. [32, 218], i.e., an EOS prior that is nonuniform in  $R_{1.4}$ , we show the results as dashed lines in Fig. 7.1. We find that the probability for NSBH<sub>2</sub> changes only very slightly for a different EOS prior, from 19% to 17%. Hence, we conclude that our findings are robust with respect to the EOS prior.

We summarize the findings for all four scenarios in Table 7.1. Our analysis strongly suggests that GW190814 was a BBH merger, as otherwise GW190814 would introduce a strong tension with the results of our NMMA analysis. Given the remnant mass of GW170817 of  $2.7M_{\odot}$ , which is very close to the inferred  $m_2$  of GW190814, and the likely scenario that the remnant of GW170817 was, in fact, a BH, this seems to be the most consistent scenario given all current observational and theoretical knowledge of the NS EOS. Our findings are consistent with Refs. [277, 284–286].

### 7.3.2 EOS constraints from GW190814

Finally, we investigate the impact of our four scenarios on the EOS by studying the MR relation. This allows us to provide testable predictions for the NS radius for these four cases, and might help to fully pin down the nature of GW190814 when more observations become available in the future.

For NSBH<sub>1</sub> ( $P(\Delta m > 0) < 0.1\%$ ), the strong tension between the different constraints on  $M_{\max}$  translates to a narrow posterior in the MR plane, which we show in the left panel of Fig. 7.3. We find that in this case  $R_{1.4}$  is constrained to be  $R_{1.4} = 12.6_{-0.5}^{+0.4}\text{km}$ . That would be the most stringent constraint on the NS radius to date. Also, the posterior on MR remains rather tight in the mass range  $(1.4 - 2.0)M_{\odot}$  and, hence, puts very strong

Scenario	NSBH <sub>1</sub>	NSBH <sub>2</sub>	BBH <sub>1</sub>	BBH <sub>2</sub>
Probability	< 0.001	~ 0.19	> 0.999	~ 0.81
$M_{\max}$	$2.53^{+0.07}_{-0.06}M_{\odot}$	$2.68^{+0.14}_{-0.11}M_{\odot}$	$2.18^{+0.15}_{-0.13}M_{\odot}$	$2.29^{+0.26}_{-0.21}M_{\odot}$
$R_{1.4}$	$12.56^{+0.38}_{-0.51}\text{km}$	$12.69^{+0.55}_{-0.55}\text{km}$	$11.76^{+0.90}_{-0.82}\text{km}$	$11.97^{+0.87}_{-0.93}\text{km}$

Table 7.1: Summary of the probabilities and the resulting posteriors on the NS maximum mass and radius of a typical NS for the four scenarios analyzed in this chapter.

constraints on the NS EOS. For NSBH<sub>2</sub> ( $P(\Delta m > 0) \sim 19\%$ ), the constraints on the MR relation are less tight and the posterior widens as expected, see middle left panel of Fig. 7.3. The radius of a typical NS is found to be  $R_{1.4} = 12.7^{+0.6}_{-0.5}\text{km}$ , in good agreement with the determinations by the LVC Refs. [277, 284] for this scenario. Both for the NSBH<sub>1</sub> and NSBH<sub>2</sub> scenarios, the EOS posterior strongly suggests that the NS MR relation does not have multiple stable branches, which would be indicative of very strong first-order phase transitions [159]. For such EOS,  $M_{\max}$  is typically much smaller, see, e.g., Refs. [148, 159, 293]. Furthermore, in particular NSBH<sub>2</sub> now prefers the stiffest EOS included in our EOS set, and its posterior is pushed against the upper bound of our EOS prior. This behavior is observed also for the pressure between  $(1 - 2)n_{\text{sat}}$ , which is pushed toward the upper prior bound. Therefore, NSBH<sub>2</sub> might imply that the QMC calculations employing local chiral EFT interactions, which we use to constrain the EOSs, might break down already below  $1.5n_{\text{sat}}$ . In particular, NSBH<sub>2</sub> would disfavor the softer Hamiltonian explored in Refs. [32, 111], although it would not exclude it. A possible explanation could be that higher-order many-body forces, that tend to stiffen the EOS [294, 295], are crucial to describe NS physics, see also Ref. [35].

Furthermore, NSBH<sub>2</sub> suggests that the EOS would need to remain stiff within the whole NS. While the original NMMA analysis finds the maximum of the speed of sound inside an NS,  $c_{s,\max}$ , to be  $c_{s,\max}^2 \geq 0.4$ , for NSBH<sub>2</sub> we find  $c_{s,\max}^2 \geq 0.6$ . Hence, GW190814 being an NS–BH merger might require us to revisit our current understanding of the EOS.

In the BBH<sub>1</sub> and BBH<sub>2</sub> scenarios, GW190814 adds another upper limit on  $M_{\max}$ , which however, is much weaker than the upper limit of Ref. [151]. Hence, for BBH<sub>1</sub>, GW190814 does not add any additional information and our result of Ch. 6,  $R_{1.4} = 11.8^{+0.9}_{-0.8}\text{km}$ , is reproduced. For BBH<sub>2</sub>, due to the limit on  $M_{\max}$  being weaker, the radius posterior shifts to slightly larger radii, and we find  $R_{1.4} = 12.0^{+0.9}_{-0.9}\text{km}$ , which remains very consistent with the findings in Ch. 6. Because this new upper limit would be more robust than the one of Ref. [151], the BBH<sub>2</sub> scenario would provide a verification of the findings of the NMMA analysis if this scenario was confirmed.

## 7.4 Summary

In this chapter, we have investigated different possible scenarios for the nature of GW190814 using our robust NMMA framework that includes a wealth of observational data. Assuming that this compact merger was, in fact, an NS–BH merger, we find strong constraints on the radius of a typical neutron star,  $R_{1.4} = 12.6^{+0.4}_{-0.5}\text{km}$  ( $R_{1.4} = 12.7^{+0.6}_{-0.5}\text{km}$ ) in case upper limits on  $M_{\max}$  from GW170817 are (not) enforced. If, on the other hand, GW190814 was a BBH merger, then it is fully consistent with our current knowledge of the EOS, and



the radius of a typical NS remains at  $R_{1.4} = 11.8_{-0.8}^{+0.9}\text{km}$  ( $R_{1.4} = 12.0_{-0.9}^{+0.9}\text{km}$ ).

Based on the low probability of  $m_2$  to lie below  $M_{\text{max}}$  inferred from the NMMA analysis of Ch. 6, less than 0.1% (19%) if the upper limit on  $M_{\text{max}}$  of Ref. [151] is (not) included, our study strongly suggests that GW190814 was a BBH merger. Similar events detected in the future will help to map out the maximum mass of NSs and enable us to pin down the EOS of dense matter.



# NUCLEAR-PHYSICS MULTI-MESSENGER ASTROPHYSICS CONSTRAINTS ON THE NEUTRON-STAR EQUATION OF STATE: ADDING NICER'S PSR J0740+6620 MEASUREMENT

## 8.1 Introduction

To explore the high-density EOS and to place constraints on the possible existence of a phase transition, it is crucial to observe isolated NSs close to the maximum mass supported by the EOS. Alternatively, the high-density part of the EOS can also be probed through binary NS mergers. Once the two stars merge, they can potentially form a hypermassive remnant even exceeding the maximum mass of individual NSs [25, 151, 221, 296]. However, such remnants have not yet been observed through GWs but only through the associated EM observations which, due to their more involved interpretation, leads to larger uncertainties for the EOS (e.g., [297] and [236]). Fortunately, the recently published second observation by NICER [65, 66, 298] provides a crucial new data point for an isolated NS close to the maximum mass.

NICER is a NASA mission on board the International Space Station that measures the X-ray pulse profile of selected pulsars which allows one to extract information on the configuration of X-ray hot spots. Additionally, the pulse profile is sensitive to the light bending around the pulsar (see Sec. 4 in Ref. [298]), and therefore, provides information on the NS compactness, which in turn allows to extract data on the NS mass and radius. The first NICER measurement was reported in December 2019 and targeted the pulsar J0030+0451, for which both mass and radius were unknown. Two independent analyses of the first NICER observation provided mass-radius constraints for this NS of  $1.34_{-0.16}^{+0.15} M_{\odot}$  and  $12.71_{-1.19}^{+1.14}$  km [64] or  $1.44_{-0.14}^{+0.15} M_{\odot}$  and  $13.02_{-1.06}^{+1.24}$  km [63] at 68% credence.

In its second observation, NICER analyzed X-ray data from the millisecond pulsar PSR J0740+6620 [65, 66]. This NS is the heaviest NS observed to date with a known mass of  $2.08 \pm 0.07 M_{\odot}$  (Ref. [62], updated from its original value reported by Ref. [135]). Combining the known mass with the pulse-profile modeling allowed the NICER collaboration to measure the radius of PSR J0740+6620. Two independent analyses by the NICER collaboration found the radius to be  $12.39_{-0.98}^{+1.30}$  km [66] or  $13.71_{-1.50}^{+2.61}$  km [65] at 68% credence. While the NICER data provide information about the modulated emission from the star, the analyses of [65] and [66] additionally used information from the X-ray Multi-Mirror (XMM)-Newton telescope [299, 300] to improve the total flux measurement from the star, due to a smaller rate of background counts.

In this chapter, we incorporate the new X-ray observation of PSR J0740+6620 and its updated mass within our existing nuclear-physics multi-messenger astrophysics (NMMA) framework, which we have developed and described in Ch. 6. This allows us to revisit

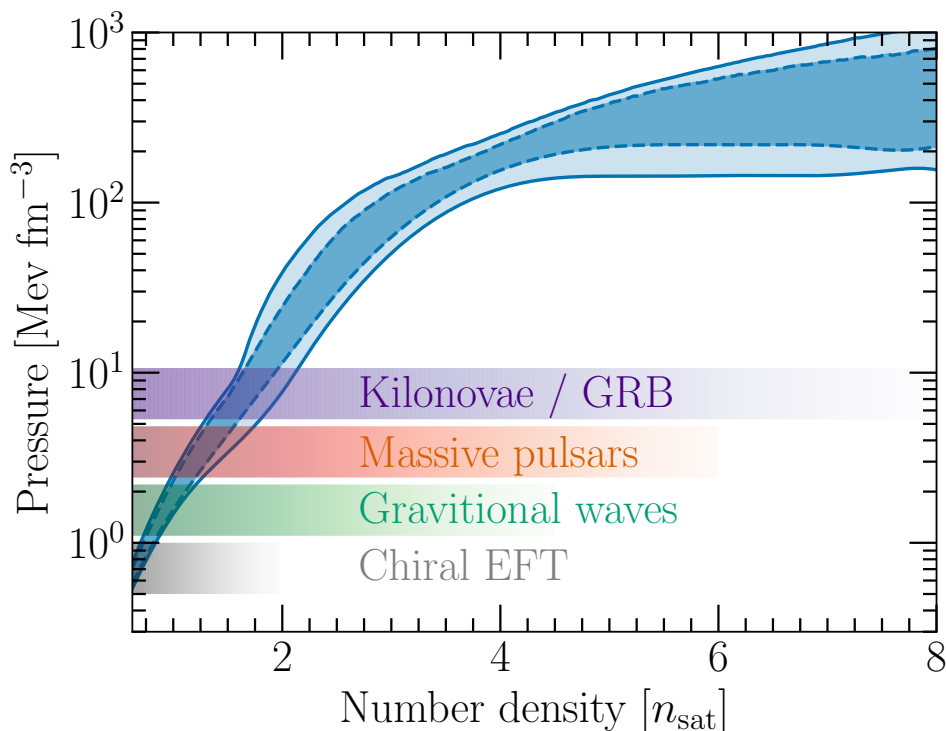


Figure 8.1: The posterior for the pressure as a function of number density for our final analysis is shown at 68% and 95% credible intervals (blue light- and dark-shaded bands, respectively). The shaded bars indicate qualitatively which density regions are probed by different NS information, while the corresponding pressures can be extracted using the pressure vs. density band. The bars refer to theoretical modeling at low densities using chiral effective field theory (gray), gravitational waves (green) where the maximum probed density is the central density of GW190425’s primary component, massive pulsars (orange) where we give the central density of PSR J0740+6620, and kilonova and GRB (purple). Because kilonova and GRB properties depend on the black hole formation mass, and therefore the maximum allowed mass by the EOS, we show the central density of the maximum mass NS.

our constraints on the NS EOS, in particular on the existence of strong first-order phase transitions, the maximum mass of neutron stars, and the nature of GW190814 (see Ch. 7).

This chapter is structured as follows. In Section 8.2 we briefly summarize our previous results and review recent works including the NICER measurement of PSR J0740+6620. In Section 8.3, we review our NMMA framework. Using the new NICER data, in Section 8.4, we discuss our prediction for the NS EOS (Sec. 8.4.1), the NS maximum mass and the probability for GW190814 [277] to be a black hole-NS merger (Sec. 8.4.2), and investigate to what extent the recent NICER observations informs us about the existence of a phase transition in the EOS (Sec. 8.4.3). We will give a summary of our results in Section 8.6.

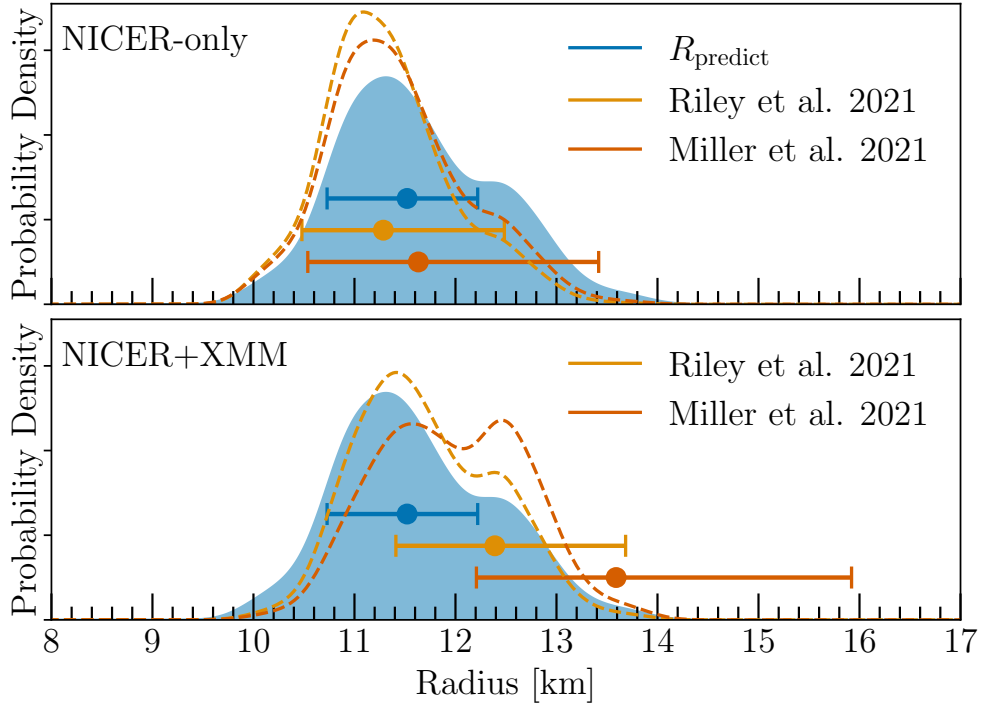


Figure 8.2: Upper panel: Posterior distribution function for  $R_{\text{predict}}$  from the NMMA framework of Ch. 6 (blue shaded). The median and 68% uncertainty for the radius prediction of PSR J0740+6620 are shown as blue error bar. We also show the NICER-only measurement of [66](yellow) and [65](red) at 68% uncertainty. The posteriors after the inclusion of the updated observations of PSR J0740+6620 are shown by dashed lines. Lower panel: Similar to the upper panel but including also XMM data.

## 8.2 Previous works

In Ch. 6, we included the pulsar mass measurements of PSR J0740+6620, PSR J0348+4042, and PSR J1614-2230 [60, 61, 134, 135], GW data from the NS mergers GW170817 and GW190425, information from the kilonova AT2017gfo, the gamma-ray burst GRB170817A as well as its afterglow [7], and the NICER observation of PSR J0030+0451 [63, 64] in a Bayesian inference framework based on systematic nuclear-physics input from chiral effective field theory (EFT). In Ch. 6, we obtained a radius of a typical NS of  $R_{1.4} = 11.75^{+0.55}_{-0.50}$  km at 68% uncertainty. Based on these results, our prediction of the radius of PSR J0740+6620 was  $R_{\text{predict}} = 11.52^{+0.70}_{-0.79}$  km at 68% credence level. We compare this prediction with the recent NICER measurements in Fig. 8.2. We find that our estimate is in excellent agreement with the results obtained in [66] and [65] using only the NICER data. Once data from the XMM-Newton observatory is additionally taken into account, the radius is pulled to larger values decreasing the agreement between our prediction and the measurement, but deviations are  $\lesssim 1\sigma$ . This effect is stronger for the Maryland-Illinois result [65], which appears to be caused by a number of differences between the individual analyses of [65] and [66]: differences in the prior on the cross-calibration uncertainty of NICER and XMM-Newton which is allowed to be two times larger than the measured deviation in [65] but an order of magnitude larger in the analysis of [66], differences in the radius prior which has an upper bound of 16 km in the

analysis of [66] and approximately 25 km in [65], differences in the sampling algorithms and their convergence that affected the posterior widths, and differences in the assumed distribution of the blank-sky counts to estimate the XMM background.

Since the first announcement of the NICER results for PSR J0740+6620 [301] there have been several studies of the implications of this radius measurement [302–305]. However, these studies did not use the full posterior samples released in [65, 66], but employed hard cuts for the radius-mass measurement, which can lead to biases during the final multi-messenger analysis, as shown in, e.g., [207]. In more detail, the studies in [302] and [303] were based on phenomenological nuclear-physics descriptions, but did not include systematic nuclear-theory calculations with uncertainty estimates, e.g., from chiral EFT, to constrain the low-density EOS. Instead, [302] studied the impact of the NICER observation of PSR J0740+6620 on the existence of a first-order phase transition or quarkyonic matter using two different models for the high-density part of the EOS. They found that the NICER observation of PSR J0740+6620 cannot rule out first-order phase transitions, but this study also did not systematically include other astrophysical constraints in a Bayesian analysis. Using a different EOS parametrization, [303] combined a hypothetical radius measurement of PSR J0740+6620 with previous GW and NICER observations and the recent result for the neutron-skin thickness of  $^{208}\text{Pb}$  from the PREX-II experiment [306]. In contrast to these works, [305] used theoretical nuclear-physics input from chiral EFT at low densities and perturbative Quantum Chromodynamics (QCD) at high densities to constrain the EOS. However, they did not perform a Bayesian analysis to constrain the EOS given available astrophysical data, but instead implemented various constraints using hard cuts; see above. None of these papers included multi-messenger constraints from a detailed modeling and parameter estimation of EM counterparts associated with binary NS mergers, e.g., from a Bayesian inference of AT2017gfo and GRB170817A.

[154] and [65] were directly based on the NICER and XMM measurements of PSR J0740+6620 and studied the influence of the new NICER data using the full posterior samples. For this purpose, [65] employed very general and conservative EOS priors that were not directly informed by nuclear-theory calculations at low densities. In addition to the NICER observations of pulsars PSR J0030+0451 and PSR J0740+6620, final EOS constraints in [65] used other heavy-pulsar mass measurements, gravitational-wave observations of GW170817 and GW190425, and constraints on the nuclear symmetry energy. Results presented in [154] were instead constrained by chiral EFT calculations up to  $1.1n_{\text{sat}}$ , comparing four different chiral EFT calculations. In addition, EM information from AT2017gfo were included as well as information from GW170817 and GW190425.

In this chapter, in contrast to the studies presented in [65] and [154], we use updated GW models [117] and different kilonova models with detailed microphysical input that also explore deviations from spherical symmetry [122, 232]; cf. [297] and Ch. 6 for details about systematic uncertainties of kilonova modelling. Again in contrast to [65], we also include low-density input from chiral EFT.

### 8.3 Methodology

Our NMMA framework uses Bayesian inference tools to analyze a set of EOSs with respect to their agreement with several astrophysical observations of NSs.

As in Ch. 6, the initial EOS set is constrained at low densities by calculations of the energy per particle of neutron matter using interactions from chiral EFT [101, 102]; see Sec. 2.2.2 for more details. We only require the EOSs to explore speeds of sound,  $c_S$ , limited by  $0 \leq c_S \leq 1$  in units of the speed of light, and to provide a maximum mass for NSs of at least  $1.9 M_\odot$ . Our EOS set explicitly includes EOS with regions of sudden stiffening or softening, e.g., strong first-order phase transitions towards exotic forms of matter. For our EOS set, we impose a uniform prior on the radius of a typical  $1.4M_\odot$  NS,  $R_{1.4}$ . To estimate the impact of the particular choice of the EOS prior, we have also investigated an EOS prior without this additional requirement, see Tab. 8.2.

As a next step, we analyze our EOS set with respect to available NS observations. We start by incorporating a constraint on the maximum mass of NSs through the radio observations of the heaviest pulsars known to date, PSR J0348+4042 [60] and PSR J1614-2230 [61]. The existence of these pulsars can only be explained if the NS EOS supports masses that lie above the individual masses of these pulsars. Hence, radio pulsar measurements of heavy NSs provide a lower bound on the maximum NS mass and the constraints of the high-density EOS; cf. Fig. 8.1. We stress that at this stage we do not include the mass measurement of PSR J0740+6620, because information will be included through the new NICER measurement. An upper bound of the maximum NS mass follows from the EM observation of GRB170817A and AT2017gfo. As outlined in, e.g., [25], the observed EM signatures indicate the formation of a black hole as the final product of the binary NS merger GW170817. Combining this information with the estimated total remnant mass from the GW observation leads to a non-rotating maximum NS mass of  $M_{\max} \leq 2.16^{+0.17}_{-0.15} M_\odot$  [151]. Incorporating the constraints on the maximum mass leads to a re-weighting of the original chiral EFT EOS set.

As a next step, we include the NICER measurement of PSR J0030+0451, for which the inferred mass-radius posterior probability distributions was not dominated by systematic uncertainties and inferred system parameters were in agreement for different analyses [63, 64]. Finally, we use the resulting EOS set for GW and kilonova parameter estimation following the methods outlined in Ch. 6.

We now include the NICER observations of PSR J0740+6620 [65, 66], which are based on a Bayesian inference approach to analyze the energy-dependent thermal X-ray signal of PSR J0740+6620. We employ the posterior samples obtained with the two-circular, uniform-temperature spot model from [65, 307] and the two disjoint, uniform-temperature spots model from [66, 308]. These models provide best agreement with the observed NICER and NICER+XMM data and, for the latter, constrain the radius of PSR J0740+6620 with a mass of  $2.08 \pm 0.07 M_\odot$  [62, 135] to be  $13.71^{+2.61}_{-1.50}$  km and  $12.39^{+1.30}_{-0.98}$  km at 68% credence for [65] and [66], respectively.

The corresponding likelihood  $\mathcal{L}_{\text{NICER}}$  is given by

$$\begin{aligned} \mathcal{L}_{\text{NICER}}(\text{EOS}) &= \int dM dR p_{\text{NICER}}(M, R) \pi(M, R | \text{EOS}) \\ &\propto \int dM dR p_{\text{NICER}}(M, R) \delta(R - R(M, \text{EOS})) \\ &\propto \int dM p_{\text{NICER}}(M, R = R(M, \text{EOS})), \end{aligned} \quad (8.1)$$

where  $p_{\text{NICER}}(M, R)$  is the joint-posterior probability distribution of mass and radius of PSR J0740+6620 as measured by NICER and we use the fact that the radius is a function

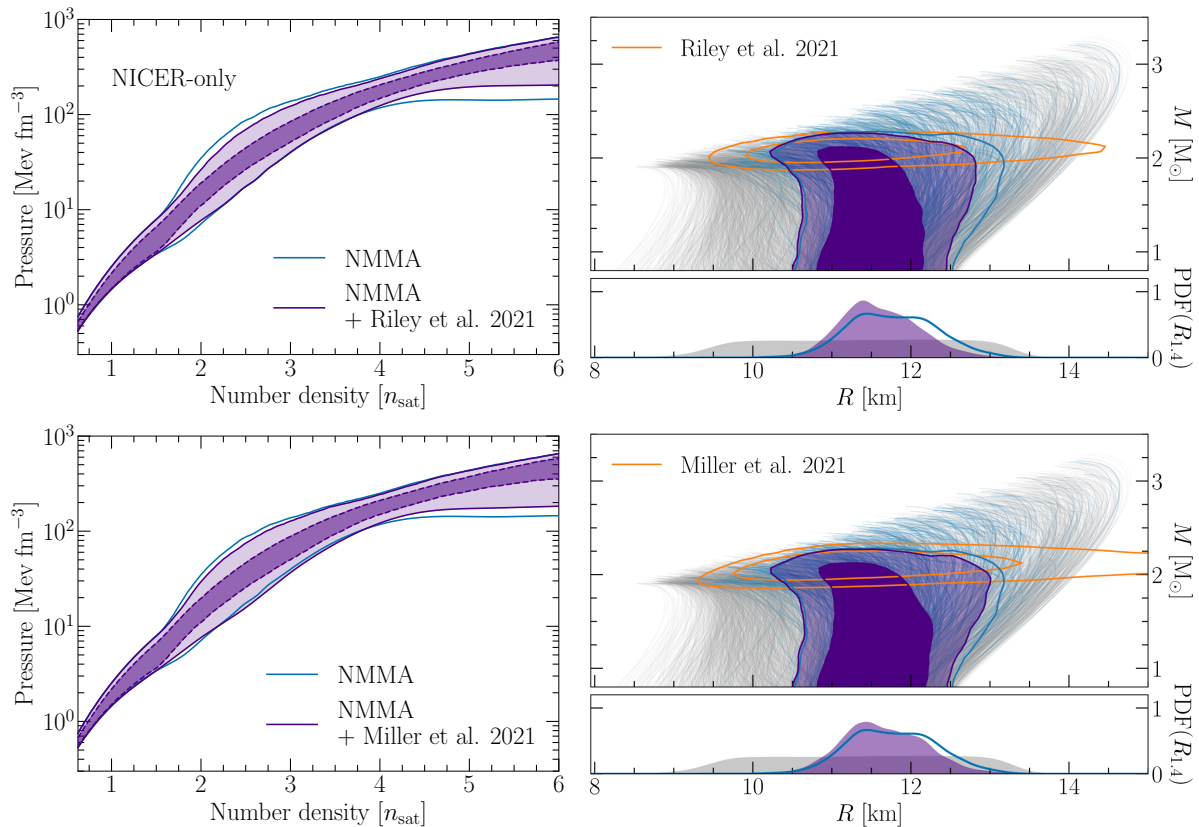


Figure 8.3: Left panels: The posterior for the pressure as a function of number density including the NICER-only observation of PSR J0740+6620 from [66] (upper panel) and from [65] (lower panel). The bands indicate 68% and 95% credible intervals. The 95% band for the NMMA result without the new NICER measurement is shown as comparison (blue line). Right panels: NICER mass-radius posteriors of PSR J0740+6620 plotted at 68% and 95% credible intervals (orange contours) and the EOSs included in the analysis (gray lines). The 95% contour for the NMMA result without including the new NICER observation is shown as thick blue line, while the individual EOSs within this credible interval of the NMMA analysis are shown as thin blue lines. The resulting mass-radius posterior after the inclusion of the new NICER-only observation is shown in purple for the NICER result of [66] (upper panel) and of [65] (lower panel) at 68% and 95% credible intervals. The 1D insets show the posteriors for  $R_{1.4}$  with (purple) and without (blue) the inclusion of the NICER-only measurement of PSR J0740+6620.

of mass for a given EOS.

## 8.4 Results

In the following, we discuss the results of our NMMA framework when the new NICER measurement is included. We give results using constraints from the X-PSI analysis by the Amsterdam group [66] or using the analysis of the Illinois-Maryland group [65] outside/inside of parentheses. The combined results refer to an analysis using the average of



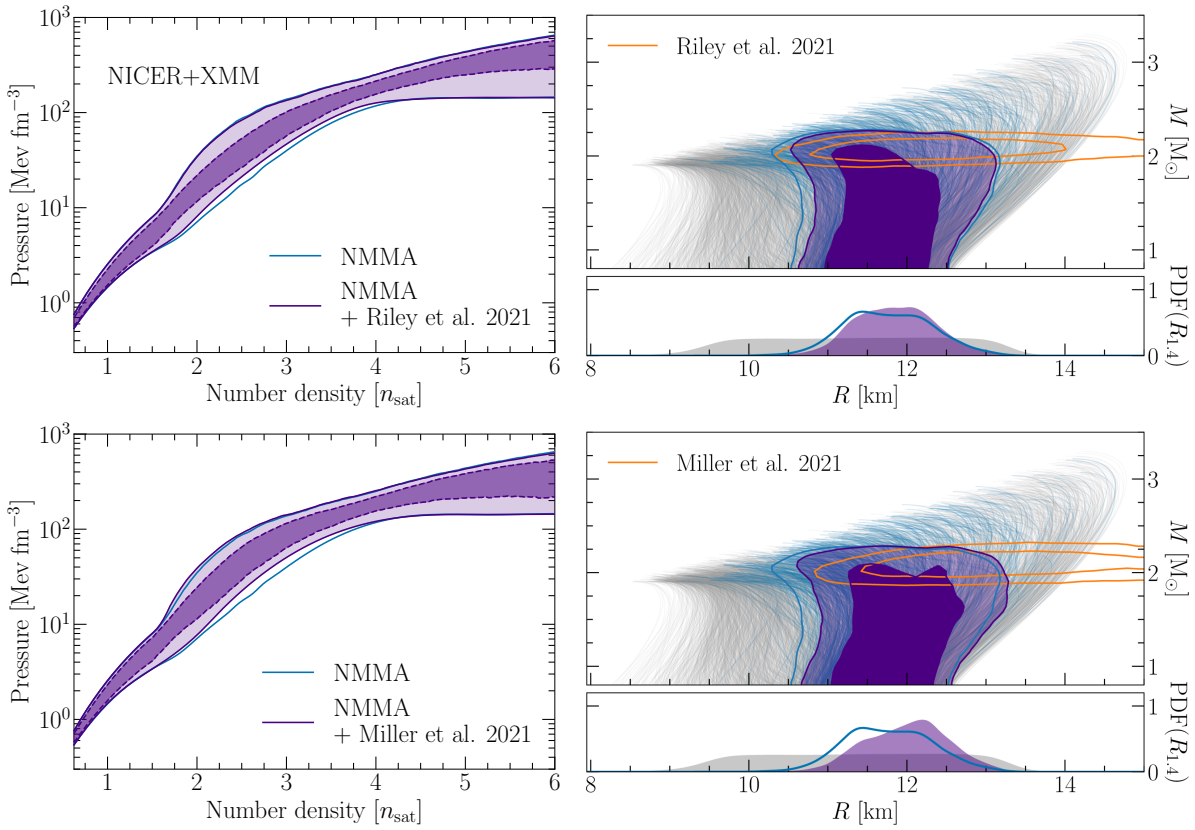


Figure 8.4: Same as Fig. 8.3 but using the NICER+XMM data.

the two  $(M, R)$  posterior distributions for PSR J0740+6620. Our findings are summarized in Tab. 8.1.

### 8.4.1 Neutron-star equation of state

In Fig. 8.3, we show the EOS and mass-radius posteriors after the inclusion of the radius measurement of PSR J0740+6620 using only NICER data. In this case, the NICER radius measurement shows excellent agreement with the NMMA prediction for the radius of PSR J0740+6620, see also Fig. 8.2. Because the NICER-only data slightly prefers softer EOS in the NMMA set, we observe a softening of our total EOS posterior. This can also be seen from the posteriors for the mass-radius relation, that is slightly shifted to lower radii. For example, the NMMA framework predicts the radius of a  $1.4M_{\odot}$  NS,  $R_{1.4}$ , to be  $11.75^{+0.86}_{-0.81}$  km without the new NICER measurement. Including the measurement, we find  $11.56^{+0.79}_{-0.76}$  km ( $11.62^{+0.85}_{-0.79}$  km) and a combined result of  $11.59^{+0.83}_{-0.76}$  km at 90% credibility. The median predictions change minimally, by  $\sim 200$  m, and the uncertainties improve slightly from 4.5% to 4.2% for the combined result at 68% credible interval (and from 7.1% to 6.9% at 90% credible interval). Similarly, the radius posteriors of PSR J0740+6620 after including the NICER-only data are shown in Fig. 8.2. The estimated radius changes from  $11.52^{+0.70}_{-0.79}$  km to  $11.26^{+0.56}_{-0.63}$  km ( $11.35^{+0.61}_{-0.72}$  km) at 68% credibility.

The situation is different when the XMM data are added. In Fig. 8.4, we show our results for the EOS and the mass-radius relation when including the NICER and XMM

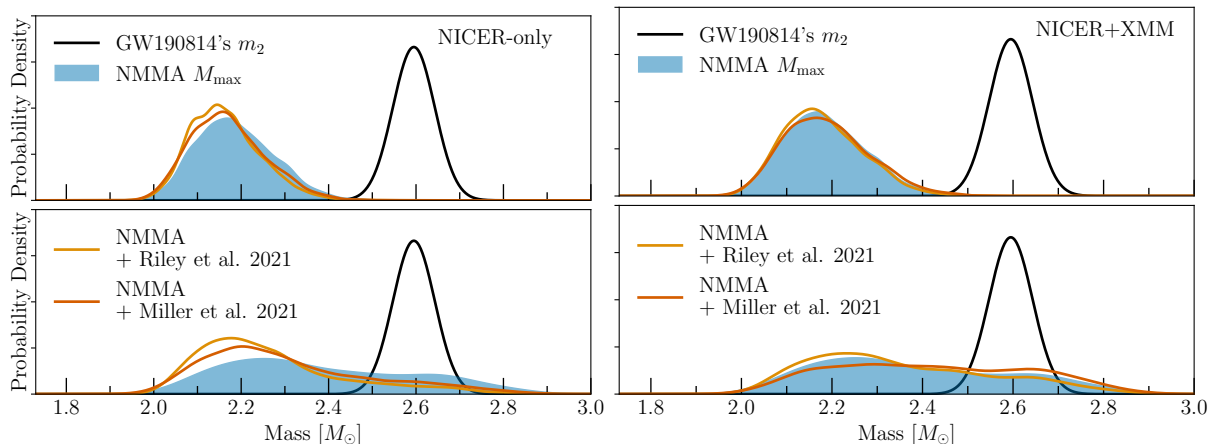


Figure 8.5: Distributions of  $M_{\max}$  without the new NICER observation (blue bands) and when including the posterior from [66] (yellow lines) and [65] (red lines). We show results for the NICER-only data (left panels) and for the NICER+XMM data (right panels), and including the  $M_{\max}$  upper limit suggested in [151] (upper panels) and when this upper limit on  $M_{\max}$  is relaxed (lower panels).

data. Now, these measurements predict larger radii compared to our initial estimation for PSR J0740+6620, see Fig. 8.2. This slightly shifts our EOS posterior to the stiffer end and the mass-radius relation to larger radii. By including the NICER-XMM measurement,  $R_{1.4}$  changes from  $11.75^{+0.86}_{-0.81}$  km without the new data to  $11.84^{+0.79}_{-0.80}$  km ( $12.03^{+0.77}_{-0.87}$  km) and a combined result of  $11.94^{+0.76}_{-0.87}$  km. Though the measured radii are well above the NMMA prediction, the uncertainties are sizable and, hence, the radius measurement of PSR J0740+6620 does not change our EOS results significantly. The medians shift to slightly larger values but remain statistically consistent with a comparable uncertainty. Similarly, the NMMA radius prediction for PSR J0740+6620 changes from  $11.52^{+0.70}_{-0.79}$  km without the new data to  $11.63^{+0.66}_{-0.79}$  km ( $11.96^{+0.80}_{-0.75}$  km) at 68% credibility.

### 8.4.2 Neutron-star maximum mass and GW190814

The radius measurement of PSR J0740+6620, and its impact on the EOS, allows us to revisit our estimate for the maximum allowed mass for NSs,  $M_{\max}$ , which we found to be  $M_{\max} = 2.18^{+0.14}_{-0.13} M_{\odot}$  without including the new NICER data as shown in Ch. 7, see Fig. 8.5. Please note that this original estimate used the previously larger mass for PSR J0740+6620 from [135], which was updated to a lower value in [62].

Because the NICER-only data favors slightly softer EOS, see the previous discussion, the maximum-mass estimate decreases slightly to  $M_{\max} = 2.15^{+0.14}_{-0.12} M_{\odot}$  ( $2.16^{+0.15}_{-0.12} M_{\odot}$ ). When additionally considering the XMM data, the new data prefers slightly stiffer EOS but the maximum mass estimate,  $2.17^{+0.15}_{-0.13} M_{\odot}$  ( $2.18^{+0.15}_{-0.15} M_{\odot}$ ), does not change significantly. The reason is that the upper limit on  $M_{\max}$  is mainly determined by the constraint of [151]. Because of the strong impact of this constraint, we also consider the scenario where this upper limit on  $M_{\max}$  is not included. In this case,  $M_{\max}$  is found to be  $2.34^{+0.34}_{-0.28} M_{\odot}$  without the new NICER data and changes to  $2.23^{+0.31}_{-0.20} M_{\odot}$  ( $2.26^{+0.36}_{-0.24} M_{\odot}$ ) including the NICER-only data and to  $2.31^{+0.37}_{-0.25} M_{\odot}$  ( $2.40^{+0.35}_{-0.32} M_{\odot}$ ) for the NICER and XMM data. The

changes are small because the increased stiffness coming from the pulsar radius measurement competes with the updated lower pulsar mass.

The posterior of  $M_{\max}$  affects the classification of the secondary component of GW190814 [277], where a  $2.6M_{\odot}$  compact object merged with a  $22M_{\odot}$  black hole. Due to its extreme mass ratio and the low primary spin, the nature of the secondary component cannot be extracted from observational data. Instead, it has to be extracted from EOS modeling, see, e.g, Ch. 7 and Ref. [274, 284, 309]. To examine the probability for the secondary component of GW190814 to be a NS, the posterior of  $M_{\max}$ ,  $p_{M_{\max}}(m)$  and that of GW190814's  $m_2$ ,  $p_{m_2}(m)$  are compared. As shown in Ch. 7, the probability for GW190814 being a NS-black hole merger is given by,

$$P(\text{GW190814 is NSBH}) = \int_0^{\infty} d\Delta m \int_{-\infty}^{\infty} dm p_{M_{\max}}(m + \Delta m) p_{m_2}(m). \quad (8.2)$$

Due to the strong tension between GW190814's  $m_2$  and the upper limit from [151], the inclusion of the NICER measurement of PSR J0740+6620 does not impact the classification of this system. With or without the new NICER measurement, the probability for GW190814 to be NS-black hole merger is estimated to be  $< 0.1\%$ . However, if we relax the upper limit on  $M_{\max}$ , i.e., do not include the analysis of [151], the probabilities change. Using the NICER-only data, the probability for GW190814 to be a NS-black hole system changes to 6.30(10.5)%, lower than the previous estimation of 19% in Ch. 7. When additionally including XMM data, the probability for GW190814 to be a NS-black hole system changes to 15.2 (24.4)%. The corresponding posterior distributions are shown in Fig. 8.5. Given all current observational and theoretical knowledge of the NS EOS, a binary black hole merger remains the most consistent scenario for GW190814.

### 8.4.3 Existence of a phase transition

QCD predicts that nucleonic matter undergoes a phase transition to quark matter at very high densities. If such a phase transition is realized in neutron stars, at which exact density such a phase transition would occur, and which properties this phase transition would exhibit is unknown [155, 157, 310]. A strong first-order phase transition, i.e., a segment in the EOS where the speed of sound vanishes, would be a 'smoking gun' signature for the existence of exotic forms of matter inside NSs.

Here, we calculate the Bayes factor  $\mathcal{B}_{\text{NPT}}^{\text{PT}}$  for the presence of such a strong first-order phase transition against the absence of it. The Bayes factor  $\mathcal{B}_{\text{NPT}}^{\text{PT}}$  is given by

$$\mathcal{B}_{\text{NPT}}^{\text{PT}} \equiv \frac{P(d|\mathcal{H}_{\text{PT}})}{P(d|\mathcal{H}_{\text{NPT}})} = \frac{P(\mathcal{H}_{\text{PT}}|d)}{P(\mathcal{H}_{\text{NPT}}|d)} \bigg/ \frac{P(\mathcal{H}_{\text{PT}})}{P(\mathcal{H}_{\text{NPT}})}, \quad (8.3)$$

where  $P(\mathcal{H}_{\text{PT}}|d)$  ( $P(\mathcal{H}_{\text{NPT}}|d)$ ) is the posterior probability for the presence (absence) of phase transition, and  $P(\mathcal{H}_{\text{PT}})$  ( $P(\mathcal{H}_{\text{NPT}})$ ) is the corresponding prior probability. A Bayes factor larger than one indicates that the presence of a phase transition is preferred, while a Bayes factor smaller than one suggests that the presence of a phase transition is disfavoured. Without information from the NICER measurement of PSR J0740+6620, we find the Bayes factor to be  $0.27 \pm 0.01$ .

When including NICER-only data, softer EOS are preferred and the Bayes factors in

Quantity	NMMA	NMMA		
		NMMA + Miller et al. 2021	NMMA + Riley et al. 2021	NMMA + Miller et al. 2021 + Riley et al. 2021
$R_{1.4}$	$11.75^{+0.86}_{-0.81}$ km	$11.62^{+0.85}_{-0.79}$ km ( $12.03^{+0.77}_{-0.87}$ km)	$11.56^{+0.79}_{-0.76}$ km ( $11.84^{+0.79}_{-0.80}$ km)	$11.59^{+0.83}_{-0.76}$ km ( $11.94^{+0.76}_{-0.87}$ km)
$M_{\max}$	$2.18^{+0.14}_{-0.13} M_{\odot}$	$2.16^{+0.15}_{-0.12} M_{\odot}$ ( $2.18^{+0.15}_{-0.15} M_{\odot}$ )	$2.15^{+0.14}_{-0.12} M_{\odot}$ ( $2.17^{+0.15}_{-0.13} M_{\odot}$ )	$2.15^{+0.15}_{-0.12} M_{\odot}$ ( $2.18^{+0.16}_{-0.13} M_{\odot}$ )
$\mathcal{B}_{\text{NPT}}^{\text{PT}}$	$0.27 \pm 0.01$	$0.29 \pm 0.01$ ( $0.21 \pm 0.01$ )	$0.30 \pm 0.01$ ( $0.23 \pm 0.01$ )	$0.29 \pm 0.01$ ( $0.23 \pm 0.01$ )

Table 8.1: Summary of the resulting posteriors for the radius of a typical NS  $R_{1.4}$ , the NS maximum mass  $M_{\max}$ , and the Bayes factor for phase transition against its absence,  $\mathcal{B}_{\text{NPT}}^{\text{PT}}$ . The values shown outside (inside) parentheses refer to the results without (with) inclusion of XMM data. All quoted errors are given at 90% credible interval.

favor of a phase transition change to  $0.30 \pm 0.01$  ( $0.29 \pm 0.01$ ). In this case, the NICER radius measurement of PSR J0740+6620 alone slightly increases the Bayes factor for the presence of a strong first-order phase transition within a NS with respect to the original NMMA analysis, but such a transition remains disfavoured considering all data. On the other hand, with the additional inclusion of the XMM data, the Bayes factor changes to  $0.23 \pm 0.01$  ( $0.21 \pm 0.01$ ). Following the interpretation of the Bayes factor described in [213], the presence of a phase transition inside a NS is disfavoured in all cases, yet it is not ruled out, in agreement with the findings of [302].

In all cases, even though a radius measurement of PSR J0740+6620 probes the EOS at the highest densities we can observe in the Cosmos to date, the NICER data adds only limited information due to its sizable uncertainties. In addition, it remains inconclusive if the radius measurement of PSR J0740+6620 itself suggests the presence of a phase transition inside a NS because the NICER-only and NICER-XMM data shift the Bayes factors in different directions; cf. last column in Tab. 8.1. Moreover, an analysis using a different EOS prior shows that the direction of the shift is prior-dependent; cf. Tab. 8.2.

## 8.5 Impact of EOS prior

In Table 8.2, we present the summary of the resulting posteriors for the quantities of interest using an EOS prior that is not uniform in  $R_{1.4}$ , i.e., a prior that is “natural” to our speed-of-sound extension scheme. The posteriors on  $R_{1.4}$  and  $M_{\max}$  are consistent with the results shown in Tab. 8.1 within the uncertainties.

In contrast, the Bayes factors  $\mathcal{B}_{\text{NPT}}^{\text{PT}}$  are prior-sensitive, and their values shift significantly from the results in Tab. 8.1. Because the non-uniform prior set does not explore as many EOS with phase transitions as the uniform  $R_{1.4}$  prior set, the shifts of the Bayes factors change. However, the presence of a phase transition inside a NS is still disfavoured in all cases, but cannot be ruled out.

Quantity	NMMA	NMMA		
		NMMA + Miller et al. 2021	NMMA + Riley et al. 2021	NMMA + Miller et al. 2021 + Riley et al. 2021
$R_{1.4}$	$11.94^{+0.58}_{-0.64}$ km	$11.86^{+0.58}_{-0.58}$ km ( $12.04^{+0.61}_{-0.61}$ km)	$11.82^{+0.56}_{-0.57}$ km ( $11.96^{+0.62}_{-0.57}$ km)	$11.84^{+0.56}_{-0.59}$ km ( $12.00^{+0.61}_{-0.60}$ km)
$M_{\max}$	$2.19^{+0.14}_{-0.13} M_{\odot}$	$2.18^{+0.15}_{-0.12} M_{\odot}$ ( $2.18^{+0.18}_{-0.13} M_{\odot}$ )	$2.17^{+0.15}_{-0.11} M_{\odot}$ ( $2.17^{+0.16}_{-0.12} M_{\odot}$ )	$2.18^{+0.14}_{-0.12} M_{\odot}$ ( $2.18^{+0.17}_{-0.13} M_{\odot}$ )
$\mathcal{B}_{\text{NPT}}^{\text{PT}}$	$0.64 \pm 0.01$	$0.62 \pm 0.01$ ( $0.67 \pm 0.01$ )	$0.60 \pm 0.01$ ( $0.64 \pm 0.01$ )	$0.61 \pm 0.01$ ( $0.65 \pm 0.01$ )

Table 8.2: Summary of the resulting posteriors without an uniform prior on  $R_{1.4}$  imposed, for the radius of a typical NS  $R_{1.4}$ , the NS maximum mass  $M_{\max}$ , and the Bayes factor for phase transition against its absence,  $\mathcal{B}_{\text{NPT}}^{\text{PT}}$ . The values shown outside (inside) parentheses refer to the results without (with) inclusion of XMM data. All quoted errors are given at 90% credible interval.

## 8.6 Summary

Using our nuclear physics – multi-messenger astronomy framework introduced in Ch. 6, we have studied the impact of the new NICER observations of PSR J0740+6620 on the neutron-star EOS. While the NICER data alone shows good agreement with our previous NMMA predictions (see Ch. 6) and therefore, validates our results, the additional inclusion of XMM data prefers slightly stiffer EOS. However, due to the large uncertainties of 10-20% in the NICER radius measurement of PSR J0740+6620, changes remain small.

In particular, the radius of a  $1.4M_{\odot}$  NS  $R_{1.4}$  changes from  $R_{1.4} = 11.75^{+0.86}_{-0.81}$  km (see Ch. 6) to  $11.56^{+0.79}_{-0.76}$  km and  $11.62^{+0.85}_{-0.79}$  km for the analyses from [66] and [65], respectively, at 90% credence without the XMM data and to  $11.84^{+0.79}_{-0.80}$  km and  $12.03^{+0.77}_{-0.87}$  km with the XMM data. Combining the latter results, we obtain a final radius estimate of  $11.94^{+0.76}_{-0.87}$  km (at 90% credence), showing excellent agreement with our initial prediction. Although the NICER-XMM data is informative, its large measurement uncertainties prevent it from significantly influencing our NMMA analysis.

We also investigated its impact on the maximum allowed NS mass,  $M_{\max}$ , and its influence on the probability for GW190814 to be a NS-black hole merger. The upper limit on the maximum mass is mainly influenced by electromagnetic observations of GW170817 [25, 151] and therefore, the NICER data does not result in an observable impact. When not enforcing this upper bound on  $M_{\max}$ , the probability for GW190814 to be a NS-black hole merger changes from 19% to 6.3% and 10.5% (15.2% and 24.4%) with the inclusion of NICER (NICER+XMM) data from [66] and [65], respectively. Based on these estimations, it remains most plausible that GW190814 originated from a binary black-hole merger.

Finally, we studied the possibility for a first-order phase transition to be present inside NSs. Following the interpretation of Bayes factors suggested in [213], the presence of phase transition inside NSs is disfavoured, yet it is not ruled out. However, this result is mainly impacted by previous multi-messenger observations of NSs and the impact of the new

NICER measurement is small.

Observation of NSs have the potential to help us answer key questions in nuclear physics but current uncertainties of individual data remain large. This highlights the importance of flexible multi-messenger frameworks that can use input from nuclear theory modeling of the EOS, laboratory experiments, and complementary observations of NSs to probe different aspects and to paint a complete picture of the EOS.

## 9.1 Introduction

As we have seen, at densities below  $1-2n_{\text{sat}}$ , the EOS and its theoretical uncertainty can be obtained from microscopic calculations based on chiral effective field theory (EFT) of QCD [109, 177, 181, 294, 311, 312]. To probe dense matter beyond these densities, additional approaches, based on experimental and observational data, are necessary. A very promising tool is the multi-messenger astrophysics analysis of neutron stars and their collisions, which provides access to dense neutron-rich matter currently not accessible in terrestrial experiments. In recent years, the advent of gravitational-wave (GW) astronomy [9] and new electromagnetic (EM) observations of neutron stars [11, 63, 64], including NASA’s Neutron Star Interior Composition Explorer (NICER) mission [63, 64], led to novel constraints on the EOS [22, 24, 27, 29–31, 33, 65, 153, 154]. However, these observations mainly probe the EOS at densities  $\gtrsim 2n_{\text{sat}}$  and still carry considerable uncertainties, reflected in the ranges for predictions of neutron-star radii. More precise or new complementary information are required to reduce the uncertainties further.

The gap between our current knowledge of the EOS stemming from nuclear theory and experiment at low densities and astrophysical observations of neutron stars at higher densities can be bridged by heavy-ion collision (HIC) experiments. These experiments, performed with heavy-ion beam energies of up to 2 GeV/nucleon, presently probe the nuclear EOS mainly in a density range between  $1-2n_{\text{sat}}$  [313–315], representing a new source of information [316].

In this chapter, we perform a global analysis of the nuclear EOS including information from nuclear theory (see Fig. 9.1A and Fig. 9.2A), astrophysical observations of neutron stars (see Fig. 9.1B and Fig. 9.2B), and results from HIC experiments that were performed at the Schwerionensynchrotron 18 (SIS-18) accelerator located at the GSI Helmholtz Centre for Heavy Ion Research [314, 315] (see Fig. 9.1C and Fig. 9.2C). We analyse the EOS and neutron-star properties by extending our Bayesian multi-messenger astrophysics framework of Ch. 6 to include information from the Four-Pi (FOPI) [314] and the Asymmetric-Matter EOS (ASY-EOS) experimental campaigns [315]. The combination of these experiments provides new constraints for neutron-rich matter between  $\sim 1-2n_{\text{sat}}$ . We additionally include the EOS constraint from Danielewicz et al. [313] for symmetric nuclear matter obtained from HIC experiments at the Bevalac accelerator at Lawrence Berkeley National Laboratory (LBL) and the Alternating Gradient Synchrotron (AGS) at Brookhaven National Laboratory (BNL). In all experiments, gold nuclei were collided. The information from this series of HIC experiments allows us to further constrain the EOS in a density range where theoretical calculations become less reliable. The final EOS constraints are obtained through the combination of both the HIC information

and astrophysical multi-messenger observations (see Fig. 9.1D and Fig. 9.2D). At 95% uncertainty, our final result for the pressure at  $1.5n_{\text{sat}}$  is  $6.25^{+1.90}_{-2.26}$  MeV fm $^{-3}$ ; a typical 1.4 solar mass neutron star is  $12.01^{+0.78}_{-0.77}$  km, see Tab. 9.1.

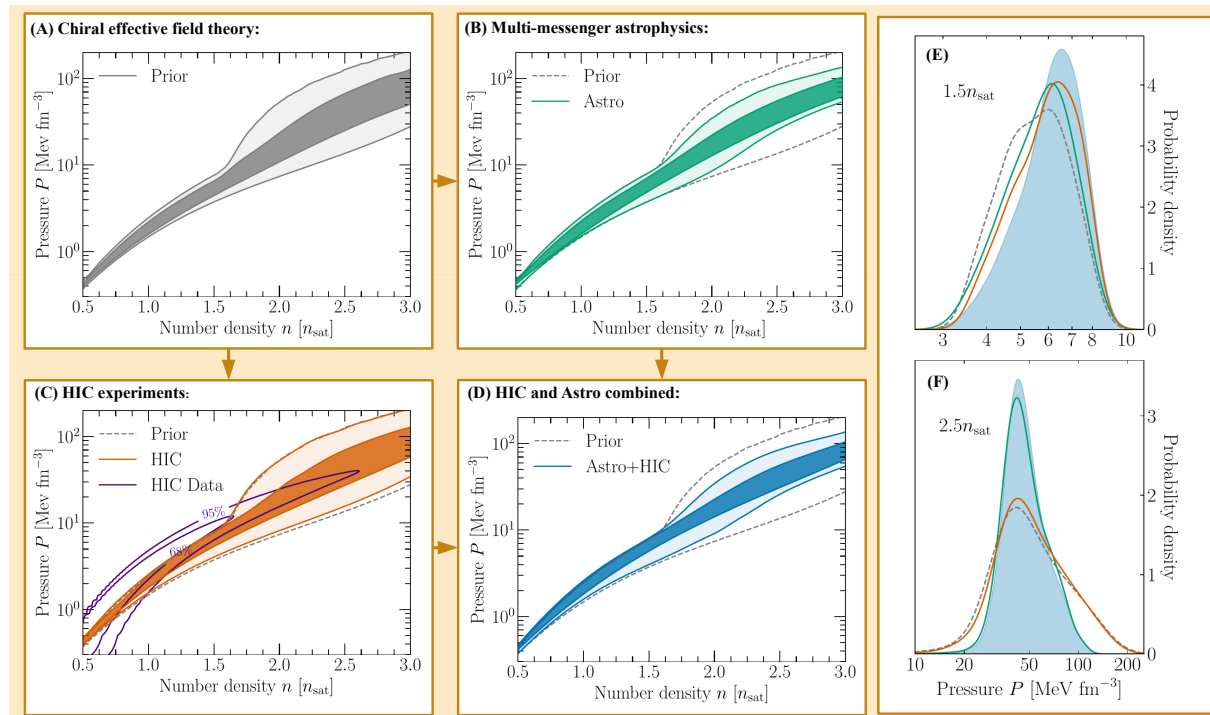


Figure 9.1: **Constraints on the EOS of neutron-star matter.** Evolution of the pressure as a function of baryon number density for the EOS prior (A, gray), when including only data from multi-messenger neutron-star observations (B, green), when including only HIC data (C, orange), and when combining both (D, blue). The shading corresponds to the 95% and 68% credible intervals (lightest to darkest). The impact of the HIC experimental constraint (HIC Data, purple lines at 95% and 68%) on the EOS is shown in panel C. In panels (B) through (D), we show the 95% prior bound for comparison (gray dashed lines). We also show posterior distributions for the pressure at  $1.5n_{\text{sat}}$  and  $2.5n_{\text{sat}}$  at different stages of our analysis (E, F), where the combined Astro+HIC region is light-blue shaded.

## 9.2 Methods

### 9.2.1 Nuclear equations of state from chiral effective field theory

Similarly to what we did in Ch. 6, 7, and 8, we make of the EOSs constrained with theoretical calculations at zero temperature employing local chiral EFT interactions [109], [107, 108, 184, 317]; see Sec. 2.2.2 for more details. As before, we use microscopic input up to  $1.5n_{\text{sat}}$  to constrain the EOS but a variation within  $1-2n_{\text{sat}}$  shows no substantial impact on our final results for neutron-star radii [35]. Above this density, we sample a set of six randomly distributed points in the speed of sound plane at baryon densities between  $1.5n_{\text{sat}}$  and  $12n_{\text{sat}}$ , enforcing  $0 \leq c_s \leq c$  at each point. A variation of the number of sampled



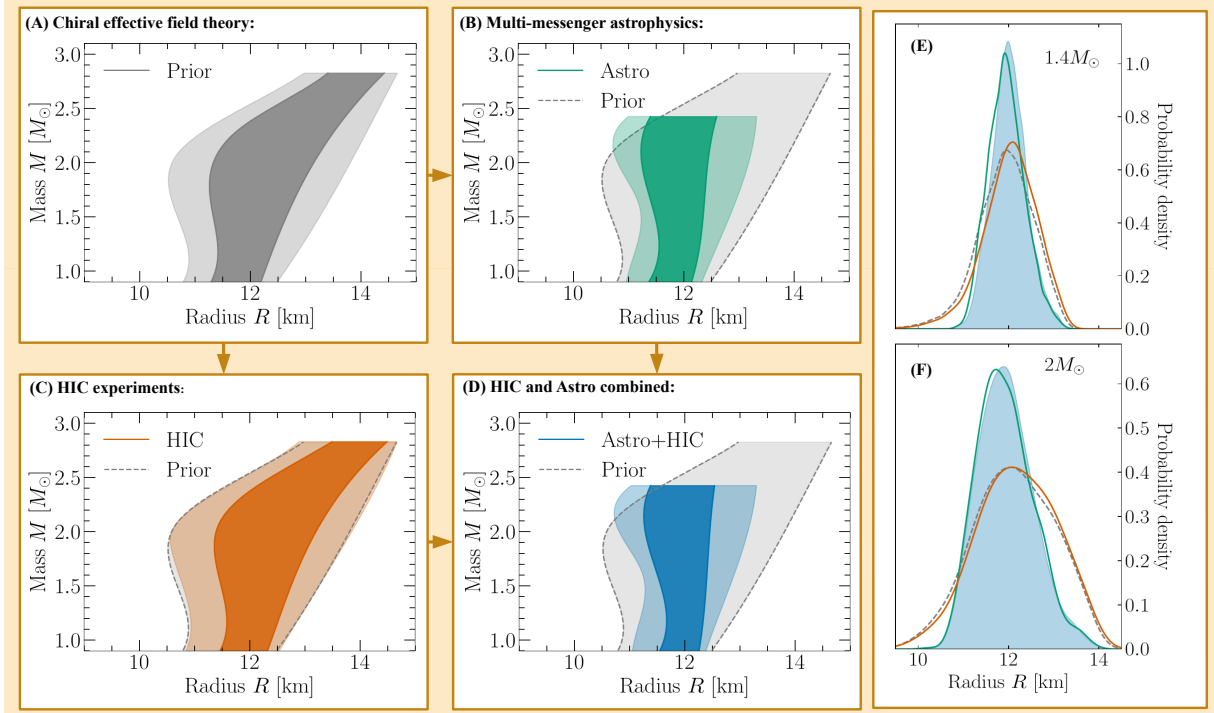


Figure 9.2: **Constraints on the mass and radius of neutron stars.** We show the 95% and 68% credible ranges for the neutron-star radius across various masses (up to the 95% upper bound on the maximum allowed mass, as only few EOSs support mass beyond that, which would result in an unrepresentative credible range) for the prior (A, gray), when including only multi-messenger constraints (B, green), when including only HIC experiment data (C, orange), and for the joint constraint (D, blue). We show the prior 95% contour in panels (B)-(D) for comparison. Posterior distributions for the radii of  $1.4M_{\odot}$  and  $2M_{\odot}$  stars are given at different stages of our analysis (E, F), where the combined Astro+HIC region is light-blue shaded.

points between 5-10 does not impact our findings. We then connect these points by line segments, reconstruct the EOS, and solve the Tolman-Oppenheimer-Volkoff equations to extract neutron-star properties. Additionally, for each EOS we construct a partner EOS that includes a segment with vanishing speed of sound to explicitly simulate strong first-order phase transitions. We sample the onset density and width of this segment randomly.

Our EOS set includes 15,000 different EOS samples where the prior on the radii of neutron stars is naturally determined by the EOS expansion scheme. We have explicitly checked the differences among a prior uniform in the radius of a typical  $1.4M_{\odot}$  neutron star and the “natural” prior and found only minor changes once astrophysical and HIC data are included, see Tab. 9.2.

Recently, first results for the EOS of symmetric nuclear matter between  $3-10n_{\text{sat}}$  from functional Renormalization Group (fRG) calculations that are based on QCD became available [318]. This offers a very promising future tool to constrain dense neutron-star matter when calculations for asymmetric matter will become available.

	Prior	Astro only	HIC only	Astro + HIC
$P_{1.5n_{\text{sat}}}$	$5.59^{+2.04}_{-1.97}$	$5.84^{+1.95}_{-2.26}$	$6.06^{+1.85}_{-2.04}$	$6.25^{+1.90}_{-2.26}$
$R_{1.4}$	$11.96^{+1.18}_{-1.15}$	$11.93^{+0.80}_{-0.75}$	$12.06^{+1.13}_{-1.18}$	$12.01^{+0.78}_{-0.77}$

Table 9.1: **Final constraints on the pressure and the radius of neutron stars.** Comparison of the pressure in  $\text{MeV fm}^{-3}$  at  $1.5n_{\text{sat}}$  and the radius in km of a  $1.4M_{\odot}$  neutron star (median with the 95% credible interval) when including only astrophysical constraints, only HIC experimental data, and for the combination of both.

## 9.2.2 Multi-messenger analysis of astrophysical data

To constrain the set of EOSs derived from chiral EFT with astrophysical data, we use a multi-step procedure in which results from individual steps are used as prior for the next part of the analysis (see Ch. 6), see Fig. 9.6. First, we incorporate constraints on the maximum mass of neutron stars. For this, we implement the mass measurements of the heavy radio pulsars PSR J0348+0432 [60] and PSR J1614-2230 [61]. Since we make use of the NICER and XMM mass-radius information of PSR J0740+6620 [65, 66] at a later stage, we do not include the mass measurement of PSR J0740+6620 [62] to avoid double counting. The combination of these observations (see Ch. 6 and Ch. 7) of high-mass neutron stars provides a lower bound on the maximum mass of neutron stars. In contrast, an upper bound of the maximum mass is obtained from the observation of the merger remnant of the neutron-star merger GW170817 [151]. Among other arguments, the observation of a bright, red kilonova component and the observation of a short gamma-ray burst 2 seconds after the merger of the two neutron stars indicate that the remnant experienced a delayed ( $\mathcal{O}(100\text{ms})$ ) collapse to a black hole, so that an upper limit on the maximum mass can be derived. The combined estimate of the maximum mass,  $2.21^{+0.10}_{-0.13}M_{\odot}$  at 68% uncertainty, already provides important information about the internal structure of neutron stars and disfavors both too stiff and too soft EOSs, i.e., EOSs with too large and too small pressures, respectively.

In the next step, we incorporate NICER’s mass and radius measurement of PSR J0030+0451 [63] and PSR J0740+6620 [65, 66]. NICER, located on board of the International Space Station, is a NASA telescope measuring the X-ray pulse profile of pulsars. By correlation of the observed profile and brightness with theoretical predictions, it is possible to extract information on the configuration, e.g., on the location and properties of hot spots on the neutron-star surface, the rotation rate of the star, as well as its compactness, which determines the light bending around the pulsar. This information enables constraints on the pulsar’s mass and radius. In addition to NICER, the XMM-Newton telescope [299, 300] has been used for the analysis of PSR J0740+6620 [65] to improve the total flux measurement. For PSR J0740+6620, we average over the results obtained by Miller et al. [65] and Riley et al. [66], while for PSR J0030+0451 we only use results of Miller et al. [63].

Next, we analyse the GW signal emitted from the binary neutron-star merger GW170817 [9], as well as its observed kilonova AT2017gfo [11]. Finally, we also incorporate the second confirmed GW signal from a binary neutron-star merger GW190425 [49]. For GW170817 and GW190425, we assumed both of them to be emitted by binary neutron star

	Natural prior on $R_{1.4}$					
$P/R$	Chiral EFT up to $1.5n_{\text{sat}}$			Chiral EFT up to $1n_{\text{sat}}$		
	HIC only	Astro only	Astro+HIC	HIC only	Astro only	Astro+HIC
$1.0n_{\text{sat}}$	$2.05^{+0.49}_{-0.45}$	$2.00^{+0.52}_{-0.49}$	$2.11^{+0.49}_{-0.52}$	$1.95^{+0.51}_{-0.39}$	$1.87^{+0.51}_{-0.41}$	$1.95^{+0.50}_{-0.43}$
$1.5n_{\text{sat}}$	$6.06^{+1.85}_{-2.04}$	$5.84^{+1.96}_{-2.26}$	$6.25^{+1.90}_{-2.26}$	$10.77^{+29.80}_{-8.81}$	$8.98^{+8.41}_{-4.30}$	$9.12^{+6.66}_{-4.36}$
$2.0n_{\text{sat}}$	$19.47^{+33.63}_{-11.67}$	$18.44^{+16.24}_{-9.69}$	$19.07^{+15.27}_{-10.53}$	$33.02^{+76.25}_{-31.06}$	$26.11^{+24.36}_{-17.81}$	$26.21^{+21.85}_{-17.16}$
$2.5n_{\text{sat}}$	$47.78^{+75.96}_{-32.96}$	$45.05^{+39.80}_{-19.62}$	$45.43^{+40.41}_{-19.11}$	$68.31^{+114.74}_{-66.35}$	$54.19^{+38.50}_{-20.67}$	$54.33^{+35.54}_{-21.69}$
$1.0M_{\odot}$	$11.89^{+0.79}_{-0.98}$	$11.76^{+0.65}_{-0.71}$	$11.88^{+0.57}_{-0.76}$	$12.68^{+1.44}_{-1.41}$	$12.36^{+0.95}_{-0.90}$	$12.40^{+0.85}_{-0.89}$
$1.4M_{\odot}$	$12.06^{+1.13}_{-1.18}$	$11.94^{+0.79}_{-0.78}$	$12.01^{+0.78}_{-0.77}$	$12.96^{+1.87}_{-1.84}$	$12.53^{+1.22}_{-1.03}$	$12.56^{+1.07}_{-1.01}$
$1.6M_{\odot}$	$12.11^{+1.33}_{-1.33}$	$11.98^{+0.93}_{-0.79}$	$12.03^{+0.98}_{-0.75}$	$13.05^{+2.11}_{-2.08}$	$12.55^{+1.31}_{-1.10}$	$12.57^{+1.22}_{-1.04}$
$2.0M_{\odot}$	$12.19^{+1.71}_{-1.59}$	$11.88^{+1.23}_{-1.10}$	$11.91^{+1.24}_{-1.11}$	$13.21^{+2.53}_{-2.38}$	$12.32^{+1.58}_{-1.49}$	$12.33^{+1.56}_{-1.44}$
	Uniform prior on $R_{1.4}$					
$P/R$	Chiral EFT up to $1.5n_{\text{sat}}$			Chiral EFT up to $1n_{\text{sat}}$		
	HIC only	Astro only	Astro+HIC	HIC only	Astro only	Astro+HIC
$1.0n_{\text{sat}}$	$2.05^{+0.46}_{-0.54}$	$1.92^{+0.64}_{-0.45}$	$2.18^{+0.43}_{-0.68}$	$1.98^{+0.49}_{-0.40}$	$1.90^{+0.52}_{-0.43}$	$2.00^{+0.49}_{-0.46}$
$1.5n_{\text{sat}}$	$6.12^{+1.75}_{-2.43}$	$5.56^{+2.45}_{-2.15}$	$6.57^{+1.66}_{-2.92}$	$9.11^{+42.6}_{-7.53}$	$8.22^{+6.51}_{-5.53}$	$8.58^{+6.62}_{-5.70}$
$2.0n_{\text{sat}}$	$17.04^{+46.81}_{-12.56}$	$18.19^{+27.15}_{-12.37}$	$19.93^{+29.61}_{-12.96}$	$23.84^{+100.12}_{-22.25}$	$22.56^{+21.12}_{-18.76}$	$23.45^{+21.97}_{-18.10}$
$2.5n_{\text{sat}}$	$38.39^{+98.48}_{-34.37}$	$44.28^{+47.06}_{-24.88}$	$47.03^{+52.26}_{-22.44}$	$48.34^{+154.87}_{-46.75}$	$46.39^{+38.20}_{-31.12}$	$47.89^{+37.10}_{-32.47}$
$1.0M_{\odot}$	$11.70^{+1.25}_{-2.23}$	$11.72^{+0.91}_{-0.89}$	$11.96^{+0.78}_{-1.02}$	$12.27^{+1.92}_{-3.01}$	$12.15^{+1.07}_{-1.39}$	$12.25^{+1.04}_{-1.41}$
$1.4M_{\odot}$	$11.81^{+1.62}_{-2.30}$	$11.90^{+1.18}_{-0.92}$	$12.08^{+1.18}_{-0.94}$	$12.32^{+2.60}_{-2.89}$	$12.22^{+1.31}_{-1.42}$	$12.33^{+1.26}_{-1.52}$
$1.6M_{\odot}$	$11.81^{+1.86}_{-2.33}$	$11.94^{+1.37}_{-0.96}$	$12.10^{+1.34}_{-1.02}$	$12.29^{+2.93}_{-2.87}$	$12.20^{+1.44}_{-1.43}$	$12.30^{+1.42}_{-1.50}$
$2.0M_{\odot}$	$12.37^{+1.82}_{-2.69}$	$11.82^{+1.71}_{-1.27}$	$11.97^{+1.80}_{-1.27}$	$12.92^{+3.04}_{-3.22}$	$11.88^{+1.85}_{-1.57}$	$11.94^{+1.85}_{-1.59}$

Table 9.2: **Impact of the EOS prior: Maximum density of chiral EFT and of prior distribution of  $R_{1.4}$ .** Comparison of the 95% credible interval for the pressure [MeV fm<sup>-3</sup>] and radius [km] of neutron stars when including only HIC experiments, only astrophysical observations, or the combined HIC and astrophysics results for chiral EFT constraints up to  $1.5n_{\text{sat}}$  and up to  $1n_{\text{sat}}$ , and for using a natural and uniform prior on  $R_{1.4}$ . We find that differences for pressures and neutron-star radii are small between both prior choices when Astro+HIC data constraints are employed. Applying constraints from chiral EFT only up to  $1n_{\text{sat}}$  allows for a broader and stiffer EOS prior at higher densities since information up to  $1.5n_{\text{sat}}$  is discarded. As a consequence, the EOSs including HIC only and to a lesser extent the combination of HIC and observational constraints become stiffer leading to an increase of neutron-star radii. This effect is larger when using a natural instead of a uniform prior in radius. Nevertheless, the impact for the natural prior is only around 5%.

mergers. To test the robustness of the GW analysis, we have explored a number of different GW models and found only a minimal impact on the final EOS constraint (see Ch. 6). Results shown in the main text are obtained using the PARALLEL BILBY software [227] and the waveform model IMRPhenomPv2\_NRTidalv2 [117] for cross-correlation with the

observed data [9]. `IMRPhenomPv2_NRTidalv2` is an updated model of the waveform model used in previous analyses by the LIGO/Virgo Collaboration [21, 49] and, hence, allows for a more accurate measurement of tidal effects.

We use Bayesian inference to analyse the observed kilonova AT2017gfo. The likelihood function for the light curve analysis  $\mathcal{L}_{\text{EM}}$  is given by [26]

$$\mathcal{L}_{\text{EM}} \propto \chi_1^2 \left( \sum_{ij} \frac{1}{n_j - 1} \left( \frac{m_i^j - m_i^{j,\text{est}}}{\sigma_i^j} \right)^2 \right), \quad (9.1)$$

where  $m_i^{j,\text{est}}$  are the estimated or theoretically predicted apparent magnitudes for a given filter  $j$  (a passband for a particular wavelength interval) at observation time  $t_i$  with  $n_j$  data points for filter  $j$ . Moreover,  $m_i^j$  and  $\sigma_i^j$  are the observed apparent magnitude and its corresponding statistical uncertainties, respectively. For this analysis, the probability distribution of a chi-squared distribution with degree of freedom of 1,  $\chi_1^2$ , is taken as the likelihood measurement. In order to reduce the systematic error of the kilonova modelling below the statistical error, an additional uncertainty of 1 mag is added to the measurement error. To analyse AT2017gfo, we employ the radiative transfer code POSSIS [122] to produce grids of light curves for multidimensional kilonova models with the following free parameters: the dynamical ejecta mass, the disk wind ejecta mass, the opening angle of the lanthanide-rich dynamical-ejecta component, and the viewing angle. To enable inference, we combine the grid with a framework combining Gaussian-Process-Regression and Singular Value Decomposition [28] to compute generic light curves for these parameters. To connect the ejecta parameters, which determine the exact properties of the light curve, with the binary neutron-star system parameters, we assume that the total ejecta mass is a sum of two components: dynamical ejecta, released during the merger process through torque and shocks, and disk-wind ejecta. Both components, the dynamical ejecta [28] and the disk-wind ejecta (see Ch. 6), are correlated to source parameters of the binary neutron-star system based on numerical relativity simulations (see Ch. 6 and Ref. [28, 234]).

### 9.2.3 Constraining the symmetric nuclear matter EOS at high density with heavy-ion collisions

Over the last two decades, major experimental efforts have been devoted to measuring the nuclear EOS with HIC experiments performed at relativistic incident energies [313]–[319, 320]. These collisions of atomic nuclei form a hot, dense fireball of hadronic matter in the overlapping region, which expands in time and reaches the surrounding detectors as baryons and mesons. The phase-space distribution of particles flowing from the fireball during the expansion phase is strongly dictated by the compression achieved in the colliding region and is, therefore, sensitive to the EOS of the hot and dense nuclear matter created in the collision. Important progress has been made recently in modeling intermediate-energy heavy-ion collisions but theoretical uncertainties still remain [321, 322]. In the present analysis, results obtained with different models are found to be compatible within their quoted errors.

The so-called elliptic flow ( $v_2$ ) of emerging particles is the main observable, which has been used to experimentally constrain symmetric nuclear matter at supranuclear

densities with HICs. It is described by the second moment of the Fourier expansion of the distribution of azimuthal angle  $\Phi$  of the emitted particles with respect to that of the reaction plane  $\Phi_{\text{RP}}$ ,

$$\frac{d\sigma(y, p_t)}{d\Phi} = C(1 + 2v_1(y, p_t) \cos(\Phi - \Phi_{\text{RP}}) + 2v_2(y, p_t) \cos 2(\Phi - \Phi_{\text{RP}}) + \dots), \quad (9.2)$$

where all expansion coefficients  $v_n$  are functions of longitudinal rapidity  $y = \frac{1}{2} \ln \left( \frac{E+p_z}{E-p_z} \right)$ , with  $p_z$  being the momentum along the beam axis and  $E$  the total energy, and of transverse momentum  $p_t = \sqrt{p_x^2 + p_y^2}$  of the particle, with  $p_x$  and  $p_y$  denoting the momentum components perpendicular to the beam axis.

In the experiment, the orientation of the reaction plane is event-wise reconstructed from the azimuthal distribution of particles recorded in the forward and backward hemispheres, and the Fourier coefficients are corrected for the finite resolution of this procedure [323]. The coincident particle and fragment emissions are also used for the reconstruction of the impact parameter of each reaction event [315]. A positive elliptic flow  $v_2$  indicates a preferred emission in the reaction plane whereas a negative flow indicates an emission out of the reaction plane.

It has been shown that the elliptic flow  $v_2$  of protons emitted at rapidities intermediate between projectile and target rapidity (mid-rapidity) in HICs at incident energies of several hundred MeV/nucleon offers the strongest sensitivity to the nuclear EOS [313, 314] [324], as evident from calculations made with various transport models. This dependence on the nuclear EOS is predicted by QMD [314] [324–326] and Boltzmann-Uehling-Uhlenbeck [313] models. The origin of the phenomenon has been investigated in detail by Le Fèvre et al. [327] As shown by Danielewicz et al. [313], at higher beam energies between 1 and 10 GeV/nucleon, the sensitivity of the directed flow  $v_1$  to the stiffness of the EOS of symmetric nuclear matter becomes comparable to that of  $v_2$ . Overall, from HICs performed at incident beam energies of a few hundred MeV/nucleon up to around 10 GeV/nucleon, the flow data indicate an EOS for symmetric nuclear matter with an incompressibility  $K$  below 260 MeV. Using FOPI data on the elliptic flow in gold-gold collisions between 400 MeV and 1.5 GeV/nucleon, thanks to the broad acceptance of the detector, an enhanced precision in the determination of the EOS could be achieved. Including the full rapidity and transverse momentum dependence of the elliptic flow of protons and heavier isotopes [314] in the analysis with the Isospin-QMD (IQMD) transport model, the incompressibility was determined as  $K = 190 \pm 30$  MeV. This result was confirmed by interpreting the same data with three Skyrme energy-density functionals introduced into the ultrarelativistic QMD (UrQMD) transport model [326], leading to  $K = 220 \pm 40$  MeV. The interval of confidence used in the present study,  $K = 200 \pm 25$  MeV, reflects both predictions. The densities probed were estimated to range between  $1-3n_{\text{sat}}$  by analyzing the densities effective in building the elliptic flow in IQMD simulations [314]. Note that the constraints deduced from the analysis of elliptic flow are compatible with earlier findings of the Kaon Spectrometer (KaoS) Collaboration obtained from comparisons of QMD predictions with experimental  $K^+$  meson production yields from gold-gold and carbon-carbon collisions performed at GSI between 0.6 and 1.5 GeV/nucleon [328, 329].

### 9.2.4 The ASY-EOS experiment to measure the symmetry energy

Nuclear experiments can help to constrain the EOS of neutron matter, see, for example, the PREX experiment measuring the neutron-skin thickness in lead nuclei [303, 306, 330, 331]. It has been suggested by Bao-An Li [332] that flows of particles in HICs can be used to constrain the EOS of neutron matter via the symmetry energy at supra-saturation density. However, nuclear matter that can be studied in laboratory experiments using HICs is not very neutron-rich. Therefore, the effect of the symmetry energy on  $v_2$  remains small, close to or below the uncertainties of the main contribution of the symmetric nuclear matter EOS. To enhance observable effects related to the symmetry energy, the use of the elliptic flow ratio of particles with large isospin difference, ideally the ratio for neutrons over protons  $v_2^{\text{np}} = v_2^{\text{n}}/v_2^{\text{p}}$ , was proposed [333]. This method has been adopted for the ASY-EOS experiment performed at GSI in Darmstadt, studying collisions of gold nuclei of 400 MeV/nucleon incident energy and gold targets. The description of the experiment and the analysis with the UrQMD transport model are given in detail in Russotto et al. [315] ASY-EOS benefited from the Large-Area Neutron Detector (LAND) [334] permitting the detection of neutrons and charged particles within the same acceptance. LAND was placed to cover mid-rapidity emissions over a large  $p_t$  interval. Its isotopic resolution in this experiment was not sufficient to uniquely identify protons. Elliptic flow ratios as a function of  $p_t$  were, therefore, determined for neutrons with respect to all charged particles within the LAND acceptance. It has been noted that for the selected collisions (central up to semi-central) and angular region, the yield of charged particles consists of light isotopes, mainly protons (around 50%) according to FOPI data for the same reaction. Confronted with UrQMD transport model predictions (and confirmed with other models, IQMD [325] and Tübingen QMD (TüQMD) [335]), the resulting flow ratio enabled deducing a constraint for the symmetry energy, which is so far the most precise for supra-saturation densities obtained from HICs. The results are detailed in the following section. As indicated by QMD model predictions, densities probed by the elliptic flow ratio in the ASY-EOS experiment extend up to about  $2n_{\text{sat}}$ .

### 9.2.5 Implementation of nuclear equation-of-state constraints from heavy-ion collisions

For analysing the experimental elliptic flow data, an EOS functional needs to be fed into the QMD simulations for both symmetric and asymmetric nuclear matter. This is given by the parameterisation for the energy per particle [314]

$$\frac{E}{A}(n, \delta) \approx \frac{E}{A}(n, 0) + S(n)\delta^2, \quad (9.3)$$

with the baryon density  $n = n_{\text{n}} + n_{\text{p}}$  and the isospin asymmetry  $\delta = (n_{\text{n}} - n_{\text{p}})/n = 1 - 2x$ , where  $n_{\text{n}}$  and  $n_{\text{p}}$  are the neutron and proton densities, respectively, and  $x = n_{\text{p}}/n$  is the proton fraction.  $E/A(n, 0)$  is the energy of symmetric nuclear matter,  $E/A(n, 1)$  corresponds to pure neutron matter, and  $S(n)$  is the symmetry energy defined here as the difference between the two. For the analysis of the FOPI experiment, the first term

in Eq. (9.3) has been parameterised with [314]

$$\frac{E}{A}(n, 0) = \frac{3}{5} \left( \frac{n}{n_{\text{sat}}} \right)^{2/3} E_F + \frac{\alpha n}{2n_{\text{sat}}} + \frac{\beta}{\gamma + 1} \left( \frac{n}{n_{\text{sat}}} \right)^\gamma, \quad (9.4)$$

with the saturation density  $n_{\text{sat}}$ , the Fermi energy  $E_F$ , and where the parameters  $\alpha$ ,  $\beta$ , and  $\gamma$  are fixed by the incompressibility  $K$ , the binding energy  $B$  of symmetric nuclear matter at  $n_{\text{sat}}$ , and the condition that the pressure of symmetric nuclear matter is zero at saturation density [314]:

$$\alpha = -2 \left( \frac{K + \frac{6E_F}{5}}{9(\gamma - 1)} + \frac{2}{5} E_F \right), \quad (9.5a)$$

$$\beta = \left( K + \frac{6}{5} E_F \right) \frac{\gamma + 1}{9\gamma(\gamma - 1)}, \quad (9.5b)$$

$$\gamma = \frac{K + \frac{6E_F}{5}}{9 \left( \frac{E_F}{5} + B \right)}. \quad (9.5c)$$

In the ASY-EOS analysis, the  $S(n)$  term of Eq. (9.3) has been parameterised as [315]

$$S(n) = E_{\text{kin},0} \left( \frac{n}{n_{\text{sat}}} \right)^{2/3} + E_{\text{pot},0} \left( \frac{n}{n_{\text{sat}}} \right)^{\gamma_{\text{asy}}}. \quad (9.6)$$

At saturation density, the kinetic part has been set to  $E_{\text{kin},0} = 12 \text{ MeV}$  and  $E_{\text{pot},0} = S_0 - E_{\text{kin},0}$ . The parameter  $\gamma_{\text{asy}}$  was extracted from fits to experimental data of the  $p_t$  dependence of the elliptic flow ratio of neutrons over charged particles around mid-rapidity. In particular, this results in  $\gamma_{\text{asy}} = 0.68 \pm 0.19$  for  $S_0 = 31 \text{ MeV}$  and  $\gamma_{\text{asy}} = 0.72 \pm 0.19$  for  $S_0 = 34 \text{ MeV}$ , see Fig. 9.7 for a comparison with microscopic neutron matter calculations. Here, we interpolate  $\gamma_{\text{asy}}$  assuming a linear function with  $S_0$ , where the uncertainty is chosen to be 0.19 independent of  $S_0$ . We have studied the behavior of  $\gamma_{\text{asy}}$  as a function of  $S_0$  for two different QMD models (see Fig. 9.3) and confirmed that the linear interpolation in the  $S_0$  range is suitable.

The pressure constraint is given by the density derivative of the energy per particle of Eq. (9.3),

$$P(n, \delta) = n^2 \frac{\partial E/A(n, \delta)}{\partial n}, \quad (9.7)$$

and depends on  $n$ ,  $\delta$ ,  $n_{\text{sat}}$ ,  $B$ ,  $K$ , and  $S_0$ . We enforce this constraint only at densities where the experiment is sensitive. The density region of the HIC constraint is set by the sensitivity of the neutrons-over-charged-particles flow ratio determined for the ASY-EOS experiment [315], see also the previous section. This sensitivity curve covers the density range from  $0.5n_{\text{sat}}$  up to  $3n_{\text{sat}}$  and peaks between  $n_{\text{sat}}$  and  $\sim 2n_{\text{sat}}$ , where the experiment is most sensitive.

Neutron-star matter is composed of neutrons, protons, electrons, and muons in  $\beta$ -equilibrium. In order to apply the ASY-EOS constraint to neutron stars, the proton fraction  $x_{\text{ASY-EOS}}$  needed to be determined accordingly. For simplicity, muons are neglected because they only have a small impact on the neutron-star EOS in the considered density range. Then, the density of electrons is equal to the proton density due to local charge neutrality, and the proton fraction  $x$  at a given baryon density  $n$  is fixed by the

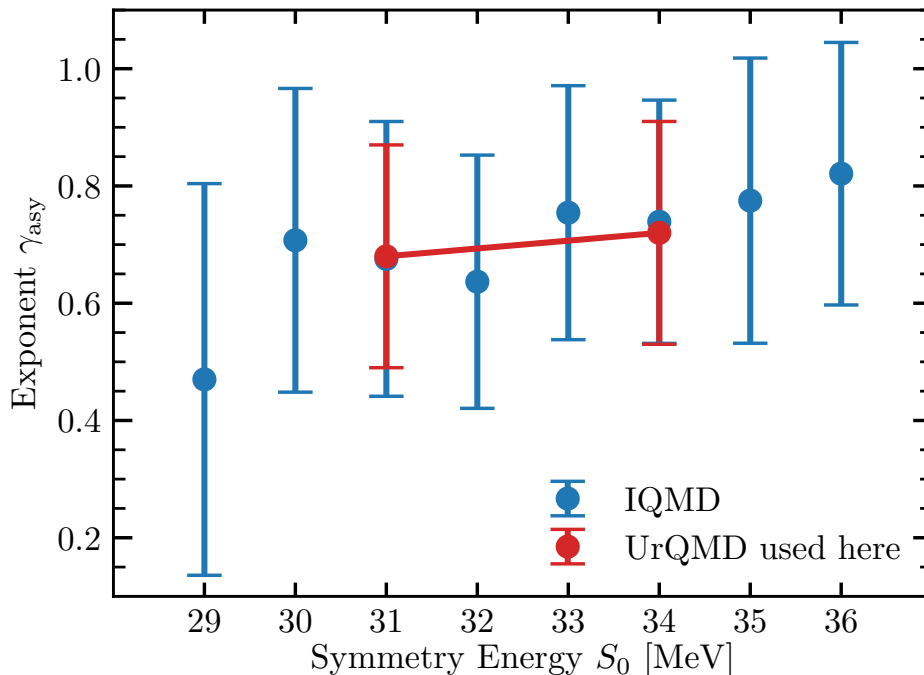


Figure 9.3: **Constraints on  $\gamma_{\text{asy}}$  versus symmetry energy  $S_0$  from two Quantum Molecular Dynamics models.** We show the exponent  $\gamma_{\text{asy}}$  of the density dependence of the potential part of the symmetry energy, see Eq. (9.6), as deduced from the analysis of ASY-EOS experimental data using the UrQMD model used in this chapter [315] (red points) and new simulations from the IQMD model (blue points). The red line indicates the mean value for  $\gamma_{\text{asy}}$  along the linear interpolation for the chosen range of  $S_0$ . Overall, the models are in good agreement with each other and the results suggest that a linear interpolation is reasonable.

$\beta$ -equilibrium condition,

$$\mu_n(n, x) = \mu_p(n, x) + \mu_e(n_e = xn), \quad (9.8)$$

where  $\mu_{n,p,e}$  is the chemical potential of the respective particle species. The neutron and proton chemical potentials are calculated consistently with Eqs. (9.3)-(9.6). Electrons are modeled as an ultrarelativistic degenerate Fermi gas with pressure  $P_e = E_e/(3V)$ , energy density  $E_e/V = \hbar c(3\pi^2 n_e)^{4/3}/(4\pi^2)$ , and chemical potential  $\mu_e = \hbar c(3\pi^2 n_e)^{1/3}$ .

The final pressure constraint is obtained using  $E_F = 37$  MeV and by varying the parameters  $n_{\text{sat}}$ ,  $B$ ,  $K$ , and  $S_0$  within specific ranges. For the parameters describing symmetric nuclear matter, we use the values consistent with the FOPI analysis given by  $n_{\text{sat}} = 0.16 \text{ fm}^{-3}$ ,  $B = 16$  MeV, and a Gaussian distribution for  $K$  with  $K = 200 \pm 25$  MeV at  $1\sigma$ . Regarding  $S_0$ , we apply a uniform prior in the range from 31 – 34 MeV. We further use results for the pressure of symmetric nuclear matter deduced by Danielewicz et al. [313] and disregard all parameter sets which lead to a pressure that is not consistent with their constraint in the overlapping density range where ASY-EOS remains sensitive, between  $2\text{--}3n_{\text{sat}}$ , see Fig. 9.4. We note that the value of  $K$  has very little influence on the observables measured by ASY-EOS to extract the symmetry energy [335]. We have



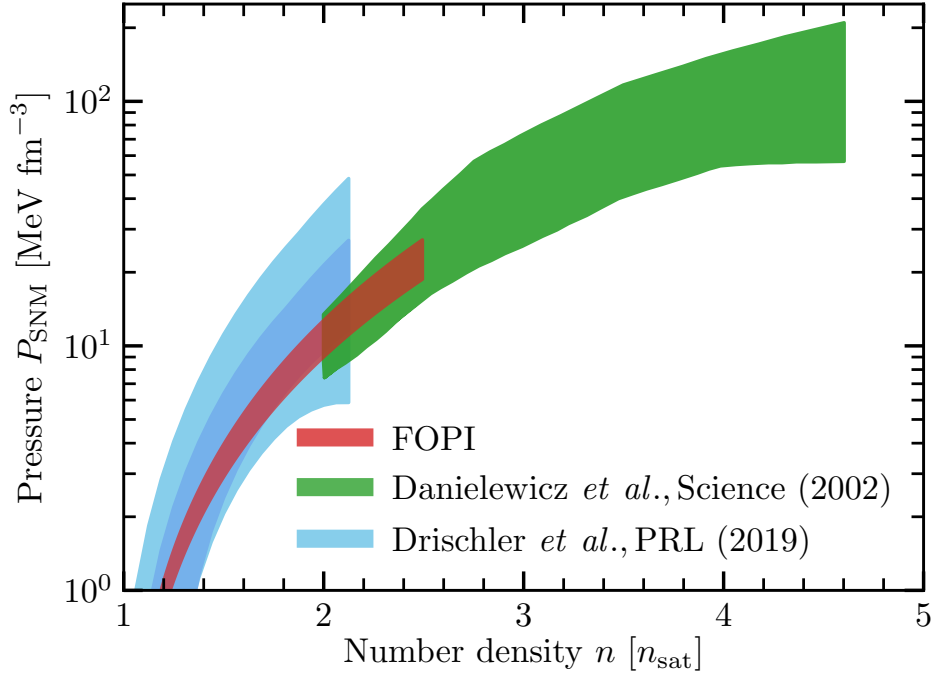


Figure 9.4: **Comparison of the pressure of symmetric nuclear matter for experiment and theory.** The pressure band from the FOPI experiment [314] at the  $1\sigma$  level (red) for the incompressibility is consistent with the chiral EFT constraint from Drischler et al. [181] [318] at N<sup>2</sup>LO (light blue) and N<sup>3</sup>LO (dark blue). The experimental uncertainty band is smaller than the theoretical one because the empirical saturation point used for extracting the experimental results has smaller uncertainties compared to theoretical estimates from chiral EFT. Between  $2-3n_{\text{sat}}$ , we additionally constrain the FOPI results with the constraint from Danielewicz et al. [313] (green), which has no statistical interpretation. This excludes the highest values for the incompressibility  $K$  from the FOPI distribution and also influences symmetric matter at smaller densities, which depends on the range of  $K$ . However, both constraints are in very good agreement with each other and the impact of the additional Danielewicz et al. constraint is small in our analysis.

explicitly checked the robustness of our results when using larger uncertainty ranges for all nuclear matter parameters in agreement with theoretical predictions [312] and found their influence on our final result to be negligible, see Tab. 9.3. In particular, we have used a larger range for  $S_0$  between 30 – 35 MeV and the following Gaussian distributions for  $n_{\text{sat}}$ ,  $B$  and  $K$ :  $n_{\text{sat}} = 0.164 \pm 0.007 \text{ fm}^{-3}$ ,  $B = 15.86 \pm 0.57 \text{ MeV}$ , and  $K = 215 \pm 40 \text{ MeV}$  at  $1\sigma$  level.

$P/R$	HIC parameters		Enlarged variations	
	HIC only	Astro+HIC	HIC only	Astro+HIC
$1.0n_{\text{sat}}$	$2.05^{+0.49}_{-0.45}$	$2.11^{+0.49}_{-0.52}$	$2.05^{+0.50}_{-0.45}$	$2.09^{+0.47}_{-0.52}$
$1.5n_{\text{sat}}$	$6.06^{+1.85}_{-2.04}$	$6.25^{+1.90}_{-2.26}$	$6.00^{+1.90}_{-2.00}$	$6.18^{+1.88}_{-2.25}$
$2.0n_{\text{sat}}$	$19.47^{+33.63}_{-11.67}$	$19.07^{+15.27}_{-10.53}$	$19.34^{+35.65}_{-11.54}$	$18.98^{+14.97}_{-9.92}$
$2.5n_{\text{sat}}$	$47.78^{+75.96}_{-32.96}$	$45.43^{+40.41}_{-19.11}$	$47.36^{+81.44}_{-28.09}$	$45.49^{+40.05}_{-20.58}$
$1.0M_{\odot}$	$11.89^{+0.79}_{-0.98}$	$11.88^{+0.57}_{-0.76}$	$11.87^{+0.81}_{-0.97}$	$11.86^{+0.58}_{-0.78}$
$1.4M_{\odot}$	$12.06^{+1.13}_{-1.18}$	$12.01^{+0.78}_{-0.77}$	$12.05^{+1.12}_{-1.20}$	$12.00^{+0.75}_{-0.80}$
$1.6M_{\odot}$	$12.11^{+1.33}_{-1.33}$	$12.03^{+0.98}_{-0.75}$	$12.10^{+1.35}_{-1.32}$	$12.03^{+0.92}_{-0.80}$
$2.0M_{\odot}$	$12.19^{+1.71}_{-1.59}$	$11.91^{+1.24}_{-1.11}$	$12.17^{+1.70}_{-1.62}$	$11.91^{+1.23}_{-1.15}$

Table 9.3: **Sensitivity on uncertainties of nuclear matter properties.** Comparison of the 95% credible interval for the pressure [ $\text{MeV fm}^{-3}$ ] and radius [km] of neutron stars when using ranges for nuclear matter properties as published for the FOPI and ASY-EOS experiments [314, 315] and when inflating the uncertainties according to theoretical calculations. We present results when including only information from HIC experiments and for the combined HIC and astrophysics information. In particular, we extend the range for the symmetry energy at saturation density to  $S_0 = 30 - 35$  MeV by extrapolating  $\gamma_{\text{asy}}$  linearly. We use Gaussian distributions for  $n_{\text{sat}}$ ,  $B$ , and  $K$  describing symmetric nuclear matter and vary these parameters within their empirical ranges (at  $1\sigma$ ):  $n_{\text{sat}} = 0.164 \pm 0.007 \text{ fm}^{-3}$ ,  $B = 15.86 \pm 0.57$  MeV [181] and  $K = 215 \pm 40$  MeV from microscopic calculations [181], [336, 337], which is in good agreement with the FOPI results.

### 9.2.6 Combination of the astronomical and heavy-ion collision constraints

In order to combine the experimental and observational EOS constraints, we use Bayesian inference. The EOS posterior is given by

$$\begin{aligned}
 p(\text{EOS}|\text{MMA}, \text{HIC}) &\propto p(\text{HIC}|\text{EOS}) \\
 &\times p(\text{MMA}|\text{EOS})p(\text{EOS}) \\
 &= p(\text{HIC}|\text{EOS})p(\text{EOS}|\text{MMA}) \\
 &\equiv \mathcal{L}_{\text{HIC}}(\text{EOS})\mathcal{P}_{\text{MMA}}(\text{EOS}),
 \end{aligned}
 \tag{9.9}$$

where MMA denotes multi-messenger astrophysics,  $\mathcal{L}_{\text{HIC}}(\text{EOS})$  is the likelihood of the HIC measurements for a given EOS, and  $\mathcal{P}_{\text{MMA}}(\text{EOS})$  is the posterior probability distribution on the EOS based on the multi-messenger observations, which acts as prior for this analysis. From the HIC experiments we obtain a posterior of the pressure at a given density,  $p(P|n, \text{HIC})$ . By combining this with the distribution of probed densities from the neutrons-over-charged particles sensitivity curve [315],  $p(n|\text{HIC})$ , the joint posterior  $p(n, P|\text{HIC}) = p(P|n, \text{HIC})p(n|\text{HIC})$  is obtained. Therefore, the relative faithfulness of the experimental results at various densities is accounted for. The likelihood  $\mathcal{L}_{\text{HIC}}(\text{EOS})$

is given by

$$\begin{aligned}
\mathcal{L}_{\text{HIC}}(\text{EOS}) &= \int dn dP p(\text{HIC}|n, P)p(n, P|\text{EOS}) \\
&\propto \int dn dP p(n, P|\text{HIC})p(n, P|\text{EOS}) \\
&\propto \int dn dP p(n, P|\text{HIC})\delta(P - P(n, \text{EOS})) \\
&= \int dn P(n, P = P(n; \text{EOS})|\text{HIC}),
\end{aligned}
\tag{9.10}$$

where we used that the pressure is a function of density for a given EOS.

## 9.3 Results

### 9.3.1 Nuclear theory input

As explained above, our analysis starts with a set of 15,000 EOSs that are constrained by nuclear theory calculations at low densities and we extend each EOS above  $1.5n_{\text{sat}}$  using an extrapolation in the speed of sound ( $c_s$ ) in neutron-star matter [32]. In addition, at this level we require all EOSs in the prior to support neutron stars with masses of at least  $1.9M_{\odot}$ , to remove EOSs that only support neutron stars with maximum masses well below the lower limit from the combined observations of heavy pulsars [60–62]. Hence, this lower bound ensures that the resulting EOS prior has reasonable support for massive-pulsar observations that we include at the first stage of our Bayesian framework as shown in Ch. 6. These general assumptions lead to a broad uncertainty for the EOS at higher densities (see Fig. 9.1A), as well as for neutron-star masses and radii (see Fig. 9.2A). The EOS prior is then used to analyse astrophysical observations and HIC experiments.

### 9.3.2 Multi-messenger astrophysics information

The astrophysical data are incorporated using a Bayesian multi-messenger framework (see Ch. 6 and Ch. 8), which analyses each EOS with respect to its agreement with a variety of observational data. We start with the mass measurements of the massive neutron stars PSR J0348+0432 [60] and PSR J1614-2230 [61] and the constraint on the maximum mass of neutron stars derived from the binary neutron-star collision GW170817 [25, 151] in which a black hole was formed after the coalescence. Information obtained from X-ray pulse-profile modeling of PSR J0030+0451 and PSR J0740+6620 using data from NICER and the X-ray Multi-Mirror Mission (XMM-Newton) [63, 65, 66] are incorporated. Moreover, we use Bayesian inference techniques to analyse GW information from the two neutron-star mergers GW170817 [9] and GW190425 [49] by matching the observed GW data with theoretical GW models that depend on neutron-star properties. Similarly to the GW analysis, we also include information from the kilonova AT2017gfo [11] associated with the GW signal.

The above astrophysical information leads to important constraints on the neutron-star EOS, as shown in Fig. 9.1B. The constraints are strongest above  $1.5n_{\text{sat}}$ , where the extrapolation in the speed of sound is used for the EOSs. The high-density astrophysical constraints affect mostly the high-mass region in the mass-radius plane and exclude the stiffest EOSs that lead to the largest radii, see Fig. 9.2B.

### 9.3.3 Data from HIC experiments

To further constrain the EOS, we implement processed data from HIC experiments provided to us by the GSI Helmholtz Centre for Heavy Ion Research. The FOPI [314] and ASY-EOS [315] experiments performed at GSI provide information respectively on the symmetric nuclear matter EOS, i.e., matter with the same amount of protons and neutrons, and on the symmetry energy, which describes the energy cost of changing protons into neutrons in nuclear matter. In addition to the GSI experiments, we include constraints on the pressure of symmetric nuclear matter at larger densities obtained from model calculations of Danielewicz et al. [313] that were used to analyze experimental data from LBL and BNL in which  $^{197}\text{Au}$  nuclei were collided at energies up to 10 GeV/nucleon. These are sensitive to higher densities,  $2\text{-}4.5n_{\text{sat}}$ , but we only include their constraints up to  $3n_{\text{sat}}$  where the sensitivity of the ASY-EOS experiment ends. We find that the inclusion of this additional constraint has only minimal impact, but keep it to ensure the completeness of our study; see Tab. 9.9.

In Fig. 9.1C, we show the combined HIC experimental constraints (labelled HIC Data) at 68% and 95% credibility as well as the resulting posterior distribution for the neutron-star EOS. Whereas the FOPI experiment delivers an EOS constraint for symmetric nuclear matter at densities between  $1\text{-}3n_{\text{sat}}$ , the ASY-EOS experiment probes the symmetry energy roughly between  $1\text{-}2n_{\text{sat}}$ . The HIC pressure-density constraint includes various sources of uncertainties. First, it includes systematic and statistical uncertainties of the experiments and the analysis of its data [314, 315]. We have explicitly checked the robustness of our results when varying the details of the analysis and employed models, and generally found that our results do not significantly depend on individual model choices; see Tabs. 9.4, 9.6, 9.7, 9.8 and Fig. 9.5. Second, when extracting the HIC constraint on neutron-star matter, we vary nuclear matter properties, such as the incompressibility parameter and the symmetry energy at  $n_{\text{sat}}$ , according to the measurements from FOPI and ASY-EOS. We have explicitly checked that increasing these uncertainties in agreement with theoretical estimates [312] only leads to minor changes of our final results, see Tab. 9.3.

To enforce the ASY-EOS constraints only at densities where the experiment is sensitive, we use the sensitivity curve for neutrons and charged particles [315] as a prior for the probed density range. We have checked the variation of our results for alternative choices of the sensitivity curve [315] and found that this has no significant impact on our final results (see Tab. 9.5). We find that the HIC constraints tend to prefer EOSs stiffer than the ones favoured by astrophysical observations, i.e., EOSs that have higher pressures at densities up to  $2n_{\text{sat}}$ , see Fig. 9.1C and Fig. 9.1E.

It has been noted that results of the ASY-EOS experiment, in their sub-saturation density extension, are compatible with recent experimental findings from isobaric analog states supplemented with additional constraints from neutron-skin data [338], HICs using isospin-diffusion observables measured in mid-peripheral collisions of Sn isotopes [339], and other nuclear structure information [340, 341]. More recently, the S $\pi$ rit campaign at RIKEN has identified spectral yield ratios of charged pions in collisions of various tin isotopes near threshold as sensitive probes of the slope of the symmetry energy near and beyond nuclear saturation density [342]. The obtained value is compatible with the ASY-EOS result but currently offers no additional strong constraint due to its large uncertainty [342, 343].

$P/R$	Speed-of-sound extension			Piecewise-polytrope extension		
	HIC only	Astro only	Astro+HIC	HIC only	Astro only	Astro+HIC
$1.0n_{\text{sat}}$	$2.05^{+0.49}_{-0.45}$	$2.00^{+0.52}_{-0.49}$	$2.11^{+0.49}_{-0.52}$	$2.06^{+0.49}_{-0.44}$	$1.96^{+0.54}_{-0.45}$	$2.10^{+0.49}_{-0.51}$
$1.5n_{\text{sat}}$	$6.06^{+1.85}_{-2.04}$	$5.84^{+1.96}_{-2.26}$	$6.25^{+1.90}_{-2.26}$	$6.06^{+1.85}_{-1.96}$	$5.66^{+2.15}_{-2.00}$	$6.20^{+1.93}_{-2.17}$
$2.0n_{\text{sat}}$	$19.47^{+33.63}_{-11.67}$	$18.44^{+16.24}_{-9.69}$	$19.07^{+15.27}_{-10.53}$	$19.00^{+17.6}_{-8.34}$	$18.96^{+15.40}_{-8.40}$	$19.64^{+15.83}_{-8.60}$
$2.5n_{\text{sat}}$	$47.78^{+75.96}_{-32.96}$	$45.05^{+39.80}_{-19.62}$	$45.43^{+40.41}_{-19.11}$	$43.72^{+39.81}_{-18.98}$	$44.77^{+35.36}_{-18.86}$	$45.27^{+36.77}_{-18.00}$
$1.0M_{\odot}$	$11.89^{+0.79}_{-0.98}$	$11.76^{+0.65}_{-0.71}$	$11.88^{+0.57}_{-0.76}$	$11.90^{+0.74}_{-0.89}$	$11.80^{+0.70}_{-0.69}$	$11.92^{+0.67}_{-0.71}$
$1.4M_{\odot}$	$12.06^{+1.13}_{-1.18}$	$11.94^{+0.79}_{-0.78}$	$12.01^{+0.78}_{-0.77}$	$12.02^{+0.96}_{-1.01}$	$11.97^{+0.84}_{-0.77}$	$12.05^{+0.83}_{-0.79}$
$1.6M_{\odot}$	$12.11^{+1.33}_{-1.33}$	$11.98^{+0.93}_{-0.79}$	$12.03^{+0.98}_{-0.75}$	$12.05^{+1.11}_{-1.11}$	$12.01^{+0.94}_{-0.83}$	$12.07^{+0.95}_{-0.84}$
$2.0M_{\odot}$	$12.19^{+1.71}_{-1.59}$	$11.88^{+1.23}_{-1.10}$	$11.91^{+1.24}_{-1.11}$	$12.02^{+1.35}_{-1.39}$	$11.88^{+1.22}_{-1.11}$	$11.92^{+1.32}_{-1.08}$

Table 9.4: **Impact of EOS extension scheme.** Comparison of the 95% credible interval for the pressure [MeV fm<sup>-3</sup>] and radius [km] of neutron stars when including only HIC results, only astrophysical observations, and for combined HIC and astrophysics results for different EOS extension schemes used. The piecewise-polytrope scheme extends the EOS beyond  $1.5n_{\text{sat}}$  with five polytropic segments with randomly chosen transition densities and polytropic indices. The differences of the pressure estimates between the two EOS extension schemes is less than 3% and the difference between the radius estimates is less than 0.5%.

### 9.3.4 Combining information from micro- and macroscopic collisions

The final EOS constraints are obtained through the combination of both the HIC information and astrophysical multi-messenger observations, see Fig. 9.1D. While the multi-messenger data rules out the most extreme EOS behavior, the HIC data favors larger pressures around  $1-1.5n_{\text{sat}}$ , where the experimental sensitivity is highest. This is similar to the effect of recent NICER observations on the EOS [65, 154]. Hence, the two complementary approaches, HIC experiments and astrophysical observations show a remarkable agreement, cf. Fig. 9.1E. At low densities, HIC results have a clear impact on the total posterior for the EOS, while the EOS at higher densities ( $\gtrsim 2n_{\text{sat}}$ ) is mostly determined by astrophysical observations. At these densities, HIC results deviate only mildly from the prior, see Fig. 9.1F. This is also reflected in the radii of neutron stars shown in Fig. 9.2E and Fig. 9.2F. Because astrophysical observations mainly probe neutron stars with  $M \gtrsim 1.4M_{\odot}$ , for which the probed densities are higher, HIC information influences the radii of these neutron stars to a smaller degree. The radius of low-mass stars with  $M \sim 1.0M_{\odot}$ , on the other hand, is also constrained by HIC information. Our final result for a typical 1.4 solar mass neutron star is  $12.01^{+0.37}_{-0.38}$  km at 68% uncertainty ( $12.01^{+0.78}_{-0.77}$  km at 95% uncertainty), see Tab. 9.1. Comparing this value to the result without any HIC information,  $11.93^{+0.39}_{-0.41}$  km at 68% credence, highlights the benefit of combining these various sources of information in a statistically robust framework. We find that the HIC information has high impact on EOS at density below  $1.5n_{\text{sat}}$ ; see Tab. 9.10. Finally, we quantify the possibility for the presence of a strong first-order phase transition to a

$P/R$	n/ch sensitivity		n/p sensitivity		Window 1- $2n_{\text{sat}}$	
	HIC only	Astro+HIC	HIC only	Astro+HIC	HIC only	Astro+HIC
$1.0n_{\text{sat}}$	$2.05^{+0.49}_{-0.45}$	$2.11^{+0.49}_{-0.52}$	$2.10^{+0.45}_{-0.49}$	$2.13^{+0.46}_{-0.54}$	$2.23^{+0.32}_{-0.50}$	$2.28^{+0.35}_{-0.55}$
$1.5n_{\text{sat}}$	$6.06^{+1.85}_{-2.04}$	$6.25^{+1.90}_{-2.26}$	$6.23^{+1.68}_{-2.16}$	$6.34^{+1.83}_{-2.30}$	$6.76^{+1.15}_{-2.13}$	$6.93^{+1.39}_{-2.17}$
$2.0n_{\text{sat}}$	$19.47^{+33.63}_{-11.67}$	$19.07^{+15.27}_{-10.53}$	$19.62^{+33.36}_{-10.81}$	$19.20^{+15.42}_{-9.21}$	$21.41^{+30.60}_{-9.02}$	$20.59^{+16.10}_{-8.36}$
$2.5n_{\text{sat}}$	$47.78^{+75.96}_{-32.96}$	$45.43^{+40.41}_{-19.11}$	$47.61^{+79.33}_{-32.61}$	$45.62^{+40.81}_{-18.61}$	$54.71^{+66.27}_{-36.26}$	$48.60^{+39.47}_{-19.32}$
$1.0M_{\odot}$	$11.89^{+0.79}_{-0.98}$	$11.88^{+0.57}_{-0.76}$	$11.92^{+0.78}_{-0.95}$	$11.91^{+0.61}_{-0.73}$	$12.09^{+0.59}_{-0.63}$	$12.06^{+0.48}_{-0.56}$
$1.4M_{\odot}$	$12.06^{+1.13}_{-1.18}$	$12.01^{+0.78}_{-0.77}$	$12.09^{+1.12}_{-1.14}$	$12.02^{+0.78}_{-0.76}$	$12.26^{+0.96}_{-0.84}$	$12.17^{+0.73}_{-0.60}$
$1.6M_{\odot}$	$12.11^{+1.33}_{-1.33}$	$12.03^{+0.98}_{-0.75}$	$12.13^{+1.31}_{-1.30}$	$12.05^{+0.91}_{-0.79}$	$12.33^{+1.14}_{-1.05}$	$12.19^{+0.81}_{-0.76}$
$2.0M_{\odot}$	$12.19^{+1.71}_{-1.59}$	$11.91^{+1.24}_{-1.11}$	$12.20^{+1.68}_{-1.60}$	$11.91^{+1.25}_{-1.11}$	$12.42^{+1.44}_{-1.48}$	$12.06^{+1.14}_{-1.20}$

Table 9.5: **Impact of the sensitivity curve for the ASY-EOS experiment.** Comparison of the 95% credible interval for the pressure [MeV fm<sup>-3</sup>] and radius [km] of neutron stars when including only HIC experiments and for combined HIC and astrophysics results for different sensitivity curves. In particular, we compare our standard results using the neutron over charged particles (n/ch) sensitivity curve [315] with the neutron over proton (n/p) sensitivity from Russotto et al. [315], which peaks at  $1.5n_{\text{sat}}$ . We find that our results are robust and differences for both sensitivity curves are small. Additionally, we compare the results to calculations where the ASY-EOS data is implemented using a uniform prior in density between 1- $2n_{\text{sat}}$  (labelled Window). For the latter choice, we generally find larger pressures and larger neutron-star radii because the n/ch and n/p sensitivity curves decrease rapidly after their maxima at 1 and  $1.5n_{\text{sat}}$ , lowering the impact of the ASY-EOS constraint at higher densities. However, differences for radii and pressures remain small once Astro+HIC data is included.

$P/R$	SNM form used here		Taylor expansion	
	HIC only	Astro+HIC	HIC only	Astro+HIC
$1.0n_{\text{sat}}$	$2.05^{+0.49}_{-0.45}$	$2.11^{+0.49}_{-0.52}$	$1.95^{+0.52}_{-0.44}$	$2.01^{+0.51}_{-0.47}$
$1.5n_{\text{sat}}$	$6.06^{+1.85}_{-2.04}$	$6.25^{+1.90}_{-2.26}$	$5.61^{+2.04}_{-2.00}$	$5.87^{+1.99}_{-2.14}$
$2.0n_{\text{sat}}$	$19.47^{+33.63}_{-11.67}$	$19.07^{+15.27}_{-10.53}$	$18.80^{+32.63}_{-12.89}$	$18.72^{+16.57}_{-9.34}$
$2.5n_{\text{sat}}$	$47.78^{+75.96}_{-32.96}$	$45.43^{+40.41}_{-19.11}$	$47.58^{+77.40}_{-31.93}$	$45.66^{+41.66}_{-19.19}$
$1.0M_{\odot}$	$11.89^{+0.79}_{-0.98}$	$11.88^{+0.57}_{-0.76}$	$11.77^{+0.84}_{-0.97}$	$11.79^{+0.60}_{-0.71}$
$1.4M_{\odot}$	$12.06^{+1.13}_{-1.18}$	$12.01^{+0.78}_{-0.77}$	$11.98^{+1.16}_{-1.18}$	$11.97^{+0.77}_{-0.74}$
$1.6M_{\odot}$	$12.11^{+1.33}_{-1.33}$	$12.03^{+0.98}_{-0.75}$	$12.05^{+1.32}_{-1.37}$	$12.00^{+0.90}_{-0.78}$
$2.0M_{\odot}$	$12.19^{+1.71}_{-1.59}$	$11.91^{+1.24}_{-1.11}$	$12.13^{+1.73}_{-1.61}$	$11.92^{+1.23}_{-1.10}$

Table 9.6: **Impact of the parameterisation for symmetric nuclear matter.** Comparison of the 95% credible interval for the pressure [ $\text{MeV fm}^{-3}$ ] and radius [km] of neutron stars when including only HIC experiments and for combined HIC and astrophysics results for two parameterisations of symmetric nuclear matter. In particular, we compare the functional form from FOPI used in this chapter, see Eq. (9.4), with a general Taylor expansion for symmetric nuclear matter with the same values for the saturation point and the incompressibility but including the third-order parameter  $Q = -150 \pm 250 \text{ MeV}$  at  $1\sigma$  using a Gaussian distribution. We find that our results are robust with respect to a variation of this parameterisation and the impact of this choice is at the 5% level for pressures and 1% level for radii.

$P/R$	$x_{\text{ASY-EOS}}$		$0 \leq x \leq 0.1$	
	HIC only	Astro+HIC	HIC only	Astro+HIC
$1.0n_{\text{sat}}$	$2.05^{+0.49}_{-0.45}$	$2.11^{+0.49}_{-0.52}$	$2.05^{+0.50}_{-0.45}$	$2.10^{+0.48}_{-0.52}$
$1.5n_{\text{sat}}$	$6.06^{+1.85}_{-2.04}$	$6.25^{+1.90}_{-2.26}$	$6.02^{+1.89}_{-2.04}$	$6.23^{+1.81}_{-2.31}$
$2.0n_{\text{sat}}$	$19.47^{+33.63}_{-11.67}$	$19.07^{+15.27}_{-10.53}$	$19.32^{+33.95}_{-11.05}$	$19.00^{+14.74}_{-10.54}$
$2.5n_{\text{sat}}$	$47.78^{+75.96}_{-32.96}$	$45.43^{+40.41}_{-19.11}$	$48.00^{+78.57}_{-34.40}$	$45.48^{+39.96}_{-19.28}$
$1.0M_{\odot}$	$11.89^{+0.79}_{-0.98}$	$11.88^{+0.57}_{-0.76}$	$11.88^{+0.79}_{-0.98}$	$11.87^{+0.59}_{-0.75}$
$1.4M_{\odot}$	$12.06^{+1.13}_{-1.18}$	$12.01^{+0.78}_{-0.77}$	$12.05^{+1.14}_{-1.17}$	$12.00^{+0.77}_{-0.77}$
$1.6M_{\odot}$	$12.11^{+1.33}_{-1.33}$	$12.03^{+0.98}_{-0.75}$	$12.10^{+1.31}_{-1.36}$	$12.03^{+0.91}_{-0.79}$
$2.0M_{\odot}$	$12.19^{+1.71}_{-1.59}$	$11.91^{+1.24}_{-1.11}$	$12.18^{+1.70}_{-1.61}$	$11.90^{+1.22}_{-1.14}$

Table 9.7: **Impact of the proton fraction in  $\beta$ -equilibrium.** Comparison of the 95% credible interval for the pressure [ $\text{MeV fm}^{-3}$ ] and radius [km] of neutron stars when including only HIC experiments and for combined HIC and astrophysics results for two choices for the proton fraction in  $\beta$ -equilibrium. For the main results, we compute the proton fraction for the HIC constraints using the EOS functional introduced by the ASY-EOS analysis ( $x_{\text{ASY-EOS}}$ ). We compare this with a more conservative choice that constrains the proton fraction to be within the range  $0 \leq x \leq 0.1$  but find only small changes.

$P/R$	HIC only	Using Refs. [65, 66]		Using Ref. [62]	
		Astro only	Astro+HIC	Astro only	Astro+HIC
$1.0n_{\text{sat}}$	$2.05^{+0.49}_{-0.45}$	$2.00^{+0.52}_{-0.49}$	$2.11^{+0.49}_{-0.52}$	$1.95^{+0.55}_{-0.45}$	$2.08^{+0.49}_{-0.53}$
$1.5n_{\text{sat}}$	$6.06^{+1.85}_{-2.04}$	$5.84^{+1.96}_{-2.26}$	$6.25^{+1.90}_{-2.26}$	$5.63^{+2.16}_{-2.05}$	$6.14^{+1.93}_{-2.28}$
$2.0n_{\text{sat}}$	$19.47^{+33.63}_{-11.67}$	$18.44^{+16.24}_{-9.69}$	$19.07^{+15.27}_{-10.53}$	$17.46^{+15.66}_{-9.27}$	$18.32^{+14.87}_{-9.60}$
$2.5n_{\text{sat}}$	$47.78^{+75.96}_{-32.96}$	$45.05^{+39.80}_{-19.62}$	$45.43^{+40.41}_{-19.11}$	$42.23^{+41.75}_{-20.47}$	$43.22^{+42.66}_{-19.18}$
$1.0M_{\odot}$	$11.89^{+0.79}_{-0.98}$	$11.76^{+0.65}_{-0.71}$	$11.88^{+0.57}_{-0.76}$	$11.68^{+0.71}_{-0.74}$	$11.82^{+0.68}_{-0.78}$
$1.4M_{\odot}$	$12.06^{+1.13}_{-1.18}$	$11.94^{+0.79}_{-0.78}$	$12.01^{+0.78}_{-0.77}$	$11.83^{+0.86}_{-0.86}$	$11.94^{+0.87}_{-0.83}$
$1.6M_{\odot}$	$12.11^{+1.33}_{-1.33}$	$11.98^{+0.93}_{-0.79}$	$12.03^{+0.98}_{-0.75}$	$11.87^{+1.01}_{-0.93}$	$11.95^{+1.01}_{-0.91}$
$2.0M_{\odot}$	$12.19^{+1.71}_{-1.59}$	$11.88^{+1.23}_{-1.10}$	$11.91^{+1.24}_{-1.11}$	$11.74^{+1.44}_{-1.25}$	$11.77^{+1.42}_{-1.23}$

Table 9.8: **Impact of the radius constraints for J0740+6220.** Comparison of the 95% credible interval for the pressure [ $\text{MeV fm}^{-3}$ ] and radius [km] of neutron stars when including only HIC results, only astrophysical observations, and for combined HIC and astrophysics results when we include the combined mass-radius measurement from NICER [65, 66] or only the radio mass measurement from Ref. [62]. The radius of J0740+6220 estimated by NICER is preferring a stiffer EOS, which agrees well with the constraint from HIC experiments.



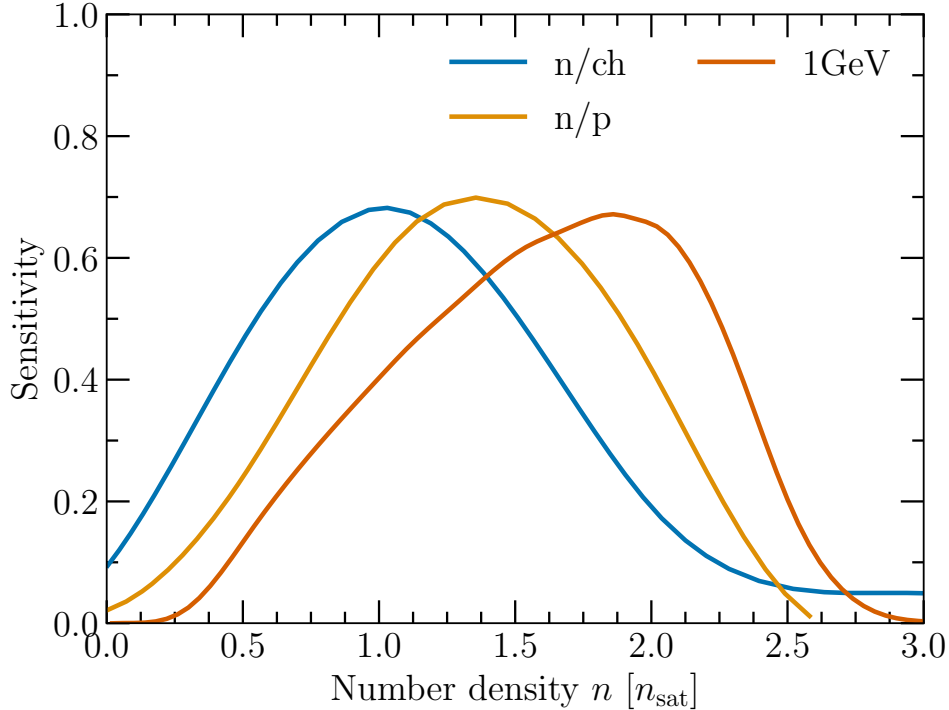


Figure 9.5: **Comparison between different sensitivity curves.** We show three sensitivity-to-density curves for different observables and incident energies. In particular, the neutron-over-charged-particle (n/ch, used here) and the neutron-over-proton (n/p) sensitivity curves for 400 MeV/nucleon incident energy from Russotto et al. [315] are compared with the density curve reported by Le Fèvre et al. [314] for the sensitivity of the elliptic flow of protons in Au+Au collisions at 1 GeV/nucleon.

new phase of QCD matter in the core of neutron stars. For this, we calculate the Bayes factor in favor of the presence of such a phase transition against its absence, and find it to be  $0.419 \pm 0.012 < 1$ . Therefore, its presence is slightly disfavoured given current astrophysical and experimental data.

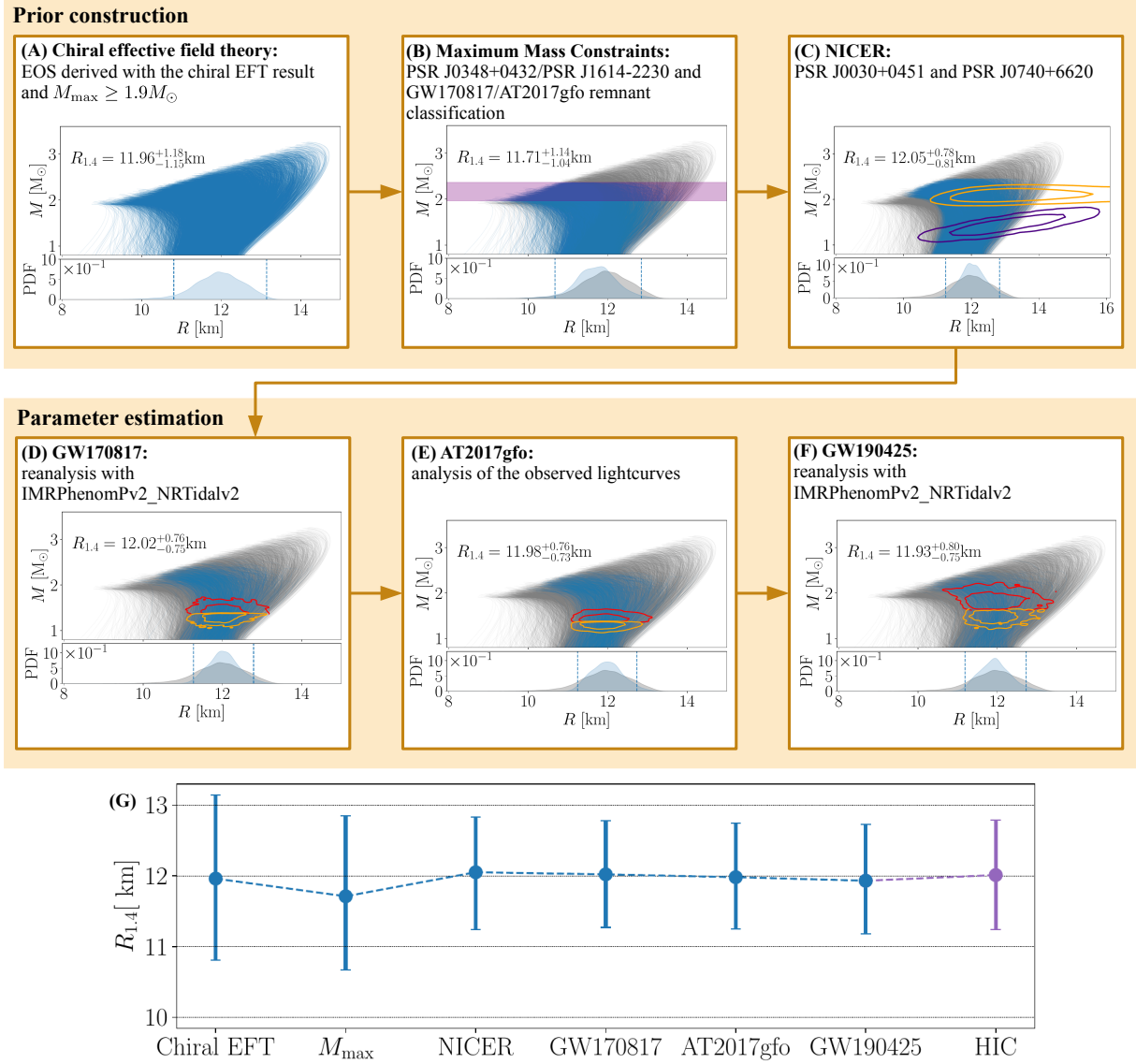
## 9.4 Conclusion

To summarize, the interdisciplinary analysis of EOS constraints from HIC experiments and multi-messenger astrophysics shows remarkable agreement between the two, and provides important information to constrain the nuclear EOS at supra-saturation densities. Going forward, it is important that both statistic and systematic sources of uncertainty for HIC experiments are further improved. For example, the impact of choosing different Quantum Molecular Dynamics (QMD) models when analyzing HIC experiments needs to be further investigated (see Fig. 9.3, 9.5), and advancing HIC experiments to probe higher densities, above  $2-3n_{\text{sat}}$ , will be key (see Tab. 9.11). Combining the latter with a reduction of experimental uncertainties, data from HICs has great potential to provide complimentary EOS information, bridging nuclear theory and astrophysical observations. In the next few years, the ASY-EOS-II and Compressed Baryonic Matter (CBM) Experiments at the upcoming Facility for Antiproton and Ion Research (FAIR) at GSI will provide a unique

$P/R$	With Danielewicz et al. [313]		Without Danielewicz et al. [313]	
	HIC only	Astro+HIC	HIC only	Astro+HIC
$1.0n_{\text{sat}}$	$2.05^{+0.49}_{-0.45}$	$2.11^{+0.49}_{-0.52}$	$2.06^{+0.49}_{-0.45}$	$2.11^{+0.48}_{-0.52}$
$1.5n_{\text{sat}}$	$6.06^{+1.85}_{-2.04}$	$6.25^{+1.90}_{-2.26}$	$6.08^{+1.83}_{-2.04}$	$6.25^{+1.89}_{-2.23}$
$2.0n_{\text{sat}}$	$19.47^{+33.63}_{-11.67}$	$19.07^{+15.27}_{-10.53}$	$19.35^{+33.66}_{-10.71}$	$19.05^{+15.33}_{-10.27}$
$2.5n_{\text{sat}}$	$47.78^{+75.96}_{-32.96}$	$45.43^{+40.41}_{-19.11}$	$47.59^{+79.68}_{-27.46}$	$45.57^{+40.87}_{-18.89}$
$1.0M_{\odot}$	$11.89^{+0.79}_{-0.98}$	$11.88^{+0.57}_{-0.76}$	$11.89^{+0.79}_{-0.98}$	$11.88^{+0.56}_{-0.78}$
$1.4M_{\odot}$	$12.06^{+1.13}_{-1.18}$	$12.01^{+0.78}_{-0.77}$	$12.06^{+1.12}_{-1.19}$	$12.01^{+0.78}_{-0.77}$
$1.6M_{\odot}$	$12.11^{+1.33}_{-1.33}$	$12.03^{+0.98}_{-0.75}$	$12.11^{+1.32}_{-1.34}$	$12.03^{+0.92}_{-0.80}$
$2.0M_{\odot}$	$12.19^{+1.71}_{-1.59}$	$11.91^{+1.24}_{-1.11}$	$12.18^{+1.70}_{-1.61}$	$11.91^{+1.17}_{-1.15}$

Table 9.9: **Impact of excluding Danielewicz et al. [313]**. Comparison of the 95% credible interval for the pressure [ $\text{MeV fm}^{-3}$ ] and radius [km] of neutron stars when including only HIC experiments and for combined HIC and astrophysics results with and without the inclusion of the constraint from Danielewicz et al. [313]. By comparing the HIC-only results, we conclude that the constraint from Danielewicz et al. [313] has a small impact on our study.

opportunity to study nuclear matter at densities probed in the core of neutron stars and their mergers, and might detect new phases of QCD matter, possibly involving hyperons and, ultimately, the transition to a deconfined quark matter phase at the highest densities (see, e.g., Orsaria et al. [344], Brandes et al. [345]). Together with experiments at the Rare Isotope Beam Facility (RIBF) at RIKEN in Japan and the Nuclotron-based Ion Collider fAcility (NICA) in Russia, the robust combination of experimental HIC constraints and astrophysical observations has the potential to revolutionise our understanding of the EOS.



$D_{\text{KL}}$	Astro only	HIC only	Astro+HIC
$1.0n_{\text{sat}}$	0.079	0.109	0.270
$1.5n_{\text{sat}}$	0.075	0.108	0.266
$2.0n_{\text{sat}}$	0.112	0.019	0.174
$2.5n_{\text{sat}}$	0.244	0.006	0.274
$1.0M_{\odot}$	0.090	0.054	0.128
$1.4M_{\odot}$	0.185	0.022	0.210
$1.6M_{\odot}$	0.225	0.015	0.251
$2.0M_{\odot}$	0.228	0.008	0.222

Table 9.10: **Kullback–Leibler divergence with different observation input.** Comparison of the Kullback–Leibler divergence (KL divergence)  $D_{\text{KL}}(\text{posterior}|\text{prior})$  of pressure and radius of a neutron star with respect to the prior in bits when including only astrophysical constraints, only HIC experimental data, and for the combination of both. The KL divergence quantifies the additional information encoded in the posterior distribution with respect to the prior distribution. A KL divergence of zero indicates that the two distributions are identical. For reference, the KL divergence  $D_{\text{KL}}(\mathcal{N}(0, 1/4)|\mathcal{N}(0, 1)) \approx 1.2\text{bits}$ , where  $\mathcal{N}(\mu, \sigma^2)$  is a normal distribution with mean  $\mu$  and variance  $\sigma^2$ . The KL divergence for the pressure at  $1.0n_{\text{sat}}$  and  $1.5n_{\text{sat}}$ , using only HIC experimental input, is higher than that of the result using only astrophysical observations. Therefore, the HIC experiment has higher impact than astrophysical observations for pressures below  $1.5n_{\text{sat}}$ .

$P/R$	Current setup				1 GeV sensitivity		1 GeV sensitivity and halved uncertainty on HIC		1 GeV sensitivity with a $1n_{\text{sat}}$ lower cutoff		
	HIC only	Astro	Astro+HIC	HIC only	Astro+HIC	HIC only	Astro+HIC	HIC only	Astro+HIC	HIC only	Astro+HIC
$1.0n_{\text{sat}}$	$2.05^{+0.49}_{-0.45}$	$2.00^{+0.52}_{-0.49}$	$2.11^{+0.49}_{-0.52}$	$2.10^{+0.49}_{-0.45}$	$2.13^{+0.47}_{-0.53}$	$2.12^{+0.43}_{-0.48}$	$2.16^{+0.43}_{-0.55}$	$2.07^{+0.48}_{-0.45}$	$2.12^{+0.47}_{-0.53}$	$2.07^{+0.48}_{-0.45}$	$2.12^{+0.47}_{-0.53}$
$1.5n_{\text{sat}}$	$6.06^{+1.85}_{-2.04}$	$5.84^{+1.96}_{-2.26}$	$6.25^{+1.90}_{-2.26}$	$6.20^{+1.71}_{-2.13}$	$6.35^{+1.80}_{-2.31}$	$5.84^{+1.96}_{-2.26}$	$6.44^{+1.77}_{-2.21}$	$6.11^{+1.80}_{-2.02}$	$6.33^{+1.82}_{-2.33}$	$6.11^{+1.80}_{-2.02}$	$6.33^{+1.82}_{-2.33}$
$2.0n_{\text{sat}}$	$19.47^{+33.63}_{-11.67}$	$18.44^{+16.24}_{-9.69}$	$19.07^{+15.27}_{-10.53}$	$19.42^{+28.90}_{-11.69}$	$19.14^{+14.24}_{-8.97}$	$19.73^{+29.32}_{-11.49}$	$19.32^{+13.93}_{-8.74}$	$18.66^{+22.18}_{-8.65}$	$18.52^{+11.08}_{-7.04}$	$18.66^{+22.18}_{-8.65}$	$18.52^{+11.08}_{-7.04}$
$2.5n_{\text{sat}}$	$47.78^{+75.96}_{-32.96}$	$45.05^{+39.80}_{-19.62}$	$45.43^{+40.41}_{-19.11}$	$47.13^{+75.65}_{-27.86}$	$45.3^{+40.52}_{-17.24}$	$48.20^{+78.30}_{-24.83}$	$45.73^{+38.03}_{-18.47}$	$44.31^{+60.85}_{-21.23}$	$43.30^{+31.65}_{-15.92}$	$44.31^{+60.85}_{-21.23}$	$43.30^{+31.65}_{-15.92}$
$1.0M_{\odot}$	$11.89^{+0.79}_{-0.98}$	$11.76^{+0.65}_{-0.71}$	$11.88^{+0.57}_{-0.76}$	$11.91^{+0.74}_{-0.93}$	$11.91^{+0.55}_{-0.76}$	$11.96^{+0.72}_{-0.85}$	$11.94^{+0.54}_{-0.71}$	$11.85^{+0.66}_{-0.78}$	$11.85^{+0.55}_{-0.70}$	$11.85^{+0.66}_{-0.78}$	$11.85^{+0.55}_{-0.70}$
$1.4M_{\odot}$	$12.06^{+1.13}_{-1.18}$	$11.94^{+0.79}_{-0.78}$	$12.01^{+0.78}_{-0.77}$	$12.08^{+1.09}_{-1.10}$	$12.02^{+0.76}_{-0.73}$	$12.11^{+1.07}_{-1.01}$	$12.04^{+0.72}_{-0.71}$	$11.97^{+0.95}_{-0.85}$	$11.96^{+0.66}_{-0.67}$	$11.97^{+0.95}_{-0.85}$	$11.96^{+0.66}_{-0.67}$
$1.6M_{\odot}$	$12.11^{+1.33}_{-1.33}$	$11.98^{+0.93}_{-0.79}$	$12.03^{+0.98}_{-0.75}$	$12.12^{+1.30}_{-1.24}$	$12.04^{+0.88}_{-0.75}$	$12.15^{+1.26}_{-1.16}$	$12.06^{+0.85}_{-0.74}$	$11.99^{+1.14}_{-0.95}$	$11.96^{+0.79}_{-0.66}$	$11.99^{+1.14}_{-0.95}$	$11.96^{+0.79}_{-0.66}$
$2.0M_{\odot}$	$12.19^{+1.71}_{-1.59}$	$11.88^{+1.23}_{-1.10}$	$11.91^{+1.24}_{-1.11}$	$12.17^{+1.71}_{-1.51}$	$11.90^{+1.21}_{-1.10}$	$12.18^{+1.66}_{-1.46}$	$11.92^{+1.19}_{-1.07}$	$11.93^{+1.61}_{-1.32}$	$11.79^{+1.08}_{-0.95}$	$11.93^{+1.61}_{-1.32}$	$11.79^{+1.08}_{-0.95}$

Table 9.11: **Future prospects for the ASY-EOS experiment.** Comparison of the 95% credible interval for the pressure [ $\text{MeV fm}^{-3}$ ] and the radius [km] of a neutron star when including only HIC experiments and for combined HIC and astrophysics results for different future improvements. In particular, we show the results with the 1 GeV sensitivity curve (see Fig. 9.5) applied to the current measurement (*second column*), when additionally halving the uncertainty on  $\gamma_{\text{asy}}$  (*third column*), and when using a lower cutoff density of  $1n_{\text{sat}}$  instead of  $0.5n_{\text{sat}}$  (*fourth column*). For all the exploratory setups, HIC data is showing a stronger impact on the EOS constraint than the current setup. The result with a density cutoff is showing a significant decrease in uncertainty compared to the result of this chapter. Therefore, to achieve a stronger constraint on the EOS, improvements to the low-density part of the HIC constraint will be most important.

Figure 9.6: **Constraint on the neutron-star mass and radius with successive astrophysics information.** In each panel (except for panel A), EOSs within (outside of) 95% credible interval are shown as blue (gray) lines. Lower panels indicate the probability distribution function (PDF) for the radius of a  $1.4M_{\odot}$  neutron star, with the 95% credible range indicated by dashed lines, in panels (B)-(F) the prior from panel (A) is shown in grey. (A) The EOS prior set constrained by chiral EFT calculations up to  $1.5n_{\text{sat}}$  and  $M_{\text{max}} \geq 1.9M_{\odot}$ . (B) The EOS set restricted by incorporating information from mass measurements of PSR J0348+0432, PSR J1614-2230, and the maximum-mass constraints obtained from GW170817/AT2017gfo. The 95% credible interval of the maximum mass posterior probability distribution is shown by the purple band. (C) The EOS set further restricted by the NICER mass-radius measurement of PSR J0030+0451 (purple contours at 68% and 95% credence) and PSR J0740+6620 (orange contours at 68% and 95% credence). Note that the latter shows the average of the results obtained by Miller et al. [65] and Riley et al. [66] (D) Further restrictions on the EOS set from a reanalysis of the GW170817 using Bayesian inference. Contours at 68% and 95% credence show the mass-radius measurements of the primary (red) and secondary (orange) neutron stars. (E) We use the chirp mass, mass ratio, and the EOSs as Bayesian prior for our analysis of AT2017gfo. (F) Further restrictions by analysing GW190425. Again, contours at 68% and 95% credence show the mass-radius measurements of the primary (red) and secondary (orange) neutron stars. (G) The radius constraint at each step of this analysis with 95% credible ranges. The radius constraint after including HIC experimental data is also shown.

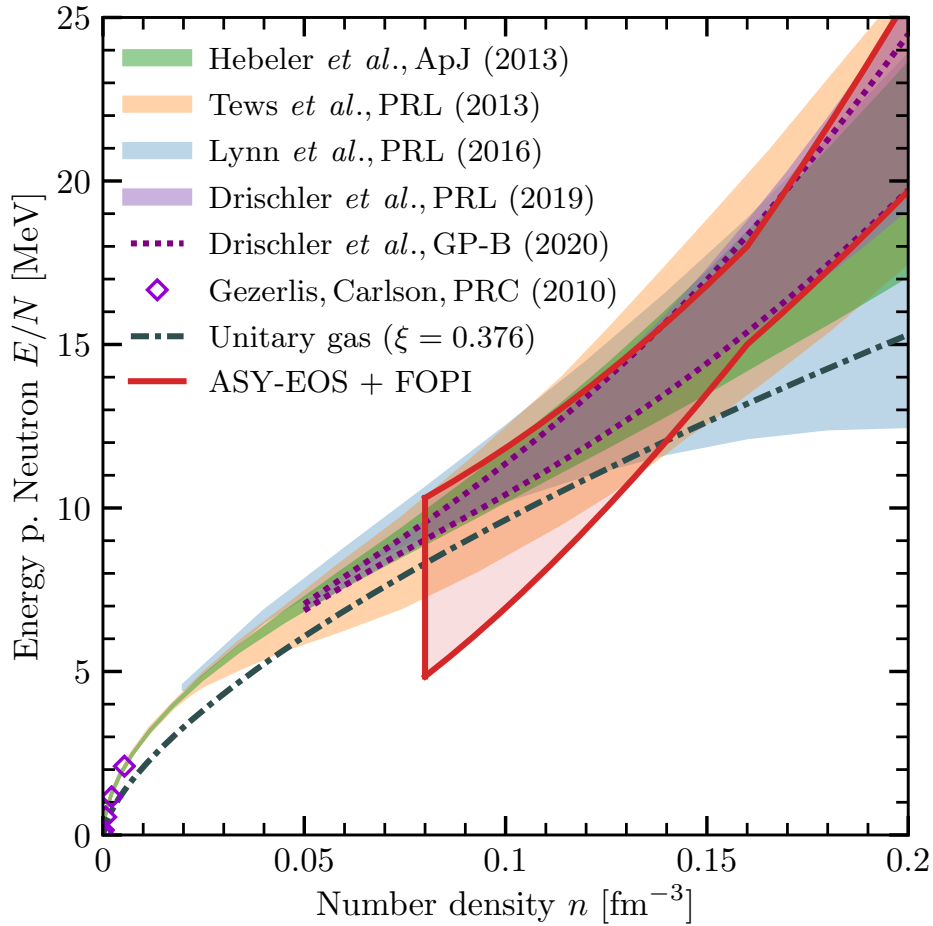


Figure 9.7: **Constraints for pure neutron matter.** Energy per particle  $E/N$  of neutron matter as a function of density  $n$  for various many-body calculations using chiral EFT interactions from Hebeler *et al.* [177], Tews *et al.* [294], Lynn *et al.* (used here) [109], Drischler *et al.* PRL [181] and GP-B [311], and low-density quantum Monte Carlo results from Gezerlis and Carlson [346]. Overall, the results from these calculations are in good agreement with each other. We also show the energy per particle of a unitary Fermi gas of neutrons, which has been proposed as a lower bound for the energy of neutron matter [347]. Finally, we compare the theoretical results with the constraint from the ASY-EOS and FOPI experiments (red), which is used as a constraint for neutron matter in the main work.





---

---

## PART III

---

# ASTROPHYSICAL IMPLICATION OF AN ACCURATE CONSTRAINT ON THE EQUATION-OF-STATE

In previous chapters, we have shown how one can arrive a robust constraint on nuclear matter equation of state via gravitational waves or multi-messenger analysis. We also demonstrated the how the constraint can answer nuclear physical questions e.g., the presence of a phase transition. In addition, an accurate constraint on the equation of state has an consequential impact on astrophysics. In Chapter 10, we will introduce a technique for identifying a gravitationally lensed binary neutron star signal with the aid of equation-of-state's information. The work is published as Ref. [40]

---

# CHAPTER 10

## LENSED OR NOT LENSED: DETERMINING LENSING MAGNIFICATIONS FOR BINARY NEUTRON STAR MERGERS FROM A SINGLE DETECTION

### 10.1 Introduction

When gravitational waves (GWs) travel near a galaxy or a galaxy cluster, their trajectories are curved, resulting in strong gravitational lensing [348–355]. The lensing magnifies the amplitude of the waves without changing their frequency evolution [356, 357]. In the case of strong lensing by galaxies, it is possible to produce multiple “images”, which would arrive to us with relative time-delays between minutes and weeks<sup>1</sup> [360, 361]. Based on predictions on the number of expected GW sources, and the distribution of lenses in the Universe, Refs. [362–364] suggest that lensed gravitational-waves may be detected in the coming years, as the LIGO/Virgo detectors reach their design sensitivities.<sup>2</sup> The number of detectable events could reach hundreds in the Einstein Telescope [365, 366]. Lensed GWs present several potential applications in fundamental physics, astrophysics, and cosmology [360, 367–373].

A number of possibilities to identify a lensed GW signal have been proposed. One can look for signatures of multiple images or microlensing within GW data [361, 367, 374–378]. Alternatively, one could search for a population of apparently high-mass binary events produced by lensing magnification [357, 364, 379]. The first combined search for all these signatures was performed recently on the O1/O2 data [380].

Here we focus on the problem of reliably identifying lensed binary neutron star signals. The overall magnification caused by lensing is degenerate with the luminosity distance measured from the GW signal and so a lensed system will appear to be closer than it truly is [357, 362, 364, 379, 381]. As the distance to the binary is biased, the estimation of the redshift to the binary will be as well. A redshifted gravitational-wave signal will appear to an observer to have higher masses than in reality.

The recent high-mass BNS detection, GW190425 [49], is therefore of particular interest. The mass of the system is higher than expected from the known galactic double neutron star population [382, 383]. Could this signal be a lensed system consistent with the known population? Unfortunately, to answer this question definitively, we would need a unique signature to discern an intrinsically high-mass binary event from a lensed event.

We note that the problem could, in principle, be resolved by lens statistics: the lensed hypothesis is disfavored *a priori*, as the rate of lensed BNSs is low within LIGO/Virgo [364, 384]. However, the prior probability of the other hypothesis (a new population of BNSs) is largely unknown, as the masses are inconsistent with the observed double neutron

---

<sup>1</sup>Let us note gravitational lensing by galaxy clusters could produce time-delays as large as months to years [358, 359]. However, we do not consider this scenario here.

<sup>2</sup>Specifically, Refs. [362–364] arrive at  $\sim 0.1 - 10 \text{ yr}^{-1}$  observable lensed events per year.

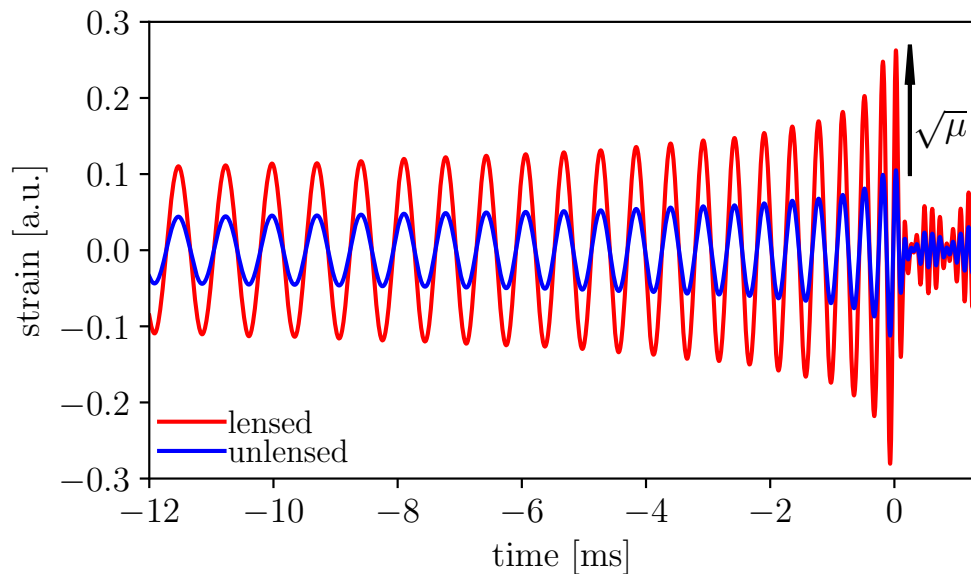


Figure 10.1: *Illustration of amplitude magnification:* GW strain of a lensed (red) and unlensed (blue) signal from an example binary neutron star system. The waveform shows the late inspiral and early postmerger phase and is adjusted from a numerical relativity simulation performed by the CoRe collaboration with the BAM code [385].

star population within the galaxy [382, 383]. Without a good grasp of the relative prior probabilities of the two hypotheses, a quantitative comparison is challenging.

In this chapter, we propose a robust method to rule out or confirm the lensing hypothesis for BNSs. While GW lensing biases the intrinsic mass measurement, it does not bias the tidal deformabilities as measured from the GW phasing. Therefore, a lensed binary would appear as a high-mass source with the tidal deformability of a lower-mass binary. We demonstrate, for the first time, that this can be used as a smoking-gun evidence of lensing, or as a way to rule out the hypothesis.

Besides eliminating magnification bias, detecting lensing will be important especially for BNS systems, considering that most strong lensing cosmography studies (such as measurements of the Hubble constant, accurate tests of the speed of gravity and polarization tests) require an electromagnetic counterpart [368–372].

The article is structured as follows. In Sec. 10.2, we describe how lensing will affect the gravitational wave signal observed from a BNS merger. Sec. 10.3 introduces the methodology to break the degeneracy between magnification and distance measurement via the tidal deformation of a BNS. Sec. 10.4 compares the recovery of magnification between the tidal measurement and assumed binary mass population from simulated signals. We then apply our methods to GW190425, finding no significant evidence to favor the lensed scenario (with a log Bayes factor  $\ln \mathcal{B}_U^L = -0.608_{-0.021}^{+0.046}$ ), and constraining the lensing magnification  $\mu \leq 86.5_{-11.2}^{+0.5}$ . Finally, we provide an outlook for future lensed gravitational-wave detections in Sec. 10.6.

## 10.2 Binary neutron star lensing

The GW signal of a non-eccentric BNS coalescence is completely described by its components' masses  $m_{1,2}$ , spins  $\vec{s}_{1,2}$  and the supranuclear equation of state(s) governing the internal physics of both neutron stars. There are a number of ways in which a signal emitted by a BNS system will differ from a BBH system with the same masses and spins, due to the presence of matter. These include the complex post-merger signal [190, 386–390], the deformation of the neutron stars due to tidal forces [171, 391], and the deformation of the neutron stars due to their own rotation [392–394]. Of these effects, the deformation of the neutron star due to tidal forces provides the best measurable constraint on the internal structure and equation of state [85, 202]. The tidal deformability determines the deformation of each neutron star in the gravitational field of the companion and is quantified by the parameter [170, 171]

$$\Lambda = \frac{2}{3}k_2 \left(\frac{R}{m}\right)^5, \quad (10.1)$$

where  $k_2$ ,  $m$ ,  $R$  are the 2<sup>nd</sup> Love number, the mass, and the radius of the individual neutron stars, respectively. The tidal deformability as a function of mass can be obtained by solving the TOV equation [171] with a given EOS. These parameters depend strongly on the equation of state.

When a gravitational wave signal is lensed by intervening galaxies or galaxy clusters, the lensing magnifies the signal, increasing its amplitude without changing the signal morphology; cf. Fig. 10.1. The effect is degenerate with the luminosity distance as measured from the gravitational-waves [362]

$$D^{\text{est}} = \frac{D}{\sqrt{\mu}}, \quad (10.2)$$

where  $D^{\text{est}}$  and  $D$  are the observed and true luminosity distances, respectively, and  $\mu$  is the magnification induced by gravitational lensing. The measured redshift  $z^{\text{est}} \equiv z(D^{\text{est}})$  is therefore also biased<sup>3</sup>. Redshift will cause a shift in the observed masses of the signal according to

$$m_i^{\text{est}} = \frac{m_i^{\text{det}}}{1 + z^{\text{est}}}, \quad (10.3)$$

where  $m_i^{\text{est}}$  and  $m_i^{\text{det}}$  is the estimated source mass and the observed detector-frame mass of each component, respectively. Therefore in the case of a lensed source not including the lensing magnification when characterizing the source will bias the inferred distance, redshift and mass of the system.

Since the gravitational-wave morphology is unchanged by lensing (Fig. 10.1), the parameters which we directly infer from the gravitational-wave phasing are unchanged [354].<sup>4</sup>

<sup>3</sup>The luminosity distance (either observed or intrinsic) is related to redshift under the assumption of standard  $\Lambda$ CDM cosmology [395].

<sup>4</sup>Let us note that Ref. [396] suggested that when the GW passes through a lensing saddle point, the signal morphology could exhibit a minor change. It was suggested that this could lead to a bias of 45 deg in the orbital line-of-sight, and possibly minor changes in the phasing for eccentric binaries and in the higher modes of merger/ringdown. We have neglected such potential effects as we consider only the inspiral part where the morphology is likely to be unchanged. However, they could be included by

That is, among others, the detector-frame masses  $m_{1,2}^{\text{det}}$  and the observed tidal deformabilities  $\Lambda_{1,2}$ , which are redshift independent [397], both remain unbiased. At leading order, the individual tidal deformabilities enter the GW phasing in a mass-weighted average  $\tilde{\Lambda}$ , as shown in Eq. (2.46), it is given by [84, 115, 170]

$$\tilde{\Lambda} = \frac{8}{13} \left( (1 + 7\eta - 31\eta^2)(\Lambda_1 + \Lambda_2) + \sqrt{1 - 4\eta}(1 + 9\eta - 11\eta^2)(\Lambda_1 - \Lambda_2) \right), \quad (10.4)$$

where  $\eta \equiv m_1 m_2 / (m_1 + m_2)^2$  is the symmetric mass ratio. Because the tidal effects can be *estimated* from the masses, we will obtain two independent measurements of the tidal effects. First, the unbiased measurement of  $\Lambda_i$  directly from the waveform phasing. Secondly, the *estimated*  $\Lambda_i^{\text{est}} = \Lambda(m_i)$ , from the estimate of the masses, combined with Eq. (10.1).

By making use of the above definitions, the hypothesis that the source is lensed corresponds to

$$\begin{aligned} \mathcal{H}_L : D &= \sqrt{\mu} D^{\text{est}}, \\ z &= z(\sqrt{\mu} D^{\text{est}}), \\ m_i &= \frac{m_i^{\text{det}}}{1+z} = m_i^{\text{est}} \frac{1+z^{\text{est}}}{1+z}, \\ \Lambda_i^{\text{est}} &= \Lambda(m_i) = \Lambda \left( m_i^{\text{est}} \frac{1+z^{\text{est}}}{1+z} \right), \end{aligned} \quad (10.5)$$

and, similarly, the hypothesis that the source is unlensed can be taken to be

$$\begin{aligned} \mathcal{H}_U : m_i &= m_i^{\text{est}}, \\ D &= D^{\text{est}}, \\ \Lambda_i^{\text{est}} &= \Lambda(m_i) = \Lambda(m_i^{\text{est}}), \end{aligned} \quad (10.6)$$

where  $z(D)$  is the redshift as a function luminosity distance  $D$  with a cosmological model given. That is, in the lensed hypothesis, the estimated masses and distances will be biased by the magnification, whereas in the unlensed one, they are their intrinsic (source-frame) quantities. We assume a high-magnification prior  $p(\mu) \propto \mu^{-3}$  for  $\mu \in [2, 6000]$ , which is generally a power-law near caustics [398].

Consequently, the effect of the lensing magnification is to increase the observed source-frame masses, while the measured tidal deformability remains unchanged. This is illustrated in Figure 10.2, where we simulate a BNS source with a luminosity distance of  $D^{\text{est}} = 100\text{Mpc}$  and source-frame masses  $(1.35, 1.35)M_\odot$ , with and without lensing magnification.

### 10.3 Breaking the lensing degeneracy

The tidal deformability of a BNS can be obtained in three ways: directly from the gravitational-wave phasing measurement, e.g. [6, 20, 170], from the observation of electro-

---

convolving the waveform with the complex magnification in a future study.

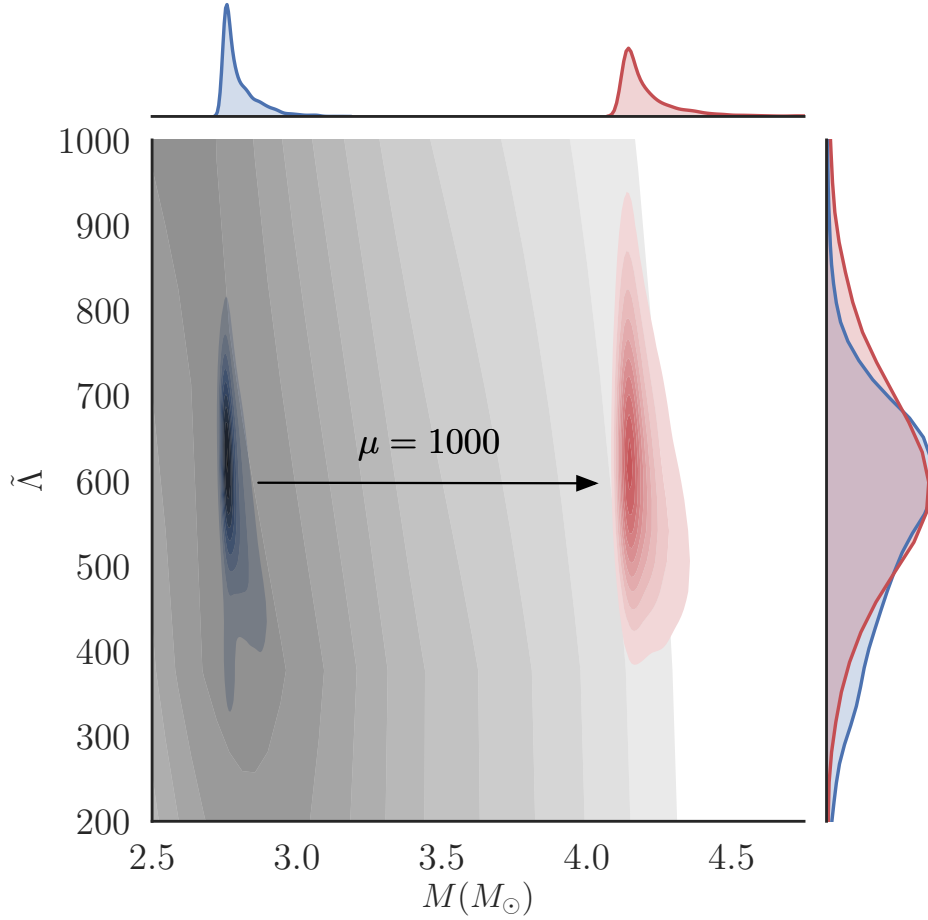


Figure 10.2: *Effect of lensing on inferred parameters:* Corner plot of the posterior distribution of the estimated source total mass  $M$  and the tidal deformability  $\tilde{\Lambda}$  of the same binary neutron star merger with (*red*) and without (*blue*) magnification. The plot demonstrates the effect of lensing on a binary neutron star merger signal. It biases the estimated source mass to larger values without affecting the observed tidal deformability. The expected distribution of  $\tilde{\Lambda}$ - $M$  with the ENG EOS [399] is also shown (*grey*), the increase of the estimated source mass due to lensing creates tension between the expected and measured values of  $\tilde{\Lambda}$ - $M$ .

magnetic counterparts [24–28, 31], or from the measured masses  $m_{1,2}$  under the assumption of a given (known) EOS.

Unfortunately, despite recent advances, the exact equation of state (EOS) governing the interior of neutron stars, i.e., cold matter at supranuclear densities, is still unknown. Information about the neutron star EOS can be obtained from nuclear physics computation, e.g., [30, 33], from the observation of radio pulsars, e.g., [135], or from the multi-messenger observation of compact binary mergers, e.g., [23]. Considering the latter, analysis of the GW signal GW170817 [9] disfavored a number of theoretically allowed EOSs, which predict large tidal deformabilities and consequently large neutron star radii. Meanwhile, the electromagnetic observation of AT2017gfo and sGRB170817 [12, 51–53, 56–58, 241–244, 400–403] disfavored EOSs with too small tidal deformabilities, i.e., too soft EOSs [23]. In the future, with a growing number of multi-messenger detections of BNS mergers, and additional experiments, e.g. NICER [404], constraints on the allowed range of EOSs will greatly improve.

Given an EOS, the posterior distribution of tidal deformabilities as estimated from the (observed) binary component masses under the *unlensed* hypothesis is

$$p(\Lambda_i^{\text{est}}|d, \text{EOS}, \mathcal{H}_U) = \int dm_i^{\text{det}} dz^{\text{est}} \delta\left(\Lambda_i^{\text{est}} - \Lambda\left(\frac{m_i^{\text{det}}}{1+z^{\text{est}}}\right)\right) p(m_i^{\text{det}}, z^{\text{est}}|d, \mathcal{H}_U), \quad (10.7)$$

where

$$p(m_i^{\text{det}}, z^{\text{est}}|d, \mathcal{H}_U) = \int dD^{\text{est}} \delta(z^{\text{est}} - z(D^{\text{est}})) p(m_i^{\text{det}}, D^{\text{est}}|d, \mathcal{H}_U). \quad (10.8)$$

The joint posterior  $p(m_i^{\text{det}}, D^{\text{est}}|d, \mathcal{H}_U)$  is the posterior inferred by `LALInference`. If the event is lensed, the lensing biases the tidal deformability under the unlensed hypothesis  $p(\Lambda_i^{\text{est}}|d, \text{EOS}, \mathcal{H}_U)$ , as predicted from the EOS, towards smaller values (as described in Sec. 10.2).

When lensing at a given magnification is taken into account, the tidal deformability estimate becomes

$$p(\Lambda_i^{\text{est}}|d, \mu, \text{EOS}, \mathcal{H}_L) = \int dm_i^{\text{det}} dz \delta\left(\Lambda_i^{\text{est}} - \Lambda\left(\frac{m_i^{\text{det}}}{1+z}\right)\right) p(m_i^{\text{det}}, z|d, \mu, \mathcal{H}_L), \quad (10.9)$$

where

$$p(m_i^{\text{det}}, z|d, \mu, \mathcal{H}_L) = \int dD^{\text{est}} \delta(z - z(\sqrt{\mu}D^{\text{est}})) p(m_i^{\text{det}}, D^{\text{est}}|d, \mathcal{H}_L). \quad (10.10)$$

However, we also obtain an *independent* posterior measurement of the tidal deformability  $p(\Lambda^{\text{phase}}|d)$  directly from the gravitational-wave phasing, which is unbiased by lensing. By doing so, we can break the magnification-induced degeneracy by matching the two independent posterior measurements ( $p(\Lambda^{\text{phase}}|d)$  and  $p(\Lambda_i^{\text{est}}|d, \mu)$ ) together, and rule out or confirm lensing.



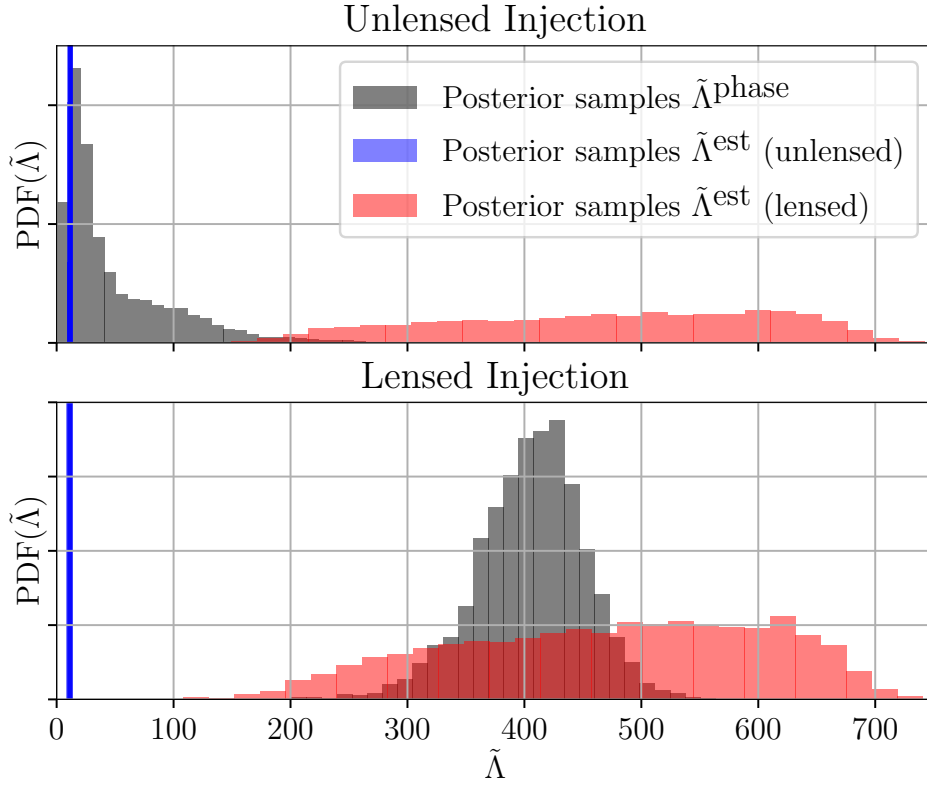


Figure 10.3: *Effect of lensing on the estimated tidal deformability:* The posterior distribution of the tidal deformability as estimated from the gravitational-wave phasing (gray), and the binary masses under the unlensed and lensed hypothesis (blue and red, respectively). In the unlensed case (top panel), the posterior measurement, as estimated from the gravitational-wave phasing, overlaps with the unlensed prediction (blue), favoring the unlensed hypothesis. Vice versa, in the lensed case (bottom panel), the posterior measurement (gray) overlaps with the lensed prediction (red), supporting the lensed hypothesis. The intrinsic binary masses  $m_1 = m_2 = 2.02 M_\odot$  ( $m_1 = m_2 = 1.35 M_\odot$ ) for the unlensed (lensed) case, while the estimated masses  $m_1^{\text{est}} = m_2^{\text{est}} = 2.02 M_\odot$  in both cases. In this illustration, we assume SFHo equation of state [175] and assume fixed magnification  $\mu = 1000$  to allow for a clear visual illustration. We show the case with variable magnification in Fig. 10.5.

EOS	Lensed ( $\mu = 1000$ )	Unlensed ( $\mu = 1$ )
SFHo	(1.35, 432.94)	(2.02, 11.84)
ENG	(1.35, 644.66)	(2.02, 24.25)

Table 10.1: Summary of the source-frame mass and the tidal deformability of the simulated binary neutron star mergers. Each cell shows the source-frame mass, tidal deformability pair  $(m, \Lambda)$  of the injection under different EOS and lensing scenario.

## 10.4 Discriminating between high-mass binaries and lensed binaries

Currently known binary neutron star systems, excluding GW observations, come from Galactic observations, which consists of relatively low-mass binaries where the total mass follows roughly a normal distribution with a  $2.69 M_{\odot}$  mean and  $0.12 M_{\odot}$  standard deviation [382]. If a high-mass BNS system was observed with GWs it could be considered that it is a lensed system consistent with the Galactic population. It would then appear as an intrinsically high-mass BNS with an apparently high tidal deformability. On the other hand, the system could belong to a new population of high-mass BNSs. If such a binary was observed, it would also appear as a high-mass BNS, but with an apparently low tidal deformability.

Let us therefore show a simple illustrative example how to distinguish between these two scenarios by use of tidal measurements. For this purpose, we simulate a gravitational-wave signal from a  $(m_1 = m_2 = 1.35 M_{\odot})$  *lensed BNS* at  $\mu = 1000$ , consistent with the Galactic double neutron star population, at an observed distance of 100 Mpc, assuming LIGO/Virgo detector network at design sensitivity, and described by the SFHo[175] and ENG[399] EOSs <sup>5</sup>.

For our analysis, we employ the standard LVC-developed nested sampling framework, LALINFERENCE (see Ch. 3 and Refs. [130, 204] for details). We recover the tidal deformability from the gravitational-wave phasing (Method-I) and from the EOS and masses (Method-II) (see Fig. 10.3, bottom panel, gray and blue bins, respectively)<sup>6</sup>. The results disagree with each other, ruling out the unlensed hypothesis. Then, we assume that the event is lensed at a magnification of  $\mu = 1000$ , and repeat the measurement (Fig. 10.3, bottom panel, gray and red bins, respectively). The posteriors overlap, supporting the lensing hypothesis.

We then demonstrate the same test for a  $(m_1 = m_2 = 2 M_{\odot})$  *unlensed but high-mass BNS* at an observed distance  $D^{\text{est}}$  of 100 Mpc. In this case, the tidal deformability from the gravitational-wave phasing and from the EOS/masses overlap (see Fig. 10.3, top panel), favoring the unlensed hypothesis. Thus, the test can be used to discriminate between intrinsically high-mass BNSs and lensed BNSs. Note that here, for the sake of illustrating the method, we have fixed the magnification; we now discuss the more general case with variable magnification below. Given a source population (which we assume to be the galactic double neutron star population), we can estimate the lensing

---

<sup>5</sup>These particular EOSs are chosen since they are broadly in agreement with joint-constraint derived from GW170817 and AT2017gfo, e.g., [23, 27, 28]

<sup>6</sup>We assume the SFHo EOS [175], for simplicity.

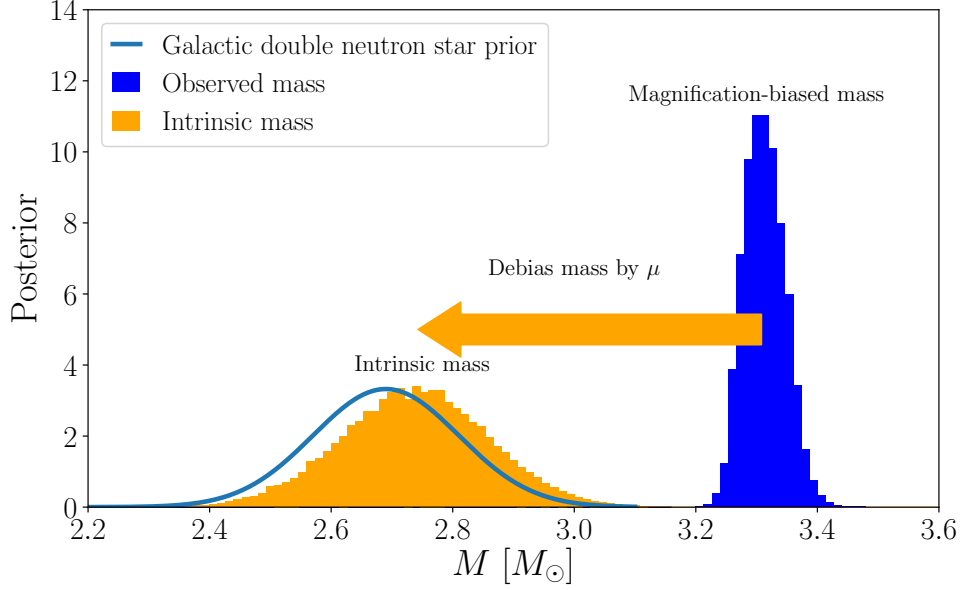


Figure 10.4: Illustration of the magnification posterior computation for GW190425 from the binary masses, assuming the galactic double neutron star population as the mass prior. The figure shows the observed total binary mass for GW190425 (orange), the galactic double neutron star population prior (green), and the mass distribution if the event was lensed (blue). By re-weighting the unlensed posterior, we can estimate the lensing magnification  $\mu$  under the lensing hypothesis. Note that we can also estimate the lensing magnification independently of the galactic double neutron star prior using tidal effects, as illustrated in Fig. 10.3.

magnification  $p(\mu|d, \mathcal{H}_L^{\text{DNS}})$  where we have explicitly defined the hypothesis  $\mathcal{H}_L^{\text{DNS}}$  to refer to the magnification estimate from the binary *masses* (see Sec. 10.7.1 for the detailed derivation). I.e., the mass prior  $p(M|\mathcal{H}_L^{\text{DNS}})$  is the one for galactic double neutron stars (a normal distribution with a  $2.69 M_\odot$  mean and  $0.12 M_\odot$  standard deviation [382]), but we make no explicit constraint on the tidal measurements. This is done by *unbiasing* the GW measurement such that it is consistent with the expected source population (see Fig. 10.4, for an illustration of the process for GW190425).

Alternatively, we can estimate the magnification  $\mu$  by combining the estimated tidal deformability with the directly measured one (see Sec. 10.7.1)

$$p(\mu|d, \text{EOS}, \mathcal{H}_L^{\text{Tidal}}) \propto \left\langle \frac{p(\tilde{\Lambda}^{\text{phase}}|d, \mathcal{H}_U)}{p(\tilde{\Lambda}^{\text{phase}}|q, \mathcal{H}_U)} \mathcal{W}_{\text{EOS}} \right\rangle_{\tilde{\Lambda}^{\text{phase}} = \tilde{\Lambda}^{\text{est}}}, \quad (10.11)$$

where  $p(\tilde{\Lambda}^{\text{phase}}|d, \mathcal{H}_U)$  is the posterior distribution of the measured tidal deformability under the unlensed hypothesis,  $q$  is the mass ratio,  $\tilde{\Lambda}^{\text{est}}$  is the estimated tidal deformability with a given magnification and EOS, and  $\langle \dots \rangle$  refers to an average over the mass and distance posterior samples. The weight  $\mathcal{W}_{\text{EOS}}$  is given by

$$\mathcal{W}_{\text{EOS}} = \frac{p(m_1^{\text{est}}, m_2^{\text{est}} | D^{\text{est}}, \mu, \mathcal{H}_L^{\text{Tidal}}, \text{EOS}) p(D^{\text{est}} | \mu, \mathcal{H}_L)}{p(m_1^{\text{est}}, m_2^{\text{est}} | D^{\text{est}}, \mathcal{H}_U) p(D^{\text{est}} | \mathcal{H}_U)} p(\mu | \mathcal{H}_L). \quad (10.12)$$

Here  $\mathcal{H}_L^{\text{Tidal}}$  refers to the lensed hypothesis that additionally enforces

$$p(\Lambda, \Lambda^{\text{est}} | \mathcal{H}_L^{\text{Tidal}}) = p(\Lambda | \mathcal{H}_L) p(\Lambda^{\text{est}} | \mathcal{H}_L) \delta(\Lambda^{\text{est}} - \Lambda) \quad (10.13)$$

in the prior. The mass prior under  $\mathcal{H}_L^{\text{Tidal}}$  hypothesis is taken to be a flat prior between  $0.5M_\odot$  and the maximum mass allowed by the EOS.

We can calculate the evidence for the lensed hypothesis  $Z_L$  and the unlensed hypothesis  $Z_U$  by

$$\begin{aligned} Z_L &= \int d\mu p(d | \mu, \text{EOS}, \mathcal{H}_L^{\text{Tidal}}) p(\mu) \\ Z_U &= p(d | \mu = 1, \text{EOS}). \end{aligned} \quad (10.14)$$

The log Bayes factor  $\ln \mathcal{B}_U^L$  is defined as the natural log of the ratio between the two evidence, therefore  $\ln \mathcal{B}_U^L \equiv \ln(Z_L/Z_U)$ . A positive  $\ln \mathcal{B}_U^L$  shows that the lensed hypothesis is more plausible than the unlensed hypothesis. For the analysis, we consider a range of EOSs, which are SFHo, ENG and MPA1. These EOSs show agreement with the joint-constraint obtained with GW170817 and AT2017gfo [23].

Since the tidal deformability measurement is not biased by lensing, we expect this secondary measurement of the magnification to be independent of any assumptions on the source population (i.e., it is completely unbiased). Therefore, we expect the magnification to be low for unlensed binaries, and high for lensed binaries.

Fig. 10.5 shows the magnification posteriors evaluated via the two methods above, for both the lensed and unlensed injections with different EOSs (Table 10.1). We observed that the required magnifications  $p(\mu | d, \mathcal{H}_L^{\text{DNS}})$ , as evaluated from the galactic double neutron star population, are in the  $\mu \sim \mathcal{O}(100) - \mathcal{O}(1000)$  range for both the lensed and unlensed injections (Fig. 10.5, gray bins). Meanwhile, the magnifications as estimated from the unbiased tidal deformabilities are different for the two scenarios, favoring the unlensed case for the unlensed injection, and lensed case for the lensed injection (solid lines, for the SFHo, ENG and MPA1 EOSs). Most notably, we find that the two magnification estimates disagree in the unlensed case, ruling out the lensed hypothesis at a log Bayes factor  $\ln \mathcal{B}_U^L$  of  $-2.72(-2.68)$ ,  $-2.75(-2.71)$  and  $-2.82(-2.83)$  for SFHo, ENG and MPA1, respectively, for SFHo(ENG) injection. They agree in the lensed case, confirming the hypothesis at a log Bayes factor  $\ln \mathcal{B}_U^L$  of  $38.5(36.26)$ ,  $31.2(32.63)$  and  $20.9(26.75)$  for SFHo, ENG and MPA1, respectively, for SFHo(ENG) injection. For the unlensed case, the posterior of the magnification  $\mu$  rails against the prior instead of peaking at the true value (therefore  $\mu = 1$ ), which result in the log Bayes factor  $\ln \mathcal{B}_U^L$  to be in different magnitude for the lensed and unlensed injections. As a supplementary analysis, we also performed the estimate on an injection set with a magnification of 100, finding that we can still disfavor lensing for the high-mass binary, but that we are unable to confirm lensing in this case (Sec. 10.7.2).

## 10.5 Beyond mock data: Discussion

Our work demonstrates a robust methodology to rule out or confirm the gravitational lensing hypothesis for BNS mergers. The methodology can be used to rule out lensing for intrinsically high mass BNS events, or confirm it for the galactic double neutron star population. The mock data was produced for two different lensed and unlensed scenario,

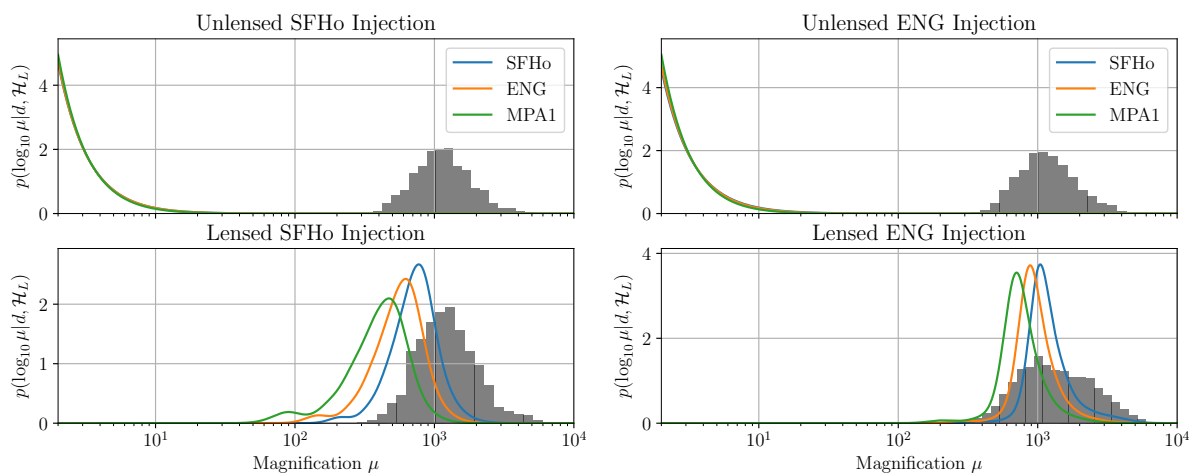


Figure 10.5: Posterior distribution of magnifications inferred with posteriors of component masses and luminosity distance (gray bins) and that with posteriors of component masses and tidal deformability for given EOSs (colored line) with various injections. We show four different injections: Unlensed SFHo (top left), unlensed ENG (top right), lensed SFHo (bottom left) and lensed ENG (bottom right) injection. The posterior of the magnification  $\mu$  inferred from the masses and from the tidal deformabilities are giving consistent results for lensed injections. Meanwhile, there exists tension between the posteriors recovered by the two means for unlensed injection. The injected BNS masses are  $(m_1 = m_2 = 1.35 M_\odot)$  and  $(m_1 = m_2 = 2.02 M_\odot)$  for the lensed and unlensed binaries, respectively. The binary neutron star is at an observed luminosity distance of  $D^{\text{est}} = 100$  Mpc, with a signal-to-noise ratio of 31.

EOS	$\ln \mathcal{B}_U^L$
SFHo	-0.610
ENG	-0.646
MPA1	-0.715

Table 10.2: The log Bayes factor for the lensed hypothesis against unlensed hypothesis of GW190425 with various EOSs given.

employing the SFHo and ENG equations of state consistent with the current GW and EM observations [23]. It is natural to wonder if the analysis could already rule out or confirm lensing for the high-mass binary neutron star event GW190425, and if not, what is required of a realistic detection to be able to make this distinction.

We evaluate the magnification posterior using both the mass estimate and the tidal deformability measurement (as in Sec. 10.4) for GW190425<sup>7</sup>, but find that both the lensed and unlensed magnification estimates overlap, allowing no clear constraints on the lens hypothesis (Fig. 10.6). However, we note that binary neutron star lensing is very unlikely within LIGO/Virgo at current sensitivity. Thus, in the absence of evidence, it is plausible that the event is not lensed. The log Bayes factor for the lensed hypothesis against unlensed hypothesis are shown in Table 10.2 for a selected set of EOSs. We deduce that the magnification  $\mu$  is less than 87.0, 86.5 and 75.3 for SFHo, ENG and MPA1, respectively, at a 99% credible level.

Had the event been observed at design sensitivity, and in the full detector network (LIGO Hanford/Livingston and Virgo), the network SNR would have been  $\sim 23$ , which is much closer to the signal strengths which we used in our mock data simulations (SNR  $\sim 30$ ). Therefore, while we can not set very stringent constraints on lensing for the GW190425 event, a similar event at a lower distance detected by LIGO/Virgo or the same event with more sensitive instruments, in the future, might allow us to probe the lensing hypothesis.

Moreover, we note that the lensing hypothesis can be ruled out more easily for higher mass events. The total mass of the GW190425 event was  $3.4_{-0.1}^{+0.3} M_\odot$ , which would already necessitate fairly large magnifications if it were lensed (Fig. 10.6). If the BNS population which produced GW190425 consists of higher mass BNS events, we will likely be able to set better constraints.

If the event is indeed lensed at a high magnification, then our method can be used to confirm that the event is lensed. It is currently unlikely that we will detect binary neutron star lensing within LIGO/Virgo. However, with future third-generation detectors such as the Einstein Telescope, lensed detections could be in the hundreds [365, 366]. We could discover these events at a much higher SNR, allowing for more robust constraints than presented here.

As we observe more BNS events, we will be able to set more stringent constraints on the EOS of neutron stars due to the combination/stacking of multiple gravitational wave sources [85, 141] and their potential EM counterparts. Therefore, our estimate of the expected tidal deformabilities will improve, which in turn will allow for improved tests of the BNS lensing. Future studies employing populations of events will answer the above questions more definitively.

---

<sup>7</sup>The parameter estimation samples released in [226] is used.

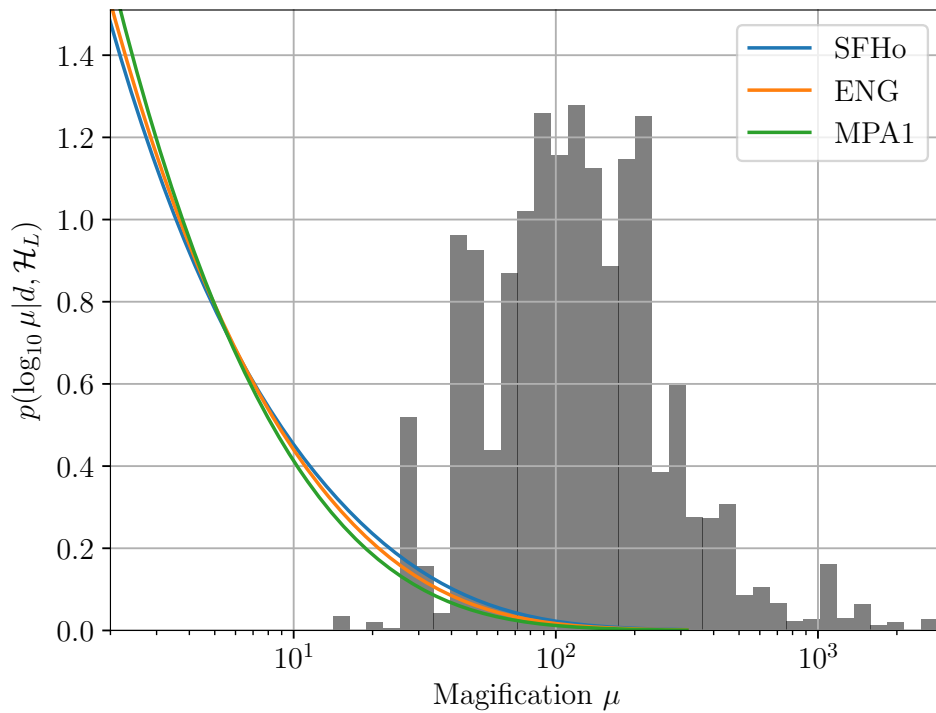


Figure 10.6: Posterior distribution of magnifications inferred with the galactic double neutron star population assumed (gray bins) and posterior distribution of magnifications inferred with different EOSs assumed (colored lines). As the lensed and unlensed magnification estimates overlap, allowing no clear constraints on the lens hypothesis. We deduce that the magnification  $\mu$  is less than 87.0, 86.5 and 75.3 for SFHo, ENG and MPA1, respectively, at a 99% confident.

## 10.6 Conclusions

If a GW from a BNS event is lensed, a combined measurement of the tidal effects and the binary masses of BNSs could be used to rule out or confirm the lensing hypothesis robustly. This test could be used to rule out lensing for intrinsically high-mass BNSs, similar to the recent GW190425 event. Lensed BNSs are one of the GW sources that can be gravitationally lensed and produce an electromagnetic counterpart. This makes them to an attractive target for multi-messenger studies. Indeed, lensed BNSs might allow for measurements of the Hubble constant [405], accurate tests of the speed of gravity [369, 371], various cosmography studies [406], and polarization tests [368]. Since our test could also be used to robustly confirm BNS lensing, it is expected to find several use-cases in these novel strong lensing avenues that utilize EM counterparts.

## 10.7 Materials and methods

### 10.7.1 Lensing analysis methods

In the lensing hypothesis  $\mathcal{H}_L$ , the magnification biases the intrinsic component masses  $m_i$  and luminosity distance  $D$  to their lensed counterparts. Accordingly, the inferred redshift will differ from the true value  $z$ .

We choose a power-law prior on the magnification and denote the PE-inferred quantities by  $m_i^{\text{est}}$ ,  $D^{\text{est}}$  and  $z^{\text{est}}$  both in the lensed and unlensed case. Hence, the assumptions which hold under  $\mathcal{H}_L$  are

$$\begin{aligned} \mathcal{H}_L : p(\mu) &\propto \mu^{-3}, \\ D &= \sqrt{\mu} D^{\text{est}}, \\ z &= z(\sqrt{\mu} D^{\text{est}}), \\ m_i &= \frac{m_i^{\text{det}}}{1+z} = m_i^{\text{est}} \frac{1+z^{\text{est}}}{1+z}, \\ \Lambda_i^{\text{est}} &= \Lambda(m_i) = \Lambda\left(m_i^{\text{est}} \frac{1+z^{\text{est}}}{1+z}\right), \end{aligned} \tag{10.15}$$

while under the unlensed hypothesis  $\mathcal{H}_U$  one finds

$$\begin{aligned} \mathcal{H}_U : m_i &= m_i^{\text{est}}, \\ D &= D^{\text{est}}, \\ \Lambda_i^{\text{est}} &= \Lambda(m_i) = \Lambda(m_i^{\text{est}}). \end{aligned} \tag{10.16}$$

The priors on  $m^{\text{est}}$  and  $D^{\text{est}}$  under  $\mathcal{H}_L$ , given  $\mu$ , are obtained by change of variables. By means of equations (10.15) one has

$$\begin{aligned} p(D^{\text{est}} | \vec{\theta}, \mu, \mathcal{H}_L) &= p(D^* | \vec{\theta}, \mu, \mathcal{H}_L) \left| \frac{\partial D}{\partial D^{\text{est}}} \right|, \\ &= p(D^* | \vec{\theta}, \mu, \mathcal{H}_L) \mu^{1/2}. \end{aligned} \tag{10.17}$$

In the above,  $\vec{\theta}$  represents all the binary parameters besides masses and distance and



$D^* = D(D^{\text{est}}, \mu)$ , as per the last one of equations (10.15). The probability that an event at redshift  $z = z(D)$  is lensed is measured by the optical depth:

$$\tau(z) = p(\mathcal{H}_L | z, \vec{\theta}, \mu). \quad (10.18)$$

The optical depth of lensing is [361]

$$\tau(z) = 4.17 \times 10^{-6} \left( \frac{D_c(z)}{\text{Gpc}} \right)^3 \quad (10.19)$$

where  $D_c(z)$  is the comoving distance. Thus, one has

$$\begin{aligned} \tau(z)p(z|\vec{\theta}, \mu) &= p(\mathcal{H}_L, z|\vec{\theta}, \mu), \\ &\propto p(z|\vec{\theta}, \mu, \mathcal{H}_L). \end{aligned} \quad (10.20)$$

By means of equation (10.20), equation (10.17) becomes:

$$\begin{aligned} p(D^{\text{est}}|\vec{\theta}, \mu, \mathcal{H}_L) &= p(z^*|\vec{\theta}, \mu, \mathcal{H}_L) \left| \frac{\partial D}{\partial z} \right| \mu^{1/2}, \\ &\propto \tau(z^*)p(z^*|\vec{\theta}, \mu, \mathcal{H}_L) \left| \frac{\partial D}{\partial z} \right| \mu^{1/2}, \\ &\propto \tau(z^*)p(z^*|\mathcal{H}_L) \left| \frac{\partial D}{\partial z} \right| \mu^{1/2}, \end{aligned} \quad (10.21)$$

where  $z^* = z(D^*)$  and we used the fact that the prior on  $z$  is independent of  $\vec{\theta}$  and  $\mu$ . In the same fashion, the lensed prior on the masses is:

$$\begin{aligned} &p(m_1^{\text{est}}, m_2^{\text{est}} | D^{\text{est}}, \vec{\theta}, \mu, \mathcal{H}_L) \\ &= p(m_1^*, m_2^* | D^{\text{est}}, \vec{\theta}, \mu, \mathcal{H}_L) \left| \frac{\partial(m_1, m_2)}{\partial(m_1^{\text{est}}, m_2^{\text{est}})} \right| \\ &= p(m_1^*, m_2^* | D^{\text{est}}, \vec{\theta}, \mu, \mathcal{H}_L) \left( \frac{1 + z^{\text{est}}}{1 + z^*} \right)^2, \end{aligned} \quad (10.22)$$

where  $z^{\text{est}} = z(D^{\text{est}})$  and  $m_i^* = m_i(m_i^{\text{est}}, z^{\text{est}}, z^*)$ .

### Magnification posterior with mass distributions

Here we demonstrate how one can estimate the magnification posterior of a given binary neutron star event, given that it comes from the galactic double neutron star population. For this purpose, we define the hypothesis  $\mathcal{H}_L^{\text{DNS}}$  to refer to the magnification estimate from the binary *masses*. I.e., the mass prior  $p(m_1, m_2 | \mathcal{H}_L^{\text{DNS}})$  is the one for galactic double neutron stars, but we make no explicit constraint on the tidal measurements.

In the lensed hypothesis, the joint posterior inferred from a dataset  $d$  is:

$$\begin{aligned} &p(\mu, D^{\text{est}}, m_1^{\text{est}}, m_2^{\text{est}}, \theta | d, \mathcal{H}_L^{\text{DNS}}) \\ &\propto \mathcal{L}(D^{\text{est}}, m_1^{\text{est}}, m_2^{\text{est}}, \vec{\theta}) p(\mu, D^{\text{est}}, m_1^{\text{est}}, m_2^{\text{est}}, \vec{\theta} | \mathcal{H}_L^{\text{DNS}}). \end{aligned} \quad (10.23)$$

Since the waveform model is unchanged, the likelihood  $\mathcal{L}$  is the same under both  $\mathcal{H}_L^{\text{DNS}}$  and  $\mathcal{H}_U$  and does not depend on  $\mu$ . The prior is:

$$\begin{aligned} & p(\mu, D^{\text{est}}, m_1^{\text{est}}, m_2^{\text{est}}, \vec{\theta} | \mathcal{H}_L^{\text{DNS}}) \\ &= p(m_1^{\text{est}}, m_2^{\text{est}} | D^{\text{est}}, \vec{\theta}, \mu, \mathcal{H}_L^{\text{DNS}}) p(D^{\text{est}} | \vec{\theta}, \mu, \mathcal{H}_L^{\text{DNS}}) \\ &\times p(\vec{\theta} | \mathcal{H}_L^{\text{DNS}}) p(\mu | \mathcal{H}_L^{\text{DNS}}), \end{aligned} \quad (10.24)$$

where we used the fact that  $\vec{\theta}$  is independent of  $\mu$ .

Inserting equation (10.24) into expression (10.23), we get:

$$\begin{aligned} & p(\mu, D^{\text{est}}, m_1^{\text{est}}, m_2^{\text{est}}, \vec{\theta} | d, \mathcal{H}_L^{\text{DNS}}) \\ &\propto \mathcal{L}(D^{\text{est}}, m_1^{\text{est}}, m_2^{\text{est}}, \vec{\theta}) p(m_1^{\text{est}}, m_2^{\text{est}} | D^{\text{est}}, \vec{\theta}, \mu, \mathcal{H}_L^{\text{DNS}}) \\ &\times p(D^{\text{est}} | \vec{\theta}, \mu, \mathcal{H}_L^{\text{DNS}}) p(\vec{\theta} | \mathcal{H}_L^{\text{DNS}}) p(\mu | \mathcal{H}_L^{\text{DNS}}). \end{aligned} \quad (10.25)$$

Similarly, the unlensed posterior samples are given by:

$$\begin{aligned} & p(D^{\text{est}}, m_1^{\text{est}}, m_2^{\text{est}}, \vec{\theta} | d, \mathcal{H}_U) \\ &\propto \mathcal{L}(D^{\text{est}}, m_1^{\text{est}}, m_2^{\text{est}}, \vec{\theta}) p(m_1^{\text{est}}, m_2^{\text{est}} | D^{\text{est}}, \vec{\theta}, \mathcal{H}_U) \\ &\times p(D^{\text{est}} | \vec{\theta}, \mathcal{H}_U) p(\vec{\theta} | \mathcal{H}_U). \end{aligned} \quad (10.26)$$

Therefore, one can rewrite equation (10.25) as follows:

$$\begin{aligned} & p(\mu, D^{\text{est}}, m_1^{\text{est}}, m_2^{\text{est}}, \theta | d, \mathcal{H}_L^{\text{DNS}}) \\ &\propto p(D^{\text{est}}, m_1^{\text{est}}, m_2^{\text{est}}, \vec{\theta} | d, \mathcal{H}_U) p(\mu | \mathcal{H}_L^{\text{DNS}}) \\ &\times \frac{p(m_1^{\text{est}}, m_2^{\text{est}} | D^{\text{est}}, \vec{\theta}, \mu, \mathcal{H}_L^{\text{DNS}}) p(D^{\text{est}} | \vec{\theta}, \mu, \mathcal{H}_L^{\text{DNS}})}{p(m_1^{\text{est}}, m_2^{\text{est}} | D^{\text{est}}, \vec{\theta}, \mathcal{H}_U) p(D^{\text{est}} | \vec{\theta}, \mathcal{H}_U)} \\ &= p(D^{\text{est}}, m_1^{\text{est}}, m_2^{\text{est}}, \vec{\theta} | d, \mathcal{H}_U) \times \mathcal{W}, \end{aligned} \quad (10.27)$$

where we used the fact that  $p(\vec{\theta} | \mathcal{H}_L^{\text{DNS}}) = p(\vec{\theta} | \mathcal{H}_U)$  and the factors in the numerator are computed as prescribed by equations (10.21) and (10.22).

Since the likelihood is unchanged, the weighting factor amounts to the prior ratio of the two scenarios,

$$\begin{aligned} \mathcal{W} &= \frac{p(m_1^{\text{est}}, m_2^{\text{est}} | D^{\text{est}}, \vec{\theta}, \mu, \mathcal{H}_L^{\text{DNS}}) p(\mu | \mathcal{H}_L^{\text{DNS}})}{p(m_1^{\text{est}}, m_2^{\text{est}} | D^{\text{est}}, \vec{\theta}, \mathcal{H}_U) p(D^{\text{est}} | \vec{\theta}, \mathcal{H}_U)} \\ &\times \tau(z^*) p(z^* | \mathcal{H}_L^{\text{DNS}}) \left| \frac{\partial D}{\partial z} \right| \mu^{1/2} \end{aligned} \quad (10.28)$$

We use a power-law prior on the magnification,  $p(\mu | \mathcal{H}_L^{\text{DNS}}) \propto \mu^{-3}$  in  $[2, 6000]$ . Prior distributions on masses and distance for the lensed case are obtained from the unlensed ones by change of variables from the unlensed to the lensed quantities. The posterior samples and the priors under  $\mathcal{H}_U$ , in turn, are the ones of the `LALInference` analysis performed by the LIGO and Virgo Collaborations [6]. All the other binary parameters are unaffected by the lensing hypothesis and their priors cancel out in the weighting factor.

### Magnification posterior with tidal measurements

To quantify the agreement between the measured tidal deformability and the estimated tidal deformability with a magnification given, we derive the posterior of the magnification  $p(\mu|d, \text{EOS})$  with a given EOS as follows.

In the following derivation, the other parameters  $\vec{\theta}$  are suppressed to ease the notation. In order to obtain the magnification via tidal measurement, we expand the posterior  $p(\mu|d, \text{EOS})$  as

$$\begin{aligned}
 p(\mu|d, \text{EOS}, \mathcal{H}_L^{\text{Tidal}}) &= p(\mu|\mathcal{H}_L^{\text{Tidal}}) \int d\tilde{\Lambda} dm_i^{\text{det}} dD^{\text{est}} \\
 &\quad \times \mathcal{L}(d|\tilde{\Lambda}, m_i^{\text{det}}, D^{\text{est}}) \\
 &\quad \times p(\tilde{\Lambda}, m_i^{\text{det}}, D^{\text{est}}|\mu, \mathcal{H}_L, \text{EOS}) \\
 &= p(\mu|\mathcal{H}_L^{\text{Tidal}}) \int d\tilde{\Lambda} dm_i^{\text{det}} dD^{\text{est}} \\
 &\quad \times \mathcal{L}(d|\tilde{\Lambda}, m_i^{\text{det}}, D^{\text{est}}) \\
 &\quad \times p(\tilde{\Lambda}|m_i^{\text{det}}, D^{\text{est}}, \mu, \mathcal{H}_L, \text{EOS}) \\
 &\quad \times p(m_i^{\text{det}}, D^{\text{est}}|\mu, \mathcal{H}_L, \text{EOS}).
 \end{aligned} \tag{10.29}$$

We notice that the tidal deformability is completely determined with a EOS and source-frame masses (therefore with detector-frame masses and luminosity distance given). Therefore  $p(\tilde{\Lambda}|m_i^{\text{det}}, D^{\text{est}}, \mu, \mathcal{H}_L, \text{EOS}) = \delta(\tilde{\Lambda} - \tilde{\Lambda}^{\text{est}})$ , where  $\tilde{\Lambda}^{\text{est}}$  is the estimated tidal deformability. Therefore,

$$\begin{aligned}
 p(\mu|d, \text{EOS}, \mathcal{H}_L^{\text{Tidal}}) &= \int d\tilde{\Lambda} dm_i^{\text{det}} dD^{\text{est}} \mathcal{L}(d|\tilde{\Lambda}, m_i^{\text{det}}, D^{\text{est}}) \\
 &\quad \times \delta(\tilde{\Lambda} - \tilde{\Lambda}^{\text{est}}) p(m_i^{\text{det}}, D^{\text{est}}|\mu, \mathcal{H}_L, \text{EOS}) \\
 &\quad \times p(\mu|\mathcal{H}_L^{\text{Tidal}}) \\
 &= \int dm_i^{\text{det}} dD^{\text{est}} \mathcal{L}(d|\tilde{\Lambda}^{\text{est}}, m_i^{\text{det}}, D^{\text{est}}) \\
 &\quad \times p(m_i^{\text{det}}, D^{\text{est}}|\mu, \mathcal{H}_L, \text{EOS}) p(\mu|\mathcal{H}_L^{\text{Tidal}}).
 \end{aligned} \tag{10.30}$$

As the likelihood is unchanged if we switch from  $\mathcal{H}_L^{\text{Tidal}}$  and  $\mathcal{H}_U$ , we then express the likelihoods in terms of the posteriors under  $\mathcal{H}_U$ ,

$$\begin{aligned}
 p(\mu|d, \text{EOS}, \mathcal{H}_L^{\text{Tidal}}) &\propto \int dm_i^{\text{det}} dD^{\text{est}} \\
 &\quad \times \frac{p(\tilde{\Lambda}^{\text{est}}, m_i^{\text{det}}, D^{\text{est}}|d, \mathcal{H}_U)}{p(\tilde{\Lambda}^{\text{est}}, m_i^{\text{det}}, D^{\text{est}}|\mathcal{H}_U)} \\
 &\quad \times p(m_i^{\text{det}}, D^{\text{est}}|\mu, \mathcal{H}_L, \text{EOS}) p(\mu|\mathcal{H}_L^{\text{Tidal}}) \\
 &= \int dm_i^{\text{det}} dD^{\text{est}} \\
 &\quad \times \frac{p(\tilde{\Lambda}^{\text{est}}, m_i^{\text{det}}, D^{\text{est}}|d, \mathcal{H}_U)}{p(\tilde{\Lambda}^{\text{est}}|m_i^{\text{det}}, D^{\text{est}}, \mathcal{H}_U)} \\
 &\quad \times \mathcal{W}_{\text{EOS}}
 \end{aligned} \tag{10.31}$$

In our study, we sample over the detector-frame masses and individual tidal deformability independently. Based on Eq. (10.4), the prior  $p(\tilde{\Lambda}^{\text{est}}|m_i^{\text{det}}, D^{\text{est}}, \mathcal{H}_U)$  is the same as the

prior  $p(\tilde{\Lambda}^{\text{est}}|q, \mathcal{H}_U)$ , where  $q \equiv m_2^{\text{det}}/m_1^{\text{det}}$ . One has

$$\begin{aligned}
 p(\mu|d, \text{EOS}, \mathcal{H}_L^{\text{Tidal}}) &\propto \int dm_i^{\text{det}} dD^{\text{est}} \\
 &\times \frac{p(\tilde{\Lambda}^{\text{est}}, m_i^{\text{det}}, D^{\text{est}}|d, \mathcal{H}_U)}{p(\tilde{\Lambda}^{\text{est}}|q, \mathcal{H}_U)} \mathcal{W}_{\text{EOS}} \\
 &= \int dm_i^{\text{det}} dD^{\text{est}} p(m_i^{\text{det}}, D^{\text{est}}|d, \mathcal{H}_U) \\
 &\times \frac{p(\tilde{\Lambda}^{\text{est}}|m_i^{\text{det}}, D^{\text{est}}, d, \mathcal{H}_U)}{p(\tilde{\Lambda}^{\text{est}}|q, \mathcal{H}_U)} \mathcal{W}_{\text{EOS}}.
 \end{aligned} \tag{10.32}$$

Finally, we approximate the integral by an average over posterior samples. As a result,

$$p(\mu|d, \text{EOS}, \mathcal{H}_L^{\text{Tidal}}) \propto \left\langle \frac{p(\tilde{\Lambda}^{\text{est}}|d, \mathcal{H}_U)}{p(\tilde{\Lambda}^{\text{est}}|q, \mathcal{H}_U)} \mathcal{W}_{\text{EOS}} \right\rangle, \tag{10.33}$$

where  $p(\tilde{\Lambda}^{\text{phase}}|d, \mathcal{H}_U)$  is the posterior distribution of the measured tidal deformability, and  $\tilde{\Lambda}^{\text{est}}$  is the estimated tidal deformability with a magnification and an EOS given.  $m_i^{\text{det}}$  and  $D^{\text{est}}$  are the observed component masses and the observed luminosity distance, respectively. The weight  $\mathcal{W}_{\text{EOS}}$  is given by

$$\begin{aligned}
 \mathcal{W}_{\text{EOS}} &= \frac{p(m_1^{\text{det}}, m_2^{\text{det}}|D^{\text{est}}, \mu, \mathcal{H}_L^{\text{Tidal}}, \text{EOS})p(D^{\text{est}}|\mu, \mathcal{H}_L^{\text{Tidal}})}{p(m_1^{\text{det}}, m_2^{\text{det}}|D^{\text{est}}, \mathcal{H}_U)p(D^{\text{est}}|\mathcal{H}_U)} \\
 &\times p(\mu|\mathcal{H}_L^{\text{Tidal}}) \\
 &= \frac{p(m_1^{\text{est}}, m_2^{\text{est}}|D^{\text{est}}, \mu, \mathcal{H}_L^{\text{Tidal}}, \text{EOS})p(D^{\text{est}}|\mu, \mathcal{H}_L^{\text{Tidal}})}{p(m_1^{\text{est}}, m_2^{\text{est}}|D^{\text{est}}, \mathcal{H}_U)p(D^{\text{est}}|\mathcal{H}_U)} \\
 &\times p(\mu|\mathcal{H}_L^{\text{Tidal}}).
 \end{aligned} \tag{10.34}$$

The difference between  $\mathcal{W}_{\text{EOS}}$  and  $\mathcal{W}$  lies in the prior on  $m_{1,2}^{\text{est}}$ . For  $\mathcal{W}_{\text{EOS}}$ , the prior on  $m_{1,2}^{\text{est}}$  is estimated based on a flat prior on the true source component mass to be uniform between  $0.5M_\odot$  and the maximum mass allowed with a given EOS, while the Galactic double neutron star population is used for the calculation of  $\mathcal{W}$  in this chapter.

## 10.7.2 Results with magnification $\mu$ of 100

In Fig. 10.7, we show the magnification posteriors evaluated with the two methods described in Sec 10.4 with injections tabulated in Tab 10.3 given.

We observed that the required magnifications  $p(\mu|d, \mathcal{H}_L^{\text{DNS}})$ , as evaluated from the galactic double neutron star population, are in the  $\mu \sim \mathcal{O}(10) - \mathcal{O}(1000)$  range for both the lensed and unlensed injections (Fig. 10.7, gray bins). Meanwhile, the magnifications as estimated from the unbiased tidal deformabilities are different for the two scenarios, favoring the unlensed case for the unlensed injection, and no clear preference for the lensed injection (solid lines, for the SFHo, ENG and MPA1 EOSs).

We find that the two magnification estimates disagree in the unlensed case, ruling out the lensed hypothesis at a log Bayes factor  $\ln \mathcal{B}_U^L$  of  $-0.62(-0.68)$ ,  $-0.77(-0.93)$  and  $-1.04(-1.24)$  for SFHo, ENG and MPA1, respectively, for SFHo(ENG) injection. The magnification estimates overlap in the lensed case, showing no clear support on lensed

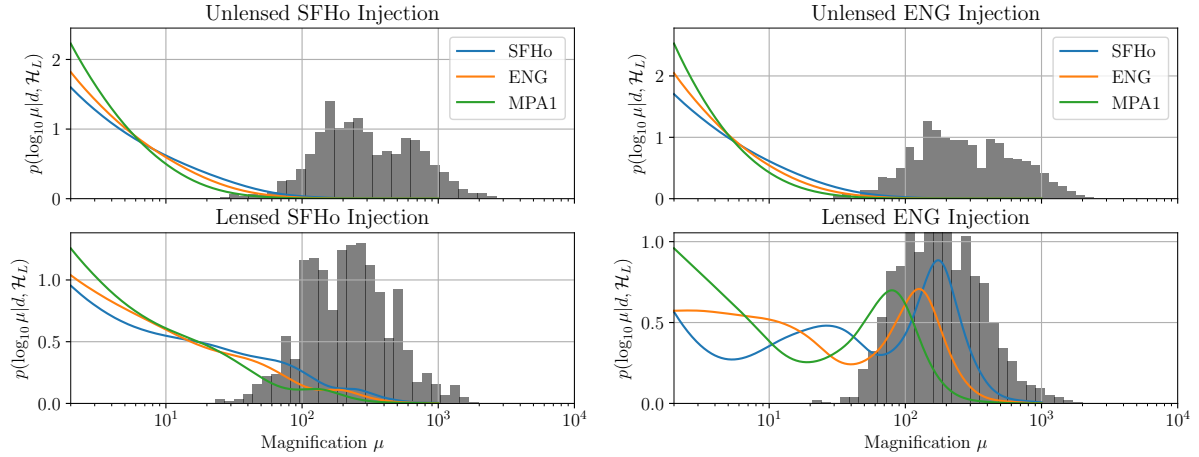


Figure 10.7: Posterior distribution of magnifications inferred with posteriors of component masses and luminosity distance (gray bins) and that with posteriors of component masses and tidal deformability for given EOSs (colored line) with various injections. We show four different injections: Unlensed SFHo (top left), unlensed ENG (top right), lensed SFHo (bottom left) and lensed ENG (bottom right) injection. The posterior of the magnification  $\mu$  inferred from the masses and from the tidal deformabilities are giving consistent results for lensed injections. Meanwhile, there exists tension between the posteriors recovered by the two means for unlensed injection. The injected BNS masses are ( $m_1 = m_2 = 1.35 M_\odot$ ) and ( $m_1 = m_2 = 1.58 M_\odot$ ) for the lensed and unlensed binaries, respectively. The binary neutron star is at an observed luminosity distance of  $D^{\text{est}} = 100$  Mpc, with a signal-to-noise ratio of 25.

EOS	Lensed ( $\mu = 100$ )	Unlensed ( $\mu = 1$ )
SFHo	(1.35, 432.94)	(1.58, 146.62)
ENG	(1.35, 644.66)	(1.58, 194.18)

Table 10.3: Summary of the source-frame mass and the tidal deformability of the simulated binary neutron star mergers. Each cell shows the source-frame mass, tidal deformability pair ( $m, \Lambda$ ) of the injection under different EOS and lensing scenario.

hypothesis at a log Bayes factor  $\ln \mathcal{B}_V^L$  of  $-0.07(0.13)$ ,  $-0.08(0.77)$  and  $-0.34(0.01)$  for SFHo, ENG and MPA1, respectively, for SFHo(ENG) injection.

These results show that the lensing hypothesis is disfavoured even for a weaker magnification with a weaker support. Meanwhile, the support for lensed hypothesis under lensed injection is too weak for us to give any statement for it.

CHAPTER 10. LENSED OR NOT LENSED: DETERMINING LENSING  
MAGNIFICATIONS FOR BINARY NEUTRON STAR MERGERS FROM A SINGLE  
DETECTION

---

---

---

## PART IV

---

# TESTING THE VALIDITY OF GENERAL RELATIVITY AND THE NATURE OF COMPACT OBJECTS

In the past several years, the Advanced LIGO observatories [4] together with Advanced Virgo [10] have been detecting gravitational wave (GW) signals from coalescing compact binaries on a regular basis. This includes a confirmed binary neutron star inspiral [9, 11, 54, 403], and more recently another possible binary neutron star [49], although most sources appear to have been binary black holes [6, 47, 48, 407–409]. The detections made during the first and second observing runs are summarized in [6]; the latter will be referred to as GWTC-1, for Gravitational Wave Transient Catalog 1. (For other detection efforts, see [410–412].)

This has enabled a variety of tests of general relativity (GR), including but not limited to the strong-field dynamics of binary coalescence [15, 16, 48, 263], the way GWs propagate over large distances [11, 16, 408], and preliminary investigations into their polarization content [263, 413, 414].

In Chapter 11, we will introduce the methods developed for probing the polarization content of the gravitational waves. In Chapter 12, a method for distinguishing binary black hole and other exotic compact objects will be described. These works are published as Refs. [41, 42].

---



# CHAPTER 11

## GENERIC SEARCHES FOR ALTERNATIVE GRAVITATIONAL WAVE POLARIZATIONS WITH NETWORKS OF INTERFEROMETRIC DETECTORS

### 11.1 Introduction

Generic metric theories of gravity allow for the existence of up to six GW polarization states for gravitational waves [415], which can be categorized into tensor modes, vector modes, and scalar modes. While GR only permits the tensor modes, some theories of gravity predict additional polarizations; see e.g. [368] and references therein. In [15, 263, 413, 414], ratios of Bayesian evidences were computed for the hypotheses that only tensor polarizations, only vector polarizations, or only scalar polarizations were present in the signals. Yet, in realistic alternative theories of gravity, typically *mixtures* occur of tensor modes together with vector and/or scalar polarization states.

In this chapter we develop methodology that will allow us to check for the existence of such mixtures, in GW signals from sources whose exact sky position is known through an electromagnetic counterpart. As shown by Gürsel and Tinto [416], it is possible to construct a specific linear combination of the outputs of multiple detectors in a network, the *null stream*, which has the property of removing any tensor signal that may be present in the data. This idea was further extended and built on in [417–419]; see also [420, 421] in the context of third-generation detectors such as Einstein Telescope. A commonly used application for LIGO-Virgo gravitational wave searches is X-Pipeline [419, 422], which assumes that only tensor polarizations can be present, and then compares the *null energy* (essentially the square of the null stream) with other combinations of detector outputs to search for GW signals that are in accordance with GR. As pointed out in [368, 423], null streams can also be used to study a signal’s non-tensorial polarization content that may result from a GR violation.

Here we introduce two concrete data analysis pipelines that make use of the fact that if there are only tensor polarizations, the null energy of [419], when evaluated at the true sky position, follows a particular  $\chi^2$  distribution, but not if extra polarizations are present. A first method to discover alternative polarization content then quantifies to what extent the null energy for the given sky position is consistent with this  $\chi^2$  distribution. In a second method the sky position is *a priori* left free, allowing us to turn the tensor-only distribution for the null energy into a probability distribution for the sky location. This sky map will be biased if alternative polarizations are present, which can be quantified by comparing it with the true position of the source on the sky.

Suppose that in a given signal, alternative polarizations are in fact present, mixed with tensor polarizations. Then to determine the precise nature and relative contributions of the additional modes, in general one would need a network of at least five detectors in

addition to the sky position [368, 423, 424].<sup>1</sup> Although in the near future KAGRA [428] will join the discovery efforts, and LIGO-India [429] is about to be built, for now only the two LIGO interferometers and Virgo are making regular detections. However, what we want to establish first of all is whether or not GW signals contain extra polarizations, *irrespective of how much each possible type contributes*, and this is what our two methods enable us to do. If we were to find evidence that GW signals tend to contain more than just tensor polarizations, then this would be a powerful motivation to extend the global detector network even further, in order to be able to study what precisely is contained in a mix of polarizations. Finally, the fact that our methodology is based on the null energy implies that no waveform models are required, so that apart from compact binary coalescences, signals from any transient source (supernovae, cosmic strings, ...) can be studied.

This chapter is structured as follows. Sec. 11.2 recalls the effects of different polarization modes on interferometric gravitational wave detectors. Sec. 11.3 explains our two methods for finding additional polarizations, one based on the null energy for the true sky position, and the other on sky maps. In Sec. 11.4 we perform a simulation whereby signals with a varying amount of scalar polarization in addition to the tensor modes are “injected” into synthetic stationary, Gaussian noise, and we compare the performance of the two analysis pipelines. The methodology is also applied to the binary neutron star signal GW170817, showing consistency with the hypothesis that only tensor polarizations were present. A summary and conclusions are given in Sec. 11.5.

## 11.2 Gravitational wave polarizations

In generic metric theories of gravity, up to six independent polarization modes can be present, namely a breathing mode, a longitudinal mode, the “X” vector mode, the “Y” vector mode, and the usual tensor modes predicted by GR [430]. The effect of different polarization modes on a ring of free-falling test mass is shown in Fig. 11.1. In all the panels of the figure, a gravitational wave is traveling in the  $z$ -direction. The solid and dotted lines illustrate the deformation of the ring in response to the various modes. Interferometric gravitational wave detectors will react accordingly, with beam pattern functions given by [430]

$$\begin{aligned}
 F_B &= -\frac{1}{2} \sin^2 \theta \cos 2\phi, \\
 F_L &= \frac{1}{2} \sin^2 \theta \cos 2\phi, \\
 F_X &= -\sin \theta (\cos \theta \cos 2\phi \cos \psi - \sin 2\phi \sin \psi), \\
 F_Y &= -\sin \theta (\cos \theta \cos 2\phi \sin \psi + \sin 2\phi \cos \psi), \\
 F_+ &= \frac{1}{2} (1 + \cos^2 \theta) \cos 2\phi \cos 2\psi - \cos \theta \sin 2\phi \sin 2\psi, \\
 F_\times &= \frac{1}{2} (1 + \cos^2 \theta) \cos 2\phi \sin 2\psi + \cos \theta \sin 2\phi \cos 2\psi.
 \end{aligned}
 \tag{11.1}$$

Here  $(\theta, \phi)$  is the sky location of the source, and  $\psi$  is the so-called polarization angle. The subscripts “B”, “L”, “X”, “Y”, “+”, and “ $\times$ ” respectively denote the breathing mode, the

---

<sup>1</sup>An exception occurs for certain special sky positions with respect to the network; see [425–427].

longitudinal mode, the X vector mode, the Y vector mode, the “+” tensor polarization, and the “×” tensor polarization. As can be seen from the expressions for  $F_B$  and  $F_L$ , there is a degeneracy between the responses of the two scalar modes; in our analyses we only consider the breathing mode.

## 11.3 Methodology

Now consider a *network* of  $D$  gravitational wave detectors labeled by  $\alpha = 0, \dots, D$ , located on the Earth at positions  $\vec{r}_\alpha$  with respect to a geocentric coordinate system, and producing strain outputs  $d_\alpha$ . A gravitational wave is assumed to originate from a source with sky location  $\hat{\Omega} = (\theta, \phi)$ , arriving at the geocenter at a time  $t$ . If only the tensor polarizations are present, one has

$$d_\alpha(t + \Delta t_\alpha) = F_{+, \alpha}(\hat{\Omega})h_+(t) + F_{\times, \alpha}(\hat{\Omega})h_\times(t) + n_\alpha(t + \Delta t_\alpha), \quad (11.2)$$

where  $F_{\alpha,+}$ ,  $F_{\alpha,\times}$  are the beam pattern functions and  $n_\alpha$  is the noise of detector  $\alpha$ . The time shifts  $\Delta t_\alpha$  are given by

$$\Delta t_\alpha = \frac{\vec{r}_\alpha}{c} \cdot (-\hat{\Omega}). \quad (11.3)$$

We can write the  $D$ -detector observation model more compactly in matrix form:

$$\mathbf{d} = \mathbf{F}\mathbf{h} + \mathbf{n}, \quad (11.4)$$

where

$$\mathbf{d} = \begin{pmatrix} d_0 \\ \vdots \\ d_{D-1} \end{pmatrix}, \quad \mathbf{h} = \begin{pmatrix} h_+ \\ h_\times \end{pmatrix}, \quad \mathbf{n} = \begin{pmatrix} n_0 \\ \vdots \\ n_{D-1} \end{pmatrix}, \quad (11.5)$$

and

$$\mathbf{F} = (\mathbf{F}_+ \quad \mathbf{F}_\times) = \begin{pmatrix} F_{+,0} & F_{\times,0} \\ \vdots & \vdots \\ F_{+,D-1} & F_{\times,D-1} \end{pmatrix}. \quad (11.6)$$

### 11.3.1 Null energy

In the above, the gravitational wave signal  $\mathbf{s} = \mathbf{F}\mathbf{h}$  can be viewed as being in a subspace of the space of detector outputs spanned by  $\mathbf{F}_+$  and  $\mathbf{F}_\times$ . We can construct the *null projector*  $\mathbf{P}_{\text{null}}(\hat{\Omega})$  [422], which projects away the signal when the projector is constructed with the true sky location. The null projector is given by

$$\mathbf{P}_{\text{null}} = \mathbf{I} - \mathbf{F}_w(\mathbf{F}_w^\dagger \mathbf{F}_w)^{-1} \mathbf{F}_w^\dagger, \quad (11.7)$$

where  $\dagger$  denotes Hermitian conjugation and  $\mathbf{F}_w$  are the noise-weighted beam pattern functions [422]. If we apply the null projector with the true sky location on the strain

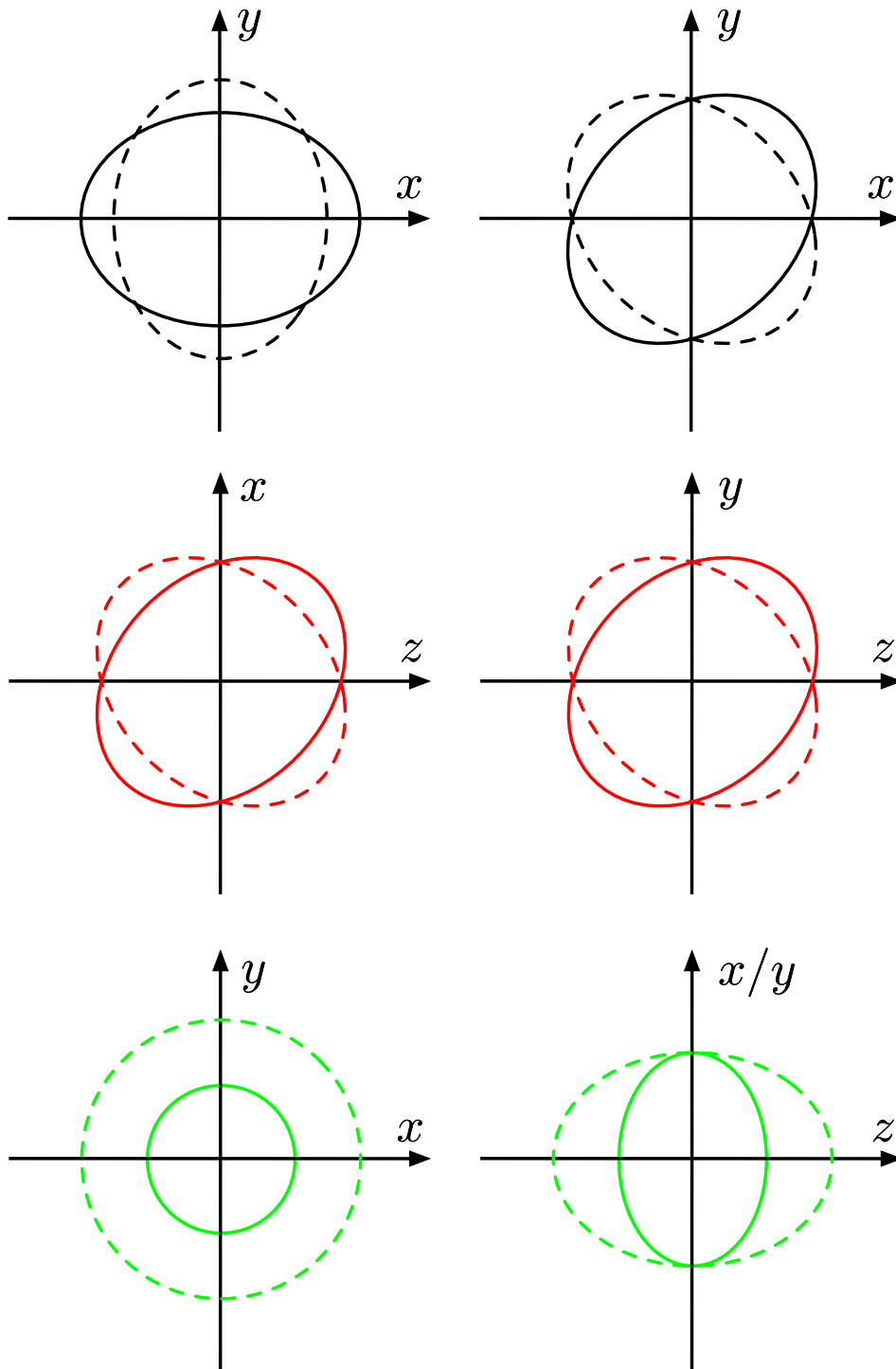


Figure 11.1: The effect on a ring of free-falling test particles of a gravitational wave in “+” tensor mode (upper left), “ $\times$ ” tensor mode (upper right), “X” vector mode (middle left), “Y” vector mode (middle right), breathing mode (lower left) and longitudinal mode (lower right). In each case the wave is traveling in the  $z$ -direction. The solid and dotted lines are the states of the ring with a phase difference of  $\pi$ .

data in Eq. (11.4), we obtain

$$\begin{aligned}
 \tilde{\mathbf{z}}(\hat{\Omega}_{\text{true}}) &= \mathbf{P}_{\text{null}}(\hat{\Omega}_{\text{true}})\tilde{\mathbf{d}}_w \\
 &= \mathbf{P}_{\text{null}}(\hat{\Omega}_{\text{true}})\mathbf{F}_w(\hat{\Omega}_{\text{true}})\tilde{\mathbf{h}} + \mathbf{P}_{\text{null}}(\hat{\Omega}_{\text{true}})\tilde{\mathbf{n}}_w \\
 &= \mathbf{P}_{\text{null}}(\hat{\Omega}_{\text{true}})\tilde{\mathbf{n}}_w
 \end{aligned} \tag{11.8}$$

where  $\tilde{\mathbf{z}}$  is the *null stream* which only consists of noise living in a subspace that is orthogonal to the one spanned by  $\mathbf{F}_{+,w}$  and  $\mathbf{F}_{\times,w}$ , and  $w$  indicates whitening.

In practice, the data are first whitened before applying the null projector. As in [422] we perform the analysis in the time-frequency domain, but using the Wilson-Daubechies-Meyer (WDM) time-frequency transform because of its superior time-frequency localization [431]. The *null energy* is then defined as [422]

$$\begin{aligned}
 E_{\text{null}} &= \sum_k \tilde{\mathbf{z}}_w^\dagger \tilde{\mathbf{z}}_w \\
 &= \sum_k \tilde{\mathbf{d}}_w^\dagger \mathbf{P}_{\text{null}}^\dagger \mathbf{P}_{\text{null}} \tilde{\mathbf{d}}_w \\
 &= \sum_k \tilde{\mathbf{d}}_w^\dagger \mathbf{P}_{\text{null}} \tilde{\mathbf{d}}_w,
 \end{aligned} \tag{11.9}$$

where  $w$  indicates whitening, a tilde refers to the data matrix resulting from the WDM transform, and  $\sum_k$  sums over the discrete time-frequency pixels. The quantity  $E_{\text{null}}$  follows a  $\chi^2$  distribution with DoF =  $N_{\tau f}(D - 2)$  degrees of freedom, where  $N_{\tau f}$  is the number of time-frequency pixels used in the analysis.<sup>2</sup>

Now let us assume that there is polarization content in the signal beyond the tensor polarizations. The whitened data matrix can then be written as

$$\tilde{\mathbf{d}}_w = \mathbf{F}_{w,t}\tilde{\mathbf{h}}_t + \mathbf{F}_{w,e}\tilde{\mathbf{h}}_e + \tilde{\mathbf{n}}_w, \tag{11.10}$$

where the index  $t$  is summed over  $+$  and  $\times$ , while the index  $e$  is summed over whatever additional polarizations are present. The null energy calculated at the source's location with pure-tensor beam pattern matrix is given by

$$\begin{aligned}
 E_{\text{null}} &= \sum_k \tilde{\mathbf{d}}_w^\dagger \mathbf{P}_{\text{null}} \tilde{\mathbf{d}}_w \\
 &= \sum_k \tilde{\mathbf{n}}_w^\dagger \mathbf{P}_{\text{null}} \tilde{\mathbf{n}}_w + \sum_k \tilde{\mathbf{h}}_e^\dagger \mathbf{F}_{e,w}^\dagger \mathbf{P}_{\text{null}} \mathbf{F}_{e',w} \tilde{\mathbf{h}}_{e'} \\
 &\quad + \sum_k 2\Re(\tilde{\mathbf{h}}_e^\dagger \mathbf{F}_{e,w}^\dagger \mathbf{P}_{\text{null}}^t \tilde{\mathbf{n}}_w),
 \end{aligned} \tag{11.11}$$

where the last two terms signify the presence of the extra polarizations. Next we explain how the  $\chi^2$  distribution which the null energy would follow in the absence of these additional polarizations, can be used to detect them, in two different ways.

---

<sup>2</sup>Note that in [422], DoF has an extra prefactor 2, which is not present here because the WDM coefficients are real.

### 11.3.2 Null energy method and sky map method

As mentioned before, we assume gravitational wave events with electromagnetic counterpart, so that the true sky position  $\hat{\Omega}_{\text{true}}$  is known. With the null energy formalism of the previous subsection, this leads to two methods for establishing whether alternative polarizations are present.

- If there are additional polarizations in the signal, then the null energy evaluated at  $\hat{\Omega}_{\text{true}}$  will no longer follow the  $\chi^2$  distribution described above. To quantify the size of the deviation, we can assign a p-value to the hypothesis that only tensor polarizations are present, given by

$$p = 1 - \int_0^{E_{\text{null}}} \chi_{\text{DoF}}^2(x) dx. \quad (11.12)$$

A small p-value indicates a strong appearance of the additional terms in the right hand side of Eq. (11.11), suggesting a deviation from GR. In the sequel this method will simply be referred to as the *null energy method*.

- Alternatively, in the definition (11.9) for the null energy one can leave  $\hat{\Omega}$  free. This leads to a sky map, or probability distribution for  $\hat{\Omega}$  through  $\mathcal{P}(\hat{\Omega}) \equiv \chi_{\text{DoF}}^2(E_{\text{null}}(\hat{\Omega}))$ . If additional polarizations are in fact present in the signal, then they will cause systematics in  $\mathcal{P}(\hat{\Omega})$  due to the detectors' responses to them. The true sky location  $\hat{\Omega}_{\text{true}}$  will fall on the boundary of some  $(1 - q)$  credible interval, where  $q$  is given by

$$q = \int d\hat{\Omega} \mathcal{P}(\hat{\Omega}) H(\mathcal{P}(\hat{\Omega}_{\text{true}}) - \mathcal{P}(\hat{\Omega})), \quad (11.13)$$

with  $H(x)$  the Heaviside step function. The quantity  $q$  can then be interpreted as a p-value for the tensor-only hypothesis. In what follows this method will be referred to as the *sky map method*.

Both methods allow us to combine information from multiple sources so as to arrive at a stronger statement on the validity of GR, or lack thereof. If GR is an accurate description of the gravitational wave polarization, then the values of  $p$  obtained from the null energy method and the values of  $q$  obtained using the sky map method should be distributed uniformly between 0 and 1. As shown by Fisher [432], if one has  $N$  samples  $\{q_i\}$  following a uniform distribution between 0 and 1, the test statistic  $S$  given by

$$S = -2 \sum_{i=1}^N \log(q_i), \quad (11.14)$$

follows a  $\chi^2$  distribution with  $2N$  degrees of freedom. Therefore, the combined p-value  $p_{\text{com}}$  is given by

$$p_{\text{com}} = 1 - \int_0^S \chi_{2N}^2(x) dx. \quad (11.15)$$

In what follows, we first test the two methods through an extensive simulation, and then apply them to the binary neutron star signal GW170817.

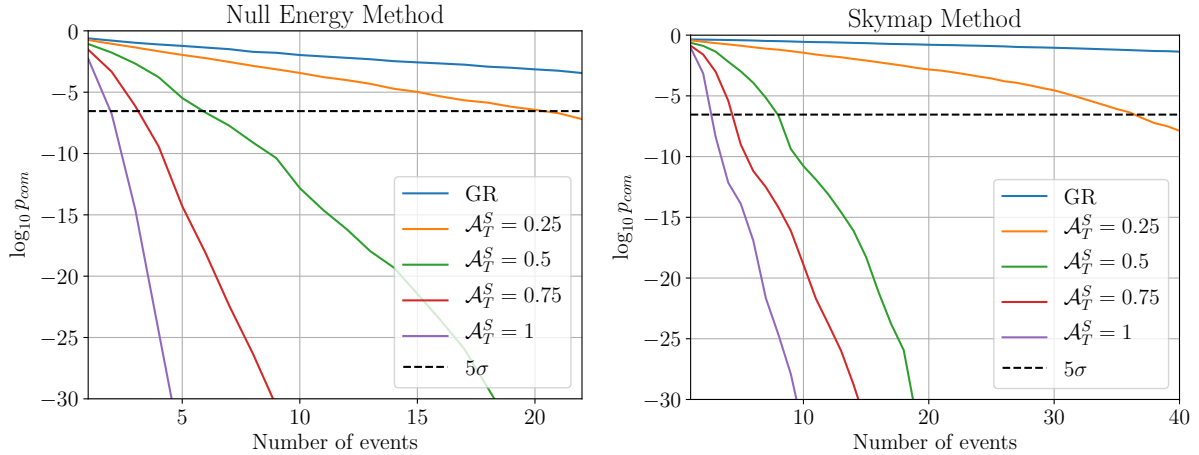


Figure 11.2:  $\log_{10}$  of combined p-values with null energy method (left panel) and skymap method (right panel) against the number of combined events, both for the GR case and for different sets of mock scalar-tensor signals as described in the main text. For all sets of non-GR injections, GR can be rejected at the  $5\sigma$  level with a few to a few tens of detections.

## 11.4 Simulations, and analyses of GW170817

In this section we evaluate the performance of the null stream and sky map methods by “injecting” simulated signals into synthetic Gaussian, stationary noise following predicted noise power spectral densities for Advanced LIGO and Advanced Virgo at their respective design sensitivities. We take the sources to be zero-spin binary neutron star inspirals with component masses uniformly distributed in  $[1, 2] M_{\odot}$ . Positions in the Universe are distributed uniformly in co-moving volume, with a network signal-to-noise threshold of 12. Binary neutron stars are chosen because of their ability to generate electromagnetic counterpart when they merge, but in principle other transient sources could be considered.

To test the sensitivities of our methods, apart from simulated signals that follow GR we also inject sets of mock scalar-tensor waveforms. The scalar component  $h_S$  of the latter signals is taken to be

$$h_S(t) = \mathcal{A}_S^T h_T(t; \text{with a } \pi/4 \text{ phase shift}), \quad (11.16)$$

where  $h_T(t)$  equals  $h_+(t)$  at zero inclination, and the  $\pi/4$  phase shift is a strawman for the more general ways in which the time evolution of the scalar component might differ from that of the tensor components in various alternative theories [368]. In each of four sets of scalar-tensor injections we let the scalar-to-tensor ratio  $\mathcal{A}_S^T$  take values of 0.25, 0.5, 0.75, or 1.0.

Fig. 11.2 shows  $\log_{10}$  of the combined p-value  $p_{\text{com}}$  calculated with the skymap method and the null energy method against the number of events. Even for  $\mathcal{A}_S^T = 0.25$ , it takes only a few tens of detections with electromagnetic counterparts to establish a  $5\sigma$  violation of GR. Comparatively, the null energy method shows a higher sensitivity since it requires fewer events to attain the  $5\sigma$  level.

We note that  $p_{\text{com}}$  for GR signals gradually approaches the  $5\sigma$  line as the number of

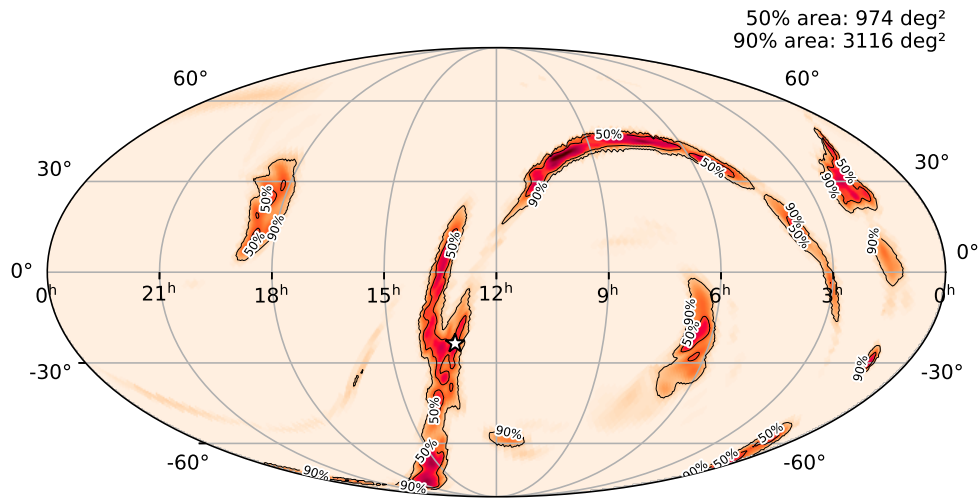


Figure 11.3: Sky map  $\mathcal{P}(\hat{\Omega})$  for GW170817. The star indicates the sky location of the corresponding counterpart SSS17a/AT 2017gfo [21]. The sky map is consistent with the counterpart location, which is enclosed in the 50% credible contour.

events increases; this is because of the systematics in the clustering algorithm used. The largest high power cluster is consistently selected to be the event candidate, but there is a non-negligible chance for high power noise pixels to be included in the periphery of the cluster. This happens especially when the burst energy of the signal is not significantly higher than the background noise. The systematic error accumulates as the number of events increases. Hence, when analyzing real data, we will have to inject large numbers of simulated GR signals into real noise to obtain a reference or “background” distribution of the test statistic to compare “foreground” results with. This procedure will automatically account for the non-stationary and non-Gaussian nature of detector noise as well as the systematics due to the clustering method.

These results show that our analysis pipelines are capable of testing the for existence of alternative polarization modes in addition to tensor modes with a 3-detector network. Given a few tens of detections with known sky position, both methods are sensitive to a scalar mode whose amplitude is a quarter of that of the tensor mode.

A binary neutron star coalescence GW170817 was observed on 17 August 2017 with merger time 12:41:04 UTC (or GPS time 1187008882.4457) [9, 225, 433]. Electromagnetic counterparts were seen, and in particular an optical counterpart was found with very precise localization at right ascension and declination  $\alpha = 13^{\text{h}}09^{\text{m}}48^{\text{s}}.085 \pm 0.018$  and  $\delta = -23^{\circ}22'53''.343 \pm 0.218$ , respectively [12], which provides us an opportunity to apply our tests for alternative polarizations. The null energy test yields a p-value of 0.315, while the sky map method gives 0.790; in the latter case, the sky map  $\mathcal{P}(\hat{\Omega})$  and true sky location  $\hat{\Omega}_{\text{true}}$  are shown in Fig. 11.3. Hence, both tests indicate consistency with the tensor-only hypothesis.



## 11.5 Summary and conclusions

We have introduced two methods to search for polarization modes in addition to the tensor modes, which can be used even with a limited network of detectors (e.g. the two LIGOs and Virgo), though an identifiable electromagnetic counterpart is needed. Both formalisms are based on the notion of null energy. In one case (the *null energy test*) we use the statistical distribution of the null energy for the given true sky location to compute p-values for the validity of the tensor-only hypothesis. The other method (the *sky map test*) first leaves the sky location to be free, turning the distribution of null energy into a sky map, for which the consistency with the true sky location can again be quantified in terms of a p-value. Apart from being able to detect mixtures of different polarization modes rather than having to consider purely tensor, purely vector, and purely scalar hypotheses, no waveform models are needed, so that any transient gravitational wave signal can be used in the tests.

By injecting mock scalar-tensor signals into synthetic stationary and Gaussian noise, we illustrated how both tests can find scalar contributions at  $5\sigma$  confidence with a few tens of signals that have electromagnetic counterparts if the scalar contribution in each signal is at the 25% level. The null energy test turns out to be slightly more sensitive than the skymap method. Both methods show a slowly accumulating bias towards a GR violation when applied to pure tensor signals, due to the null energy clustering algorithm picking up high-energy noise pixels. Thus there is scope for improvement, although even if tens of signals with counterparts were available today, we would certainly be able to already use either method by constructing a reference distribution for our detection statistic and compare “foreground” results with this “background” distribution.

Finally, we have applied our methods to GW170817, finding consistency with the pure-tensor hypothesis. To our knowledge this is the first time a search for a mixture of gravitational wave polarizations has been performed.



## 12.1 Introduction

A number of alternatives to the Kerr black holes of classical general relativity have been proposed, called exotic compact objects (ECOs). For instance, if dark matter is composed of fermionic particles then they may form star-like objects supported by degeneracy pressure: dark matter stars [434]. Boson stars [435] are macroscopic objects made out of scalar fields, as motivated by the discovery of the Higgs, cosmological inflation, axions as a solution of the strong CP problem, moduli in string theory, as well as dark matter. It has also been speculated that there may be gravastars [436]: objects with a so-called de Sitter core where spacetime is self-repulsive – much like dark energy – and held together by a shell of matter. As far as quantum gravity is concerned, fundamental considerations such as Hawking’s information paradox have led some to postulate quantum modifications of the black holes of general relativity, such as firewalls [437] and fuzzballs [438]. For an overview of the various ECOs that have been proposed in the literature, see *e.g.* [439].

When ECOs are part of a binary system that undergoes coalescence, they can make their presence known through a variety of effects that may get imprinted upon the gravitational wave signal, and which would not be there in the case of “standard” binary black holes. These include tidal effects [440, 441], dynamical friction as well as resonant excitations due to dark matter clouds in the vicinity of the objects [442], violations of the no-hair conjecture [443, 444], and gravitational wave “echoes” following a merger [445–452].

Here we will focus on another possible signature of ECOs, namely resonant excitations during inspiral. Such effects have been well-studied in the context of neutron stars [453–457]: as the gravitational wave frequency increases monotonically, at one or more points in time it can become equal to an internal resonant frequency of a compact object. The resulting excitation takes away part of the orbital energy, leading to a speed-up of the orbital motion, which in turn affects the phasing of the gravitational wave signal. As pointed out in [458, 459], for inspiraling boson stars the gravitational wave signature of such effects can potentially be detected.

Thus, it is natural to ask whether there is any sign of resonant excitations in the signals of the presumed binary black hole coalescences of GWTC-1. In this chapter we develop a concrete data analysis framework to search for these signatures in data from Advanced LIGO and Advanced Virgo, and apply it on events from GWTC-1. In particular, in Sec. 12.2 we outline our basic set-up for the effect of resonant excitations on the gravitational wave phase, together with the methodology to search for resonances in gravitational wave signals. This is then applied to simulated signals in Sec. 12.3, where we assess the detectability of the effect. The signals in GWTC-1 are analyzed in Sec. 12.4.

Finally, Sec. 12.5 provides a summary and future directions.

## 12.2 Methodology

### 12.2.1 Imprint of resonant excitations on the gravitational wave phase

Our model of how resonant excitations modify the gravitational wave signal from inspiraling ECOs will be based on that of Flanagan et al. [456]; the context of that work was resonant r-modes in binary neutron star inspiral, but the basic assumptions carry over to the case at hand. For simplicity, let us begin by assuming that only one of the two inspiraling objects undergoes a resonance, at some time  $t_0$ . The excitation takes away part of the orbital energy, causing the gravitational wave phase  $\Phi(t)$  to undergo an apparent advance in time  $\Delta t$  relative to the point particle inspiral phase  $\Phi_{\text{pp}}(t)$ :

$$\Phi(t) = \begin{cases} \Phi_{\text{pp}}(t) & \text{if } t < t_0, \\ \Phi_{\text{pp}}(t + \Delta t) - \Delta\Phi & \text{if } t \geq t_0, \end{cases} \quad (12.1)$$

where the phase shift  $\Delta\Phi$  is such that  $\Phi(t)$  remains continuous at  $t = t_0$ . Assuming  $\Delta t$  to be sufficiently small, we may write

$$\Delta\Phi = \dot{\Phi}_{\text{pp}}(t_0)\Delta t. \quad (12.2)$$

Expanding  $\Phi(t)$  in Eq. (12.1) to linear order in  $\Delta t$ , we then obtain

$$\Phi(t) = \Phi_{\text{pp}}(t) + \dot{\Phi}_{\text{pp}}(t)\Delta t - \dot{\Phi}_{\text{pp}}(t_0)\Delta t. \quad (12.3)$$

The instantaneous gravitational wave frequency is  $\omega = \dot{\Phi}$ ; using this and Eq. (12.2) leads to

$$\Phi(t) = \Phi_{\text{pp}}(t) + \theta(t - t_0) \left[ \frac{\omega(t)}{\omega(t_0)} - 1 \right] \Delta\Phi, \quad (12.4)$$

with  $\theta(t - t_0)$  the usual step function. (Clearly we are assuming that the resonant excitation is of sufficiently short duration so as to be near-instantaneous. At least in the boson star examples of [459] this is a reasonable approximation, but it may not be typical.) In the stationary phase approximation [196], this implies that the phase  $\phi(f)$  of the frequency domain waveform becomes

$$\phi(f) = \phi_{\text{pp}}(f) + \theta(f - f_0) \left[ \frac{f}{f_0} - 1 \right] \Delta\Phi, \quad (12.5)$$

where  $\phi_{\text{pp}}(f)$  is the point particle phase in the Fourier domain, and  $f_0$  the frequency at which the resonance occurs.

In practice, both objects in the binary system may experience resonant excitation; moreover, an individual object may be subject to several resonant excitations at different frequencies during the time the signal is in the detectors' sensitive frequency band [459]. In order to keep the data analysis problem tractable in terms of computational requirements as well as the dimensionality of parameter space, in this chapter we will allow for up to

two main instances of resonance, with associated frequencies  $f_{01}$  and  $f_{02}$ , assuming other resonances to have a negligible effect. The frequency domain phase then becomes

$$\begin{aligned}\phi(f) &= \phi_{\text{pp}}(f) \\ &+ \theta(f - f_{01}) \left[ \frac{f}{f_{01}} - 1 \right] \Delta\phi_{01} \\ &+ \theta(f - f_{02}) \left[ \frac{f}{f_{02}} - 1 \right] \Delta\phi_{02}.\end{aligned}\tag{12.6}$$

In what follows, we will assume that the values of resonance frequencies are ordered such that  $f_{01} < f_{02}$ .

In order for resonances to be observable, it is necessary that (a) the cumulative dephasing with respect to the point particle case is sufficiently large (for second-generation detectors this can be taken to mean larger than  $\sim 1$  radian), and (b) the resonance frequencies are within the detectors' sensitive frequency band. As shown in [460], it is hard to meet both of these criteria simultaneously for ECOs whose horizon modification scale is microscopic (as would be the case for e.g. fuzzballs [438]). On the other hand, the analysis of [458, 459] indicates that for boson stars, it is possible to satisfy both conditions at the same time.

### 12.2.2 Bayesian analysis

Our expression (12.6) for the phase in the presence of resonances leads to a Fourier domain waveform model  $\tilde{h}_{\text{ECO}}(f)$  (which is discussed in more detail below), and this in turn defines a Bayesian hypothesis  $H_{\text{ECO}}$  which states that resonances took place in a given coalescence event. This can be compared with the hypothesis  $H_{\text{BBH}}$  stating that no resonances took place; the associated waveform model  $\tilde{h}_{\text{BBH}}(f)$  just describes the signal from binary black hole coalescence.

Using the techniques introduced in Ch. 3, we can compute the ratio of evidences, or Bayes factor, for the hypotheses  $H_{\text{ECO}}$  and  $H_{\text{BBH}}$ :

$$\mathcal{B}_{\text{BBH}}^{\text{ECO}} \equiv \frac{p(d|H_{\text{ECO}}, I)}{p(d|H_{\text{BBH}}, I)}.\tag{12.7}$$

If for a given gravitational wave signal the (log) Bayes factor  $\ln \mathcal{B}_{\text{BBH}}^{\text{ECO}}$  is high, then this may be indicative of resonances having occurred. However, also noise artefacts can cause  $\ln \mathcal{B}_{\text{BBH}}^{\text{ECO}}$  to be elevated. In order to establish a statistical significance, we add a large number of simulated binary black hole signals to the detector noise and compute the log Bayes factor for all of them, leading to a so-called background distribution  $\mathcal{P}_{\text{BBH}}(\ln \mathcal{B}_{\text{BBH}}^{\text{ECO}})$ . Given a real signal with a particular value for  $\ln \mathcal{B}_{\text{BBH}}^{\text{ECO}}$ , the associated *false alarm probability* (FAP) is given by

$$\text{FAP} = \int_{\ln \mathcal{B}_{\text{BBH}}^{\text{ECO}}}^{\infty} \mathcal{P}_{\text{BBH}}(x) dx.\tag{12.8}$$

Next, consider a large number of simulated signals containing resonant effects, with given ranges for parameters like masses, resonance frequencies, and induced phase shifts for the component objects. Let the distribution of  $\ln \mathcal{B}_{\text{BBH}}^{\text{ECO}}$  for these signals be  $\mathcal{P}_{\text{ECO}}(\ln \mathcal{B}_{\text{BBH}}^{\text{ECO}})$ . Given a threshold  $p_{\text{th}}$  for the false alarm probability, the *efficiency* in uncovering the res-

Sensitivity and IFOs	Event	$\ln \mathcal{B}_{\text{BBH}}^{\text{ECO}}$	FAP
O1 HL	GW150914	-1.76	0.94
	GW151012	-2.18	0.97
	GW151226	-2.66	0.98
O2 HL	GW170104	-1.90	0.96
	GW170608	-4.04	1.00
	GW170823	-1.09	0.59
O2 HLV	GW170729	-0.81	0.25
	GW170809	-1.85	0.85
	GW170814	-2.14	0.93
	GW170818	-1.58	0.75

Table 12.1: Values of log Bayes factors for the GWTC-1 events, together with false alarm probabilities with respect to the background distributions computed for the three kinds of data sets.

onant effects is defined as

$$\epsilon = \int_{\ln \mathcal{B}_{\text{th}}}^{\infty} \mathcal{P}_{\text{ECO}}(y) dy, \quad (12.9)$$

where the threshold  $\ln \mathcal{B}_{\text{th}}$  on the log Bayes factor is obtained through

$$p_{\text{th}} = \int_{\ln \mathcal{B}_{\text{th}}}^{\infty} \mathcal{P}_{\text{BBH}}(x) dx. \quad (12.10)$$

Apart from hypothesis testing we also measure the parameters associated with a hypothesis with the methods introduced in Ch. 3. Finally, the one-dimensional posterior density function for a given parameter is obtained by integrating out all the other parameters.

The baseline of the waveform model was taken to be the frequency domain inspiral-merger-ringdown approximant IMRPhenomPv2 [86, 87, 92], and modifications arising from resonances were added on top of that; in particular, the phase was changed according to Eq. (12.6). Priors for  $\Delta\phi_{01}$  and  $\Delta\phi_{02}$  were chosen to be uniform in  $[0, 100]$ . Those for  $f_{01}$ ,  $f_{02}$  were taken to be uniform in the interval  $[20, 440]$  Hz, where the lower limit of the range is the detectors'  $f_{\text{low}}$  and the upper limit corresponds to the innermost stable circular orbit (ISCO) for a total mass of  $M = 10 M_{\odot}$ . For sources with a higher total mass this implies that our analyses will in practice also be searching for non-standard effects in the phase past the end of inspiral. In principle we could have restricted  $f_{01}$ ,  $f_{02}$  to be below the ISCO frequency; however, allowing for an extended range has the benefit that we can be sensitive to more general departures from BBH behavior in the inspiral-merger-postmerger phase evolution than just resonant excitations of the component objects during inspiral.

Finally, the software implementation of our methodology was based on the LIGO Algorithm Library Suite (LALSuite); the likelihood calculation was performed using the nested sampling algorithm in the `lalInference` package of LALSuite [204].

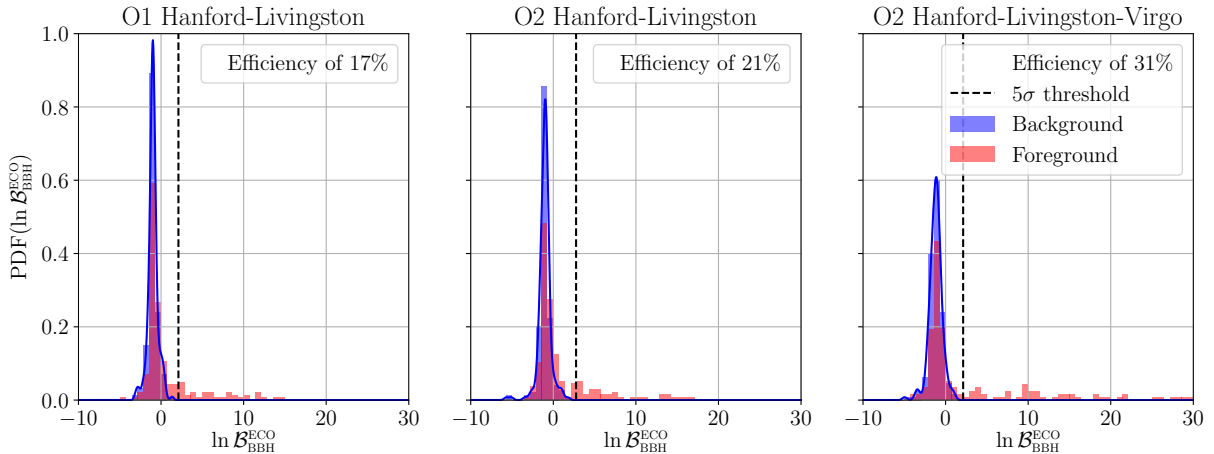


Figure 12.1: Distributions of log Bayes factors for the ECO hypothesis over the BBH hypothesis for BBH injections (blue) and ECO injections (red), with parameter ranges as described in the main text. For the BBH injections, we also show Gaussian KDE fits (the smooth curves) to the background distribution, with respect to which a  $5\sigma$  threshold for detectability of resonances is established (the dashed vertical lines). The left panel shows results for injections in O1 data from LIGO Hanford and LIGO Livingston; the middle panel uses O2 data where only the two LIGO detectors were active; and the right panel is for O2 when the two LIGO detectors as well as Virgo were on. For the chosen  $5\sigma$  threshold, the log Bayes factor distributions for ECOs lead to efficiencies of, respectively, 17%, 21%, and 31%.

## 12.3 Simulations

### 12.3.1 Measurability of resonance effects in the O1 and O2 observing runs

First we want to gain some basic insight into the size of the resonance effects that could be measurable with Advanced LIGO and Advanced Virgo. To this effect we compute  $\ln \mathcal{B}_{\text{BBH}}^{\text{ECO}}$  for two sets of simulated signals, or *injections*, in LIGO-Virgo data from the first two observing runs (O1 and O2) [6, 433, 461, 462], with one set corresponding to BBHs and the other to ECOs. For both sets, component masses are drawn uniformly from  $m_1, m_2 \in [5, 70] M_\odot$ , but total masses are restricted to  $m_1 + m_2 \in [15, 110] M_\odot$ , consistent with the mass estimates for the BBH-like events in GWTC-1 [6]. The latter leads to a maximum ISCO frequency of  $f_{\text{ISCO},\text{max}} = 293$  Hz, and a median of  $f_{\text{ISCO},\text{median}} = 83$  Hz. Sources are distributed uniformly in volume, with a lower cut-off on the network signal-to-noise ratio of  $\text{SNR} \geq 8$ .

In the set of injections corresponding to ECOs, the induced phase shifts due to resonances are taken to be uniform in  $\Delta\phi_{01}, \Delta\phi_{02} \in (0, 10]$  rad, and possible resonance frequencies are chosen uniformly in  $f_{01} \in [20, 50]$  Hz,  $f_{02} \in [20, 100]$  Hz. We only implement phase modifications for frequencies below  $f_{\text{ISCO}}$ . We reject injections for which both  $f_{01}$  and  $f_{02}$  are above  $f_{\text{ISCO}}$ ; of those remaining, 59% will exhibit only one resonance during inspiral, and the rest will have two of them. Finally, spin directions are chosen to be uniform on the sphere, with dimensionless spin magnitudes in the interval  $[0, 1)$ .

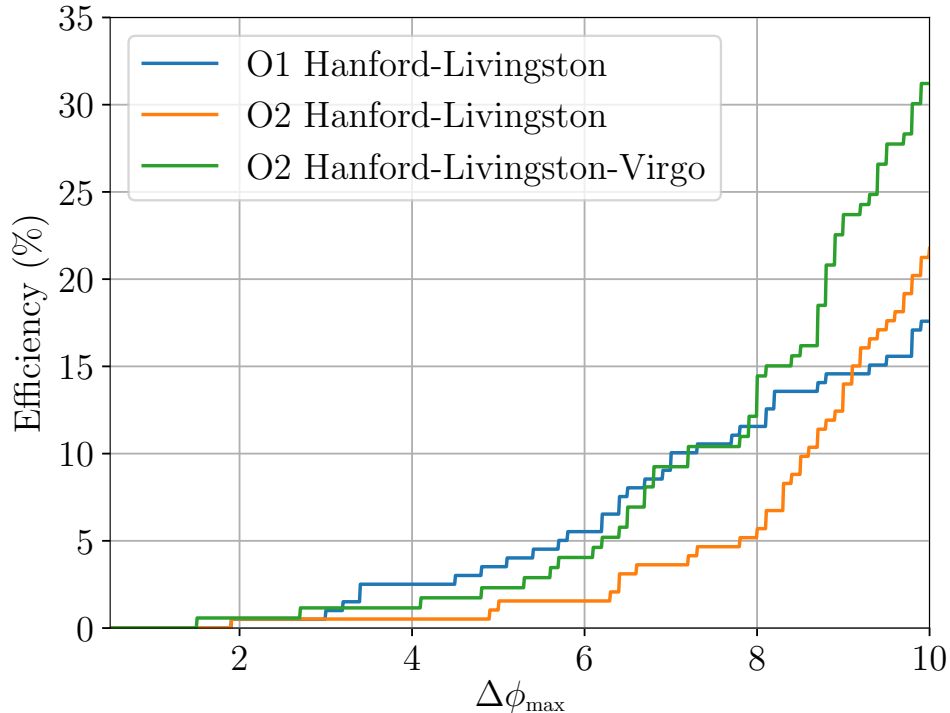


Figure 12.2: Efficiencies with respect to a  $5\sigma$  threshold as function of the size of the phase shifts associated with resonances. We consider subsets of foreground samples in which the  $\Delta\phi_{0i}$ ,  $i = 1, 2$  do not exceed some given  $\Delta\phi_{\max}$ , and progressively increase this maximum value.

Results are shown in Fig. 12.1, for 200 BBH injections and an equal number of ECO injections. Distributions of  $\ln \mathcal{B}_{\text{BBH}}^{\text{ECO}}$  are displayed separately for the case of two LIGO detectors active in O1, two LIGO detectors active in O2, and two LIGO detectors *and* Virgo active in O2. In each scenario, the blue and red histograms respectively refer to the distributions  $\mathcal{P}_{\text{BBH}}(\ln \mathcal{B}_{\text{BBH}}^{\text{ECO}})$  and  $\mathcal{P}_{\text{ECO}}(\ln \mathcal{B}_{\text{BBH}}^{\text{ECO}})$  defined in the previous section. The background distributions  $\mathcal{P}_{\text{BBH}}(\ln \mathcal{B}_{\text{BBH}}^{\text{ECO}})$  are sufficiently well-behaved to allow for accurate Gaussian KDE approximations, with respect to which we calculate threshold values  $\ln \mathcal{B}_{\text{th}}$  as in Eq. (12.10), for  $p_{\text{th}}$  corresponding to a significance of  $5\sigma$ . In each of the three cases, we then estimate the efficiency for  $5\sigma$  detection of resonances by counting the fraction of foreground  $\ln \mathcal{B}_{\text{BBH}}^{\text{ECO}}$  samples that exceed  $\ln \mathcal{B}_{\text{th}}$ . This leads to efficiencies of, respectively, 17%, 21%, and 31% for analyses in the three data sets; as expected, the three-detector network with O2 sensitivity returns the highest efficiency. This indicates that O1 and O2 would have allowed for observations of resonance-induced phase shifts with  $\Delta\phi_{01}, \Delta\phi_{02} \lesssim 10$  rad.

To assess how low a phase shift can be detectable, we can look at subsets of foreground injections for which neither  $\Delta\phi_{0i}$ ,  $i = 1, 2$  exceeds some given value  $\Delta\phi_{\max}$ , and in each of the subsets determine efficiencies for  $5\sigma$  detection of resonances. The results are shown in Fig. 12.2. We conclude that the chance of confidently detecting a resonance with *e.g.*  $\Delta\phi_{0i} \leq 5$  is relatively low ( $< 5\%$ ), and the signature of resonances mainly starts to be picked up from  $\Delta\phi_{0i} \gtrsim 8$ .



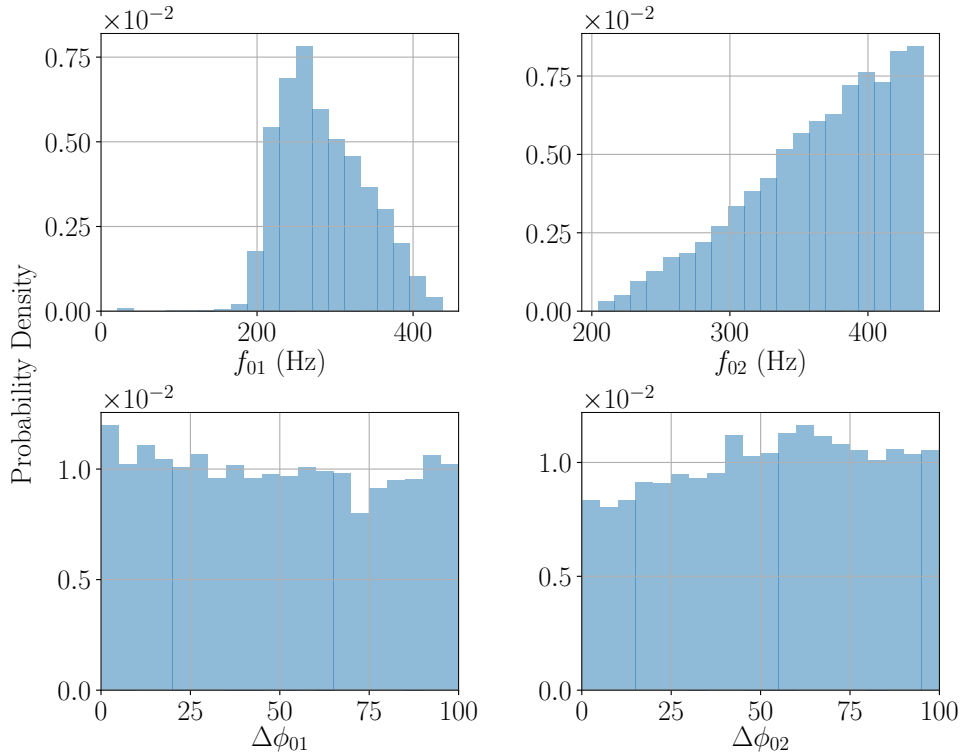


Figure 12.3: Posterior density functions for  $f_{01}$ ,  $f_{02}$ ,  $\Delta\phi_{01}$ , and  $\Delta\phi_{02}$ , in a case where no resonances are present and the signal corresponds to a BBH. For this event the inspiral ended at  $f_{\text{ISCO}} = 94.7$  Hz; the posteriors for  $f_{01}$  and  $f_{02}$  mainly have support for frequencies well above that, and the  $\Delta\phi_{01}$ ,  $\Delta\phi_{02}$  distributions largely return the prior.

### 12.3.2 A note on parameter estimation

Now let us turn to parameter estimation for resonance frequencies and phase shifts. Our Bayesian hypothesis  $H_{\text{ECO}}$  effectively assumes the presence of two resonances. Of course, in reality a binary coalescence involving ECOs may have zero instances of resonance in the detectors' sensitive frequency band, or only one, or more than two. Thus, though it is always possible to arrive at posterior density distributions for the two resonance frequencies  $f_{01}$ ,  $f_{02}$  and associated phase shifts  $\Delta\phi_{01}$ ,  $\Delta\phi_{02}$ , these should be taken with a grain of salt. Indeed, our real tool for assessing the presence of resonances is  $\ln \mathcal{B}_{\text{BBH}}^{\text{ECO}}$  together with its background distribution  $\mathcal{P}_{\text{BBH}}(\ln \mathcal{B}_{\text{BBH}}^{\text{ECO}})$ . Nevertheless, for completeness we show some representative example parameter estimation results for different cases.

First of all, Fig. 12.3 shows posterior densities for the case of a binary black hole injection. No resonance frequencies are in band, and indeed the sampling puts most of the posterior weight for  $f_{01}$ ,  $f_{02}$  at frequencies well above ISCO (where in this case  $f_{\text{ISCO}} = 97.4$  Hz). The distributions for  $\Delta\phi_{01}$  and  $\Delta\phi_{02}$  largely return the prior.

In Fig. 12.4, we show posteriors for an ECO case with two resonance frequencies in band, for an event whose  $\ln \mathcal{B}_{\text{BBH}}^{\text{ECO}}$  is above the  $5\sigma$  threshold for detectability of resonances. The parameters related to resonances are estimated reasonably well.

Finally, Fig. 12.5 shows posteriors for an example ECO with only a *single* resonance. Though in this case parameter estimation cannot be fully reliable, the posteriors for  $f_{01}$  and  $\Delta\phi_{01}$  reasonably capture the true resonance frequency and phase shift. The posterior

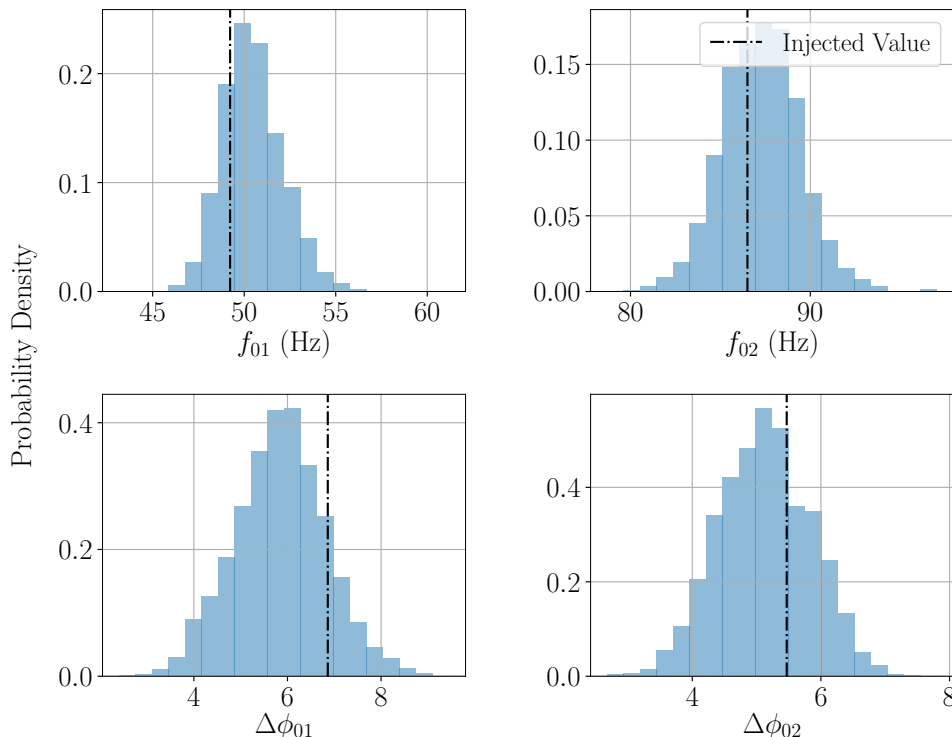


Figure 12.4: Posterior density functions for an example ECO with two resonances during inspiral; the dashed-dotted vertical lines indicate the true values of  $f_{01}$ ,  $f_{02}$ ,  $\Delta\phi_{01}$ , and  $\Delta\phi_{02}$ . In this case  $\ln \mathcal{B}_{\text{BBH}}^{\text{ECO}} = 19.98$ , *i.e.* above our  $5\sigma$  detection threshold for resonances.

for  $\Delta f_{02}$  only has support well above the ISCO frequency (here  $f_{\text{ISCO}} = 45.4$  Hz), reminiscent of the BBH case of Fig. 12.3. However, we stress again that our “detection statistic”  $\ln \mathcal{B}_{\text{BBH}}^{\text{ECO}}$  and its background distribution are what provide the means to establish the presence of resonances; and indeed, the log Bayes factor for this injection is comfortably above the  $5\sigma$  threshold.

## 12.4 Searching for resonances in GWTC-1 events

Next we turn to analyzing the presumed binary black hole events of GWTC-1 [433, 463]. The main results are given by Fig. 12.6 and Table 12.1. The Figure shows the values of  $\ln \mathcal{B}_{\text{BBH}}^{\text{ECO}}$  for the various events in the three kinds of data sets. We also show again the background distributions  $\mathcal{P}_{\text{BBH}}(\ln \mathcal{B}_{\text{BBH}}^{\text{ECO}})$ , which the “foreground” log Bayes factors are clearly consistent with. In the Table, for each event we explicitly list log Bayes factors, as well as the false alarm probability with respect to the background distribution.

Two caveats are in order regarding the false alarm probabilities that we list. First, a larger number of BBH injections than the ones performed here will of course result in a more accurate assessment of the background  $\mathcal{P}_{\text{BBH}}(\ln \mathcal{B}_{\text{BBH}}^{\text{ECO}})$ . Secondly, the background will depend upon the distributions of masses and spins that were chosen for the injected BBH signals (specified in the previous section), but the astrophysical parameter distributions for the population of heavy compact objects in the Universe are likely to differ from these. In the future one could use the *measured* parameter distributions [13], whose

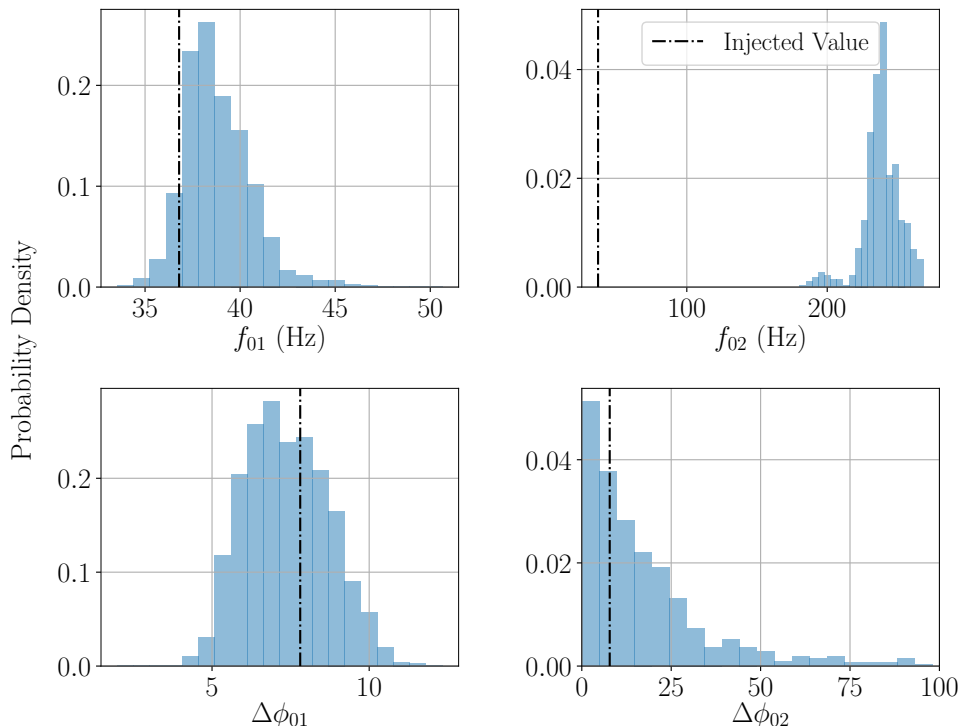


Figure 12.5: Posterior density functions for an example ECO with *only one* resonance. The dashed-dotted vertical lines indicate the true values of frequency and phase shift. The posteriors for  $f_{01}$  and  $\Delta\phi_{01}$  capture these reasonably well, but the posterior for  $f_{02}$  again has support at values much above  $f_{\text{ISCO}} = 45.4$  Hz, similar to the BBH case of Fig. 12.3. Also, the  $\Delta\phi_{02}$  distribution is consistent with 0. In this example  $\ln \mathcal{B}_{\text{BBH}}^{\text{ECO}} = 10.18$ , well above the  $5\sigma$  threshold.

accuracy will increase as more detections are made. That said, all of the values of  $\ln \mathcal{B}_{\text{BBH}}^{\text{ECO}}$  that we obtain for individual events in GWTC-1 are anyway negative, thus favoring the BBH hypothesis.

Though we find no evidence for the presence of resonances in any of the GWTC-1 events, for completeness we show posterior density functions obtained for the resonance frequencies  $f_{01}$ ,  $f_{02}$  (Fig. 12.7), and for the phase shifts  $\Delta\phi_{01}$ ,  $\Delta\phi_{02}$  (Fig. 12.8). The posteriors for  $f_{01}$ ,  $f_{02}$  tend to be rather similar to the ones for the BBH injection of Fig. 12.3, having most of their support at high frequencies, beyond ISCO. Also, the posteriors for  $\Delta\phi_{01}$ ,  $\Delta\phi_{02}$  are for the most part consistent with the priors.

## 12.5 Summary and future directions

Exotic compact objects may exhibit resonant excitations during inspiral, thereby taking away orbital energy from a binary system, leading to a speed-up of the orbital phase evolution relative to the binary black hole case. We have set up a Bayesian framework to look for such resonances under the assumption that they are of short duration, and that up to two resonant frequencies can be present in the part of the inspiral that is in the sensitive band of the Advanced LIGO and Advanced Virgo detectors. The associated model for the modification of the phase evolution allows one to compute a log Bayes factor

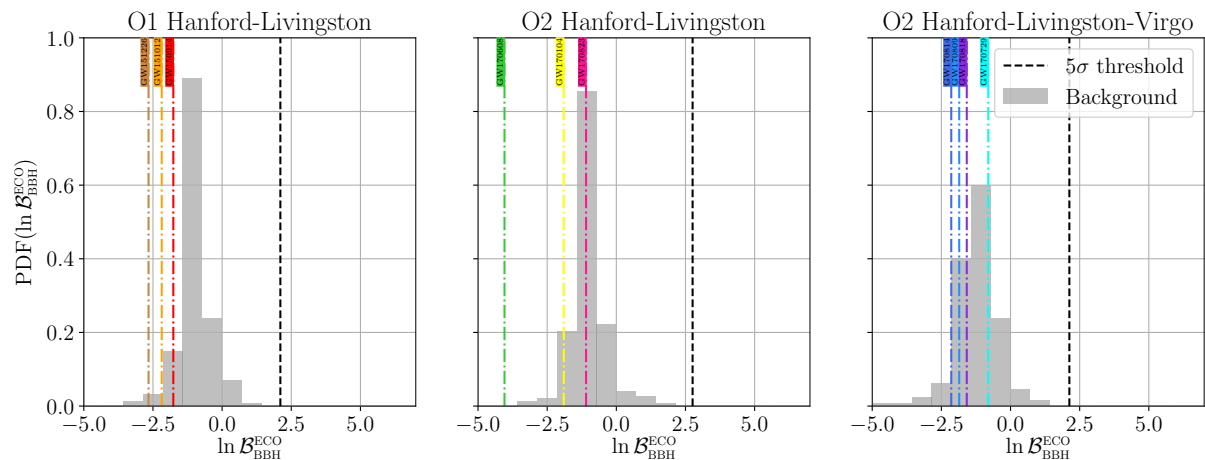


Figure 12.6: log Bayes factors for the presumed binary black hole events of GWTC-1 (vertical dashed-dotted lines). For reference we also show the BBH background distributions of Fig. 12.1 again distinguishing between the case of two detectors in O1 (left), the two LIGO detectors in O2 (middle), and the two LIGOs together with Virgo in O2 (right); vertical dashed lines again indicate  $5\sigma$  significance thresholds as in Fig. 12.1. It will be clear that for none of the GWTC-1 events, observable resonances are present in any statistically significant way.

$\ln \mathcal{B}_{\text{BBH}}^{\text{ECO}}$  quantifying the ratio of evidences for the hypothesis that resonances occurred and the hypothesis that none were present.

We calculated log Bayes factors for two sets of simulated signals embedded in data from the O1 and O2 observing runs, one in which the signals were from BBHs, and another where resonances were present. Using the distribution of  $\ln \mathcal{B}_{\text{BBH}}^{\text{ECO}}$  from the former set as background and from the latter as foreground, we were able to conclude that the effect of resonance-induced phase shifts of  $\Delta\phi_{01}, \Delta\phi_{02} \lesssim 10$  rad can be detectable at  $5\sigma$  significance with an efficiency as large as  $\sim 30\%$ .

We then turned to the presumed binary black hole events of GWTC-1. In all cases the  $\ln \mathcal{B}_{\text{BBH}}^{\text{ECO}}$  were found to be consistent with background, and moreover they were all negative, thus favoring the hypothesis that no resonances had occurred while the signals were in the detectors' sensitive frequency band. Posterior density functions for resonance frequencies and induced phase shifts were consistent with these non-detections of resonant excitations.

Although so far we have found no evidence for resonances in binary black hole-like signals, it is possible that this will happen in the future. In that case one will want to also characterize the resonant excitations. The example framework presented here assumed two resonances in the ECO hypothesis  $H_{\text{ECO}}$ . However, one could envisage Bayesian ranking within a list of ECO hypotheses  $H_{\text{ECO}}^{(n)}$  that assume there to be  $n$  resonances in band, with  $n = 1, 2, 3, \dots$ . Alternatively, one could have a single ECO hypothesis allowing for a variable number of resonances, with this number itself being sampled over. These further improvements are left for future work.

Finally, with minor modifications our methodology could be used to search for resonant r-modes in binary neutron star inspirals [456, 464]. In that case the induced phase shifts are expected to be below detectable levels with existing instruments, but they may be in

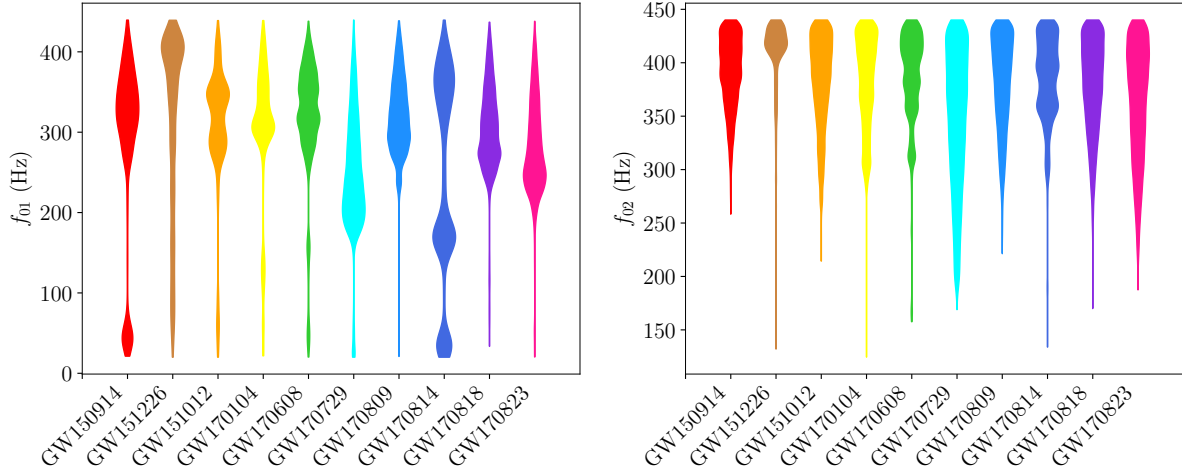


Figure 12.7: Posterior density functions for the resonance frequencies  $f_{02}$  (*left*) and  $f_{01}$  (*right*), for each of the GWTC-1 events.

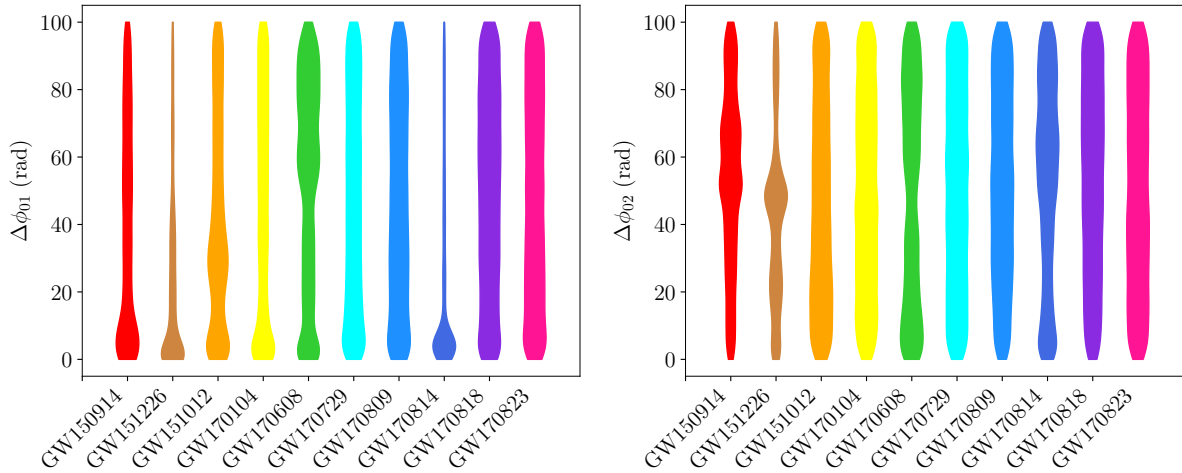


Figure 12.8: Posterior density functions for the phase shifts  $\Delta\phi_{02}$  (*left*) and  $\Delta\phi_{01}$  (*right*), for each of the GWTC-1 events.

reach of more sensitive detectors in the foreseeable future [465]. Note that for r-modes the relevant parameters can be related to other properties of the neutron stars [456]; for example the resonance frequencies are proportional to the spin frequencies, so that they need not be treated as completely free parameters. Setting up appropriate measurements then deserves a separate, in-depth treatment; this is work in progress.



Since Albert Einstein predicted the existence of gravitational waves, people have been trying to detect them for years. Luckily, we were born in a fantastic time when we could regularly detect gravitational waves, marking the beginning of gravitational-wave astronomy and multi-messenger astronomy. With such a novel tool, we can look into the Universe like never before. This thesis presented different aspects of physics probed with gravitational waves. First, we showcased how the equation-of-state (EOS) of neutron star matter is constrained by astrophysical observations, theoretical nuclear calculations, and terrestrial nuclear experiments. Subsequently, we presented how nuclear physics knowledge can help answer astrophysical questions. Finally, we introduced methods to test the validity of general relativity and applied them to the observations.

### **Constraining the equation-of-state of supranuclear matter**

Because Quantum Chromodynamics (QCD) calculations become very difficult at the density of a neutron star's core, the exact nature of matter at such a density is still unknown. In Part II, we presented how to estimate the properties of neutron star matter via observational constraints. In particular, constraints on the supranuclear matter based on astrophysical observations (Ch. 5), including nuclear theoretical calculation (Ch. 6, Ch. 8), and including terrestrial nuclear experiments (Ch. 9) were presented.

In Ch. 5, we demonstrated how one could probe the existence and the nature of a first-order phase transition in supranuclear matter with gravitational-wave signals from binary neutron star (BNS) mergers. Applying our methodology on the two BNS detections made so far, no decisive conclusion could be drawn, but in future our methodology may indicate the presence of a phase transition, or exclude it in the accessible density range.

In Ch. 7, we demonstrated how one could distinguish between a low mass black hole and a neutron star with the aid of EOS constraints and concluded that GW190814 is very likely ( $> 99.9\%$ ) to be a binary black hole merger instead of a neutron star-black hole merger.

In Ch. 6, Ch. 8 and Ch. 9, we presented a versatile multi-messenger framework, which allows information on the EOS from vastly different channels to be included. Such a framework enables us to put an accurate and precise constraint on the EOS. In particular, we have arrived at the state-of-the-art constraint of  $R_{1.4} = 12.01_{-0.77}^{+0.78}$  km (95% credibility) and demonstrated an excellent agreement between astrophysical observations and terrestrial experiments. This framework also laid the foundation for the future of probing nuclear physics via multi-messenger astronomy.

### **Astrophysical implications of an accurate constraint on the EOS**

Besides the interest of the nuclear physics community, an accurate understanding of the EOS can also benefit the astrophysics community. In Ch. 10, we developed a method to

tell if a BNS signal is gravitationally lensed even if we have only one image. The method relies on the difference between the measured and intrinsic neutron star matter properties, which is impossible without a proper understanding of the EOS.

### **Testing the validity of general relativity**

Besides the EOS, one can also test the strong field dynamics of the spacetime using gravitational-wave observations. This part described how one can probe the nature of spacetime and the nature of black-hole-like compact objects.

In Ch. 11, we developed the method for probing the presence of polarizations beyond the ones of general relativity with a limited number of detectors. The method was applied to GW170817 and showed no evidence of non-tensor polarizations.

In Ch. 12, we demonstrated how one can distinguish an exotic compact object (ECO) from a black hole by looking for the signatures of resonances. We developed a framework for 1) assigning statistically robust statements on the presence of resonance and 2) measuring the properties of the resonance. Using this method on the GWTC-1 catalog, we found no evidence of the presence of an ECO.

### **The age of statistics**

**“New physics will be discovered by the best statisticians.”**  
— Prof. Kenneth Young, 2012.

I believe this thesis is a hint of the above statement. Without a carefully constructed statistical framework, one will not be able to robustly extract physics from detections, observations, and experiments. Especially in the age of observational physics, one has to attach great importance to statistics. With a correct attitude toward statistics and data analysis, I believe a bright future in physics is awaiting.



## Astronomy

Since the existence of humanity, we have been looking up to the sky and wondering what those stars are. The word “Astronomy” literally means the science of studying the laws of stars. Such interest in the stars was shared by many ancient civilizations, e.g., Babylonians, Greeks, Indians, Egyptians, Chinese, and Maya. Ancient civilizations arrived at an initial understanding of celestial phenomena by studying the stars, the Moon, and the Sun.

During the Renaissance, our understanding of the celestial mechanics was revolutionized. Nicolaus Copernicus (1473-1543) proposed a heliocentric model of the solar system, which was defended by Galileo Galilei (1564-1642), and which acted as the foundation for the discoveries by Johannes Kepler (1571-1630). Kepler was the first to come up with the laws that accurately explained the motion of the planets around the Sun. On the other hand, Kepler could not develop the underlying framework to explain the rules he recorded. With his creation of celestial dynamics and the law of universal gravitation, Isaac Newton (1642-1726) finally explained the motions of the planets.

However, at 19<sup>th</sup> century, Newtonian gravity was challenged by observation, the precession of Mercury’s perihelion (The closest point to the Sun on Mercury’s orbit). Urbain Le Verrier (1811-1877) discovered the precession of Mercury’s perihelion in 1859, which cannot be explained by Newtonian gravity. It was not until Albert Einstein (1879-1955) introduced the general theory of relativity that this phenomenon could be properly understood.

## The general theory of relativity and gravitational waves

Newton’s law of universal gravitation describes gravity as an attractive force between objects with masses. This point of view was changed by the general theory of relativity introduced by Albert Einstein in 1915. In general relativity, space and time are combined into one continuum, spacetime. Spacetime is not solid but flexible, and can be curved and bent. This curvature is caused by energy, and momentum.

Despite general relativity’s complexity and counter-intuitiveness, it became “the law of gravitation” as it successfully explained observations that deviate from Newtonian gravity, e.g., deflection of light by gravity. In addition, it also predicts many novel phenomena, e.g., gravitational lensing, black holes, and neutron stars. In particular, the understanding of gravitational time delay turns out to be essential for the Global Positioning System (GPS) to work. Among all predictions, the presence of gravitational waves was the latest to be directly verified.

Gravitational waves are ripples in the fabric of spacetime caused by accelerating masses and that propagate at the speed of light outward from their source. They carry energy and momentum and stretch spacetime and everything in it while propagating. The measured orbital decay of the Hulse–Taylor binary pulsar, which matched the decay predicted by general relativity as energy is lost to gravitational radiation, provided the first indirect proof for the presence of gravitational waves.

## Detection of gravitational waves

Detection of gravitational waves is very challenging due to their tremendously small effect. To detect gravitational waves, one needs to measure length changes that are more than 1000 times smaller than a proton. After years of development and innovation, the Laser Interferometer Gravitational-wave Observatory (LIGO) was constructed.

On September 14, 2015, humankind made its first direct detection of a gravitational-wave signal. The waveform of the detected signal matched the prediction of general relativity, and it was emitted by a pair of black holes of around 36 and 29 solar masses. The event named GW150914 directly confirmed the existence of gravitational waves. It demonstrated the existence of a binary stellar-mass black holes and the fact that such mergers could occur within the universe's current age. After that, signals from binary black hole mergers started being detected on a regularly basis, marking the beginning of gravitational-wave astronomy.

On August 17, 2017, the first gravitational-wave signal emitted by binary neutron stars was detected by LIGO together with Virgo, the gravitational-wave detector at Italy. Moreover, numerous telescopes worldwide also saw the light of that merger. With its gamma-ray burst detected by the Fermi Gamma-ray Space Telescope and the INTERNATIONAL Gamma-Ray Astrophysics Laboratory (INTEGRAL) spacecraft and the kilonova transient observed, multi-messenger astronomy began on that day.

## The nature of neutron star matter

Neutron stars are the collapsed cores of massive stars made of neutrons or other forms of nuclear matter. They are the densest objects in the Universe. With a mass of 1-2 solar masses and the size of Amsterdam, it is the best laboratory for studying strong gravity and nuclear interaction.

Suppose you give a bunch of nuclear astrophysicist neutron star mass and ask them what the corresponding radius would be; instead of a single answer, you will receive a few tens of different responses. This is because the nature of neutron matter is not precisely known due to the theoretical difficulties associated with calculations in Quantum Chromodynamics (QCD), the theory that described the strong nuclear interaction. Different approximations and approaches have been taken, resulting in vastly different results. With the aid of gravitational and multi-messenger observations of neutron stars, we can tackle this long-standing problem from the observational side.

This thesis demonstrated how one could probe the properties of the neutron star matter using gravitational waves, light, theoretical nuclear calculation, and nuclear experiments on Earth. Using this versatile framework on supercomputers, we arrived at a state-of-the-art understanding of neutron star matter. We provided an accurate measurement of the size of a neutron star at 1.4 solar masses, which is about 12 km. This discovery significantly impacts the nuclear physics community. It allows us to understand better how nuclear physics behaves at such densities.

Besides the nuclear physics community, the astrophysics community also benefits from an accurate understanding of neutron star matter. This thesis showcases two such applications. First, we have shown how one can distinguish a low mass black hole and a neutron star when no light is emitted. Second, we introduced methods to check if a binary neutron star merger signal is gravitationally lensed even if we only see one image.

---

## Testing Einstein's general relativity

Karl Popper (1902-1994) stated that any scientific statement must be falsifiable. Even though Einstein's general relativity has been a great success, in this tradition, we have to put general relativity to the test and see if it holds.

This thesis proposed and applied two tests of general relativity. In general relativity, a gravitational wave has only two polarizations. However, in alternative theories of gravity, one can have up to four additional polarizations, and we introduced methods to look for them. We applied the methods to GW170817, and found no evidence of non-GR polarizations.

Moreover, we also looked into the nature of the black holes. In particular, we checked whether the gravitational wave signals that are seemingly emitted by binary black holes may actually have been due to even more exotic objects, by looking for particular types of vibrations that might occur in them. We checked all ten presumed binary black hole signals observed by LIGO and Virgo during their first and second observation runs with this framework. We did not find any evidence for such effects, and the sources of the signals were likely to be ordinary black holes.



## Astronomie

Sinds het bestaan van de mensheid kijken we naar de lucht en vragen we ons af wat die sterren zijn. Het woord “astronomie” betekent letterlijk de wetenschap van het bestuderen van de wetten van sterren. Een dergelijke interesse in de sterren werd gedeeld door veel oude beschavingen, bijvoorbeeld Babyloniërs, Grieken, Indiërs, Egyptenaren, Chinezen en Maya’s. Oude beschavingen kwamen tot een eerste begrip van hemelverschijnselen door de sterren, de maan en de zon te bestuderen.

Tijdens de Renaissance werd ons begrip van de hemelmechanica radicaal veranderd. Nicolaus Copernicus (1473-1543) stelde een heliocentrisch model van het zonnestelsel voor, dat werd verdedigd door Galileo Galilei (1564-1642), en dat als basis diende voor de ontdekkingen door Johannes Kepler (1571-1630). Kepler was de eerste die wetten voorstelde die de beweging van de planeten rond de zon nauwkeurig verklaarden. Aan de andere kant kon Kepler het onderliggende raamwerk niet ontwikkelen om de regels die hij vastlegde uit te leggen. Met zijn schepping van de hemeldynamiek en de wet van de universele zwaartekracht verklaarde Isaac Newton (1642-1726) eindelijk de bewegingen van de planeten.

In de 19e eeuw kwam de zwaartekracht van Newton echter onder druk te staan door een waarneming, de precessie van het perihelium van Mercurius (het punt dat het dichtst bij de zon staat in de baan van Mercurius). Urbain Le Verrier (1811-1877) ontdekte deze precessie in 1859, die niet kan worden verklaard door de zwaartekracht van Newton. Pas toen Albert Einstein (1879-1955) de algemene relativiteitstheorie introduceerde, kon dit fenomeen goed worden begrepen.

## De algemene relativiteitstheorie en zwaartekrachtsgolven

Newton’s wet van universele zwaartekracht beschrijft zwaartekracht als een aantrekkingskracht tussen objecten met massa’s. Dit standpunt werd veranderd door de algemene relativiteitstheorie die in 1915 door Albert Einstein werd geïntroduceerd. In de algemene relativiteitstheorie worden ruimte en tijd gecombineerd tot één continuüm, ruimtetijd. Ruimtetijd is niet solide maar flexibel en kan worden gekromd en gebogen. Deze kromming wordt veroorzaakt door energie en momentum.

Ondanks de complexiteit en het tegen-intuïtieve karakter van de algemene relativiteitstheorie, werd het de ‘wet van de zwaartekracht’ omdat het met succes waarnemingen verklaarde die afwijken van de Newtoniaanse zwaartekracht, bijvoorbeeld afbuiging van licht door zwaartekracht. Daarnaast voorspelt het ook veel nieuwe fenomenen, zoals zwaartekrachtlenzsvorming, zwarte gaten en neutronensterren. Vooral het begrip van gravitationele tijdsvertraging blijkt essentieel te zijn om het Global Positioning System (GPS) te laten werken. Van alle voorspellingen was de aanwezigheid van zwaartekrachtsgolven de laatste die rechtstreeks werd geverifieerd.

Zwaartekrachtsgolven zijn rimpelingen in het weefsel van de ruimtetijd die worden veroorzaakt door versnellende massa’s en die zich voortplanten met de snelheid van het licht, naar buiten toe vanaf hun bron. Ze dragen energie en momentum en rekken de ruimtetijd en alles erin terwijl ze zich voortplanten. Het gemeten orbitale verval van de

Hulse-Taylor binaire pulsar, dat overeenkwam met het verval voorspeld door de algemene relativiteitstheorie als energie verloren gaat aan zwaartekrachtstraling, leverde het eerste indirecte bewijs voor de aanwezigheid van zwaartekrachtsgolven.

## Detectie van zwaartekrachtsgolven

De detectie van zwaartekrachtsgolven is zeer uitdagend vanwege hun enorm kleine effect. Om zwaartekrachtsgolven te detecteren, moet men lengteveranderingen meten die meer dan 1000 keer kleiner zijn dan de afmetingen van een proton. Na jaren van ontwikkeling en innovatie werd de Laser Interferometer Gravitational-wave Observatory (LIGO) gebouwd.

Op 14 september 2015 deed de mensheid zijn eerste directe detectie van een zwaartekrachtgolf signaal. De golfvorm van het gedetecteerde signaal kwam overeen met de voorspelling van de algemene relativiteitstheorie en werd uitgezonden door een paar zwarte gaten van ongeveer 36 en 29 zonsmassa's. De gebeurtenis genaamd GW150914 bevestigde direct het bestaan van zwaartekrachtsgolven. Het toonde het bestaan aan van dubbele zwarte gaten en het feit dat dergelijke samensmeltingen zouden kunnen plaatsvinden binnen de huidige leeftijd van het universum. Daarna werden regelmatig signalen van binaire samensmeltingen van zwarte gaten gedetecteerd, wat het begin markeerde van de astronomie met zwaartekrachtgolven.

Op 17 augustus 2017 werd het eerste zwaartekrachtgolf signaal uitgezonden door binaire neutronensterren gedetecteerd door LIGO samen met Virgo, de zwaartekrachtgolfdetector in Italië. Bovendien zagen ook tal van telescopen wereldwijd het licht van die fusie. Met zijn gammastraaluitbarsting gedetecteerd door de Fermi Gamma-ray Space Telescope en het INTERNational Gamma-Ray Astrophysics Laboratory (INTEGRAL) ruimtevaartuig en de waargenomen 'kilonova'-nagloed, begon de multi-messenger-astronomie op die dag.

## De aard van de materie van neutronensterren

Neutronensterren zijn de ingestorte kernen van massieve sterren die bestaan uit neutronen of andere vormen van nucleaire materie. Het zijn de dichtste objecten in het heelal. Met een massa van 1-2 zonsmassa's en de grootte van Amsterdam is het het beste laboratorium voor het bestuderen van sterke zwaartekracht en nucleaire interactie.

Stel dat je een stel kern-astrofysici een waarde geeft voor de massa van een neutronenster en hen vraagt wat de overeenkomstige straal zou zijn; dan krijg je in plaats van één antwoord wel enkele tientallen verschillende antwoorden. Dit komt omdat de aard van neutronenmaterie niet precies bekend is vanwege de theoretische problemen die gepaard gaan met berekeningen in Quantum Chromodynamica (QCD), de theorie die de sterke nucleaire interactie beschrijft. Er worden uiteenlopende aannames gedaan en benaderingen gevolgd, wat tot zeer verschillende resultaten heeft geleid. Met behulp van gravitatie- en multi-messenger-waarnemingen van neutronensterren kunnen we dit al lang bestaande probleem van de waarnemingskant aanpakken.

Dit proefschrift heeft laten zien hoe men de eigenschappen van de materie van de neutronenster kan onderzoeken met behulp van zwaartekrachtsgolven, licht, theoretische nucleaire berekeningen en nucleaire experimenten op aarde. Met behulp van supercomputers kwamen we tot een state-of-the-art begrip van de materie van neutronensterren. We hebben een nauwkeurige meting gedaan van de straal van een neutronenster met een

---

massa van 1,4 zonsmassa's, wat ongeveer 12 km is. Dit heeft een aanzienlijke impact op de kernfysica-gemeenschap; het stelt ons in staat om beter te begrijpen hoe materie zich gedraagt bij dergelijke dichtheden.

Naast de kernfysica-gemeenschap, heeft de astrofysica-gemeenschap ook baat bij een nauwkeurig begrip van de materie van neutronensterren. Dit proefschrift laat twee van dergelijke toepassingen zien. Ten eerste hebben we laten zien hoe je een zwart gat met een lage massa kan onderscheiden van een neutronenster als er geen licht wordt uitgezonden. Ten tweede hebben we methoden geïntroduceerd om te controleren of een zwaartekrachtsgolfsignaal van samensmeltende neutronensterren door de zwaartekracht wordt 'gelensd', zelfs als we maar één afbeelding zien van de golf.

## **De algemene relativiteitstheorie van Einstein testen**

Karl Popper (1902-1994) stelde dat elke wetenschappelijke verklaring falsifieerbaar moet zijn. Ook al is de algemene relativiteitstheorie van Einstein een groot succes geweest, in deze traditie moeten we de algemene relativiteitstheorie op de proef stellen en kijken of deze standhoudt.

In dit proefschrift werden twee tests van de algemene relativiteitstheorie voorgesteld en toegepast. In de algemene relativiteitstheorie heeft een zwaartekrachtgolf slechts twee polarisaties. In alternatieve zwaartekrachttheorieën kan men echter tot vier extra polarisaties hebben, en we hebben methoden geïntroduceerd om ernaar te zoeken. We hebben de methoden toegepast op GW170817 en hebben geen bewijs gevonden van andere polarisaties dan die van de algemene relativiteit.

Bovendien hebben we ook gekeken naar de aard van de zwarte gaten. We hebben in het bijzonder gecontroleerd of de gravitatiegolfsignalen die schijnbaar door binaire zwarte gaten worden uitgezonden, mogelijk te wijten zijn aan nog meer exotische objecten, door te zoeken naar bepaalde soorten trillingen die daarin kunnen voorkomen. Met het door ons ontwikkelde formalisme hebben we alle tien signalen van veronderstelde dubbele zwarte gaten gecontroleerd die zijn waargenomen door LIGO en Virgo tijdens hun eerste en tweede observatieperiodes. We hebben geen bewijs gevonden voor dergelijke effecten en de bronnen van de signalen waren waarschijnlijk gewone zwarte gaten.





## Personal information

Name           Tsun Ho (Peter) Pang  
Nationality    Hong Kong  
Email           t.h.pang@uu.nl / t.h.pang@nikhef.nl / tsunhopang@gmail.com

## Education

2018 - 2022    Ph.D. in Physics  
                  GRASP, Utrecht University; Prof. dr. C. Van Den Broeck  
2016 - 2018    M.Phil in Physics  
                  Department of Physics, The Chinese University of Hong Kong;  
                  Prof. dr. T. G. F. Li  
2012 - 2016    B.Sc. in Physics (First class honours)  
                  Department of Physics, The Chinese University of Hong Kong

## Selected publications

1. Peter T. H. Pang et al. “NMMA: A nuclear-physics and multi-messenger astrophysics framework to analyze binary neutron star mergers”. In: (May 2022). arXiv: 2205.08513 [astro-ph.HE]
2. Pawan Kumar Gupta, Anna Puecher, Peter T. H. Pang, et al. “Determining the equation of state of neutron stars with Einstein Telescope using tidal effects and r-mode excitations from a population of binary inspirals”. In: (May 2022). arXiv: 2205.01182 [gr-qc]
3. Nina Kunert, Peter T. H. Pang, Ingo Tews, et al. “Quantifying modeling uncertainties when combining multiple gravitational-wave detections from binary neutron star sources”. In: *Phys. Rev. D* 105.6 (2022), p. L061301. DOI: 10.1103/PhysRevD.105.L061301. arXiv: 2110.11835 [astro-ph.HE]
4. Pawan Kumar Gupta, Thomas F. M. Spijksma, Peter T. H. Pang, et al. “Bounding dark charges on binary black holes using gravitational waves”. In: *Phys. Rev. D* 104.6 (2021), p. 063041. DOI: 10.1103/PhysRevD.104.063041. arXiv: 2107.12111 [gr-qc]

5. S. Huth, P. T. H. Pang, I. Tews, et al. “Constraining Neutron-Star Matter with Microscopic and Macroscopic Collisions”. In: *Nature* 606 (2022), pp. 276–280. DOI: 10.1038/s41586-022-04750-w. arXiv: 2107.06229 [nucl-th]
  - joint first authorship
6. Isaac C. F. Wong, Peter T. H. Pang, Rico K. L. Lo, et al. “Null-stream-based Bayesian Unmodeled Framework to Probe Generic Gravitational-wave Polarizations”. In: (May 2021). arXiv: 2105.09485 [gr-qc]
7. Peter T. H. Pang, Ingo Tews, Michael W. Coughlin, et al. “Nuclear Physics Multimessenger Astrophysics Constraints on the Neutron Star Equation of State: Adding NICER’s PSR J0740+6620 Measurement”. In: *Astrophys. J.* 922.1 (2021), p. 14. DOI: 10.3847/1538-4357/ac19ab. arXiv: 2105.08688 [astro-ph.HE]
8. Tomas Ahumada et al. “Discovery and confirmation of the shortest gamma-ray burst from a collapsar”. In: *Nature Astron.* 5.9 (2021), pp. 917–927. DOI: 10.1038/s41550-021-01428-7. arXiv: 2105.05067 [astro-ph.HE]
9. Igor Andreoni et al. “Fast-transient Searches in Real Time with ZTFReST: Identification of Three Optically Discovered Gamma-Ray Burst Afterglows and New Constraints on the Kilonova Rate”. In: *Astrophys. J.* 918.2 (2021), p. 63. DOI: 10.3847/1538-4357/ac0bc7. arXiv: 2104.06352 [astro-ph.HE]
10. Ingo Tews, Peter T. H. Pang, Tim Dietrich, et al. “On the Nature of GW190814 and Its Impact on the Understanding of Supranuclear Matter”. In: *Astrophys. J. Lett.* 908.1 (2021), p. L1. DOI: 10.3847/2041-8213/abdaae. arXiv: 2007.06057 [astro-ph.HE]
11. Peter T. H. Pang, Tim Dietrich, Ingo Tews, et al. “Parameter estimation for strong phase transitions in supranuclear matter using gravitational-wave astronomy”. In: *Phys. Rev. Res.* 2.3 (2020), p. 033514. DOI: 10.1103/PhysRevResearch.2.033514. arXiv: 2006.14936 [astro-ph.HE]
12. Yasmeeen Asali, Peter T. H. Pang, Anuradha Samajdar, et al. “Probing resonant excitations in exotic compact objects via gravitational waves”. In: *Phys. Rev. D* 102.2 (2020), p. 024016. DOI: 10.1103/PhysRevD.102.024016. arXiv: 2004.05128 [gr-qc]
13. Peter T. H. Pang, Rico K. L. Lo, Isaac C. F. Wong, et al. “Generic searches for alternative gravitational wave polarizations with networks of interferometric detectors”. In: *Phys. Rev. D* 101.10 (2020), p. 104055. DOI: 10.1103/PhysRevD.101.104055. arXiv: 2003.07375 [gr-qc]
14. Tim Dietrich, Michael W. Coughlin, Peter T. H. Pang, et al. “Multimessenger constraints on the neutron-star equation of state and the Hubble constant”. In: *Science* 370.6523 (2020), pp. 1450–1453. DOI: 10.1126/science.abb4317. arXiv: 2002.11355 [astro-ph.HE]

- 
15. Peter T. H. Pang, Otto A. Hannuksela, Tim Dietrich, et al. “Lensed or not lensed: Determining lensing magnifications for binary neutron star mergers from a single detection”. In: (Feb. 2020). DOI: 10.1093/mnras/staa1430. arXiv: 2002.04893 [astro-ph.HE]
  16. Gregorio Carullo et al. “Empirical tests of the black hole no-hair conjecture using gravitational-wave observations”. In: *Phys. Rev. D* 98.10 (2018), p. 104020. DOI: 10.1103/PhysRevD.98.104020. arXiv: 1805.04760 [gr-qc]
  17. Peter T. H. Pang, Juan Calderón Bustillo, Yifan Wang, et al. “Potential observations of false deviations from general relativity in gravitational wave signals from binary black holes”. In: *Phys. Rev. D* 98.2 (2018), p. 024019. DOI: 10.1103/PhysRevD.98.024019. arXiv: 1802.03306 [gr-qc]
  18. Peter T. H. Pang and Tjonnie G. F. Li. “Prospects of Constraining the Nuclear Equation of State with Gravitational-Wave Signals in the Advanced Detector Era and Beyond”. In: *JPS Conf. Proc.* 20 (2018). Ed. by Toshitaka Tatsumi, Toshiki Maruyama, and Takumi Muto, p. 011048. DOI: 10.7566/JPSCP.20.011048
  19. Peter T. H. Pang and Tjonnie G. F. Li. “Phenomenological Model of Hyper-Massive Neutron Star Phase Gravitational Wave of Binary Neutron Star”. In: *JPS Conf. Proc.* 20 (2018). Ed. by Toshitaka Tatsumi, Toshiki Maruyama, and Takumi Muto, p. 011052. DOI: 10.7566/JPSCP.20.011052



## LIST OF ACRONYMS

**BBH** binary black hole.

**BH** black hole.

**BNS** binary neutron star.

**CBC** compact binary coalescence.

**CEFT** chiral effective field theory.

**ECO** exotic compact object.

**EFT** effective field theory.

**EM** electromagnetic.

**EOS** equation of state.

**GR** general relativity.

**GRB** gamma-ray burst.

**GW** gravitational wave.

**IMR** inspiral-merger-ringdown.

**ISCO** innermost stable circular orbit.

**LIGO** Laser Interferometer Gravitational-wave Observatory.

**LVC** LIGO Virgo Scientific Collaboration.

**LVK** LIGO Virgo KAGRA Scientific Collaboration.

**MAP** maximum *a posteriori*.

**MCMC** Markov chain Monte Carlo.

**NICER** Neutron Star Interior Composition Explorer.

**NS** neutron star.

**O1** first observation run.

**O2** second observation run.

## List of acronyms

---

**O3a** first half of the third observation run.

**O3b** second half of the third observation run.

**PDF** probability density function.

**PN** post Newtonian.

**PSD** power spectral density.

**SNR** signal-to-noise ratio.

**SPA** stationary phase approximation.

**TOV** Tolman-Oppenheimer-Volkoff.

**TT** traceless transverse.

## BIBLIOGRAPHY

- [1] Isaac Newton. *Philosophiæ Naturalis Principia Mathematica*. England, 1687.
- [2] Albert Einstein. “The Foundation of the General Theory of Relativity”. In: *Annalen Phys.* 49.7 (1916). Ed. by Jong-Ping Hsu and D. Fine, pp. 769–822. DOI: 10.1002/andp.19163540702.
- [3] Joel M. Weisberg and Joseph H. Taylor. “Relativistic binary pulsar B1913+16: Thirty years of observations and analysis”. In: *ASP Conf. Ser.* 328 (2005), p. 25. arXiv: astro-ph/0407149.
- [4] J. Aasi et al. “Advanced LIGO”. In: *Class. Quant. Grav.* 32 (2015), p. 074001. DOI: 10.1088/0264-9381/32/7/074001. arXiv: 1411.4547 [gr-qc].
- [5] B. P. Abbott et al. “Observation of Gravitational Waves from a Binary Black Hole Merger”. In: *Phys. Rev. Lett.* 116.6 (2016), p. 061102. DOI: 10.1103/PhysRevLett.116.061102. arXiv: 1602.03837 [gr-qc].
- [6] B. P. Abbott et al. “GWTC-1: A Gravitational-Wave Transient Catalog of Compact Binary Mergers Observed by LIGO and Virgo during the First and Second Observing Runs”. In: *Phys. Rev. X* 9.3 (2019), p. 031040. DOI: 10.1103/PhysRevX.9.031040. arXiv: 1811.12907 [astro-ph.HE].
- [7] R. Abbott et al. “GWTC-2: Compact Binary Coalescences Observed by LIGO and Virgo During the First Half of the Third Observing Run”. In: *Phys. Rev. X* 11 (2021), p. 021053. DOI: 10.1103/PhysRevX.11.021053. arXiv: 2010.14527 [gr-qc].
- [8] R. Abbott et al. “GWTC-3: Compact Binary Coalescences Observed by LIGO and Virgo During the Second Part of the Third Observing Run”. In: (Nov. 2021). arXiv: 2111.03606 [gr-qc].
- [9] Benjamin P. Abbott et al. “GW170817: Observation of Gravitational Waves from a Binary Neutron Star Inspiral”. In: *Phys. Rev. Lett.* 119.16 (2017), p. 161101. DOI: 10.1103/PhysRevLett.119.161101. arXiv: 1710.05832 [gr-qc].
- [10] F. Acernese et al. “Advanced Virgo: a second-generation interferometric gravitational wave detector”. In: *Class. Quant. Grav.* 32.2 (2015), p. 024001. DOI: 10.1088/0264-9381/32/2/024001. arXiv: 1408.3978 [gr-qc].
- [11] B. P. Abbott et al. “Gravitational Waves and Gamma-rays from a Binary Neutron Star Merger: GW170817 and GRB 170817A”. In: *Astrophys. J. Lett.* 848.2 (2017), p. L13. DOI: 10.3847/2041-8213/aa920c. arXiv: 1710.05834 [astro-ph.HE].
- [12] B. P. Abbott et al. “Multi-messenger Observations of a Binary Neutron Star Merger”. In: *Astrophys. J. Lett.* 848.2 (2017), p. L12. DOI: 10.3847/2041-8213/aa91c9. arXiv: 1710.05833 [astro-ph.HE].

## BIBLIOGRAPHY

---

- [13] B. P. Abbott et al. “Binary Black Hole Population Properties Inferred from the First and Second Observing Runs of Advanced LIGO and Advanced Virgo”. In: *Astrophys. J. Lett.* 882.2 (2019), p. L24. DOI: 10.3847/2041-8213/ab3800. arXiv: 1811.12940 [astro-ph.HE].
- [14] R. Abbott et al. “Population Properties of Compact Objects from the Second LIGO-Virgo Gravitational-Wave Transient Catalog”. In: *Astrophys. J. Lett.* 913.1 (2021), p. L7. DOI: 10.3847/2041-8213/abe949. arXiv: 2010.14533 [astro-ph.HE].
- [15] B. P. Abbott et al. “Tests of general relativity with GW150914”. In: *Phys. Rev. Lett.* 116.22 (2016). [Erratum: Phys.Rev.Lett. 121, 129902 (2018)], p. 221101. DOI: 10.1103/PhysRevLett.116.221101. arXiv: 1602.03841 [gr-qc].
- [16] B. P. Abbott et al. “Tests of General Relativity with the Binary Black Hole Signals from the LIGO-Virgo Catalog GWTC-1”. In: *Phys. Rev. D* 100.10 (2019), p. 104036. DOI: 10.1103/PhysRevD.100.104036. arXiv: 1903.04467 [gr-qc].
- [17] R. Abbott et al. “Tests of general relativity with binary black holes from the second LIGO-Virgo gravitational-wave transient catalog”. In: *Phys. Rev. D* 103.12 (2021), p. 122002. DOI: 10.1103/PhysRevD.103.122002. arXiv: 2010.14529 [gr-qc].
- [18] R. Abbott et al. “Tests of General Relativity with GWTC-3”. In: (Dec. 2021). arXiv: 2112.06861 [gr-qc].
- [19] Liang Dai, Tejaswi Venumadhav, and Barak Zackay. “Parameter Estimation for GW170817 using Relative Binning”. In: (June 2018). arXiv: 1806.08793 [gr-qc].
- [20] Soumi De, Daniel Finstad, James M. Lattimer, et al. “Tidal Deformabilities and Radii of Neutron Stars from the Observation of GW170817”. In: *Phys. Rev. Lett.* 121.9 (2018). [Erratum: Phys.Rev.Lett. 121, 259902 (2018)], p. 091102. DOI: 10.1103/PhysRevLett.121.091102. arXiv: 1804.08583 [astro-ph.HE].
- [21] B. P. Abbott et al. “Properties of the binary neutron star merger GW170817”. In: *Phys. Rev. X* 9.1 (2019), p. 011001. DOI: 10.1103/PhysRevX.9.011001. arXiv: 1805.11579 [gr-qc].
- [22] B. P. Abbott et al. “GW170817: Measurements of neutron star radii and equation of state”. In: *Phys. Rev. Lett.* 121.16 (2018), p. 161101. DOI: 10.1103/PhysRevLett.121.161101. arXiv: 1805.11581 [gr-qc].
- [23] David Radice, Albino Perego, Francesco Zappa, et al. “GW170817: Joint Constraint on the Neutron Star Equation of State from Multimessenger Observations”. In: *Astrophys. J. Lett.* 852.2 (2018), p. L29. DOI: 10.3847/2041-8213/aaa402. arXiv: 1711.03647 [astro-ph.HE].
- [24] Andreas Bauswein, Oliver Just, Hans-Thomas Janka, et al. “Neutron-star radius constraints from GW170817 and future detections”. In: *Astrophys. J. Lett.* 850.2 (2017), p. L34. DOI: 10.3847/2041-8213/aa9994. arXiv: 1710.06843 [astro-ph.HE].
- [25] Ben Margalit and Brian D. Metzger. “Constraining the Maximum Mass of Neutron Stars From Multi-Messenger Observations of GW170817”. In: *Astrophys. J. Lett.* 850.2 (2017), p. L19. DOI: 10.3847/2041-8213/aa991c. arXiv: 1710.05938 [astro-ph.HE].



- 
- [26] Michael W. Coughlin et al. “Constraints on the neutron star equation of state from AT2017gfo using radiative transfer simulations”. In: *Mon. Not. Roy. Astron. Soc.* 480.3 (2018), pp. 3871–3878. DOI: 10.1093/mnras/sty2174. arXiv: 1805.09371 [astro-ph.HE].
- [27] David Radice and Liang Dai. “Multimessenger Parameter Estimation of GW170817”. In: *Eur. Phys. J. A* 55.4 (2019), p. 50. DOI: 10.1140/epja/i2019-12716-4. arXiv: 1810.12917 [astro-ph.HE].
- [28] Michael W. Coughlin, Tim Dietrich, Ben Margalit, et al. “Multimessenger Bayesian parameter inference of a binary neutron star merger”. In: *Mon. Not. Roy. Astron. Soc.* 489.1 (2019), pp. L91–L96. DOI: 10.1093/mnrasl/slz133. arXiv: 1812.04803 [astro-ph.HE].
- [29] Tim Dietrich, Michael W. Coughlin, Peter T. H. Pang, et al. “Multimessenger constraints on the neutron-star equation of state and the Hubble constant”. In: *Science* 370.6523 (2020), pp. 1450–1453. DOI: 10.1126/science.abb4317. arXiv: 2002.11355 [astro-ph.HE].
- [30] Eemeli Annala, Tyler Gorda, Alekski Kurkela, et al. “Gravitational-wave constraints on the neutron-star-matter Equation of State”. In: *Phys. Rev. Lett.* 120.17 (2018), p. 172703. DOI: 10.1103/PhysRevLett.120.172703. arXiv: 1711.02644 [astro-ph.HE].
- [31] Elias R. Most, Lukas R. Weih, Luciano Rezzolla, et al. “New constraints on radii and tidal deformabilities of neutron stars from GW170817”. In: *Phys. Rev. Lett.* 120.26 (2018), p. 261103. DOI: 10.1103/PhysRevLett.120.261103. arXiv: 1803.00549 [gr-qc].
- [32] I. Tews, J. Margueron, and S. Reddy. “Critical examination of constraints on the equation of state of dense matter obtained from GW170817”. In: *Phys. Rev. C* 98.4 (2018), p. 045804. DOI: 10.1103/PhysRevC.98.045804. arXiv: 1804.02783 [nucl-th].
- [33] Collin D. Capano, Ingo Tews, Stephanie M. Brown, et al. “Stringent constraints on neutron-star radii from multimessenger observations and nuclear theory”. In: *Nature Astron.* 4.6 (2020), pp. 625–632. DOI: 10.1038/s41550-020-1014-6. arXiv: 1908.10352 [astro-ph.HE].
- [34] G. Raaijmakers et al. “Constraining the dense matter equation of state with joint analysis of NICER and LIGO/Virgo measurements”. In: *Astrophys. J. Lett.* 893.1 (2020), p. L21. DOI: 10.3847/2041-8213/ab822f. arXiv: 1912.11031 [astro-ph.HE].
- [35] Reed Essick, Ingo Tews, Philippe Landry, et al. “Direct Astrophysical Tests of Chiral Effective Field Theory at Supranuclear Densities”. In: *Phys. Rev. C* 102.5 (2020), p. 055803. DOI: 10.1103/PhysRevC.102.055803. arXiv: 2004.07744 [astro-ph.HE].
- [36] Peter T. H. Pang, Tim Dietrich, Ingo Tews, et al. “Parameter estimation for strong phase transitions in supranuclear matter using gravitational-wave astronomy”. In: *Phys. Rev. Res.* 2.3 (2020), p. 033514. DOI: 10.1103/PhysRevResearch.2.033514. arXiv: 2006.14936 [astro-ph.HE].

## BIBLIOGRAPHY

---

- [37] Ingo Tews, Peter T. H. Pang, Tim Dietrich, et al. “On the Nature of GW190814 and Its Impact on the Understanding of Supranuclear Matter”. In: *Astrophys. J. Lett.* 908.1 (2021), p. L1. DOI: 10.3847/2041-8213/abdaae. arXiv: 2007.06057 [astro-ph.HE].
- [38] Peter T. H. Pang, Ingo Tews, Michael W. Coughlin, et al. “Nuclear Physics Multimessenger Astrophysics Constraints on the Neutron Star Equation of State: Adding NICER’s PSR J0740+6620 Measurement”. In: *Astrophys. J.* 922.1 (2021), p. 14. DOI: 10.3847/1538-4357/ac19ab. arXiv: 2105.08688 [astro-ph.HE].
- [39] S. Huth, P. T. H. Pang, I. Tews, et al. “Constraining Neutron-Star Matter with Microscopic and Macroscopic Collisions”. In: *Nature* 606 (2022), pp. 276–280. DOI: 10.1038/s41586-022-04750-w. arXiv: 2107.06229 [nucl-th].
- [40] Peter T. H. Pang, Otto A. Hannuksela, Tim Dietrich, et al. “Lensed or not lensed: Determining lensing magnifications for binary neutron star mergers from a single detection”. In: (Feb. 2020). DOI: 10.1093/mnras/staa1430. arXiv: 2002.04893 [astro-ph.HE].
- [41] Peter T. H. Pang, Rico K. L. Lo, Isaac C. F. Wong, et al. “Generic searches for alternative gravitational wave polarizations with networks of interferometric detectors”. In: *Phys. Rev. D* 101.10 (2020), p. 104055. DOI: 10.1103/PhysRevD.101.104055. arXiv: 2003.07375 [gr-qc].
- [42] Yasmeeen Asali, Peter T. H. Pang, Anuradha Samajdar, et al. “Probing resonant excitations in exotic compact objects via gravitational waves”. In: *Phys. Rev. D* 102.2 (2020), p. 024016. DOI: 10.1103/PhysRevD.102.024016. arXiv: 2004.05128 [gr-qc].
- [43] B. S. Sathyaprakash and B. F. Schutz. “Physics, Astrophysics and Cosmology with Gravitational Waves”. In: *Living Rev. Rel.* 12 (2009), p. 2. DOI: 10.12942/lrr-2009-2. arXiv: 0903.0338 [gr-qc].
- [44] David J.C. MacKay. *Information theory, inference, and learning algorithms*. Cambridge University Press, 2003.
- [45] Neil J. Cornish and Tyson B. Littenberg. “BayesWave: Bayesian Inference for Gravitational Wave Bursts and Instrument Glitches”. In: *Class. Quant. Grav.* 32.13 (2015), p. 135012. DOI: 10.1088/0264-9381/32/13/135012. arXiv: 1410.3835 [gr-qc].
- [46] <https://gracedb.ligo.org/superevents/public/03/>.
- [47] B. P. Abbott et al. “GW151226: Observation of Gravitational Waves from a 22-Solar-Mass Binary Black Hole Coalescence”. In: *Phys. Rev. Lett.* 116.24 (2016), p. 241103. DOI: 10.1103/PhysRevLett.116.241103. arXiv: 1606.04855 [gr-qc].
- [48] B. P. Abbott et al. “Binary Black Hole Mergers in the first Advanced LIGO Observing Run”. In: *Phys. Rev. X* 6.4 (2016). [Erratum: Phys.Rev.X 8, 039903 (2018)], p. 041015. DOI: 10.1103/PhysRevX.6.041015. arXiv: 1606.04856 [gr-qc].
- [49] B. P. Abbott et al. “GW190425: Observation of a Compact Binary Coalescence with Total Mass  $\sim 3.4M_{\odot}$ ”. In: *Astrophys. J. Lett.* 892.1 (2020), p. L3. DOI: 10.3847/2041-8213/ab75f5. arXiv: 2001.01761 [astro-ph.HE].

- 
- [50] R. Abbott et al. “Observation of Gravitational Waves from Two Neutron Star–Black Hole Coalescences”. In: *Astrophys. J. Lett.* 915.1 (2021), p. L5. DOI: 10.3847/2041-8213/ac082e. arXiv: 2106.15163 [astro-ph.HE].
- [51] D. A. Coulter et al. “Swope Supernova Survey 2017a (SSS17a), the Optical Counterpart to a Gravitational Wave Source”. In: *Science* 358 (2017), p. 1556. DOI: 10.1126/science.aap9811. arXiv: 1710.05452 [astro-ph.HE].
- [52] R. Chornock et al. “The Electromagnetic Counterpart of the Binary Neutron Star Merger LIGO/VIRGO GW170817. IV. Detection of Near-infrared Signatures of r-process Nucleosynthesis with Gemini-South”. In: *Astrophys. J. Lett.* 848.2 (2017), p. L19. DOI: 10.3847/2041-8213/aa905c. arXiv: 1710.05454 [astro-ph.HE].
- [53] M. Nicholl et al. “The Electromagnetic Counterpart of the Binary Neutron Star Merger LIGO/VIRGO GW170817. III. Optical and UV Spectra of a Blue Kilonova From Fast Polar Ejecta”. In: *Astrophys. J. Lett.* 848.2 (2017), p. L18. DOI: 10.3847/2041-8213/aa9029. arXiv: 1710.05456 [astro-ph.HE].
- [54] P. S. Cowperthwaite et al. “The Electromagnetic Counterpart of the Binary Neutron Star Merger LIGO/Virgo GW170817. II. UV, Optical, and Near-infrared Light Curves and Comparison to Kilonova Models”. In: *Astrophys. J. Lett.* 848.2 (2017), p. L17. DOI: 10.3847/2041-8213/aa8fc7. arXiv: 1710.05840 [astro-ph.HE].
- [55] E. Pian et al. “Spectroscopic identification of r-process nucleosynthesis in a double neutron star merger”. In: *Nature* 551 (2017), pp. 67–70. DOI: 10.1038/nature24298. arXiv: 1710.05858 [astro-ph.HE].
- [56] S. J. Smartt et al. “A kilonova as the electromagnetic counterpart to a gravitational-wave source”. In: *Nature* 551.7678 (2017), pp. 75–79. DOI: 10.1038/nature24303. arXiv: 1710.05841 [astro-ph.HE].
- [57] N. R. Tanvir et al. “The Emergence of a Lanthanide-Rich Kilonova Following the Merger of Two Neutron Stars”. In: *Astrophys. J. Lett.* 848.2 (2017), p. L27. DOI: 10.3847/2041-8213/aa90b6. arXiv: 1710.05455 [astro-ph.HE].
- [58] Masaomi Tanaka et al. “Kilonova from post-merger ejecta as an optical and near-infrared counterpart of GW170817”. In: *Publ. Astron. Soc. Jap.* 69.6 (2017), psx12. DOI: 10.1093/pasj/psx121. arXiv: 1710.05850 [astro-ph.HE].
- [59] Stefano Valenti, David J. Sand, Sheng Yang, et al. “The discovery of the electromagnetic counterpart of GW170817: kilonova AT 2017gfo/DLT17ck”. In: *Astrophys. J. Lett.* 848.2 (2017), p. L24. DOI: 10.3847/2041-8213/aa8edf. arXiv: 1710.05854 [astro-ph.HE].
- [60] John Antoniadis et al. “A Massive Pulsar in a Compact Relativistic Binary”. In: *Science* 340 (2013), p. 6131. DOI: 10.1126/science.1233232. arXiv: 1304.6875 [astro-ph.HE].
- [61] Zaven Arzoumanian et al. “The NANOGrav 11-year Data Set: High-precision timing of 45 Millisecond Pulsars”. In: *Astrophys. J. Suppl.* 235.2 (2018), p. 37. DOI: 10.3847/1538-4365/aab5b0. arXiv: 1801.01837 [astro-ph.HE].
- [62] E. Fonseca et al. “Refined Mass and Geometric Measurements of the High-mass PSR J0740+6620”. In: *Astrophys. J. Lett.* 915.1 (2021), p. L12. DOI: 10.3847/2041-8213/ac03b8. arXiv: 2104.00880 [astro-ph.HE].

## BIBLIOGRAPHY

---

- [63] M. C. Miller et al. “PSR J0030+0451 Mass and Radius from *NICER* Data and Implications for the Properties of Neutron Star Matter”. In: *Astrophys. J. Lett.* 887.1 (2019), p. L24. DOI: 10.3847/2041-8213/ab50c5. arXiv: 1912.05705 [astro-ph.HE].
- [64] Thomas E. Riley et al. “A *NICER* View of PSR J0030+0451: Millisecond Pulsar Parameter Estimation”. In: *Astrophys. J. Lett.* 887.1 (2019), p. L21. DOI: 10.3847/2041-8213/ab481c. arXiv: 1912.05702 [astro-ph.HE].
- [65] M. C. Miller et al. “The Radius of PSR J0740+6620 from *NICER* and XMM-Newton Data”. In: *Astrophys. J. Lett.* 918.2 (2021), p. L28. DOI: 10.3847/2041-8213/ac089b. arXiv: 2105.06979 [astro-ph.HE].
- [66] Thomas E. Riley et al. “A *NICER* View of the Massive Pulsar PSR J0740+6620 Informed by Radio Timing and XMM-Newton Spectroscopy”. In: *Astrophys. J. Lett.* 918.2 (2021), p. L27. DOI: 10.3847/2041-8213/ac0a81. arXiv: 2105.06980 [astro-ph.HE].
- [67] Charles W Misner, etc., Kip S Thorne, et al. *Gravitation*. New York, NY: W.H. Freeman, Jan. 1973.
- [68] Michele Maggiore. *Gravitational waves: Volume 1: Theory and Experiments*. London, England: Oxford University Press, Oct. 2007.
- [69] Alessandra Buonanno, Bala Iyer, Evan Ochsner, et al. “Comparison of post-Newtonian templates for compact binary inspiral signals in gravitational-wave detectors”. In: *Phys. Rev. D* 80 (2009), p. 084043. DOI: 10.1103/PhysRevD.80.084043. arXiv: 0907.0700 [gr-qc].
- [70] Thibault Damour, Piotr Jaranowski, and Gerhard Schaefel. “Dimensional regularization of the gravitational interaction of point masses”. In: *Phys. Lett. B* 513 (2001), pp. 147–155. DOI: 10.1016/S0370-2693(01)00642-6. arXiv: gr-qc/0105038.
- [71] Luc Blanchet, Thibault Damour, and Gilles Esposito-Farese. “Dimensional regularization of the third postNewtonian dynamics of point particles in harmonic coordinates”. In: *Phys. Rev. D* 69 (2004), p. 124007. DOI: 10.1103/PhysRevD.69.124007. arXiv: gr-qc/0311052.
- [72] Luc Blanchet, Thibault Damour, Gilles Esposito-Farese, et al. “Gravitational radiation from inspiralling compact binaries completed at the third post-Newtonian order”. In: *Phys. Rev. Lett.* 93 (2004), p. 091101. DOI: 10.1103/PhysRevLett.93.091101. arXiv: gr-qc/0406012.
- [73] Luc Blanchet, Thibault Damour, Gilles Esposito-Farese, et al. “Dimensional regularization of the third post-Newtonian gravitational wave generation from two point masses”. In: *Phys. Rev. D* 71 (2005), p. 124004. DOI: 10.1103/PhysRevD.71.124004. arXiv: gr-qc/0503044.
- [74] Thibault Damour, Piotr Jaranowski, and Gerhard Schaefel. “Equivalence between the ADM-Hamiltonian and the harmonic coordinates approaches to the third post-Newtonian dynamics of compact binaries”. In: *Phys. Rev. D* 63 (2001). [Erratum: *Phys.Rev.D* 66, 029901 (2002)], p. 044021. DOI: 10.1103/PhysRevD.63.044021. arXiv: gr-qc/0010040.

- 
- [75] Vanessa C. de Andrade, Luc Blanchet, and Guillaume Faye. “Third postNewtonian dynamics of compact binaries: Noetherian conserved quantities and equivalence between the harmonic coordinate and ADM Hamiltonian formalisms”. In: *Class. Quant. Grav.* 18 (2001), pp. 753–778. DOI: 10.1088/0264-9381/18/5/301. arXiv: gr-qc/0011063.
- [76] Luc Blanchet and Bala R. Iyer. “Third postNewtonian dynamics of compact binaries: Equations of motion in the center-of-mass frame”. In: *Class. Quant. Grav.* 20 (2003), p. 755. DOI: 10.1088/0264-9381/20/4/309. arXiv: gr-qc/0209089.
- [77] Yousuke Itoh and Toshifumi Futamase. “New derivation of a third postNewtonian equation of motion for relativistic compact binaries without ambiguity”. In: *Phys. Rev. D* 68 (2003), p. 121501. DOI: 10.1103/PhysRevD.68.121501. arXiv: gr-qc/0310028.
- [78] Luc Blanchet, Bala R. Iyer, and Benoit Joguet. “Gravitational waves from inspiralling compact binaries: Energy flux to third postNewtonian order”. In: *Phys. Rev. D* 65 (2002). [Erratum: *Phys.Rev.D* 71, 129903 (2005)], p. 064005. DOI: 10.1103/PhysRevD.65.064005. arXiv: gr-qc/0105098.
- [79] Luc Blanchet, Guillaume Faye, Bala R. Iyer, et al. “Gravitational wave inspiral of compact binary systems to  $7/2$  postNewtonian order”. In: *Phys. Rev. D* 65 (2002). [Erratum: *Phys.Rev.D* 71, 129902 (2005)], p. 061501. DOI: 10.1103/PhysRevD.71.129902. arXiv: gr-qc/0105099.
- [80] Luc Blanchet and Bala R. Iyer. “Hadamard regularization of the third post-Newtonian gravitational wave generation of two point masses”. In: *Phys. Rev. D* 71 (2005), p. 024004. DOI: 10.1103/PhysRevD.71.024004. arXiv: gr-qc/0409094.
- [81] Balazs Mikoczi, Matyas Vasuth, and Laszlo A. Gergely. “Self-interaction spin effects in inspiralling compact binaries”. In: *Phys. Rev. D* 71 (2005), p. 124043. DOI: 10.1103/PhysRevD.71.124043. arXiv: astro-ph/0504538.
- [82] K. G. Arun, Alessandra Buonanno, Guillaume Faye, et al. “Higher-order spin effects in the amplitude and phase of gravitational waveforms emitted by inspiralling compact binaries: Ready-to-use gravitational waveforms”. In: *Phys. Rev. D* 79 (2009). [Erratum: *Phys.Rev.D* 84, 049901 (2011)], p. 104023. DOI: 10.1103/PhysRevD.79.104023. arXiv: 0810.5336 [gr-qc].
- [83] Alejandro Bohé, Sylvain Marsat, and Luc Blanchet. “Next-to-next-to-leading order spin-orbit effects in the gravitational wave flux and orbital phasing of compact binaries”. In: *Class. Quant. Grav.* 30 (2013), p. 135009. DOI: 10.1088/0264-9381/30/13/135009. arXiv: 1303.7412 [gr-qc].
- [84] Leslie Wade, Jolien D. E. Creighton, Evan Ochsner, et al. “Systematic and statistical errors in a bayesian approach to the estimation of the neutron-star equation of state using advanced gravitational wave detectors”. In: *Phys. Rev. D* 89.10 (2014), p. 103012. DOI: 10.1103/PhysRevD.89.103012. arXiv: 1402.5156 [gr-qc].
- [85] Michalis Agathos, Jeroen Meidam, Walter Del Pozzo, et al. “Constraining the neutron star equation of state with gravitational wave signals from coalescing binary neutron stars”. In: *Phys. Rev. D* 92.2 (2015), p. 023012. DOI: 10.1103/PhysRevD.92.023012. arXiv: 1503.05405 [gr-qc].

## BIBLIOGRAPHY

---

- [86] Sascha Husa, Sebastian Khan, Mark Hannam, et al. “Frequency-domain gravitational waves from nonprecessing black-hole binaries. I. New numerical waveforms and anatomy of the signal”. In: *Phys. Rev. D* 93.4 (2016), p. 044006. DOI: 10.1103/PhysRevD.93.044006. arXiv: 1508.07250 [gr-qc].
- [87] Sebastian Khan, Sascha Husa, Mark Hannam, et al. “Frequency-domain gravitational waves from nonprecessing black-hole binaries. II. A phenomenological model for the advanced detector era”. In: *Phys. Rev. D* 93.4 (2016), p. 044007. DOI: 10.1103/PhysRevD.93.044007. arXiv: 1508.07253 [gr-qc].
- [88] Sebastian Khan, Katerina Chatziioannou, Mark Hannam, et al. “Phenomenological model for the gravitational-wave signal from precessing binary black holes with two-spin effects”. In: *Phys. Rev. D* 100.2 (2019), p. 024059. DOI: 10.1103/PhysRevD.100.024059. arXiv: 1809.10113 [gr-qc].
- [89] Curt Cutler and Eanna E. Flanagan. “Gravitational waves from merging compact binaries: How accurately can one extract the binary’s parameters from the inspiral wave form?” In: *Phys. Rev. D* 49 (1994), pp. 2658–2697. DOI: 10.1103/PhysRevD.49.2658. arXiv: gr-qc/9402014.
- [90] Eric Poisson and Clifford M. Will. “Gravitational waves from inspiraling compact binaries: Parameter estimation using second postNewtonian wave forms”. In: *Phys. Rev. D* 52 (1995), pp. 848–855. DOI: 10.1103/PhysRevD.52.848. arXiv: gr-qc/9502040.
- [91] P. Ajith. “Addressing the spin question in gravitational-wave searches: Waveform templates for inspiraling compact binaries with nonprecessing spins”. In: *Phys. Rev. D* 84 (2011), p. 084037. DOI: 10.1103/PhysRevD.84.084037. arXiv: 1107.1267 [gr-qc].
- [92] Mark Hannam, Patricia Schmidt, Alejandro Bohé, et al. “Simple Model of Complete Precessing Black-Hole-Binary Gravitational Waveforms”. In: *Phys. Rev. Lett.* 113.15 (2014), p. 151101. DOI: 10.1103/PhysRevLett.113.151101. arXiv: 1308.3271 [gr-qc].
- [93] Richard C. Tolman. “Static solutions of Einstein’s field equations for spheres of fluid”. In: *Phys. Rev.* 55 (1939), pp. 364–373.
- [94] J. R. Oppenheimer and G. M. Volkoff. “On Massive neutron cores”. In: *Phys. Rev.* 55 (1939), pp. 374–381.
- [95] *Relativistic EOS Table for supernovae*. <https://user.numazu-ct.ac.jp/~sumi/eos/>. (Accessed on 02/22/2022).
- [96] *Compact Star Online Supernovae Equation of State (CompOSE)*. <https://compose.obspm.fr/>. (Accessed on 02/22/2022).
- [97] *Dense matter EoS*. <http://xtreme.as.arizona.edu/NeutronStars/index.php/dense-matter-eos/>. (Accessed on 02/22/2022).
- [98] Steven Weinberg. “Nuclear forces from chiral Lagrangians”. In: *Phys. Lett. B* 251 (1990), pp. 288–292. DOI: 10.1016/0370-2693(90)90938-3.
- [99] Steven Weinberg. “Effective chiral Lagrangians for nucleon - pion interactions and nuclear forces”. In: *Nucl. Phys. B* 363 (1991), pp. 3–18. DOI: 10.1016/0550-3213(91)90231-L.

- 
- [100] U. van Kolck. “Few nucleon forces from chiral Lagrangians”. In: *Phys. Rev. C* 49 (1994), pp. 2932–2941. DOI: 10.1103/PhysRevC.49.2932.
- [101] Evgeny Epelbaum, Hans-Werner Hammer, and Ulf-G. Meissner. “Modern Theory of Nuclear Forces”. In: *Rev. Mod. Phys.* 81 (2009), pp. 1773–1825. DOI: 10.1103/RevModPhys.81.1773. arXiv: 0811.1338 [nucl-th].
- [102] R. Machleidt and D. R. Entem. “Chiral effective field theory and nuclear forces”. In: *Phys. Rept.* 503 (2011), pp. 1–75. DOI: 10.1016/j.physrep.2011.02.001. arXiv: 1105.2919 [nucl-th].
- [103] E. Epelbaum, H. Krebs, and U. G. Meißner. “Improved chiral nucleon-nucleon potential up to next-to-next-to-next-to-leading order”. In: *Eur. Phys. J. A* 51.5 (2015), p. 53. DOI: 10.1140/epja/i2015-15053-8. arXiv: 1412.0142 [nucl-th].
- [104] J. A. Melendez, S. Wesolowski, and R. J. Furnstahl. “Bayesian truncation errors in chiral effective field theory: nucleon-nucleon observables”. In: *Phys. Rev. C* 96.2 (2017), p. 024003. DOI: 10.1103/PhysRevC.96.024003. arXiv: 1704.03308 [nucl-th].
- [105] J. Carlson, S. Gandolfi, F. Pederiva, et al. “Quantum Monte Carlo methods for nuclear physics”. In: *Rev. Mod. Phys.* 87 (2015), p. 1067. DOI: 10.1103/RevModPhys.87.1067. arXiv: 1412.3081 [nucl-th].
- [106] J. E. Lynn, I. Tews, S. Gandolfi, et al. “Quantum Monte Carlo Methods in Nuclear Physics: Recent Advances”. In: *Ann. Rev. Nucl. Part. Sci.* 69 (2019), pp. 279–305. DOI: 10.1146/annurev-nucl-101918-023600. arXiv: 1901.04868 [nucl-th].
- [107] A. Gezerlis, I. Tews, E. Epelbaum, et al. “Quantum Monte Carlo Calculations with Chiral Effective Field Theory Interactions”. In: *Phys. Rev. Lett.* 111.3 (2013), p. 032501. DOI: 10.1103/PhysRevLett.111.032501. arXiv: 1303.6243 [nucl-th].
- [108] A. Gezerlis, I. Tews, E. Epelbaum, et al. “Local chiral effective field theory interactions and quantum Monte Carlo applications”. In: *Phys. Rev. C* 90.5 (2014), p. 054323. DOI: 10.1103/PhysRevC.90.054323. arXiv: 1406.0454 [nucl-th].
- [109] J. E. Lynn, I. Tews, J. Carlson, et al. “Chiral Three-Nucleon Interactions in Light Nuclei, Neutron- $\alpha$  Scattering, and Neutron Matter”. In: *Phys. Rev. Lett.* 116.6 (2016), p. 062501. DOI: 10.1103/PhysRevLett.116.062501. arXiv: 1509.03470 [nucl-th].
- [110] Ingo Tews, Zohreh Davoudi, Andreas Ekström, et al. “New Ideas in Constraining Nuclear Forces”. In: *J. Phys. G* 47.10 (2020), p. 103001. DOI: 10.1088/1361-6471/ab9079. arXiv: 2001.03334 [nucl-th].
- [111] Ingo Tews, Joseph Carlson, Stefano Gandolfi, et al. “Constraining the speed of sound inside neutron stars with chiral effective field theory interactions and observations”. In: *Astrophys. J.* 860.2 (2018), p. 149. DOI: 10.3847/1538-4357/aac267. arXiv: 1801.01923 [nucl-th].
- [112] Tanja Hinderer. “Tidal Love numbers of neutron stars”. In: *Astrophys. J.* 677 (2008), pp. 1216–1220. DOI: 10.1086/533487. arXiv: 0711.2420 [astro-ph].

## BIBLIOGRAPHY

---

- [113] Justin Vines, Eanna E. Flanagan, and Tanja Hinderer. “Post-1-Newtonian tidal effects in the gravitational waveform from binary inspirals”. In: *Phys. Rev. D* 83 (2011), p. 084051. DOI: 10.1103/PhysRevD.83.084051. arXiv: 1101.1673 [gr-qc].
- [114] Thibault Damour, Alessandro Nagar, and Loic Villain. “Measurability of the tidal polarizability of neutron stars in late-inspiral gravitational-wave signals”. In: *Phys. Rev. D* 85 (2012), p. 123007. DOI: 10.1103/PhysRevD.85.123007. arXiv: 1203.4352 [gr-qc].
- [115] Marc Favata. “Systematic parameter errors in inspiraling neutron star binaries”. In: *Phys. Rev. Lett.* 112 (2014), p. 101101. DOI: 10.1103/PhysRevLett.112.101101. arXiv: 1310.8288 [gr-qc].
- [116] Tim Dietrich et al. “Matter imprints in waveform models for neutron star binaries: Tidal and self-spin effects”. In: *Phys. Rev. D* 99.2 (2019), p. 024029. DOI: 10.1103/PhysRevD.99.024029. arXiv: 1804.02235 [gr-qc].
- [117] Tim Dietrich, Anuradha Samajdar, Sebastian Khan, et al. “Improving the NRTidal model for binary neutron star systems”. In: *Phys. Rev. D* 100.4 (2019), p. 044003. DOI: 10.1103/PhysRevD.100.044003. arXiv: 1905.06011 [gr-qc].
- [118] Kent Yagi and Nicolas Yunes. “I-Love-Q Relations in Neutron Stars and their Applications to Astrophysics, Gravitational Waves and Fundamental Physics”. In: *Phys. Rev. D* 88.2 (2013), p. 023009. DOI: 10.1103/PhysRevD.88.023009. arXiv: 1303.1528 [gr-qc].
- [119] Kent Yagi and Nicolás Yunes. “Approximate Universal Relations for Neutron Stars and Quark Stars”. In: *Phys. Rept.* 681 (2017), pp. 1–72. DOI: 10.1016/j.physrep.2017.03.002. arXiv: 1608.02582 [gr-qc].
- [120] Kent Yagi and Nicolas Yunes. “Binary Love Relations”. In: *Class. Quant. Grav.* 33.13 (2016), 13LT01. DOI: 10.1088/0264-9381/33/13/13LT01. arXiv: 1512.02639 [gr-qc].
- [121] Katerina Chatziioannou, Carl-Johan Haster, and Aaron Zimmerman. “Measuring the neutron star tidal deformability with equation-of-state-independent relations and gravitational waves”. In: *Phys. Rev. D* 97.10 (2018), p. 104036. DOI: 10.1103/PhysRevD.97.104036. arXiv: 1804.03221 [gr-qc].
- [122] Mattia Bulla. “POSSIS: predicting spectra, light curves and polarization for multi-dimensional models of supernovae and kilonovae”. In: *Mon. Not. Roy. Astron. Soc.* 489.4 (2019), pp. 5037–5045. DOI: 10.1093/mnras/stz2495. arXiv: 1906.04205 [astro-ph.HE].
- [123] Ilya Mandel, Will M. Farr, and Jonathan R. Gair. “Extracting distribution parameters from multiple uncertain observations with selection biases”. In: *Mon. Not. Roy. Astron. Soc.* 486.1 (2019), pp. 1086–1093. DOI: 10.1093/mnras/stz896. arXiv: 1809.02063 [physics.data-an].
- [124] Nicholas Metropolis, Arianna W. Rosenbluth, Marshall N. Rosenbluth, et al. “Equation of State Calculations by Fast Computing Machines”. In: *The Journal of Chemical Physics* 21.6 (June 1953), pp. 1087–1092. DOI: 10.1063/1.1699114. URL: <https://doi.org/10.1063/1.1699114>.



- 
- [125] W. K. Hastings. “Monte Carlo sampling methods using Markov chains and their applications”. In: *Biometrika* 57.1 (Apr. 1970), pp. 97–109. DOI: 10.1093/biomet/57.1.97. URL: <https://doi.org/10.1093/biomet/57.1.97>.
- [126] W.R. Gilks, S. Richardson, and David Spiegelhalter, eds. *Markov Chain Monte Carlo in Practice*. Chapman and Hall/CRC, Dec. 1995. DOI: 10.1201/b14835. URL: <https://doi.org/10.1201/b14835>.
- [127] David J. Earl and Michael W. Deem. “Parallel tempering: Theory, applications, and new perspectives”. In: *Physical Chemistry Chemical Physics* 7.23 (2005), p. 3910. DOI: 10.1039/b509983h. URL: <https://doi.org/10.1039/b509983h>.
- [128] John Skilling. “Nested Sampling”. In: *AIP Conference Proceedings*. AIP, 2004. DOI: 10.1063/1.1835238. URL: <https://doi.org/10.1063/1.1835238>.
- [129] Pia Mukherjee, David Parkinson, and Andrew R. Liddle. “A nested sampling algorithm for cosmological model selection”. In: *Astrophys. J. Lett.* 638 (2006), pp. L51–L54. DOI: 10.1086/501068. arXiv: astro-ph/0508461.
- [130] J. Veitch et al. “Parameter estimation for compact binaries with ground-based gravitational-wave observations using the LALInference software library”. In: *Phys. Rev. D* 91.4 (2015), p. 042003. DOI: 10.1103/PhysRevD.91.042003. arXiv: 1409.7215 [gr-qc].
- [131] F. Feroz, M. P. Hobson, and M. Bridges. “MultiNest: an efficient and robust Bayesian inference tool for cosmology and particle physics”. In: *Mon. Not. Roy. Astron. Soc.* 398 (2009), pp. 1601–1614. DOI: 10.1111/j.1365-2966.2009.14548.x. arXiv: 0809.3437 [astro-ph].
- [132] Michael J. Williams, John Veitch, and Chris Messenger. “Nested sampling with normalizing flows for gravitational-wave inference”. In: *Phys. Rev. D* 103.10 (2021), p. 103006. DOI: 10.1103/PhysRevD.103.103006. arXiv: 2102.11056 [gr-qc].
- [133] Robert Salomone, Leah F. South, Christopher C. Drovandi, et al. *Unbiased and Consistent Nested Sampling via Sequential Monte Carlo*. 2018. arXiv: 1805.03924 [stat.CO].
- [134] Paul Demorest, Tim Pennucci, Scott Ransom, et al. “Shapiro Delay Measurement of A Two Solar Mass Neutron Star”. In: *Nature* 467 (2010), pp. 1081–1083. DOI: 10.1038/nature09466. arXiv: 1010.5788 [astro-ph.HE].
- [135] H. T. Cromartie et al. “Relativistic Shapiro delay measurements of an extremely massive millisecond pulsar”. In: *Nature Astron.* 4.1 (2019), pp. 72–76. DOI: 10.1038/s41550-019-0880-2. arXiv: 1904.06759 [astro-ph.HE].
- [136] Andrew W. Steiner, James M. Lattimer, and Edward F. Brown. “The Neutron Star Mass-Radius Relation and the Equation of State of Dense Matter”. In: *Astrophys. J. Lett.* 765 (2013), p. L5. DOI: 10.1088/2041-8205/765/1/L5. arXiv: 1205.6871 [nucl-th].
- [137] Jocelyn S. Read, Charalampos Markakis, Masaru Shibata, et al. “Measuring the neutron star equation of state with gravitational wave observations”. In: *Phys. Rev. D* 79 (2009), p. 124033. DOI: 10.1103/PhysRevD.79.124033. arXiv: 0901.3258 [gr-qc].

## BIBLIOGRAPHY

---

- [138] Charalampos Markakis, Jocelyn S. Read, Masaru Shibata, et al. “Inferring the neutron star equation of state from binary inspiral waveforms”. In: *12th Marcel Grossmann Meeting on General Relativity*. Aug. 2010, pp. 743–745. DOI: 10.1142/9789814374552\_0046. arXiv: 1008.1822 [gr-qc].
- [139] Charalampos Markakis, Jocelyn S. Read, Masaru Shibata, et al. “Neutron star equation of state via gravitational wave observations”. In: *J. Phys. Conf. Ser.* 189 (2009), p. 012024. DOI: 10.1088/1742-6596/189/1/012024. arXiv: 1110.3759 [gr-qc].
- [140] Jocelyn S. Read, Luca Baiotti, Jolien D. E. Creighton, et al. “Matter effects on binary neutron star waveforms”. In: *Phys. Rev. D* 88 (2013), p. 044042. DOI: 10.1103/PhysRevD.88.044042. arXiv: 1306.4065 [gr-qc].
- [141] Walter Del Pozzo, Tjonnie G. F. Li, Michalis Agathos, et al. “Demonstrating the feasibility of probing the neutron star equation of state with second-generation gravitational wave detectors”. In: *Phys. Rev. Lett.* 111.7 (2013), p. 071101. DOI: 10.1103/PhysRevLett.111.071101. arXiv: 1307.8338 [gr-qc].
- [142] Benjamin D. Lackey and Leslie Wade. “Reconstructing the neutron-star equation of state with gravitational-wave detectors from a realistic population of inspiralling binary neutron stars”. In: *Phys. Rev. D* 91.4 (2015), p. 043002. DOI: 10.1103/PhysRevD.91.043002. arXiv: 1410.8866 [gr-qc].
- [143] F. J. Fattoyev, J. Piekarewicz, and C. J. Horowitz. “Neutron Skins and Neutron Stars in the Multimessenger Era”. In: *Phys. Rev. Lett.* 120.17 (2018), p. 172702. DOI: 10.1103/PhysRevLett.120.172702. arXiv: 1711.06615 [nucl-th].
- [144] Yeunhwan Lim and Jeremy W. Holt. “Neutron star tidal deformabilities constrained by nuclear theory and experiment”. In: *Phys. Rev. Lett.* 121.6 (2018), p. 062701. DOI: 10.1103/PhysRevLett.121.062701. arXiv: 1803.02803 [nucl-th].
- [145] S. K. Greif, G. Raaijmakers, K. Hebeler, et al. “Equation of state sensitivities when inferring neutron star and dense matter properties”. In: *Mon. Not. Roy. Astron. Soc.* 485.4 (2019), pp. 5363–5376. DOI: 10.1093/mnras/stz654. arXiv: 1812.08188 [astro-ph.HE].
- [146] Reed Essick, Philippe Landry, and Daniel E. Holz. “Nonparametric Inference of Neutron Star Composition, Equation of State, and Maximum Mass with GW170817”. In: *Phys. Rev. D* 101.6 (2020), p. 063007. DOI: 10.1103/PhysRevD.101.063007. arXiv: 1910.09740 [astro-ph.HE].
- [147] Philippe Landry, Reed Essick, and Katerina Chatziioannou. “Nonparametric constraints on neutron star matter with existing and upcoming gravitational wave and pulsar observations”. In: *Phys. Rev. D* 101.12 (2020), p. 123007. DOI: 10.1103/PhysRevD.101.123007. arXiv: 2003.04880 [astro-ph.HE].
- [148] Katerina Chatziioannou and Sophia Han. “Studying strong phase transitions in neutron stars with gravitational waves”. In: *Phys. Rev. D* 101.4 (2020), p. 044019. DOI: 10.1103/PhysRevD.101.044019. arXiv: 1911.07091 [gr-qc].
- [149] Daniel Wysocki, Richard O’Shaughnessy, Leslie Wade, et al. “Inferring the neutron star equation of state simultaneously with the population of merging neutron stars”. In: (Jan. 2020). arXiv: 2001.01747 [gr-qc].

- 
- [150] Katerina Chatziioannou. “Neutron star tidal deformability and equation of state constraints”. In: *Gen. Rel. Grav.* 52.11 (2020), p. 109. DOI: 10.1007/s10714-020-02754-3. arXiv: 2006.03168 [gr-qc].
- [151] Luciano Rezzolla, Elias R. Most, and Lukas R. Weih. “Using gravitational-wave observations and quasi-universal relations to constrain the maximum mass of neutron stars”. In: *Astrophys. J. Lett.* 852.2 (2018), p. L25. DOI: 10.3847/2041-8213/aaa401. arXiv: 1711.00314 [astro-ph.HE].
- [152] Masaru Shibata, Sho Fujibayashi, Kenta Hotokezaka, et al. “Modeling GW170817 based on numerical relativity and its implications”. In: *Phys. Rev. D* 96.12 (2017), p. 123012. DOI: 10.1103/PhysRevD.96.123012. arXiv: 1710.07579 [astro-ph.HE].
- [153] Isaac Legred, Katerina Chatziioannou, Reed Essick, et al. “Impact of the PSR J0740+6620 radius constraint on the properties of high-density matter”. In: *Phys. Rev. D* 104.6 (2021), p. 063003. DOI: 10.1103/PhysRevD.104.063003. arXiv: 2106.05313 [astro-ph.HE].
- [154] G. Raaijmakers, S. K. Greif, K. Hebeler, et al. “Constraints on the Dense Matter Equation of State and Neutron Star Properties from NICER’s Mass–Radius Estimate of PSR J0740+6620 and Multimessenger Observations”. In: *Astrophys. J. Lett.* 918.2 (2021), p. L29. DOI: 10.3847/2041-8213/ac089a. arXiv: 2105.06981 [astro-ph.HE].
- [155] Norman K. Glendenning. “First order phase transitions with more than one conserved charge: Consequences for neutron stars”. In: *Phys. Rev. D* 46 (1992), pp. 1274–1287. DOI: 10.1103/PhysRevD.46.1274.
- [156] Mark G. Alford. “Color superconducting quark matter”. In: *Ann. Rev. Nucl. Part. Sci.* 51 (2001), pp. 131–160. DOI: 10.1146/annurev.nucl.51.101701.132449. arXiv: hep-ph/0102047.
- [157] Mark Alford, David Blaschke, Alessandro Drago, et al. “Quark matter in compact stars?” In: *Nature* 445 (2007), E7–E8. DOI: 10.1038/nature05582. arXiv: astro-ph/0606524.
- [158] Mark Alford, Matt Braby, M. W. Paris, et al. “Hybrid stars that masquerade as neutron stars”. In: *Astrophys. J.* 629 (2005), pp. 969–978. DOI: 10.1086/430902. arXiv: nucl-th/0411016.
- [159] Mark G. Alford, Sophia Han, and Madappa Prakash. “Generic conditions for stable hybrid stars”. In: *Phys. Rev. D* 88.8 (2013), p. 083013. DOI: 10.1103/PhysRevD.88.083013. arXiv: 1302.4732 [astro-ph.SR].
- [160] Sanjin Benic, David Blaschke, David E. Alvarez-Castillo, et al. “A new quark-hadron hybrid equation of state for astrophysics - I. High-mass twin compact stars”. In: *Astron. Astrophys.* 577 (2015), A40. DOI: 10.1051/0004-6361/201425318. arXiv: 1411.2856 [astro-ph.HE].
- [161] Mark G. Alford and Armen Sedrakian. “Compact stars with sequential QCD phase transitions”. In: *Phys. Rev. Lett.* 119.16 (2017), p. 161104. DOI: 10.1103/PhysRevLett.119.161104. arXiv: 1706.01592 [astro-ph.HE].

## BIBLIOGRAPHY

---

- [162] Andreas Bauswein, Niels-Uwe F. Bastian, David B. Blaschke, et al. “Identifying a first-order phase transition in neutron star mergers through gravitational waves”. In: *Phys. Rev. Lett.* 122.6 (2019), p. 061102. DOI: 10.1103/PhysRevLett.122.061102. arXiv: 1809.01116 [astro-ph.HE].
- [163] Elias R. Most, L. Jens Papenfort, Veronica Dexheimer, et al. “Signatures of quark-hadron phase transitions in general-relativistic neutron-star mergers”. In: *Phys. Rev. Lett.* 122.6 (2019), p. 061101. DOI: 10.1103/PhysRevLett.122.061101. arXiv: 1807.03684 [astro-ph.HE].
- [164] Andreas Bauswein, Niels-Uwe Friedrich Bastian, David Blaschke, et al. “Equation-of-state Constraints and the QCD Phase Transition in the Era of Gravitational-Wave Astronomy”. In: *AIP Conf. Proc.* 2127.1 (2019). Ed. by Ang Li, Bao-An Li, and Furong Xu, p. 020013. DOI: 10.1063/1.5117803. arXiv: 1904.01306 [astro-ph.HE].
- [165] Elias R. Most, L. Jens Papenfort, Veronica Dexheimer, et al. “On the deconfinement phase transition in neutron-star mergers”. In: *Eur. Phys. J. A* 56.2 (2020), p. 59. DOI: 10.1140/epja/s10050-020-00073-4. arXiv: 1910.13893 [astro-ph.HE].
- [166] Lukas R. Weih, Matthias Hanauske, and Luciano Rezzolla. “Postmerger Gravitational-Wave Signatures of Phase Transitions in Binary Mergers”. In: *Phys. Rev. Lett.* 124.17 (2020), p. 171103. DOI: 10.1103/PhysRevLett.124.171103. arXiv: 1912.09340 [gr-qc].
- [167] Sebastian Blacker, Niels-Uwe F. Bastian, Andreas Bauswein, et al. “Constraining the onset density of the hadron-quark phase transition with gravitational-wave observations”. In: *Phys. Rev. D* 102.12 (2020), p. 123023. DOI: 10.1103/PhysRevD.102.123023. arXiv: 2006.03789 [astro-ph.HE].
- [168] Gloria Montana, Laura Tolos, Matthias Hanauske, et al. “Constraining twin stars with GW170817”. In: *Phys. Rev. D* 99.10 (2019), p. 103009. DOI: 10.1103/PhysRevD.99.103009. arXiv: 1811.10929 [astro-ph.HE].
- [169] Henrique Gieg, Tim Dietrich, and Maximiliano Ujevic. “Simulating Binary Neutron Stars with Hybrid Equation of States: Gravitational Waves, Electromagnetic Signatures, and Challenges for Numerical Relativity”. In: *Particles* 2.3 (2019), pp. 365–384. DOI: 10.3390/particles2030023. arXiv: 1908.03135 [gr-qc].
- [170] Eanna E. Flanagan and Tanja Hinderer. “Constraining neutron star tidal Love numbers with gravitational wave detectors”. In: *Phys. Rev. D* 77 (2008), p. 021502. DOI: 10.1103/PhysRevD.77.021502. arXiv: 0709.1915 [astro-ph].
- [171] Tanja Hinderer, Benjamin D. Lackey, Ryan N. Lang, et al. “Tidal deformability of neutron stars with realistic equations of state and their gravitational wave signatures in binary inspiral”. In: *Phys. Rev. D* 81 (2010), p. 123016. DOI: 10.1103/PhysRevD.81.123016. arXiv: 0911.3535 [astro-ph.HE].
- [172] Eemeli Annala, Tyler Gorda, Alekski Kurkela, et al. “Evidence for quark-matter cores in massive neutron stars”. In: *Nature Phys.* 16.9 (2020), pp. 907–910. DOI: 10.1038/s41567-020-0914-9. arXiv: 1903.09121 [astro-ph.HE].
- [173] F. Douchin and P. Haensel. “A unified equation of state of dense matter and neutron star structure”. In: *Astron. Astrophys.* 380 (2001), p. 151. DOI: 10.1051/0004-6361:20011402. arXiv: astro-ph/0111092.

- 
- [174] S. Typel, G. Ropke, T. Klahn, et al. “Composition and thermodynamics of nuclear matter with light clusters”. In: *Phys. Rev. C* 81 (2010), p. 015803. DOI: 10.1103/PhysRevC.81.015803. arXiv: 0908.2344 [nucl-th].
- [175] Andrew W. Steiner, Matthias Hempel, and Tobias Fischer. “Core-collapse supernova equations of state based on neutron star observations”. In: *Astrophys. J.* 774 (2013), p. 17. DOI: 10.1088/0004-637X/774/1/17. arXiv: 1207.2184 [astro-ph.SR].
- [176] S. Gandolfi, J. Carlson, and Sanjay Reddy. “The maximum mass and radius of neutron stars and the nuclear symmetry energy”. In: *Phys. Rev. C* 85 (2012), p. 032801. DOI: 10.1103/PhysRevC.85.032801. arXiv: 1101.1921 [nucl-th].
- [177] K. Hebeler, J. M. Lattimer, C. J. Pethick, et al. “Equation of state and neutron star properties constrained by nuclear physics and observation”. In: *Astrophys. J.* 773 (2013), p. 11. DOI: 10.1088/0004-637X/773/1/11. arXiv: 1303.4662 [astro-ph.SR].
- [178] Arianna Carbone, Andrea Cipollone, Carlo Barbieri, et al. “Self-consistent Green’s functions formalism with three-body interactions”. In: *Phys. Rev. C* 88.5 (2013), p. 054326. DOI: 10.1103/PhysRevC.88.054326. arXiv: 1310.3688 [nucl-th].
- [179] G. Hagen, T. Papenbrock, A. Ekström, et al. “Coupled-cluster calculations of nucleonic matter”. In: *Phys. Rev. C* 89.1 (2014), p. 014319. DOI: 10.1103/PhysRevC.89.014319. arXiv: 1311.2925 [nucl-th].
- [180] J. W. Holt and N. Kaiser. “Equation of state of nuclear and neutron matter at third-order in perturbation theory from chiral effective field theory”. In: *Phys. Rev. C* 95.3 (2017), p. 034326. DOI: 10.1103/PhysRevC.95.034326. arXiv: 1612.04309 [nucl-th].
- [181] C. Drischler, K. Hebeler, and A. Schwenk. “Chiral interactions up to next-to-next-to-next-to-leading order and nuclear saturation”. In: *Phys. Rev. Lett.* 122.4 (2019), p. 042501. DOI: 10.1103/PhysRevLett.122.042501. arXiv: 1710.08220 [nucl-th].
- [182] Jocelyn S. Read, Benjamin D. Lackey, Benjamin J. Owen, et al. “Constraints on a phenomenologically parameterized neutron-star equation of state”. In: *Phys. Rev. D* 79 (2009), p. 124032. DOI: 10.1103/PhysRevD.79.124032. arXiv: 0812.2163 [astro-ph].
- [183] Philippe Landry and Reed Essick. “Nonparametric inference of the neutron star equation of state from gravitational wave observations”. In: *Phys. Rev. D* 99.8 (2019), p. 084049. DOI: 10.1103/PhysRevD.99.084049. arXiv: 1811.12529 [gr-qc].
- [184] Ingo Tews. “Spectrum of shear modes in the neutron-star crust: Estimating the nuclear-physics uncertainties”. In: *Phys. Rev. C* 95.1 (2017), p. 015803. DOI: 10.1103/PhysRevC.95.015803. arXiv: 1607.06998 [nucl-th].
- [185] D. Shoemaker et al. “Advanced LIGO anticipated sensitivity curves”. In: *LIGO-T0900288*, <https://dcc.ligo.org/cgi-bin/DocDB/ShowDocument?docid=2974> (2010).

## BIBLIOGRAPHY

---

- [186] Katerina Chatziioannou, James Alexander Clark, Andreas Bauswein, et al. “Inferring the post-merger gravitational wave emission from binary neutron star coalescences”. In: *Phys. Rev. D* 96.12 (2017), p. 124035. DOI: 10.1103/PhysRevD.96.124035. arXiv: 1711.00040 [gr-qc].
- [187] Sukanta Bose, Kabir Chakravarti, Luciano Rezzolla, et al. “Neutron-star Radius from a Population of Binary Neutron Star Mergers”. In: *Phys. Rev. Lett.* 120.3 (2018), p. 031102. DOI: 10.1103/PhysRevLett.120.031102. arXiv: 1705.10850 [gr-qc].
- [188] Andoni Torres-Rivas, Katerina Chatziioannou, Andreas Bauswein, et al. “Observing the post-merger signal of GW170817-like events with improved gravitational-wave detectors”. In: *Phys. Rev. D* 99.4 (2019), p. 044014. DOI: 10.1103/PhysRevD.99.044014. arXiv: 1811.08931 [gr-qc].
- [189] Paul J. Easter, Paul D. Lasky, Andrew R. Casey, et al. “Computing Fast and Reliable Gravitational Waveforms of Binary Neutron Star Merger Remnants”. In: *Phys. Rev. D* 100.4 (2019), p. 043005. DOI: 10.1103/PhysRevD.100.043005. arXiv: 1811.11183 [gr-qc].
- [190] Ka Wa Tsang, Tim Dietrich, and Chris Van Den Broeck. “Modeling the post-merger gravitational wave signal and extracting binary properties from future binary neutron star detections”. In: *Phys. Rev. D* 100.4 (2019), p. 044047. DOI: 10.1103/PhysRevD.100.044047. arXiv: 1907.02424 [gr-qc].
- [191] Matteo Breschi, Sebastiano Bernuzzi, Francesco Zappa, et al. “kiloHertz gravitational waves from binary neutron star remnants: time-domain model and constraints on extreme matter”. In: *Phys. Rev. D* 100.10 (2019), p. 104029. DOI: 10.1103/PhysRevD.100.104029. arXiv: 1908.11418 [gr-qc].
- [192] Gordon Baym, Christopher Pethick, and Peter Sutherland. “The Ground state of matter at high densities: Equation of state and stellar models”. In: *Astrophys. J.* 170 (1971), pp. 299–317. DOI: 10.1086/151216.
- [193] John W. Negele and D. Vautherin. “Neutron star matter at subnuclear densities”. In: *Nucl. Phys. A* 207 (1973), pp. 298–320. DOI: 10.1016/0375-9474(73)90349-7.
- [194] Matthew F. Carney, Leslie E. Wade, and Burke S. Irwin. “Comparing two models for measuring the neutron star equation of state from gravitational-wave signals”. In: *Phys. Rev. D* 98.6 (2018), p. 063004. DOI: 10.1103/PhysRevD.98.063004. arXiv: 1805.11217 [gr-qc].
- [195] Rossella Gamba, Jocelyn S. Read, and Leslie E. Wade. “The impact of the crust equation of state on the analysis of GW170817”. In: *Class. Quant. Grav.* 37.2 (2020), p. 025008. DOI: 10.1088/1361-6382/ab5ba4. arXiv: 1902.04616 [gr-qc].
- [196] B. S. Sathyaprakash and S. V. Dhurandhar. “Choice of filters for the detection of gravitational waves from coalescing binaries”. In: *Phys. Rev. D* 44 (1991), pp. 3819–3834. DOI: 10.1103/PhysRevD.44.3819.
- [197] Luc Blanchet, Thibault Damour, Bala R. Iyer, et al. “Gravitational radiation damping of compact binary systems to second postNewtonian order”. In: *Phys. Rev. Lett.* 74 (1995), pp. 3515–3518. DOI: 10.1103/PhysRevLett.74.3515. arXiv: gr-qc/9501027.

- 
- [198] Walter D. Goldberger and Ira Z. Rothstein. “An Effective field theory of gravity for extended objects”. In: *Phys. Rev. D* 73 (2006), p. 104029. DOI: 10.1103/PhysRevD.73.104029. arXiv: hep-th/0409156.
- [199] Alejandro Bohé, Guillaume Faye, Sylvain Marsat, et al. “Quadratic-in-spin effects in the orbital dynamics and gravitational-wave energy flux of compact binaries at the 3PN order”. In: *Class. Quant. Grav.* 32.19 (2015), p. 195010. DOI: 10.1088/0264-9381/32/19/195010. arXiv: 1501.01529 [gr-qc].
- [200] Chandra Kant Mishra, Aditya Kela, K. G. Arun, et al. “Ready-to-use post-Newtonian gravitational waveforms for binary black holes with nonprecessing spins: An update”. In: *Phys. Rev. D* 93.8 (2016), p. 084054. DOI: 10.1103/PhysRevD.93.084054. arXiv: 1601.05588 [gr-qc].
- [201] Anuradha Samajdar and Tim Dietrich. “Constructing Love-Q-Relations with Gravitational Wave Detections”. In: *Phys. Rev. D* 101.12 (2020), p. 124014. DOI: 10.1103/PhysRevD.101.124014. arXiv: 2002.07918 [gr-qc].
- [202] Anuradha Samajdar and Tim Dietrich. “Waveform systematics for binary neutron star gravitational wave signals: Effects of spin, precession, and the observation of electromagnetic counterparts”. In: *Phys. Rev. D* 100.2 (2019), p. 024046. DOI: 10.1103/PhysRevD.100.024046. arXiv: 1905.03118 [gr-qc].
- [203] Richard W. O’Shaughnessy, C. Kim, V. Kalogera, et al. “Constraining population synthesis models via empirical binary compact object merger and supernovae rates”. In: *Astrophys. J.* 672 (2008), pp. 479–488. DOI: 10.1086/523620. arXiv: astro-ph/0610076.
- [204] LIGO Scientific Collaboration. *LIGO Algorithm Library - LALSuite*. free software (GPL). 2018. DOI: 10.7935/GT1W-FZ16.
- [205] J. Buchner, A. Georgakakis, K. Nandra, et al. “X-ray spectral modelling of the AGN obscuring region in the CDFS: Bayesian model selection and catalogue”. In: *Astron. Astrophys.* 564 (2014), A125. DOI: 10.1051/0004-6361/201322971. arXiv: 1402.0004 [astro-ph.HE].
- [206] Johannes Buchner. *PyMultiNest 2.9 documentation*. URL: <https://johannesbuchner.github.io/PyMultiNest/pymultinest.html>.
- [207] M. Coleman Miller, Cecilia Chirenti, and Frederick K. Lamb. “Constraining the equation of state of high-density cold matter using nuclear and astronomical measurements”. In: (Apr. 2019). DOI: 10.3847/1538-4357/ab4ef9. arXiv: 1904.08907 [astro-ph.HE].
- [208] Ryan J. Foley, David A. Coulter, Charles D. Kilpatrick, et al. “Updated Parameter Estimates for GW190425 Using Astrophysical Arguments and Implications for the Electromagnetic Counterpart”. In: *Mon. Not. Roy. Astron. Soc.* 494.1 (2020), pp. 190–198. DOI: 10.1093/mnras/staa725. arXiv: 2002.00956 [astro-ph.HE].
- [209] Ming-Zhe Han, Shao-Peng Tang, Yi-Ming Hu, et al. “Is GW190425 consistent with being a neutron star–black hole merger?” In: *Astrophys. J. Lett.* 891.1 (2020), p. L5. DOI: 10.3847/2041-8213/ab745a. arXiv: 2001.07882 [astro-ph.HE].

## BIBLIOGRAPHY

---

- [210] Koutarou Kyutoku, Sho Fujibayashi, Kota Hayashi, et al. “On the Possibility of GW190425 Being a Black Hole–Neutron Star Binary Merger”. In: *Astrophys. J. Lett.* 890.1 (2020), p. L4. DOI: 10.3847/2041-8213/ab6e70. arXiv: 2001.04474 [astro-ph.HE].
- [211] The LIGO Scientific Collaboration and the Virgo Collaboration. *Parameter estimation sample release for GWTC-1*. 2019. URL: <https://dcc.ligo.org/LIGO-P1800370/public>.
- [212] The LIGO Scientific Collaboration and the Virgo Collaboration. *Parameter estimation sample release for GW190425*. 2020. URL: <https://dcc.ligo.org/LIGO-P2000026/public>.
- [213] H. Jeffreys. *Theory of Probability*. Third. Oxford, England: Oxford, 1961.
- [214] B. P. Abbott et al. “A gravitational-wave standard siren measurement of the Hubble constant”. In: *Nature* 551.7678 (2017), pp. 85–88. DOI: 10.1038/nature24471. arXiv: 1710.05835 [astro-ph.CO].
- [215] Michael W. Coughlin, Tim Dietrich, Sarah Antier, et al. “Implications of the search for optical counterparts during the first six months of the Advanced LIGO’s and Advanced Virgo’s third observing run: possible limits on the ejecta mass and binary properties”. In: *Mon. Not. Roy. Astron. Soc.* 492.1 (2020), pp. 863–876. DOI: 10.1093/mnras/stz3457. arXiv: 1910.11246 [astro-ph.HE].
- [216] G. Raaijmakers et al. “A *NICER* view of PSR J0030+0451: Implications for the dense matter equation of state”. In: *Astrophys. J. Lett.* 887.1 (2019), p. L22. DOI: 10.3847/2041-8213/ab451a. arXiv: 1912.05703 [astro-ph.HE].
- [217] Jin-Liang Jiang, Shao-Peng Tang, Yuan-Zhu Wang, et al. “PSR J0030+0451, GW170817 and the nuclear data: joint constraints on equation of state and bulk properties of neutron stars”. In: *Astrophys. J.* 892 (2020), p. 1. DOI: 10.3847/1538-4357/ab77cf. arXiv: 1912.07467 [astro-ph.HE].
- [218] I. Tews, J. Margueron, and S. Reddy. “Confronting gravitational-wave observations with modern nuclear physics constraints”. In: *Eur. Phys. J. A* 55.6 (2019), p. 97. DOI: 10.1140/epja/i2019-12774-6. arXiv: 1901.09874 [nucl-th].
- [219] D. Alvarez-Castillo, A. Ayriyan, S. Benic, et al. “New class of hybrid EoS and Bayesian M-R data analysis”. In: *Eur. Phys. J. A* 52.3 (2016), p. 69. DOI: 10.1140/epja/i2016-16069-2. arXiv: 1603.03457 [nucl-th].
- [220] Masaru Shibata, Enping Zhou, Kenta Kiuchi, et al. “Constraint on the maximum mass of neutron stars using GW170817 event”. In: *Phys. Rev. D* 100.2 (2019), p. 023015. DOI: 10.1103/PhysRevD.100.023015. arXiv: 1905.03656 [astro-ph.HE].
- [221] Milton Ruiz, Stuart L. Shapiro, and Antonios Tsokaros. “GW170817, General Relativistic Magnetohydrodynamic Simulations, and the Neutron Star Maximum Mass”. In: *Phys. Rev. D* 97.2 (2018), p. 021501. DOI: 10.1103/PhysRevD.97.021501. arXiv: 1711.00473 [astro-ph.HE].



- [222] Slavko Bogdanov et al. “Constraining the Neutron Star Mass–Radius Relation and Dense Matter Equation of State with *NICER*. II. Emission from Hot Spots on a Rapidly Rotating Neutron Star”. In: *Astrophys. J. Lett.* 887.1 (2019), p. L26. DOI: 10.3847/2041-8213/ab5968. arXiv: 1912.05707 [astro-ph.HE].
- [223] M. C. Miller, F. K. Lamb, A. J. Dittmann, et al. *NICER PSR J0030+0451 Illinois-Maryland MCMC Samples*. Version 1.0.0. Dec. 2019. DOI: 10.5281/zenodo.3473466. URL: <https://doi.org/10.5281/zenodo.3473466>.
- [224] Gregory Ashton et al. “BILBY: A user-friendly Bayesian inference library for gravitational-wave astronomy”. In: *Astrophys. J. Suppl.* 241.2 (2019), p. 27. DOI: 10.3847/1538-4365/ab06fc. arXiv: 1811.02042 [astro-ph.IM].
- [225] LIGO Scientific Collaboration and Virgo Collaboration. <https://www.gw-openscience.org/events/GW170817/>. 2017.
- [226] LIGO Scientific Collaboration and Virgo Collaboration. [https://www.gw-openscience.org/eventapi/html/03\\_Discovery\\_Papers/GW190425/v1](https://www.gw-openscience.org/eventapi/html/03_Discovery_Papers/GW190425/v1). 2020.
- [227] Rory J. E. Smith, Gregory Ashton, Avi Vajpeyi, et al. “Massively parallel Bayesian inference for transient gravitational-wave astronomy”. In: *Mon. Not. Roy. Astron. Soc.* 498.3 (2020), pp. 4492–4502. DOI: 10.1093/mnras/staa2483. arXiv: 1909.11873 [gr-qc].
- [228] Farr B. Farr W. M. and Littenberg T. “Modelling Calibration Errors in CBC Waveforms”. In: *Collaboration Technical Report* No. LIGO-T1400682 ().
- [229] Craig Cahillane et al. “Calibration uncertainty for Advanced LIGO’s first and second observing runs”. In: *Phys. Rev. D* 96.10 (2017), p. 102001. DOI: 10.1103/PhysRevD.96.102001. arXiv: 1708.03023 [astro-ph.IM].
- [230] Aaron Viets et al. “Reconstructing the calibrated strain signal in the Advanced LIGO detectors”. In: *Class. Quant. Grav.* 35.9 (2018), p. 095015. DOI: 10.1088/1361-6382/aab658. arXiv: 1710.09973 [astro-ph.IM].
- [231] Tyson B. Littenberg and Neil J. Cornish. “Bayesian inference for spectral estimation of gravitational wave detector noise”. In: *Phys. Rev. D* 91.8 (2015), p. 084034. DOI: 10.1103/PhysRevD.91.084034. arXiv: 1410.3852 [gr-qc].
- [232] Daniel Kasen, Brian Metzger, Jennifer Barnes, et al. “Origin of the heavy elements in binary neutron-star mergers from a gravitational wave event”. In: *Nature* 551 (2017), p. 80. DOI: 10.1038/nature24453. arXiv: 1710.05463 [astro-ph.HE].
- [233] Jennifer Barnes, Daniel Kasen, Meng-Ru Wu, et al. “Radioactivity and thermalization in the ejecta of compact object mergers and their impact on kilonova light curves”. In: *Astrophys. J.* 829.2 (2016), p. 110. DOI: 10.3847/0004-637X/829/2/110. arXiv: 1605.07218 [astro-ph.HE].
- [234] Tim Dietrich and Maximiliano Ujevic. “Modeling dynamical ejecta from binary neutron star mergers and implications for electromagnetic counterparts”. In: *Class. Quant. Grav.* 34.10 (2017), p. 105014. DOI: 10.1088/1361-6382/aa6bb0. arXiv: 1612.03665 [gr-qc].

## BIBLIOGRAPHY

---

- [235] Albino Perego, David Radice, and Sebastiano Bernuzzi. “AT 2017gfo: An Anisotropic and Three-component Kilonova Counterpart of GW170817”. In: *Astrophys. J. Lett.* 850.2 (2017), p. L37. DOI: 10.3847/2041-8213/aa9ab9. arXiv: 1711.03982 [astro-ph.HE].
- [236] Kyohei Kawaguchi, Masaru Shibata, and Masaomi Tanaka. “Diversity of kilonova light curves”. In: (Aug. 2019). DOI: 10.3847/1538-4357/ab61f6. arXiv: 1908.05815 [astro-ph.HE].
- [237] Zoheyr Doctor, Ben Farr, Daniel E. Holz, et al. “Statistical Gravitational Waveform Models: What to Simulate Next?”. In: *Phys. Rev. D* 96.12 (2017), p. 123011. DOI: 10.1103/PhysRevD.96.123011. arXiv: 1706.05408 [astro-ph.HE].
- [238] Michael Pürrer. “Frequency domain reduced order models for gravitational waves from aligned-spin compact binaries”. In: *Class. Quant. Grav.* 31.19 (2014), p. 195010. DOI: 10.1088/0264-9381/31/19/195010. arXiv: 1402.4146 [gr-qc].
- [239] I. Andreoni et al. “Follow up of GW170817 and its electromagnetic counterpart by Australian-led observing programs”. In: *Publ. Astron. Soc. Austral.* 34 (2017), e069. DOI: 10.1017/pasa.2017.65. arXiv: 1710.05846 [astro-ph.HE].
- [240] Iair Arcavi et al. “Optical emission from a kilonova following a gravitational-wave-detected neutron-star merger”. In: *Nature* 551 (2017), p. 64. DOI: 10.1038/nature24291. arXiv: 1710.05843 [astro-ph.HE].
- [241] M. R. Drout et al. “Light Curves of the Neutron Star Merger GW170817/SSS17a: Implications for R-Process Nucleosynthesis”. In: *Science* 358 (2017), pp. 1570–1574. DOI: 10.1126/science.aaq0049. arXiv: 1710.05443 [astro-ph.HE].
- [242] P. A. Evans et al. “Swift and NuSTAR observations of GW170817: detection of a blue kilonova”. In: *Science* 358 (2017), p. 1565. DOI: 10.1126/science.aap9580. arXiv: 1710.05437 [astro-ph.HE].
- [243] M. M. Kasliwal et al. “Illuminating Gravitational Waves: A Concordant Picture of Photons from a Neutron Star Merger”. In: *Science* 358 (2017), p. 1559. DOI: 10.1126/science.aap9455. arXiv: 1710.05436 [astro-ph.HE].
- [244] E. Troja et al. “The X-ray counterpart to the gravitational wave event GW 170817”. In: *Nature* 551 (2017), pp. 71–74. DOI: 10.1038/nature24290. arXiv: 1710.05433 [astro-ph.HE].
- [245] Yousuke Utsumi et al. “J-GEM observations of an electromagnetic counterpart to the neutron star merger GW170817”. In: *Publ. Astron. Soc. Jap.* 69.6 (2017), p. 101. DOI: 10.1093/pasj/psx118. arXiv: 1710.05848 [astro-ph.HE].
- [246] Kenta Kiuchi, Koutarou Kyutoku, Masaru Shibata, et al. “Revisiting the lower bound on tidal deformability derived by AT 2017gfo”. In: *Astrophys. J. Lett.* 876.2 (2019), p. L31. DOI: 10.3847/2041-8213/ab1e45. arXiv: 1903.01466 [astro-ph.HE].
- [247] David Radice, Albino Perego, Kenta Hotokezaka, et al. “Binary Neutron Star Mergers: Mass Ejection, Electromagnetic Counterparts and Nucleosynthesis”. In: *Astrophys. J.* 869.2 (2018), p. 130. DOI: 10.3847/1538-4357/aaf054. arXiv: 1809.11161 [astro-ph.HE].

- [248] Tim Dietrich, Maximiliano Ujevic, Wolfgang Tichy, et al. “Gravitational waves and mass ejecta from binary neutron star mergers: Effect of the mass-ratio”. In: *Phys. Rev. D* 95.2 (2017), p. 024029. DOI: 10.1103/PhysRevD.95.024029. arXiv: 1607.06636 [gr-qc].
- [249] Kenta Hotokezaka, Koutarou Kyutoku, Hirotada Okawa, et al. “Binary Neutron Star Mergers: Dependence on the Nuclear Equation of State”. In: *Phys. Rev. D* 83 (2011), p. 124008. DOI: 10.1103/PhysRevD.83.124008. arXiv: 1105.4370 [astro-ph.HE].
- [250] Michalis Agathos, Francesco Zappa, Sebastiano Bernuzzi, et al. “Inferring Prompt Black-Hole Formation in Neutron Star Mergers from Gravitational-Wave Data”. In: *Phys. Rev. D* 101.4 (2020), p. 044006. DOI: 10.1103/PhysRevD.101.044006. arXiv: 1908.05442 [gr-qc].
- [251] G. Hinshaw et al. “Five-Year Wilkinson Microwave Anisotropy Probe (WMAP) Observations: Data Processing, Sky Maps, and Basic Results”. In: *Astrophys. J. Suppl.* 180 (2009), pp. 225–245. DOI: 10.1088/0067-0049/180/2/225. arXiv: 0803.0732 [astro-ph].
- [252] Aidan C. Crook, John P. Huchra, Nathalie Martimbeau, et al. “Groups of Galaxies in the Two Micron All-Sky Redshift Survey”. In: *Astrophys. J.* 655 (2007), pp. 790–813. DOI: 10.1086/510201. arXiv: astro-ph/0610732.
- [253] Christopher M. Springob, Christina Magoulas, Matthew Colless, et al. “The 6dF Galaxy Survey: Peculiar Velocity Field and Cosmography”. In: *Mon. Not. Roy. Astron. Soc.* 445.3 (2014), pp. 2677–2697. DOI: 10.1093/mnras/stu1743. arXiv: 1409.6161 [astro-ph.CO].
- [254] Jonathan Carrick, Stephen J. Turnbull, Guilhem Lavaux, et al. “Cosmological parameters from the comparison of peculiar velocities with predictions from the 2M++ density field”. In: *Mon. Not. Roy. Astron. Soc.* 450.1 (2015), pp. 317–332. DOI: 10.1093/mnras/stv547. arXiv: 1504.04627 [astro-ph.CO].
- [255] Michael W. Coughlin, Tim Dietrich, Jack Heinzl, et al. “Standardizing kilonovae and their use as standard candles to measure the Hubble constant”. In: *Phys. Rev. Res.* 2.2 (2020), p. 022006. DOI: 10.1103/PhysRevResearch.2.022006. arXiv: 1908.00889 [astro-ph.HE].
- [256] Rahul Kashyap, Gayathri Raman, and Parameswaran Ajith. “Can Kilonova Light curves be Standardized?” In: *Astrophys. J. Lett.* 886.1 (2019), p. L19. DOI: 10.3847/2041-8213/ab543f. arXiv: 1908.02168 [astro-ph.SR].
- [257] Daniel Foreman-Mackey, David W. Hogg, Dustin Lang, et al. “emcee: The MCMC Hammer”. In: *Publ. Astron. Soc. Pac.* 125 (2013), pp. 306–312. DOI: 10.1086/670067. arXiv: 1202.3665 [astro-ph.IM].
- [258] Kenta Hotokezaka, Ehud Nakar, Ore Gottlieb, et al. “A Hubble constant measurement from superluminal motion of the jet in GW170817”. In: *Nature Astron.* 3.10 (2019), pp. 940–944. DOI: 10.1038/s41550-019-0820-1. arXiv: 1806.10596 [astro-ph.CO].
- [259] Adam G. Riess et al. “A 2.4% Determination of the Local Value of the Hubble Constant”. In: *Astrophys. J.* 826.1 (2016), p. 56. DOI: 10.3847/0004-637X/826/1/56. arXiv: 1604.01424 [astro-ph.CO].

## BIBLIOGRAPHY

---

- [260] P. A. R. Ade et al. “Planck 2015 results. XIII. Cosmological parameters”. In: *Astron. Astrophys.* 594 (2016), A13. DOI: 10.1051/0004-6361/201525830. arXiv: 1502.01589 [astro-ph.CO].
- [261] Tim Dietrich, Sebastiano Bernuzzi, and Wolfgang Tichy. “Closed-form tidal approximants for binary neutron star gravitational waveforms constructed from high-resolution numerical relativity simulations”. In: *Phys. Rev. D* 96.12 (2017), p. 121501. DOI: 10.1103/PhysRevD.96.121501. arXiv: 1706.02969 [gr-qc].
- [262] Benjamin P Abbott et al. “Model comparison from LIGO–Virgo data on GW170817’s binary components and consequences for the merger remnant”. In: *Class. Quant. Grav.* 37.4 (2020), p. 045006. DOI: 10.1088/1361-6382/ab5f7c. arXiv: 1908.01012 [gr-qc].
- [263] B. P. Abbott et al. “Tests of General Relativity with GW170817”. In: *Phys. Rev. Lett.* 123.1 (2019), p. 011102. DOI: 10.1103/PhysRevLett.123.011102. arXiv: 1811.00364 [gr-qc].
- [264] Tanja Hinderer et al. “Effects of neutron-star dynamic tides on gravitational waveforms within the effective-one-body approach”. In: *Phys. Rev. Lett.* 116.18 (2016), p. 181101. DOI: 10.1103/PhysRevLett.116.181101. arXiv: 1602.00599 [gr-qc].
- [265] Benjamin D. Lackey, Michael Pürrer, Andrea Taracchini, et al. “Surrogate model for an aligned-spin effective one body waveform model of binary neutron star inspirals using Gaussian process regression”. In: *Phys. Rev. D* 100.2 (2019), p. 024002. DOI: 10.1103/PhysRevD.100.024002. arXiv: 1812.08643 [gr-qc].
- [266] O. McBrien, S. Smartt, K. W. Smith, et al. “LIGO/Virgo S190425z: ATLAS observations of the S190425z skymap.” In: *GRB Coordinates Network* 24197 (Jan. 2019), p. 1.
- [267] B. P. Gompertz et al. “Searching for Electromagnetic Counterparts to Gravitational-wave Merger Events with the Prototype Gravitational-wave Optical Transient Observer (GOTO-4)”. In: *Mon. Not. Roy. Astron. Soc.* 497.1 (2020), pp. 726–738. DOI: 10.1093/mnras/staa1845. arXiv: 2004.00025 [astro-ph.HE].
- [268] V. Lipunov, E. Gorbovskoy, V. Kornilov, et al. “LIGO/Virgo S190425z Global MASTER-Net observations report.” In: *GRB Coordinates Network* 24167 (Jan. 2019), p. 1.
- [269] Michael W. Coughlin et al. “GROWTH on S190425z: Searching thousands of square degrees to identify an optical or infrared counterpart to a binary neutron star merger with the Zwicky Transient Facility and Palomar Gattini IR”. In: *Astrophys. J. Lett.* 885.1 (2019), p. L19. DOI: 10.3847/2041-8213/ab4ad8. arXiv: 1907.12645 [astro-ph.HE].
- [270] James M. Lattimer. “The nuclear equation of state and neutron star masses”. In: *Ann. Rev. Nucl. Part. Sci.* 62 (2012), pp. 485–515. DOI: 10.1146/annurev-nucl-102711-095018. arXiv: 1305.3510 [nucl-th].
- [271] Justin Alsing, Hector O. Silva, and Emanuele Berti. “Evidence for a maximum mass cut-off in the neutron star mass distribution and constraints on the equation of state”. In: *Mon. Not. Roy. Astron. Soc.* 478.1 (2018), pp. 1377–1391. DOI: 10.1093/mnras/sty1065. arXiv: 1709.07889 [astro-ph.HE].

- 
- [272] Maya Fishbach, Reed Essick, and Daniel E. Holz. “Does Matter Matter? Using the mass distribution to distinguish neutron stars and black holes”. In: *Astrophys. J. Lett.* 899 (2020), p. L8. DOI: 10.3847/2041-8213/aba7b6. arXiv: 2006.13178 [astro-ph.HE].
- [273] Will M. Farr and Katerina Chatziioannou. “A Population-Informed Mass Estimate for Pulsar J0740+6620”. In: *Research Notes of the AAS* 4.5 (May 2020), p. 65. DOI: 10.3847/2515-5172/ab9088. URL: <https://doi.org/10.3847%2F2515-5172%2Fab9088>.
- [274] Vassiliki Kalogera and Gordon Baym. “The maximum mass of a neutron star”. In: *Astrophys. J. Lett.* 470 (1996), pp. L61–L64. DOI: 10.1086/310296. arXiv: astro-ph/9608059.
- [275] Ramandeep Gill, Antonios Nathanail, and Luciano Rezzolla. “When Did the Remnant of GW170817 Collapse to a Black Hole?” In: *Astrophys. J.* 876.2 (2019), p. 139. DOI: 10.3847/1538-4357/ab16da. arXiv: 1901.04138 [astro-ph.HE].
- [276] Tim Dietrich, Tanja Hinderer, and Anuradha Samajdar. “Interpreting Binary Neutron Star Mergers: Describing the Binary Neutron Star Dynamics, Modelling Gravitational Waveforms, and Analyzing Detections”. In: *Gen. Rel. Grav.* 53.3 (2021), p. 27. DOI: 10.1007/s10714-020-02751-6. arXiv: 2004.02527 [gr-qc].
- [277] R. Abbott et al. “GW190814: Gravitational Waves from the Coalescence of a 23 Solar Mass Black Hole with a 2.6 Solar Mass Compact Object”. In: *Astrophys. J. Lett.* 896.2 (2020), p. L44. DOI: 10.3847/2041-8213/ab960f. arXiv: 2006.12611 [astro-ph.HE].
- [278] An Chen, Nathan K. Johnson-McDaniel, Tim Dietrich, et al. “Distinguishing high-mass binary neutron stars from binary black holes with second- and third-generation gravitational wave observatories”. In: *Phys. Rev. D* 101.10 (2020), p. 103008. DOI: 10.1103/PhysRevD.101.103008. arXiv: 2001.11470 [astro-ph.HE].
- [279] Margherita Fasano, Kaze W. K. Wong, Andrea Maselli, et al. “Distinguishing double neutron star from neutron star-black hole binary populations with gravitational wave observations”. In: *Phys. Rev. D* 102.2 (2020), p. 023025. DOI: 10.1103/PhysRevD.102.023025. arXiv: 2005.01726 [astro-ph.HE].
- [280] Francois Foucart. “Black Hole-Neutron Star Mergers: Disk Mass Predictions”. In: *Phys. Rev. D* 86 (2012), p. 124007. DOI: 10.1103/PhysRevD.86.124007. arXiv: 1207.6304 [astro-ph.HE].
- [281] Christian Jürgen Krüger and Francois Foucart. “Estimates for Disk and Ejecta Masses Produced in Compact Binary Mergers”. In: *Phys. Rev. D* 101.10 (2020), p. 103002. DOI: 10.1103/PhysRevD.101.103002. arXiv: 2002.07728 [astro-ph.HE].
- [282] Lee Lindblom. “Spectral Representations of Neutron-Star Equations of State”. In: *Phys. Rev. D* 82 (2010), p. 103011. DOI: 10.1103/PhysRevD.82.103011. arXiv: 1009.0738 [astro-ph.HE].
- [283] Lee Lindblom and Nathaniel M. Indik. “A Spectral Approach to the Relativistic Inverse Stellar Structure Problem”. In: *Phys. Rev. D* 86 (2012), p. 084003. DOI: 10.1103/PhysRevD.86.084003. arXiv: 1207.3744 [astro-ph.HE].

## BIBLIOGRAPHY

---

- [284] Reed Essick and Philippe Landry. “Discriminating between Neutron Stars and Black Holes with Imperfect Knowledge of the Maximum Neutron Star Mass”. In: *Astrophys. J.* 904.1 (2020), p. 80. DOI: 10.3847/1538-4357/abbd3b. arXiv: 2007.01372 [astro-ph.HE].
- [285] Elias R. Most, L. Jens Papenfort, Lukas R. Weih, et al. “A lower bound on the maximum mass if the secondary in GW190814 was once a rapidly spinning neutron star”. In: *Mon. Not. Roy. Astron. Soc.* 499.1 (2020), pp. L82–L86. DOI: 10.1093/mnrasl/slaa168. arXiv: 2006.14601 [astro-ph.HE].
- [286] Hung Tan, Jacquelyn Noronha-Hostler, and Nico Yunes. “Neutron Star Equation of State in light of GW190814”. In: *Phys. Rev. Lett.* 125.26 (2020), p. 261104. DOI: 10.1103/PhysRevLett.125.261104. arXiv: 2006.16296 [astro-ph.HE].
- [287] F. J. Fattoyev, C. J. Horowitz, J. Piekarewicz, et al. “GW190814: Impact of a 2.6 solar mass neutron star on the nucleonic equations of state”. In: *Phys. Rev. C* 102.6 (2020), p. 065805. DOI: 10.1103/PhysRevC.102.065805. arXiv: 2007.03799 [nucl-th].
- [288] Nai-Bo Zhang and Bao-An Li. “GW190814’s Secondary Component with Mass 2.50–2.67  $M_{\odot}$  as a Superfast Pulsar”. In: *Astrophys. J.* 902.1 (2020), p. 38. DOI: 10.3847/1538-4357/abb470. arXiv: 2007.02513 [astro-ph.HE].
- [289] Antonios Tsokaros, Milton Ruiz, and Stuart L. Shapiro. “GW190814: Spin and equation of state of a neutron star companion”. In: *Astrophys. J.* 905.1 (2020), p. 48. DOI: 10.3847/1538-4357/abc421. arXiv: 2007.05526 [astro-ph.HE].
- [290] Kyriakos Vattis, Isabelle S. Goldstein, and Savvas M. Koushiappas. “Could the 2.6  $M_{\odot}$  object in GW190814 be a primordial black hole?” In: *Phys. Rev. D* 102.6 (2020), p. 061301. DOI: 10.1103/PhysRevD.102.061301. arXiv: 2006.15675 [astro-ph.HE].
- [291] The LIGO Scientific Collaboration and the Virgo Collaboration. *GW190814 parameter estimation samples*. 2020. URL: <https://dcc.ligo.org/P2000183/public>.
- [292] I. Tews and A. Schwenk. “Spin-polarized neutron matter, the maximum mass of neutron stars, and GW170817”. In: *Astrophys. J.* 892 (2020), p. 14. DOI: 10.3847/1538-4357/ab7232. arXiv: 1908.02638 [nucl-th].
- [293] D. E. Alvarez-Castillo and D. B. Blaschke. “High-mass twin stars with a multipolytropic equation of state”. In: *Phys. Rev. C* 96.4 (2017), p. 045809. DOI: 10.1103/PhysRevC.96.045809. arXiv: 1703.02681 [nucl-th].
- [294] I. Tews, T. Krüger, K. Hebeler, et al. “Neutron matter at next-to-next-to-next-to-leading order in chiral effective field theory”. In: *Phys. Rev. Lett.* 110.3 (2013), p. 032504. DOI: 10.1103/PhysRevLett.110.032504. arXiv: 1206.0025 [nucl-th].
- [295] C. Drischler, J. A. Melendez, R. J. Furnstahl, et al. “Quantifying uncertainties and correlations in the nuclear-matter equation of state”. In: *Phys. Rev. C* 102.5 (2020), p. 054315. DOI: 10.1103/PhysRevC.102.054315. arXiv: 2004.07805 [nucl-th].

- 
- [296] David Radice, Sebastiano Bernuzzi, Walter Del Pozzo, et al. “Probing Extreme-Density Matter with Gravitational Wave Observations of Binary Neutron Star Merger Remnants”. In: *Astrophys. J. Lett.* 842.2 (2017), p. L10. DOI: 10.3847/2041-8213/aa775f. arXiv: 1612.06429 [astro-ph.HE].
- [297] J. Heinzl, M. W. Coughlin, T. Dietrich, et al. “Comparing inclination dependent analyses of kilonova transients”. In: *Mon. Not. Roy. Astron. Soc.* 502.2 (2021), pp. 3057–3065. DOI: 10.1093/mnras/stab221. arXiv: 2010.10746 [astro-ph.HE].
- [298] Michael T. Wolff et al. “NICER Detection of Thermal X-Ray Pulsations from the Massive Millisecond Pulsars PSR J0740+6620 and PSR J1614–2230”. In: *Astrophys. J. Lett.* 918.2 (2021), p. L26. DOI: 10.3847/2041-8213/ac158e. arXiv: 2105.06978 [astro-ph.HE].
- [299] L. Struder et al. “The European Photon Imaging Camera on XMM-Newton: The pn-CCD camera”. In: *Astron. Astrophys.* 365 (2001), pp. L18–26. DOI: 10.1051/0004-6361:20000066.
- [300] Martin J. L. Turner et al. “The European Photon Imaging Camera on XMM-Newton: The MOS cameras”. In: *Astron. Astrophys.* 365 (2001), pp. L27–35. DOI: 10.1051/0004-6361:20000087. arXiv: astro-ph/0011498.
- [301] NICER. “Nicer Press Release”. In: (2021). URL: <https://www.nasa.gov/feature/goddard/2021/nasa-s-nicer-probes-the-squeezability-of-neutron-stars/>.
- [302] Rahul Somasundaram and Jérôme Margueron. “Impact of massive neutron star radii on the nature of phase transitions in dense matter”. In: (Apr. 2021). arXiv: 2104.13612 [astro-ph.HE].
- [303] Bhaskar Biswas. “Impact of PREX-II and Combined Radio/NICER/XMM-Newton’s Mass-radius Measurement of PSR J0740+6620 on the Dense-matter Equation of State”. In: *Astrophys. J.* 921.1 (2021), p. 63. DOI: 10.3847/1538-4357/ac1c72. arXiv: 2105.02886 [astro-ph.HE].
- [304] Bao-An Li, Bao-Jun Cai, Wen-Jie Xie, et al. “Progress in Constraining Nuclear Symmetry Energy Using Neutron Star Observables Since GW170817”. In: *Universe* 7.6 (2021), p. 182. DOI: 10.3390/universe7060182. arXiv: 2105.04629 [nucl-th].
- [305] Eemeli Annala, Tyler Gorda, Evangelia Katerini, et al. “Multimessenger constraints for ultra-dense matter”. In: (May 2021). arXiv: 2105.05132 [astro-ph.HE].
- [306] D. Adhikari et al. “Accurate Determination of the Neutron Skin Thickness of  $^{208}\text{Pb}$  through Parity-Violation in Electron Scattering”. In: *Phys. Rev. Lett.* 126.17 (2021), p. 172502. DOI: 10.1103/PhysRevLett.126.172502. arXiv: 2102.10767 [nucl-ex].
- [307] M.C. Miller, F. K. Lamb, A. J. Dittmann, et al. *NICER PSR J0740+6620 Illinois-Maryland MCMC Samples*. Apr. 2021. DOI: 10.5281/zenodo.4670689. URL: <https://doi.org/10.5281/zenodo.4670689>.

## BIBLIOGRAPHY

---

- [308] Thomas E. Riley, Anna L. Watts, Paul S. Ray, et al. *A NICER View of the Massive Pulsar PSR J0740+6620 Informed by Radio Timing and XMM-Newton Spectroscopy: Nested Samples for Millisecond Pulsar Parameter Estimation*. Version v1.0.0. Apr. 2021. DOI: 10.5281/zenodo.4697625. URL: <https://doi.org/10.5281/zenodo.4697625>.
- [309] Bhaskar Biswas, Rana Nandi, Prasanta Char, et al. “GW190814: on the properties of the secondary component of the binary”. In: *Mon. Not. Roy. Astron. Soc.* 505.2 (2021), pp. 1600–1606. DOI: 10.1093/mnras/stab1383. arXiv: 2010.02090 [astro-ph.HE].
- [310] Mark Alford. “Color superconducting quark matter in compact stars”. In: *eConf C010815* (2002). Ed. by R. Ouyed and F. Sannino, pp. 137–148. arXiv: hep-ph/0110150.
- [311] C. Drischler, R. J. Furnstahl, J. A. Melendez, et al. “How Well Do We Know the Neutron-Matter Equation of State at the Densities Inside Neutron Stars? A Bayesian Approach with Correlated Uncertainties”. In: *Phys. Rev. Lett.* 125.20 (2020), p. 202702. DOI: 10.1103/PhysRevLett.125.202702. arXiv: 2004.07232 [nucl-th].
- [312] S. Huth, C. Wellenhofer, and A. Schwenk. “New equations of state constrained by nuclear physics, observations, and QCD calculations of high-density nuclear matter”. In: *Phys. Rev. C* 103.2 (2021), p. 025803. DOI: 10.1103/PhysRevC.103.025803. arXiv: 2009.08885 [nucl-th].
- [313] Pawel Danielewicz, Roy Lacey, and William G. Lynch. “Determination of the equation of state of dense matter”. In: *Science* 298 (2002), pp. 1592–1596. DOI: 10.1126/science.1078070. arXiv: nucl-th/0208016.
- [314] A. Le Fèvre, Y. Leifels, W. Reisdorf, et al. “Constraining the nuclear matter equation of state around twice saturation density”. In: *Nucl. Phys. A* 945 (2016), pp. 112–133. DOI: 10.1016/j.nuclphysa.2015.09.015. arXiv: 1501.05246 [nucl-ex].
- [315] P. Russotto et al. “Results of the ASY-EOS experiment at GSI: The symmetry energy at suprasaturation density”. In: *Phys. Rev. C* 94.3 (2016), p. 034608. DOI: 10.1103/PhysRevC.94.034608. arXiv: 1608.04332 [nucl-ex].
- [316] M. B. Tsang, W. G. Lynch, P. Danielewicz, et al. “Symmetry energy constraints from GW170817 and laboratory experiments”. In: *Phys. Lett. B* 795 (2019), pp. 533–536. DOI: 10.1016/j.physletb.2019.06.059. arXiv: 1906.02180 [nucl-ex].
- [317] I. Tews, S. Gandolfi, A. Gezerlis, et al. “Quantum Monte Carlo calculations of neutron matter with chiral three-body forces”. In: *Phys. Rev. C* 93.2 (2016), p. 024305. DOI: 10.1103/PhysRevC.93.024305. arXiv: 1507.05561 [nucl-th].
- [318] M. Leonhardt, M. Pospiech, B. Schallmo, et al. “Symmetric nuclear matter from the strong interaction”. In: *Phys. Rev. Lett.* 125.14 (2020), p. 142502. DOI: 10.1103/PhysRevLett.125.142502. arXiv: 1907.05814 [nucl-th].
- [319] C. Fuchs and H. H. Wolter. “Modelization of the EOS”. In: *Eur. Phys. J. A* 30 (2006), pp. 5–21. DOI: 10.1140/epja/i2005-10313-x. arXiv: nucl-th/0511070.



- 
- [320] Yingxun Zhang, Ning Wang, Qing-Feng Li, et al. “Progress of quantum molecular dynamics model and its applications in heavy ion collisions”. In: *Front. Phys. (Beijing)* 15 (2020), p. 54301. DOI: 10.1007/s11467-020-0961-9. arXiv: 2005.12877 [nucl-th].
- [321] Xin An et al. “The BEST framework for the search for the QCD critical point and the chiral magnetic effect”. In: *Nucl. Phys. A* 1017 (2022), p. 122343. DOI: 10.1016/j.nuclphysa.2021.122343. arXiv: 2108.13867 [nucl-th].
- [322] Maria Colonna et al. “Comparison of heavy-ion transport simulations: Mean-field dynamics in a box”. In: *Phys. Rev. C* 104.2 (2021), p. 024603. DOI: 10.1103/PhysRevC.104.024603. arXiv: 2106.12287 [nucl-th].
- [323] A. Andronic, J. Lukasik, W. Reisdorf, et al. “Systematics of Stopping and Flow in Au+Au Collisions”. In: *Eur. Phys. J. A* 30 (2006), pp. 31–46. DOI: 10.1140/epja/i2006-10101-2. arXiv: nucl-ex/0608015.
- [324] W. Reisdorf et al. “Systematics of azimuthal asymmetries in heavy ion collisions in the 1 A GeV regime”. In: *Nucl. Phys. A* 876 (2012), pp. 1–60. DOI: 10.1016/j.nuclphysa.2011.12.006. arXiv: 1112.3180 [nucl-ex].
- [325] C. Hartnack, Rajeev K. Puri, J. Aichelin, et al. “Modeling the many body dynamics of heavy ion collisions: Present status and future perspective”. In: *Eur. Phys. J. A* 1 (1998), pp. 151–169. DOI: 10.1007/s100500050045. arXiv: nucl-th/9811015.
- [326] Yongjia Wang, Chenchen Guo, Qingfeng Li, et al. “Determination of the nuclear incompressibility from the rapidity-dependent elliptic flow in heavy-ion collisions at beam energies 0.4 A –1.0 A GeV”. In: *Phys. Lett. B* 778 (2018), pp. 207–212. DOI: 10.1016/j.physletb.2018.01.035. arXiv: 1804.04293 [nucl-th].
- [327] A. Le Fèvre, Y. Leifels, C. Hartnack, et al. “Origin of elliptic flow and its dependence on the equation of state in heavy ion reactions at intermediate energies”. In: *Phys. Rev. C* 98.3 (2018), p. 034901. DOI: 10.1103/PhysRevC.98.034901. arXiv: 1611.07500 [nucl-th].
- [328] Christian Thomas Sturm et al. “Evidence for a soft nuclear equation of state from kaon production in heavy ion collisions”. In: *Phys. Rev. Lett.* 86 (2001), pp. 39–42. DOI: 10.1103/PhysRevLett.86.39. arXiv: nucl-ex/0011001.
- [329] C. Fuchs, Amand Faessler, S. El-Basaouny, et al. “The Nuclear equation of state probed by K+ production in heavy ion collisions”. In: *J. Phys. G* 28 (2002). Ed. by I. Iori and A. Moroni, pp. 1615–1622. DOI: 10.1088/0954-3899/28/7/313. arXiv: nucl-th/0103036.
- [330] Brendan T. Reed, F. J. Fattoyev, C. J. Horowitz, et al. “Implications of PREX-2 on the Equation of State of Neutron-Rich Matter”. In: *Phys. Rev. Lett.* 126.17 (2021), p. 172503. DOI: 10.1103/PhysRevLett.126.172503. arXiv: 2101.03193 [nucl-th].
- [331] Reed Essick, Ingo Tews, Philippe Landry, et al. “Astrophysical Constraints on the Symmetry Energy and the Neutron Skin of Pb208 with Minimal Modeling Assumptions”. In: *Phys. Rev. Lett.* 127.19 (2021), p. 192701. DOI: 10.1103/PhysRevLett.127.192701. arXiv: 2102.10074 [nucl-th].

- [332] Bao-An Li. “Probing the high density behavior of nuclear symmetry energy with high-energy heavy ion collisions”. In: *Phys. Rev. Lett.* 88 (2002), p. 192701. DOI: 10.1103/PhysRevLett.88.192701. arXiv: nucl-th/0205002.
- [333] P. Russotto et al. “Symmetry energy from elliptic flow in  $^{197}\text{Au} + ^{197}\text{Au}$ ”. In: *Phys. Lett. B* 697 (2011), pp. 471–476. DOI: 10.1016/j.physletb.2011.02.033. arXiv: 1101.2361 [nucl-ex].
- [334] Th. Blaich et al. “A Large area detector for high-energy neutrons”. In: *Nucl. Instrum. Meth. A* 314 (1992), pp. 136–154. DOI: 10.1016/0168-9002(92)90507-Z.
- [335] M. D. Cozma. “Feasibility of constraining the curvature parameter of the symmetry energy using elliptic flow data”. In: *Eur. Phys. J. A* 54.3 (2018), p. 40. DOI: 10.1140/epja/i2018-12470-1. arXiv: 1706.01300 [nucl-th].
- [336] K. Hebeler, S. K. Bogner, R. J. Furnstahl, et al. “Improved nuclear matter calculations from chiral low-momentum interactions”. In: *Phys. Rev. C* 83 (2011), p. 031301. DOI: 10.1103/PhysRevC.83.031301. arXiv: 1012.3381 [nucl-th].
- [337] Christian Drischler, Kai Hebeler, and Achim Schwenk. “Asymmetric nuclear matter based on chiral two- and three-nucleon interactions”. In: *Phys. Rev. C* 93.5 (2016), p. 054314. DOI: 10.1103/PhysRevC.93.054314. arXiv: 1510.06728 [nucl-th].
- [338] Pawel Danielewicz and Jenny Lee. “Symmetry Energy II: Isobaric Analog States”. In: *Nucl. Phys. A* 922 (2014), pp. 1–70. DOI: 10.1016/j.nuclphysa.2013.11.005. arXiv: 1307.4130 [nucl-th].
- [339] M. B. Tsang, Yingxun Zhang, P. Danielewicz, et al. “Constraints on the density dependence of the symmetry energy”. In: *Phys. Rev. Lett.* 102 (2009), p. 122701. DOI: 10.1103/PhysRevLett.102.122701. arXiv: 0811.3107 [nucl-ex].
- [340] Zhen Zhang and Lie-Wen Chen. “Constraining the symmetry energy at subsaturation densities using isotope binding energy difference and neutron skin thickness”. In: *Phys. Lett. B* 726 (2013), pp. 234–238. DOI: 10.1016/j.physletb.2013.08.002. arXiv: 1302.5327 [nucl-th].
- [341] B. Alex Brown. “Constraints on the Skyrme Equations of State from Properties of Doubly Magic Nuclei”. In: *Phys. Rev. Lett.* 111.23 (2013), p. 232502. DOI: 10.1103/PhysRevLett.111.232502. arXiv: 1308.3664 [nucl-th].
- [342] J. Estee et al. “Probing the Symmetry Energy with the Spectral Pion Ratio”. In: *Phys. Rev. Lett.* 126.16 (2021), p. 162701. DOI: 10.1103/PhysRevLett.126.162701. arXiv: 2103.06861 [nucl-ex].
- [343] Gao-Chan Yong. “Symmetry energy extracted from the S $\pi$ RIT pion data in Sn+Sn systems”. In: *Phys. Rev. C* 104.1 (2021), p. 014613. DOI: 10.1103/PhysRevC.104.014613. arXiv: 2104.12098 [nucl-th].
- [344] Milva G. Orsaria, Germán Malfatti, Mauro Mariani, et al. “Phase transitions in neutron stars and their links to gravitational waves”. In: *J. Phys. G* 46.7 (2019), p. 073002. DOI: 10.1088/1361-6471/ab1d81. arXiv: 1907.04654 [astro-ph.HE].
- [345] Len Brandes, Norbert Kaiser, and Wolfram Weise. “Fluctuations and phases in baryonic matter”. In: *Eur. Phys. J. A* 57.7 (2021), p. 243. DOI: 10.1140/epja/s10050-021-00528-2. arXiv: 2103.06096 [nucl-th].

- 
- [346] Alexandros Gezerlis and J. Carlson. “Low-density neutron matter”. In: *Phys. Rev. C* 81 (2010), p. 025803. DOI: 10.1103/PhysRevC.81.025803. arXiv: 0911.3907 [nucl-th].
- [347] Ingo Tews, James M. Lattimer, Akira Ohnishi, et al. “Symmetry Parameter Constraints from a Lower Bound on Neutron-matter Energy”. In: *Astrophys. J.* 848.2 (2017), p. 105. DOI: 10.3847/1538-4357/aa8db9. arXiv: 1611.07133 [nucl-th].
- [348] Hans C Ohanian. “On the focusing of gravitational radiation”. In: *International Journal of Theoretical Physics* 9.6 (1974), pp. 425–437.
- [349] PV Bliokh and AA Minakov. “Diffraction of light and lens effect of the stellar gravitation field”. In: *Astrophysics and Space Science* 34.2 (1975), pp. L7–L9.
- [350] Robert J Bontz and Mark P Haugan. “A diffraction limit on the gravitational lens effect”. In: *Astrophysics and Space Science* 78.1 (1981), pp. 199–210.
- [351] Kip S Thorne. “The theory of gravitational radiation-an introductory review”. In: *Gravitational radiation*. 1983, pp. 1–57.
- [352] Sh Deguchi and WD Watson. “Diffraction in gravitational lensing for compact objects of low mass”. In: *The Astrophysical Journal* 307 (1986), pp. 30–37.
- [353] Takahiro T Nakamura. “Gravitational lensing of gravitational waves from inspiraling binaries by a point mass lens”. In: *Physical review letters* 80.6 (1998), p. 1138.
- [354] Ryuichi Takahashi and Takashi Nakamura. “Wave effects in gravitational lensing of gravitational waves from chirping binaries”. In: *Astrophys. J.* 595 (2003), pp. 1039–1051. DOI: 10.1086/377430. arXiv: astro-ph/0305055.
- [355] Masamune Oguri. “Strong gravitational lensing of explosive transients”. In: *Rept. Prog. Phys.* 82.12 (2019), p. 126901. DOI: 10.1088/1361-6633/ab4fc5. arXiv: 1907.06830 [astro-ph.CO].
- [356] Yun Wang, Albert Stebbins, and Edwin L. Turner. “Gravitational lensing of gravitational waves from merging neutron star binaries”. In: *Phys. Rev. Lett.* 77 (1996), pp. 2875–2878. DOI: 10.1103/PhysRevLett.77.2875. arXiv: astro-ph/9605140.
- [357] Liang Dai, Tejaswi Venumadhav, and Kris Sigurdson. “Effect of lensing magnification on the apparent distribution of black hole mergers”. In: *Phys. Rev. D* 95.4 (2017), p. 044011. DOI: 10.1103/PhysRevD.95.044011. arXiv: 1605.09398 [astro-ph.CO].
- [358] Graham P. Smith, Mathilde Jauzac, John Veitch, et al. “What if LIGO’s gravitational wave detections are strongly lensed by massive galaxy clusters?” In: *Mon. Not. Roy. Astron. Soc.* 475.3 (2018), pp. 3823–3828. DOI: 10.1093/mnras/sty031. arXiv: 1707.03412 [astro-ph.HE].
- [359] G. P. Smith et al. “Strong-lensing of Gravitational Waves by Galaxy Clusters”. In: *IAU Symp.* 338 (2017). Ed. by Gabriela González and Robert Hynes, pp. 98–102. DOI: 10.1017/S1743921318003757. arXiv: 1803.07851 [astro-ph.CO].
- [360] M. Sereno, Ph. Jetzer, A. Sesana, et al. “Cosmography with strong lensing of LISA gravitational wave sources”. In: *Mon. Not. Roy. Astron. Soc.* 415 (2011), p. 2773. DOI: 10.1111/j.1365-2966.2011.18895.x. arXiv: 1104.1977 [astro-ph.CO].

## BIBLIOGRAPHY

---

- [361] K. Haris, Ajit Kumar Mehta, Sumit Kumar, et al. “Identifying strongly lensed gravitational wave signals from binary black hole mergers”. In: (July 2018). arXiv: 1807.07062 [gr-qc].
- [362] Ken K. Y. Ng, Kaze W. K. Wong, Tom Broadhurst, et al. “Precise LIGO Lensing Rate Predictions for Binary Black Holes”. In: *Phys. Rev. D* 97.2 (2018), p. 023012. DOI: 10.1103/PhysRevD.97.023012. arXiv: 1703.06319 [astro-ph.CO].
- [363] Shun-Sheng Li, Shude Mao, Yuetong Zhao, et al. “Gravitational lensing of gravitational waves: A statistical perspective”. In: *Mon. Not. Roy. Astron. Soc.* 476.2 (2018), pp. 2220–2229. DOI: 10.1093/mnras/sty411. arXiv: 1802.05089 [astro-ph.CO].
- [364] Masamune Oguri. “Effect of gravitational lensing on the distribution of gravitational waves from distant binary black hole mergers”. In: *Mon. Not. Roy. Astron. Soc.* 480.3 (2018), pp. 3842–3855. DOI: 10.1093/mnras/sty2145. arXiv: 1807.02584 [astro-ph.CO].
- [365] Marek Biesiada, Xuheng Ding, Aleksandra Piorkowska, et al. “Strong gravitational lensing of gravitational waves from double compact binaries - perspectives for the Einstein Telescope”. In: *JCAP* 10 (2014), p. 080. DOI: 10.1088/1475-7516/2014/10/080. arXiv: 1409.8360 [astro-ph.HE].
- [366] Xuheng Ding, Marek Biesiada, and Zong-Hong Zhu. “Strongly lensed gravitational waves from intrinsically faint double compact binaries—prediction for the Einstein Telescope”. In: *JCAP* 12 (2015), p. 006. DOI: 10.1088/1475-7516/2015/12/006. arXiv: 1508.05000 [astro-ph.HE].
- [367] Kwun-Hang Lai, Otto A. Hannuksela, Antonio Herrera-Martin, et al. “Discovering intermediate-mass black hole lenses through gravitational wave lensing”. In: *Phys. Rev. D* 98.8 (2018), p. 083005. DOI: 10.1103/PhysRevD.98.083005. arXiv: 1801.07840 [gr-qc].
- [368] Katerina Chatziioannou, Nicolas Yunes, and Neil Cornish. “Model-Independent Test of General Relativity: An Extended post-Einsteinian Framework with Complete Polarization Content”. In: *Phys. Rev. D* 86 (2012). [Erratum: *Phys.Rev.D* 95, 129901 (2017)], p. 022004. DOI: 10.1103/PhysRevD.86.022004. arXiv: 1204.2585 [gr-qc].
- [369] Thomas E. Collett and David Bacon. “Testing the speed of gravitational waves over cosmological distances with strong gravitational lensing”. In: *Phys. Rev. Lett.* 118.9 (2017), p. 091101. DOI: 10.1103/PhysRevLett.118.091101. arXiv: 1602.05882 [astro-ph.HE].
- [370] Tessa Baker and Mark Trodden. “Multimessenger time delays from lensed gravitational waves”. In: *Phys. Rev. D* 95.6 (2017), p. 063512. DOI: 10.1103/PhysRevD.95.063512. arXiv: 1612.02004 [astro-ph.CO].
- [371] Xi-Long Fan, Kai Liao, Marek Biesiada, et al. “Speed of Gravitational Waves from Strongly Lensed Gravitational Waves and Electromagnetic Signals”. In: *Phys. Rev. Lett.* 118.9 (2017), p. 091102. DOI: 10.1103/PhysRevLett.118.091102. arXiv: 1612.04095 [gr-qc].
- [372] H. Yu and F. Y. Wang. “Testing Weak Equivalence Principle with Strongly Lensed Cosmic Transients”. In: *Eur. Phys. J. C* 78.9 (2018), p. 692. DOI: 10.1140/epjc/s10052-018-6162-9. arXiv: 1801.01257 [astro-ph.HE].

- 
- [373] Suvodip Mukherjee, Benjamin D. Wandelt, and Joseph Silk. “Multimessenger tests of gravity with weakly lensed gravitational waves”. In: *Phys. Rev. D* 101.10 (2020), p. 103509. DOI: 10.1103/PhysRevD.101.103509. arXiv: 1908.08950 [astro-ph.CO].
- [374] Pierre Christian, Salvatore Vitale, and Abraham Loeb. “Detecting Stellar Lensing of Gravitational Waves with Ground-Based Observatories”. In: *Phys. Rev. D* 98.10 (2018), p. 103022. DOI: 10.1103/PhysRevD.98.103022. arXiv: 1802.02586 [astro-ph.HE].
- [375] Liang Dai, Shun-Sheng Li, Barak Zackay, et al. “Detecting Lensing-Induced Diffraction in Astrophysical Gravitational Waves”. In: *Phys. Rev. D* 98.10 (2018), p. 104029. DOI: 10.1103/PhysRevD.98.104029. arXiv: 1810.00003 [gr-qc].
- [376] Alvin K. Y. Li, Rico K. L. Lo, Surabhi Sachdev, et al. “Finding diamonds in the rough: Targeted Sub-threshold Search for Strongly-lensed Gravitational-wave Events”. In: (Apr. 2019). arXiv: 1904.06020 [gr-qc].
- [377] Connor McIsaac, David Keitel, Thomas Collett, et al. “Search for strongly lensed counterpart images of binary black hole mergers in the first two LIGO observing runs”. In: *Phys. Rev. D* 102.8 (2020), p. 084031. DOI: 10.1103/PhysRevD.102.084031. arXiv: 1912.05389 [gr-qc].
- [378] Pablo Marchant, Katelyn Breivik, Christopher P. L. Berry, et al. “Eclipses of continuous gravitational waves as a probe of stellar structure”. In: *Phys. Rev. D* 101.2 (2020), p. 024039. DOI: 10.1103/PhysRevD.101.024039. arXiv: 1912.04268 [astro-ph.SR].
- [379] Tom Broadhurst, Jose M. Diego, and George Smoot. “Reinterpreting Low Frequency LIGO/Virgo Events as Magnified Stellar-Mass Black Holes at Cosmological Distances”. In: (Feb. 2018). arXiv: 1802.05273 [astro-ph.CO].
- [380] O. A. Hannuksela, K. Haris, K. K. Y. Ng, et al. “Search for gravitational lensing signatures in LIGO-Virgo binary black hole events”. In: *Astrophys. J. Lett.* 874.1 (2019), p. L2. DOI: 10.3847/2041-8213/ab0c0f. arXiv: 1901.02674 [gr-qc].
- [381] O. Contigiani. “Lensing efficiency for gravitational wave mergers”. In: *Mon. Not. Roy. Astron. Soc.* 492.3 (2020), pp. 3359–3363. DOI: 10.1093/mnras/staa026. arXiv: 2001.01135 [astro-ph.CO].
- [382] Nicholas Farrow, Xing-Jiang Zhu, and Eric Thrane. “The mass distribution of Galactic double neutron stars”. In: *Astrophys. J.* 876.1 (2019), p. 18. DOI: 10.3847/1538-4357/ab12e3. arXiv: 1902.03300 [astro-ph.HE].
- [383] Mohammadtaher Safarzadeh, Enrico Ramirez-Ruiz, and Edo Berger. “Does GW190425 require an alternative formation pathway than a fast-merging channel?” In: *Astrophys. J.* 900.1 (2020), p. 13. DOI: 10.3847/1538-4357/aba596. arXiv: 2001.04502 [astro-ph.HE].
- [384] Graham P. Smith, Andrew Robertson, Matteo Bianconi, et al. “Discovery of Strongly-lensed Gravitational Waves - Implications for the LSST Observing Strategy”. In: (Feb. 2019). arXiv: 1902.05140 [astro-ph.HE].
- [385] Tim Dietrich, David Radice, Sebastiano Bernuzzi, et al. “CoRe database of binary neutron star merger waveforms”. In: *Class. Quant. Grav.* 35.24 (2018), 24LT01. DOI: 10.1088/1361-6382/aaebc0. arXiv: 1806.01625 [gr-qc].

## BIBLIOGRAPHY

---

- [386] A. Bauswein, H. T. Janka, K. Hebeler, et al. “Equation-of-state dependence of the gravitational-wave signal from the ring-down phase of neutron-star mergers”. In: *Phys. Rev. D* 86 (2012), p. 063001. DOI: 10.1103/PhysRevD.86.063001. arXiv: 1204.1888 [astro-ph.SR].
- [387] Kentaro Takami, Luciano Rezzolla, and Luca Baiotti. “Constraining the Equation of State of Neutron Stars from Binary Mergers”. In: *Phys. Rev. Lett.* 113.9 (2014), p. 091104. DOI: 10.1103/PhysRevLett.113.091104. arXiv: 1403.5672 [gr-qc].
- [388] A. Bauswein, N. Stergioulas, and H. -T. Janka. “Revealing the high-density equation of state through binary neutron star mergers”. In: *Phys. Rev. D* 90.2 (2014), p. 023002. DOI: 10.1103/PhysRevD.90.023002. arXiv: 1403.5301 [astro-ph.SR].
- [389] Sebastiano Bernuzzi, Tim Dietrich, and Alessandro Nagar. “Modeling the complete gravitational wave spectrum of neutron star mergers”. In: *Phys. Rev. Lett.* 115.9 (2015), p. 091101. DOI: 10.1103/PhysRevLett.115.091101. arXiv: 1504.01764 [gr-qc].
- [390] Luciano Rezzolla and Kentaro Takami. “Gravitational-wave signal from binary neutron stars: a systematic analysis of the spectral properties”. In: *Phys. Rev. D* 93.12 (2016), p. 124051. DOI: 10.1103/PhysRevD.93.124051. arXiv: 1604.00246 [gr-qc].
- [391] Thibault Damour and Alessandro Nagar. “Relativistic tidal properties of neutron stars”. In: *Phys. Rev. D* 80 (2009), p. 084035. DOI: 10.1103/PhysRevD.80.084035. arXiv: 0906.0096 [gr-qc].
- [392] William G. Laarakkers and Eric Poisson. “Quadrupole moments of rotating neutron stars”. In: *Astrophys. J.* 512 (1999), pp. 282–287. DOI: 10.1086/306732. arXiv: gr-qc/9709033.
- [393] Eric Poisson. “Gravitational waves from inspiraling compact binaries: The Quadrupole moment term”. In: *Phys. Rev. D* 57 (1998), pp. 5287–5290. DOI: 10.1103/PhysRevD.57.5287. arXiv: gr-qc/9709032.
- [394] Ian Harry and Tanja Hinderer. “Observing and measuring the neutron-star equation-of-state in spinning binary neutron star systems”. In: *Class. Quant. Grav.* 35.14 (2018), p. 145010. DOI: 10.1088/1361-6382/aac7e3. arXiv: 1801.09972 [gr-qc].
- [395] P. A. R. Ade et al. “Planck 2013 results. XVI. Cosmological parameters”. In: *Astron. Astrophys.* 571 (2014), A16. DOI: 10.1051/0004-6361/201321591. arXiv: 1303.5076 [astro-ph.CO].
- [396] Liang Dai and Tejaswi Venumadhav. “On the waveforms of gravitationally lensed gravitational waves”. In: (Feb. 2017). arXiv: 1702.04724 [gr-qc].
- [397] C. Messenger and J. Read. “Measuring a cosmological distance-redshift relationship using only gravitational wave observations of binary neutron star coalescences”. In: *Phys. Rev. Lett.* 108 (2012), p. 091101. DOI: 10.1103/PhysRevLett.108.091101. arXiv: 1107.5725 [gr-qc].
- [398] Roger Blandford and Ramesh Narayan. “Fermat’s principle, caustics, and the classification of gravitational lens images”. In: *Astrophys. J.* 310 (1986), pp. 568–582. DOI: 10.1086/164709.

- 
- [399] L. Engvik, G. Bao, M. Hjorth-Jensen, et al. “Asymmetric nuclear matter and neutron star properties”. In: *Astrophys. J.* 469 (1996), p. 794. DOI: 10.1086/177827. arXiv: nucl-th/9509016.
- [400] Iair Arcavi et al. “Optical Follow-up of Gravitational-wave Events with Las Cumbres Observatory”. In: *Astrophys. J. Lett.* 848.2 (2017), p. L33. DOI: 10.3847/2041-8213/aa910f. arXiv: 1710.05842 [astro-ph.HE].
- [401] G. Hallinan et al. “A Radio Counterpart to a Neutron Star Merger”. In: *Science* 358 (2017), p. 1579. DOI: 10.1126/science.aap9855. arXiv: 1710.05435 [astro-ph.HE].
- [402] A. Murguia-Berthier et al. “A Neutron Star Binary Merger Model for GW170817/GRB 170817A/SSS17a”. In: *Astrophys. J. Lett.* 848.2 (2017), p. L34. DOI: 10.3847/2041-8213/aa91b3. arXiv: 1710.05453 [astro-ph.HE].
- [403] M. Soares-Santos et al. “The Electromagnetic Counterpart of the Binary Neutron Star Merger LIGO/Virgo GW170817. I. Discovery of the Optical Counterpart Using the Dark Energy Camera”. In: *Astrophys. J. Lett.* 848.2 (2017), p. L16. DOI: 10.3847/2041-8213/aa9059. arXiv: 1710.05459 [astro-ph.HE].
- [404] Keith C. Gendreau, Zaven Arzoumanian, and Takashi Okajima. “The Neutron star Interior Composition Explorer (NICER): an Explorer mission of opportunity for soft x-ray timing spectroscopy”. In: *Space Telescopes and Instrumentation 2012: Ultraviolet to Gamma Ray*. Ed. by Tadayuki Takahashi, Stephen S. Murray, and Jan-Willem A. den Herder. Vol. 8443. International Society for Optics and Photonics. SPIE, 2012, pp. 322–329. DOI: 10.1117/12.926396. URL: <https://doi.org/10.1117/12.926396>.
- [405] Kai Liao, Xi-Long Fan, Xu-Heng Ding, et al. “Precision cosmology from future lensed gravitational wave and electromagnetic signals”. In: *Nature Commun.* 8.1 (2017). [Erratum: *Nature Commun.* 8, 2136 (2017)], p. 1148. DOI: 10.1038/s41467-017-01152-9. arXiv: 1703.04151 [astro-ph.CO].
- [406] G. P. Smith, M. Bianconi, M. Jauzac, et al. “Deep and rapid observations of strong-lensing galaxy clusters within the sky localization of GW170814”. In: *Mon. Not. Roy. Astron. Soc.* 485.4 (2019), pp. 5180–5191. DOI: 10.1093/mnras/stz675. arXiv: 1805.07370 [astro-ph.HE].
- [407] B. P. Abbott et al. “Observation of Gravitational Waves from a Binary Black Hole Merger”. In: *Centennial of General Relativity: A Celebration*. Ed. by César Augusto Zen Vasconcellos. 2017, pp. 291–311. DOI: 10.1142/9789814699662\_0011.
- [408] Benjamin P. Abbott et al. “GW170104: Observation of a 50-Solar-Mass Binary Black Hole Coalescence at Redshift 0.2”. In: *Phys. Rev. Lett.* 118.22 (2017). [Erratum: *Phys.Rev.Lett.* 121, 129901 (2018)], p. 221101. DOI: 10.1103/PhysRevLett.118.221101. arXiv: 1706.01812 [gr-qc].
- [409] B. . P. . Abbott et al. “GW170608: Observation of a 19-solar-mass Binary Black Hole Coalescence”. In: *Astrophys. J. Lett.* 851 (2017), p. L35. DOI: 10.3847/2041-8213/aa9f0c. arXiv: 1711.05578 [astro-ph.HE].

## BIBLIOGRAPHY

---

- [410] Alexander H. Nitz, Collin Capano, Alex B. Nielsen, et al. “1-OGC: The first open gravitational-wave catalog of binary mergers from analysis of public Advanced LIGO data”. In: *Astrophys. J.* 872.2 (2019), p. 195. DOI: 10.3847/1538-4357/ab0108. arXiv: 1811.01921 [gr-qc].
- [411] Tejaswi Venumadhav, Barak Zackay, Javier Roulet, et al. “New search pipeline for compact binary mergers: Results for binary black holes in the first observing run of Advanced LIGO”. In: *Phys. Rev. D* 100.2 (2019), p. 023011. DOI: 10.1103/PhysRevD.100.023011. arXiv: 1902.10341 [astro-ph.IM].
- [412] Tejaswi Venumadhav, Barak Zackay, Javier Roulet, et al. “New binary black hole mergers in the second observing run of Advanced LIGO and Advanced Virgo”. In: *Phys. Rev. D* 101.8 (2020), p. 083030. DOI: 10.1103/PhysRevD.101.083030. arXiv: 1904.07214 [astro-ph.HE].
- [413] Maximiliano Isi and Alan J. Weinstein. “Probing gravitational wave polarizations with signals from compact binary coalescences”. In: (Oct. 2017). arXiv: 1710.03794 [gr-qc].
- [414] B. P. Abbott et al. “GW170814: A Three-Detector Observation of Gravitational Waves from a Binary Black Hole Coalescence”. In: *Phys. Rev. Lett.* 119.14 (2017), p. 141101. DOI: 10.1103/PhysRevLett.119.141101. arXiv: 1709.09660 [gr-qc].
- [415] D. M. Eardley, D. L. Lee, and A. P. Lightman. “Gravitational-wave observations as a tool for testing relativistic gravity”. In: *Phys. Rev. D* 8 (1973), pp. 3308–3321. DOI: 10.1103/PhysRevD.8.3308.
- [416] Y. Guersel and M. Tinto. “Near optimal solution to the inverse problem for gravitational wave bursts”. In: *Phys. Rev. D* 40 (1989), pp. 3884–3938. DOI: 10.1103/PhysRevD.40.3884.
- [417] Linqing Wen and Bernard F Schutz. “Coherent network detection of gravitational waves: The Redundancy veto”. In: *Class. Quant. Grav.* 22 (2005). Ed. by B. Mours and F. Marion, S1321–S1336. DOI: 10.1088/0264-9381/22/18/S46. arXiv: gr-qc/0508042.
- [418] Parameswaran Ajith, M. Hewitson, and I. S. Heng. “Null-stream veto for two co-located detectors: Implementation issues”. In: *Class. Quant. Grav.* 23 (2006). Ed. by M. Diaz and S. Mohanty, S741–S749. DOI: 10.1088/0264-9381/23/19/S13. arXiv: gr-qc/0604004.
- [419] Shourov Chatterji, Albert Lazzarini, Leo Stein, et al. “Coherent network analysis technique for discriminating gravitational-wave bursts from instrumental noise”. In: *Phys. Rev. D* 74 (2006), p. 082005. DOI: 10.1103/PhysRevD.74.082005. arXiv: gr-qc/0605002.
- [420] A. Freise, S. Chelkowski, S. Hild, et al. “Triple Michelson Interferometer for a Third-Generation Gravitational Wave Detector”. In: *Class. Quant. Grav.* 26 (2009), p. 085012. DOI: 10.1088/0264-9381/26/8/085012. arXiv: 0804.1036 [gr-qc].
- [421] Tania Regimbau et al. “A Mock Data Challenge for the Einstein Gravitational-Wave Telescope”. In: *Phys. Rev. D* 86 (2012), p. 122001. DOI: 10.1103/PhysRevD.86.122001. arXiv: 1201.3563 [gr-qc].



- 
- [422] Patrick J. Sutton et al. “X-Pipeline: An Analysis package for autonomous gravitational-wave burst searches”. In: *New J. Phys.* 12 (2010), p. 053034. DOI: 10.1088/1367-2630/12/5/053034. arXiv: 0908.3665 [gr-qc].
- [423] Kazuhiro Hayama and Atsushi Nishizawa. “Model-independent test of gravity with a network of ground-based gravitational-wave detectors”. In: *Phys. Rev. D* 87.6 (2013), p. 062003. DOI: 10.1103/PhysRevD.87.062003. arXiv: 1208.4596 [gr-qc].
- [424] Chris Van Den Broeck. “Probing dynamical spacetimes with gravitational waves”. In: *Springer Handbook of Spacetime*. Ed. by Abhay Ashtekar and Vesselin Petkov. 2014, pp. 589–613. DOI: 10.1007/978-3-642-41992-8\_27. arXiv: 1301.7291 [gr-qc].
- [425] Yuki Hagihara, Naoya Era, Daisuke Iikawa, et al. “Probing gravitational wave polarizations with Advanced LIGO, Advanced Virgo and KAGRA”. In: *Phys. Rev. D* 98.6 (2018), p. 064035. DOI: 10.1103/PhysRevD.98.064035. arXiv: 1807.07234 [gr-qc].
- [426] Yuki Hagihara, Naoya Era, Daisuke Iikawa, et al. “Constraining extra gravitational wave polarizations with Advanced LIGO, Advanced Virgo and KAGRA and upper bounds from GW170817”. In: *Phys. Rev. D* 100.6 (2019), p. 064010. DOI: 10.1103/PhysRevD.100.064010. arXiv: 1904.02300 [gr-qc].
- [427] Yuki Hagihara, Naoya Era, Daisuke Iikawa, et al. “Condition for directly testing scalar modes of gravitational waves by four detectors”. In: *Phys. Rev. D* 101.4 (2020), p. 041501. DOI: 10.1103/PhysRevD.101.041501. arXiv: 1912.06340 [gr-qc].
- [428] Yoichi Aso, Yuta Michimura, Kentaro Somiya, et al. “Interferometer design of the KAGRA gravitational wave detector”. In: *Phys. Rev. D* 88.4 (2013), p. 043007. DOI: 10.1103/PhysRevD.88.043007. arXiv: 1306.6747 [gr-qc].
- [429] B. Iyer et al. *LIGO India*. Tech. rep. LIGO-M1100296. <https://dcc.ligo.org/LIGO-M1100296/public>. 2011.
- [430] Eric Poisson and Clifford M Will. *Gravity: Newtonian, Post-Newtonian, Relativistic*. Cambridge, England: Cambridge University Press, May 2014.
- [431] V. Necula, S. Klimentenko, and G. Mitselmakher. “Transient analysis with fast Wilson-Daubechies time-frequency transform”. In: *J. Phys. Conf. Ser.* 363 (2012). Ed. by Mark Hannam, Patrick Sutton, Stefan Hild, et al., p. 012032. DOI: 10.1088/1742-6596/363/1/012032.
- [432] Ronald Fisher. *Statistical methods for research workers*. Darien, Conn: Hafner Pub. Co, 1970. ISBN: 0-05-002170-2.
- [433] Michele Vallisneri, Jonah Kanner, Roy Williams, et al. “The LIGO Open Science Center”. In: *J. Phys. Conf. Ser.* 610.1 (2015). Ed. by Giacomo Ciani, John W. Conklin, and Guido Mueller, p. 012021. DOI: 10.1088/1742-6596/610/1/012021. arXiv: 1410.4839 [gr-qc].
- [434] Chris Kouvaris and Niklas Grønlund Nielsen. “Asymmetric Dark Matter Stars”. In: *Phys. Rev. D* 92.6 (2015), p. 063526. DOI: 10.1103/PhysRevD.92.063526. arXiv: 1507.00959 [hep-ph].

## BIBLIOGRAPHY

---

- [435] Steven L. Liebling and Carlos Palenzuela. “Dynamical Boson Stars”. In: *Living Rev. Rel.* 15 (2012), p. 6. DOI: 10.12942/lrr-2012-6. arXiv: 1202.5809 [gr-qc].
- [436] P. O. Mazur and E. Mottola. “Dark energy and condensate stars: A quantum alternative to classical black holes”. In: *10th Marcel Grossmann Meeting on Recent Developments in Theoretical and Experimental General Relativity, Gravitation and Relativistic Field Theories (MG X MMIII)*. July 2003, pp. 1041–1047.
- [437] Ahmed Almheiri, Donald Marolf, Joseph Polchinski, et al. “Black Holes: Complementarity or Firewalls?” In: *JHEP* 02 (2013), p. 062. DOI: 10.1007/JHEP02(2013)062. arXiv: 1207.3123 [hep-th].
- [438] Oleg Lunin and Samir D. Mathur. “AdS / CFT duality and the black hole information paradox”. In: *Nucl. Phys. B* 623 (2002), pp. 342–394. DOI: 10.1016/S0550-3213(01)00620-4. arXiv: hep-th/0109154.
- [439] Leor Barack et al. “Black holes, gravitational waves and fundamental physics: a roadmap”. In: *Class. Quant. Grav.* 36.14 (2019), p. 143001. DOI: 10.1088/1361-6382/ab0587. arXiv: 1806.05195 [gr-qc].
- [440] Vitor Cardoso, Edgardo Franzin, Andrea Maselli, et al. “Testing strong-field gravity with tidal Love numbers”. In: *Phys. Rev. D* 95.8 (2017). [Addendum: *Phys.Rev.D* 95, 089901 (2017)], p. 084014. DOI: 10.1103/PhysRevD.95.084014. arXiv: 1701.01116 [gr-qc].
- [441] Nathan K. Johnson-Mcdaniel, Arunava Mukherjee, Rahul Kashyap, et al. “Constraining black hole mimickers with gravitational wave observations”. In: *Phys. Rev. D* 102 (2020), p. 123010. DOI: 10.1103/PhysRevD.102.123010. arXiv: 1804.08026 [gr-qc].
- [442] Daniel Baumann, Horng Sheng Chia, and Rafael A. Porto. “Probing Ultralight Bosons with Binary Black Holes”. In: *Phys. Rev. D* 99.4 (2019), p. 044001. DOI: 10.1103/PhysRevD.99.044001. arXiv: 1804.03208 [gr-qc].
- [443] Gregorio Carullo et al. “Empirical tests of the black hole no-hair conjecture using gravitational-wave observations”. In: *Phys. Rev. D* 98.10 (2018), p. 104020. DOI: 10.1103/PhysRevD.98.104020. arXiv: 1805.04760 [gr-qc].
- [444] Richard Brito, Alessandra Buonanno, and Vivien Raymond. “Black-hole Spectroscopy by Making Full Use of Gravitational-Wave Modeling”. In: *Phys. Rev. D* 98.8 (2018), p. 084038. DOI: 10.1103/PhysRevD.98.084038. arXiv: 1805.00293 [gr-qc].
- [445] Vitor Cardoso, Edgardo Franzin, and Paolo Pani. “Is the gravitational-wave ringdown a probe of the event horizon?” In: *Phys. Rev. Lett.* 116.17 (2016). [Erratum: *Phys.Rev.Lett.* 117, 089902 (2016)], p. 171101. DOI: 10.1103/PhysRevLett.116.171101. arXiv: 1602.07309 [gr-qc].
- [446] Vitor Cardoso, Seth Hopper, Caio F. B. Macedo, et al. “Gravitational-wave signatures of exotic compact objects and of quantum corrections at the horizon scale”. In: *Phys. Rev. D* 94.8 (2016), p. 084031. DOI: 10.1103/PhysRevD.94.084031. arXiv: 1608.08637 [gr-qc].

- [447] Vitor Cardoso and Paolo Pani. “Tests for the existence of black holes through gravitational wave echoes”. In: *Nature Astron.* 1.9 (2017), pp. 586–591. DOI: 10.1038/s41550-017-0225-y. arXiv: 1709.01525 [gr-qc].
- [448] Vitor Cardoso, Valentino F. Foit, and Matthew Kleban. “Gravitational wave echoes from black hole area quantization”. In: *JCAP* 08 (2019), p. 006. DOI: 10.1088/1475-7516/2019/08/006. arXiv: 1902.10164 [hep-th].
- [449] Baoyi Chen, Yanbei Chen, Yiqiu Ma, et al. “Instability of Exotic Compact Objects and Its Implications for Gravitational-Wave Echoes”. In: (Feb. 2019). arXiv: 1902.08180 [gr-qc].
- [450] Andrea Addazi, Antonino Marcianò, and Nicolás Yunes. “Gravitational Instability of Exotic Compact Objects”. In: *Eur. Phys. J. C* 80.1 (2020), p. 36. DOI: 10.1140/epjc/s10052-019-7575-9. arXiv: 1905.08734 [gr-qc].
- [451] Vitor Cardoso and Paolo Pani. “The observational evidence for horizons: from echoes to precision gravitational-wave physics”. In: (July 2017). arXiv: 1707.03021 [gr-qc].
- [452] Vitor Cardoso and Paolo Pani. “Testing the nature of dark compact objects: a status report”. In: *Living Rev. Rel.* 22.1 (2019), p. 4. DOI: 10.1007/s41114-019-0020-4. arXiv: 1904.05363 [gr-qc].
- [453] Kostas D. Kokkotas and Gerhard Schaefer. “Tidal and tidal resonant effects in coalescing binaries”. In: *Mon. Not. Roy. Astron. Soc.* 275 (1995), p. 301. DOI: 10.1093/mnras/275.2.301. arXiv: gr-qc/9502034.
- [454] Dong Lai. “Resonant oscillations and tidal heating in coalescing binary neutron stars”. In: *Mon. Not. Roy. Astron. Soc.* 270 (1994), p. 611. DOI: 10.1093/mnras/270.3.611. arXiv: astro-ph/9404062.
- [455] Masaru Shibata. “Effects of tidal resonances in coalescing compact binary systems”. In: *Prog. Theor. Phys.* 91 (1994), pp. 871–884. DOI: 10.1143/PTP.91.871.
- [456] Eanna E. Flanagan and Etienne Racine. “Gravitomagnetic resonant excitation of Rossby modes in coalescing neutron star binaries”. In: *Phys. Rev. D* 75 (2007), p. 044001. DOI: 10.1103/PhysRevD.75.044001. arXiv: gr-qc/0601029.
- [457] Hang Yu and Nevin N. Weinberg. “Resonant tidal excitation of superfluid neutron stars in coalescing binaries”. In: *Mon. Not. Roy. Astron. Soc.* 464.3 (2017), pp. 2622–2637. DOI: 10.1093/mnras/stw2552. arXiv: 1610.00745 [astro-ph.HE].
- [458] Caio F. B. Macedo, Paolo Pani, Vitor Cardoso, et al. “Into the lair: gravitational-wave signatures of dark matter”. In: *Astrophys. J.* 774 (2013), p. 48. DOI: 10.1088/0004-637X/774/1/48. arXiv: 1302.2646 [gr-qc].
- [459] Caio F. B. Macedo, Paolo Pani, Vitor Cardoso, et al. “Astrophysical signatures of boson stars: quasinormal modes and inspiral resonances”. In: *Phys. Rev. D* 88.6 (2013), p. 064046. DOI: 10.1103/PhysRevD.88.064046. arXiv: 1307.4812 [gr-qc].
- [460] Vitor Cardoso, Adrian del Rio, and Masashi Kimura. “Distinguishing black holes from horizonless objects through the excitation of resonances during inspiral”. In: *Phys. Rev. D* 100 (2019). [Erratum: Phys.Rev.D 101, 069902 (2020)], p. 084046. DOI: 10.1103/PhysRevD.100.084046. arXiv: 1907.01561 [gr-qc].

## BIBLIOGRAPHY

---

- [461] LIGO Scientific Collaboration and Virgo Collaboration. <https://www.gw-openscience.org/01/>. 2018.
- [462] LIGO Scientific Collaboration and Virgo Collaboration. <https://www.gw-openscience.org/02/>. 2019.
- [463] LIGO Scientific Collaboration and Virgo Collaboration. <https://www.gw-openscience.org/GWTC-1/>. 2019.
- [464] Prakash Balachandran and Eanna E. Flanagan. “Detectability of mode resonances in coalescing neutron star binaries”. In: (Jan. 2007). arXiv: [gr-qc/0701076](https://arxiv.org/abs/gr-qc/0701076).
- [465] Eric Poisson. “Gravitomagnetic tidal resonance in neutron-star binary inspirals”. In: *Phys. Rev. D* 101.10 (2020), p. 104028. DOI: [10.1103/PhysRevD.101.104028](https://doi.org/10.1103/PhysRevD.101.104028). arXiv: [2003.10427](https://arxiv.org/abs/2003.10427) [[gr-qc](#)].
- [466] Peter T. H. Pang et al. “NMMA: A nuclear-physics and multi-messenger astrophysics framework to analyze binary neutron star mergers”. In: (May 2022). arXiv: [2205.08513](https://arxiv.org/abs/2205.08513) [[astro-ph.HE](#)].
- [467] Pawan Kumar Gupta, Anna Puecher, Peter T. H. Pang, et al. “Determining the equation of state of neutron stars with Einstein Telescope using tidal effects and r-mode excitations from a population of binary inspirals”. In: (May 2022). arXiv: [2205.01182](https://arxiv.org/abs/2205.01182) [[gr-qc](#)].
- [468] Nina Kunert, Peter T. H. Pang, Ingo Tews, et al. “Quantifying modeling uncertainties when combining multiple gravitational-wave detections from binary neutron star sources”. In: *Phys. Rev. D* 105.6 (2022), p. L061301. DOI: [10.1103/PhysRevD.105.L061301](https://doi.org/10.1103/PhysRevD.105.L061301). arXiv: [2110.11835](https://arxiv.org/abs/2110.11835) [[astro-ph.HE](#)].
- [469] Pawan Kumar Gupta, Thomas F. M. Spiekma, Peter T. H. Pang, et al. “Bounding dark charges on binary black holes using gravitational waves”. In: *Phys. Rev. D* 104.6 (2021), p. 063041. DOI: [10.1103/PhysRevD.104.063041](https://doi.org/10.1103/PhysRevD.104.063041). arXiv: [2107.12111](https://arxiv.org/abs/2107.12111) [[gr-qc](#)].
- [470] Isaac C. F. Wong, Peter T. H. Pang, Rico K. L. Lo, et al. “Null-stream-based Bayesian Unmodeled Framework to Probe Generic Gravitational-wave Polarizations”. In: (May 2021). arXiv: [2105.09485](https://arxiv.org/abs/2105.09485) [[gr-qc](#)].
- [471] Tomas Ahumada et al. “Discovery and confirmation of the shortest gamma-ray burst from a collapsar”. In: *Nature Astron.* 5.9 (2021), pp. 917–927. DOI: [10.1038/s41550-021-01428-7](https://doi.org/10.1038/s41550-021-01428-7). arXiv: [2105.05067](https://arxiv.org/abs/2105.05067) [[astro-ph.HE](#)].
- [472] Igor Andreoni et al. “Fast-transient Searches in Real Time with ZTFReST: Identification of Three Optically Discovered Gamma-Ray Burst Afterglows and New Constraints on the Kilonova Rate”. In: *Astrophys. J.* 918.2 (2021), p. 63. DOI: [10.3847/1538-4357/ac0bc7](https://doi.org/10.3847/1538-4357/ac0bc7). arXiv: [2104.06352](https://arxiv.org/abs/2104.06352) [[astro-ph.HE](#)].
- [473] Peter T. H. Pang, Juan Calderón Bustillo, Yifan Wang, et al. “Potential observations of false deviations from general relativity in gravitational wave signals from binary black holes”. In: *Phys. Rev. D* 98.2 (2018), p. 024019. DOI: [10.1103/PhysRevD.98.024019](https://doi.org/10.1103/PhysRevD.98.024019). arXiv: [1802.03306](https://arxiv.org/abs/1802.03306) [[gr-qc](#)].

- [474] Peter T. H. Pang and Tjonnie G. F. Li. “Prospects of Constraining the Nuclear Equation of State with Gravitational-Wave Signals in the Advanced Detector Era and Beyond”. In: *JPS Conf. Proc.* 20 (2018). Ed. by Toshitaka Tatsumi, Toshiki Maruyama, and Takumi Muto, p. 011048. DOI: 10.7566/JPSCP.20.011048.
- [475] Peter T. H. Pang and Tjonnie G. F. Li. “Phenomenological Model of Hyper-Massive Neutron Star Phase Gravitational Wave of Binary Neutron Star”. In: *JPS Conf. Proc.* 20 (2018). Ed. by Toshitaka Tatsumi, Toshiki Maruyama, and Takumi Muto, p. 011052. DOI: 10.7566/JPSCP.20.011052.